The Magnetic Quadrupole Transition in Neutral Strontium

Jan Trautmann

München 2022

The Magnetic Quadrupole Transition in Neutral Strontium

Dissertation an der Fakultät für Physik
Ludwig-Maximilians-Universität München

vorgelegt von

Jan Trautmann

aus Bensheim

München, den 07. September 2022

Tag der mündlichen Prüfung: 20. Oktober 2022
Erstgutachter: Prof. Immanuel Bloch
Zweitgutachter: Prof. Thomas Udem
Weitere Prüfungskommissionsmitglieder: Prof. Jan von Delft, Prof. Rudolf Gross

Zusammenfassung

Analoge Quantensimulatoren ermöglichen die experimentelle Untersuchung von stark wechselwirkenden Quantenvielteilchensystemen, die auf klassischen Computern nicht mehr numerisch berechnet werden können. Eine bemerkenswert erfolgreiche Erfindung bei der Entwicklung dieser Simulatoren ist das Quantengasmikroskop. Diese Mikroskope mit hoher numerischer Apertur ermöglichen es ultrakalte Atome in optischen Gittern zu detektieren und können dabei einzelne Gitterplätze auflösen. Bisher verwenden die meisten Experimente mit Quantengasmikroskopen Alkaliatome, jedoch zielen kürzlich realisierte Experimente darauf ab, die besonderen Eigenschaften von Erdalkaliatomen zu nutzen.

Erdalkaliatome besitzen zwei Valenzelektronen, was zu einer vielfältigen Struktur atomarer Zustände mit Singulett- und metastabilen Triplettzuständen führt. Diese Atomstruktur beinhaltet ultraschmale Interkombinationsübergänge im optischen Bereich, die zahlreiche Anwendungen in den Quantenwissenschaften finden. Die bekannteste Anwendung von Strontium ist die optische Gitteruhr, die auf dem $^1S_0$-$^3P_0$-Übergang basiert. Diese Erfolgsgeschichte trieb kürzlich Entwicklungen im Bereich der Quantensimulation und Quantencomputer voran, die die metastabilen Zustände und die im Sekundenbereich liegenden Kohärenzzeiten nutzen.

Unser Ansatz besteht darin, stark zustandsabhängige optische Gitter für die Grund- und metastabilen Triplettzustände zu erzeugen und die darin auftretenden Quantenvielteilchenphänomene mit einem Quantengasmikroskop zu untersuchen. Erdalkaliatome unter einem Quantengasmikroskop zu verwenden, erfordert es Atome oder Qubits lokal auslesen oder manipulieren zu können. Dieses Adressieren kann man dadurch erreichen, dass ein optischer Strahl mit dem Mikroskop fokussiert wird. Die beugungsbegrenzte Auflösung führt jedoch dazu, dass benachbarte Gitterplätze ebenfalls angesprochen werden. Durch die Verwendung von Magnetfeldgradienten in Kombination mit magnetfeldempfindlichen Übergängen kann die Auflösung über die Beugungsgrenze hinaus gesteigert werden. Dadurch können der Spin oder der elektronische Zustand der Atome auf den gewünschten Gitterplätzen innerhalb eines größeren Systems von Hunderten von Atomen verändert werden. Lokales Adressieren von Strontiumatomen zu realisieren ist technisch anspruchsvoll, da die meisten magnetfeldempfindlichen Übergänge zu breit sind. Eine vielversprechende Lösung ist den Millihertz breiten und magnetisch sensitiven $^1S_0$-$^3P_2$ magnetischen Quadrupolübergang zu verwenden, der durch seine schmale Linienbreite eine hervorragende Frequenzdiskriminierung selbst bei moderate Magnetfeldgradienten aufweist. Obwohl dieser Übergang einzigartige Anwendungen ermöglicht, wurden viele Eigenschaften des Übergangs, wie die exakte Übergangsfrequenz oder das Fallenpotential des $^3P_2$-Zustands, vor der in dieser Dissertation beschriebenen Arbeit nicht untersucht.

Diese Arbeit berichtet über die erste hochauflösende und dopplerfreie Laserspektroskopie des $^1S_0$-$^3P_2$-Übergangs mit Kilohertz-Präzision in einem optischen Gitter frei von Linienverschiebungen durch das Lichtfeld. Wir unterdrücken die Linienverschiebung, indem wir die Vektor- und Tensorpolarisierbarkeit des angeregten $^3P_2$-Zustands einstellen.

Wir messen die absolute Übergangsfrequenz mit drei Größenordnungen kleineren Fehlerbalken als alle Messungen zuvor. Abschließend zeigen wir lokales Adressieren im optischen Gitter unter Verwendung des $^1S_0$-$^3P_2$-Übergangs. Dies ist ein erster entscheidender Schritt auf dem Weg zur Kontrolle einzelner Atome unter dem Quantengasmikroskop. Das Adressieren wird es uns in naher Zukunft ermöglichen, eine einzelne Ebene des optischen Gitters im Fokus des ersten Strontium-Quantengasmikroskops zu isolieren.

Die demonstrierte experimentelle Kontrolle über den $^1S_0$-$^3P_2$-Übergang ebnet den Weg, das entsprechende optische Qubit in Quantencomputern mit neutralen Atomen zu verwenden, bei denen einzelne Qubits lokal manipuliert und ausgelesen werden können.

Abstract

Analog quantum simulators enable the experimental investigation of strongly interacting quantum many-body systems, for which numerical calculations are often out of reach for classical computers. One remarkably successful invention in the development of these simulators is the quantum gas microscope. These high-numerical-aperture microscopes enable the detection of ultracold atoms in optical lattices and can resolve individual lattice sites. Until now, most quantum gas microscope experiments use alkali atoms, but recent experiments aim to make use of the special properties of alkaline earth atoms.

Alkaline earth atoms possess two valence electrons, giving rise to a rich electronic-level structure featuring singlet and metastable triplet states. This internal structure results in ultranarrow optical intercombination transitions, opening up numerous applications in quantum sciences. The most prominent application of strontium is the optical lattice clock based on the $^1S_0$-$^3P_0$ transition. Based on this success story, there has been a recent effort to use the metastable states and the achieved second-scale coherence time for quantum computing and quantum simulation.

Our approach is to implement highly state-dependent optical lattices for the ground and metastable triplet states and to study the emerging quantum many-body phenomena using a quantum gas microscope. Working with alkaline earth atoms under a quantum gas microscope requires developing local readout and manipulation of atoms or qubits. This addressing can be realized by focusing an optical beam through the microscope. However, the diffraction-limited resolution results in cross-talk between adjacent lattice sites. The addressing resolution can be enhanced beyond the diffraction limit by applying magnetic field gradients in combination with magnetic-field-sensitive transitions. Doing so allows controlling the atoms' spin or electronic state on dedicated lattice sites within a larger sample of hundreds of atoms. Implementing local addressability for strontium atoms is technically challenging since most magnetic-field-sensitive transitions are too broad. A promising solution is to use the millihertz-wide and magnetically-sensitive $^1S_0$-$^3P_2$ magnetic quadrupole transition, which features excellent frequency discrimination for even moderate magnetic field gradients due to its narrow linewidth. Although this transition opens up unique applications, many of the key features of the transition, such as the exact transition frequency, or the $^3P_2$ state's trapping potential have not been investigated prior to the work described in this thesis.

This thesis reports on the first high-resolution and Doppler-free laser spectroscopy of the $^1S_0$-$^3P_2$ transition with kilohertz precision in a light-shift-compensated optical lattice. We engineer the light-shift-free lattice by tuning the vector and tensor polarizability of the excited $^3P_2$ state. We measure the absolute transition frequency with an improvement of three orders of magnitude compared to previously reported values. Finally, we demonstrate local addressing on the $^1S_0$-$^3P_2$ transition in the optical lattice, a first crucial step towards single-particle control under the quantum gas microscope. In the near future, the addressing will allow us to isolate a single layer of the optical lattice in the focus of the first strontium quantum gas microscope.

The demonstrated experimental control over the $^1S_0$-$^3P_2$ transition paves the way to

use the corresponding optical qubit for neutral atom quantum computation, where single qubits can be locally manipulated and read out.

Contents

List of Tables

List of Figures

Chapter 1

Introduction

Understanding systems of many interacting quantum particles is one of the major outstanding challenges in quantum physics. Such systems can be found in many research areas like unconventional superconductors [1], quantum chemistry [2], or the quantum mechanical states of a nucleon [3]. The many-body interactions in these systems determine their physical properties.

In quantum mechanics, the number of possible states scales exponentially with the number of particles in the system. Due to this scaling, calculating or simulating quantum many-body systems quickly becomes prohibitively difficult to impossible on classical computers. Richard Feynman offered a solution to this problem by proposing to use a well-controllable quantum system to simulate the more "inaccessible" quantum system of interest [4, 5].

The developments in cooling and trapping neutral atoms [6–8] allow to prepare bosonic and fermionic atoms at ultracold temperatures and to use their interactions for quantum simulations [9]. At ultracold temperatures, atoms stop behaving like classical particles and enter the regime of quantum mechanics, where atoms can form quantum degenerate states of matter such as Bose-Einstein condensates [10, 11] and degenerate Fermi gases [12].

However, cooling atoms to ultracold temperatures is only the starting point for most quantum simulation experiments. Simulating quantum systems also requires the ability to engineer the interactions between the constituent particles to enter the regime of strongly correlated quantum systems. One approach to directly control the interatomic interactions is using Feshbach resonances [13]. This technique was used to realize strongly interacting ultracold Bose [14] and Fermi gases [15]. Various experiments exploited Feshbach resonances to study the pairing of fermions in the BEC to BCS crossover regime [16–18], which possesses analogies to the pairing mechanisms of electrons in superconductors [19]. Another very successful approach to realizing strongly-correlated quantum gases is trapping ultracold atoms in an optical lattice [20]. Using optical lattices one can tune the ratio of the atoms' kinetic to the on-site interaction by adjusting the lattice depth. If the on-site interaction dominates the energy scales, the atoms trapped in the lattice enter the strongly-correlated regime. For increasing lattice depth the kinetic energy given the tunneling energy decreases while the on-site interaction increases. This behavior has been demonstrated by observing a phase transition between the weakly interacting superfluid and the strongly interacting Mott insulator phase in an optical lattice [21]. The excellent control over ultracold atoms and their isolation from the envi-

ronment make ultracold quantum gases in optical lattices an ideal platform for quantum simulation [20, 22–24].

Experimentally studying strongly correlated systems of ultracold atoms requires suitable detection methods. Typically, the atoms are imaged after their release from the trap, giving access to the momentum distribution [25] containing information about the initial quantum state [20]. Absorption or fluorescence imaging techniques allow detection of the in situ density distribution. However, the resolution of these techniques are insufficient to measure observables on the scale of a few lattice sites preventing one from obtaining the full information about the quantum state.

Obtaining the full information about a quantum many-body system requires detecting each of the constituents [26]. For ultracold atoms, this detection can be achieved by confining atoms in deep optical lattices and taking fluorescence images through a microscope objective with a high numerical aperture resulting in images that resolve individual lattice sites [27–36]. These systems are known as quantum gas microscopes. The single-site resolution enables the detection of quantum fluctuations and measuring local density-density correlations characterizing the quantum many-body system. Combining the high resolution with spin-sensitive imaging gives access to spin correlations. Hence, quantum gas microscope experiments are very well suited to experimentally investigate strongly correlated quantum systems such as the Bose-Hubbard or Fermi-Hubbard model [24, 37, 38]. Using the microscopes, one can fully access the quantum statistics [28], detect excitations [39] and investigate local dynamics [40]. These experiments were extremely successful in studying entanglement entropy [41], antiferromagnetic spin correlations [42, 43] and many more phenomena, see e.g., Refs. [44–48].

Until now, most quantum gas microscope experiments use alkali atoms, but recent experiments aim to make use of the special properties of alkaline earth atoms. Alkaline-earth atoms also have applications in quantum technologies like metrology and quantum computing. In the following, we will discuss these applications.

Quantum technologies with ultracold strontium

We briefly introduce alkaline-earth atomic clocks and discuss the properties of these elements concerning their application in quantum simulation and quantum computation. Afterwards, we discuss how we will use strontium atoms in optical lattices to simulate open quantum systems.

Metrology Alkaline-earth atoms have two valence electrons where the electron spins can form singlet and triplet states. The presence of spin-singlet and triplet states results in a rich atomic-level structure depicted for strontium in Fig. 1.1. In strontium, the intercombination transition between the $^1S_0$ ground state and the $^3P_0$ excited state has an extremely narrow linewidth of $1.35(3)$ mHz [49] and a transition wavelength of 698 nm in the visible spectrum. Hence, the $^1S_0$-$^3P_0$ transition in strontium provides one of the highest atomic quality factors in nature with $6.5(1.1) \times 10^{16}$ [50, 51]. Moreover, due to

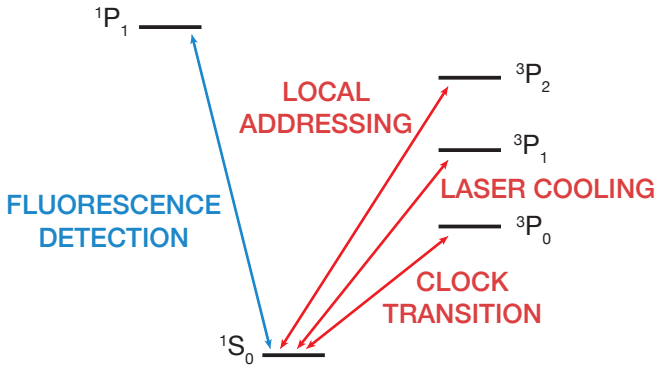

Fig. 1.1 Simplified electronic level structure of strontium. A detailed diagram of the level structure and corresponding transition properties can be found in Fig. 2.1.

this vanishing angular momentum, these states are insensitive to magnetic field fluctuations. The development of the optical frequency comb [52, 53], which provides a link between optical and radio frequencies, enables using such ultranarrow optical transitions for precision metrology.

Nowadays, the most precise atomic clocks are based on ultracold strontium atoms trapped in optical lattices [54, 55]. The lattice confinement results in many micro-traps for the atoms [56]. The individual atoms act as independent simultaneously interrogated oscillators. The simultaneous interrogation enables averaging their response and allows reaching a lower fractional uncertainty. Creating the lattices with light at the so-called *magic wavelength* minimizes the perturbing effects of the trapping potential. At this wavelength, the transition states have equal polarizability, resulting in a vanishing differential light shift and thus a vanishing shift of the transition frequency.

Very recently, strontium optical lattice clocks reached a precision with a fractional uncertainty of 7.6×10^{-21} [57, 58], enabling measurements of the gravitational red-shift over a distance of 1 mm. Further improving the accuracy and precision of optical clocks will enable testing of fundamental physics [57], such as the search for possible variations in the fundamental constants [59]. The spectral resolution of clock experiments also allows to study weak interactions in quantum many-body systems [60] like the dipole-dipole interaction of atoms in neighboring lattice sites [61].

Quantum computing Besides alkaline-earth atoms being used in optical atomic clocks, they also offer advantageous properties for quantum computing applications. One can encode a qubit in the $^1S_0$ ground state and the $^3P_0$ state. Due to the excited state's lifetime of 120 s and the insensitivity of both states to environmental effects, the $^1S_0$-$^3P_0$ qubit of strontium can have coherence times of several tens of seconds, as demonstrated in recent experiments [50, 51, 57, 58, 62]. Because the energy separation of the states is in the optical domain, the qubit is a so-called optical qubit. Optical qubits provide faster manipulation and detection schemes than hyperfine qubits [63–66], used in quantum

computing schemes with alkali atoms. In optical qubits, one can realize single-qubit gates with single-photon transitions, while hyperfine qubits require two-photon Raman transitions.

In neutral atom systems, one can realize multi-qubit gates via the interaction of Rydberg states [67]. In alkali atoms, the excitation to the Rydberg state is a two-photon process, where the spontaneous decay from the intermediate state shortens the coherence time [68]. An advantage of the optical qubit in alkaline-earth atoms is that the Rydberg excitation is a single-photon transition [69, 70], allowing long coherence times and fast qubit rotations.

The fermionic alkaline-earth isotopes have a non-vanishing nuclear spin. Due to the vanishing angular momentum of the $^1S_0$ state and the $^3P_0$ state, the nuclear spin is decoupled from the electronic structure [71]. This decoupling enables encoding qubits in the well-protected nuclear spin states [72–75] and allows manipulating the atom optically without influencing the qubit.

In alkaline-earth atoms, one can also encode information in the $^3P_0$-$^3P_2$ fine-structure states [76]. This qubit configuration offers faster single-qubit gates than the optical qubit. Additionally, the fine-structure qubit also allows fast, Rydberg-mediated two-qubit gates.

Several research groups have built quantum information experiments with neutral strontium and ytterbium atoms [77–81]. The capabilities already demonstrated in these experiments have led to many more quantum computing setups based on alkaline-earth atoms being currently constructed.

All current quantum information experiments using neutral atoms trap individual atoms in tightly focused laser beams, so-called optical tweezers. These tweezers offer microscopic control and detection similar to quantum gas microscopes [82] but at much larger atom distances of several µm. In addition, these platforms can run with roughly ten times higher repetition rates than quantum gas microscope experiments. However, the available laser power to generate the tweezers currently limits the system size to several hundreds of tweezers [83, 84]. Furthermore, the trap depths in a tweezer array are not as homogeneously distributed as in an optical lattice. Therefore, some new experiments are starting to combine tweezers and optical lattices by preparing the atoms in tweezer arrays and loading them into an optical lattice [85].

Quantum simulation The properties of alkaline-earth atoms also pave the way for novel analog quantum simulation schemes that go beyond the possibilities of alkali atoms. These simulations make use of the well-protected nuclear states [72] or the ability to generate state-dependent optical traps at several wavelengths [74, 86].

The decoupling of the nuclear spin in the fermionic isotopes from the electronic structure results in a scattering length and thus an interaction energy that is independent of the nuclear spin state [60]. Mathematically, this dependence leads to a system Hamiltonian with an SU(N) symmetry, where $N = 2I + 1 = 10$ for ^{87}Sr. For fermions, collisions between the same spin states are forbidden by the Pauli exclusion principle. These symmetric interactions can be used to simulate a wider range of many-body systems than possible with alkali atoms with two spin states [87]. For example the SU(N) symmetric

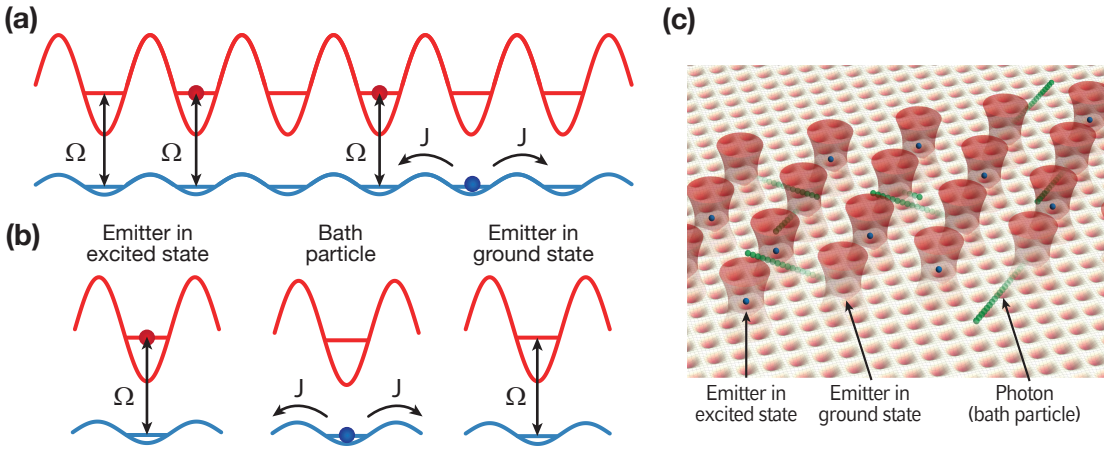

Fig. 1.2 Quantum simulation of light-matter interfaces (adapted from Ref. [94]). (a) The ground g (blue circles) and the excited state e (red circles) of strontium atoms are trapped in state-dependent lattices, where e experiences strong confinement, while g can tunnel through the lattice. The tunneling rate is described by the parameter J. A resonant laser beam can couple g and e with the coupling strength Ω. (b) Mapping between ultracold strontium atoms in state-dependent lattices and light-matter interactions. (c) Extending the simulation of light-matter interfaces to two dimensions. The beam coupling ground and excited state is depicted in red.

Mott insulator is predicted to give rise to exotic quantum magnetism [88–90]. A recent experiment investigated the thermodynamics of a degenerate SU($N = 10$)-symmetric Fermi gas using ultracold strontium atoms demonstrating enhanced interactions [91].

Because the $^1S_0$ ground state and the $^3P_0$ ($^3P_2$) metastable states are energetically separated by optical frequencies, the states' polarizabilities depend differently on the trapping light wavelength. Due to the different dependency, we can find wavelengths where the polarizability of one state vanishes while the other state has a finite polarizability. At these so-called tune-out wavelengths, we can realize highly state-dependent optical traps [92]. Due to the extremely narrow transition linewidths in strontium, the tune-out wavelengths are far detuned from atomic resonances, resulting in lower photon scattering rates than possible in state-dependent traps for Rb [93].

Quantum simulation of light-matter interfaces

Our experiment is mostly tailored toward using ultracold atoms in a state-dependent optical lattice to simulate strongly coupled light-matter interfaces [95] and open quantum systems [96–98]. Naturally, we can find such systems in the field of nanophotonics. The simulation using ultracold atoms allows us to study regimes that are difficult to realize in nanophotonic systems. The simulation requires a mapping between light-matter interactions and ultracold atoms, which we will discuss briefly in the following. We start by generating an optical lattice close to the ground state tune-out wavelength. This state-dependent lattice strongly confines the $^3P_1$ state (e) and only weakly traps the $^1S_0$ state

(g) as shown in Fig. 1.2(a). The strong confinement of e atoms results in the localization of these atoms in the lattice wells. Atoms in g experience a weak trapping potential, allowing them free propagation through the lattice with the tunneling parameter J. The absence (presence) of an e atom at a given lattices site maps to an emitter in its ground (excited state), playing the role of matter in the light-matter interactions as shown in Fig. 1.2(b). The moving g atoms map to bath particles and play the role of light. We realize the coupling of light and matter of strength Ω by driving the $^1S_0$-$^3P_0$ transition with a laser beam. The de-excitation from e to g results in a matter-wave emission. This emission corresponds to a photon emission in the nanophotonic system. Using two orthogonal state-dependent lattices, we can extend the simulations to two dimensions, as shown in Fig. 1.2(c).

Using the scheme above to simulate light-matter interfaces with ultracold atoms gives us control over various experimental parameters that are difficult to adjust in a nanophotonic system. We can tune the coupling strength between light and matter by varying the intensity of the $^1S_0$-$^3P_0$ laser beam. Choosing a laser detuning corresponding to a transition into the band gap of the optical lattice, we can simulate an atom-photon bound state [95]. In the simulation, this bound state is a trapped-untrapped atom bound state where the g atom remains exponentially localized around e's initial position. Furthermore, we can also vary the optical lattice band structure by adjusting the lattice power. The Schneble group already demonstrated simulations using rubidium atoms trapped in a 1D state-dependent lattice [99, 100]. Extending the simulations to ultracold strontium in 2D optical lattices will enable the study of even richer physical phenomena.

To enable these quantum simulations, we require state-dependent lattices, large 2D optical lattices, and a quantum gas microscope for detection and manipulation. In the following, we discuss these three technical challenges in more detail, where we demonstrated the feasibility of the first two in previous experiments.

State-dependent lattice We can generate highly state-dependent optical lattices for the optically separated $^1S_0$ ground state and the excited $^3P_0$ clock state, using the ground state tune-out wavelength [92, 94]. At this wavelength, the polarizability of the ground state vanishes, and the polarizability of the clock state is finite. Using this wavelength to generate optical traps, we can obtain highly-independent control over the $^1S_0$-$^3P_0$ optical qubit.

To realize the simulation of light-matter interfaces discussed above, we generate a lattice close to the tune-out wavelength of the $^1S_0$ ground state. Doing so results in weak confinement of atoms in the $^1S_0$ state, while atoms in the $^3P_0$ clock state experience a strong trapping potential localizing them. In previous experiments, we have experimentally measured the ground state tune-out wavelength [92] and demonstrated trapping $^3P_0$ atoms in the tune-out lattice. These results show that we can successfully implement state-dependent lattices allowing us to focus on the challenge of generating large and uniform optical lattices.

Large optical lattice systems In quantum technology, scaling the system size is one of the major outstanding challenges for all currently available experimental platforms, where ultracold atoms in optical lattices offer the largest systems. These lattices are generated by overlapping Gaussian laser beams and, because the beams have a finite extent, also the lattices have a finite system size. Due to the limited available laser power, an increased beam size results in a smaller potential depth, and the atoms are not confined tightly enough for imaging with the quantum gas microscope. Typically, optical lattice experiments contain $\sim 30 \times 30$ usable lattice sites [32, 101, 102]. Apart from the general applications, simulating the light-matter interfaces in large lattice systems allows observing matter-wave propagation over much longer distances than possible in other systems.

We overcome the limitation by using a 2D buildup cavity to generate our lattices [103]. Our cavity assembly enhances the circulating power in the cavity at certain design wavelengths by up to a factor of $1,000$. The combination of power enhancement and a mode size of ~ 450 µm allows us to create optical lattices with $\sim 200 \times 200$ usable sites [93]. We experimentally characterized the resulting system by performing high-resolution spectroscopy confirming the expected mode size and homogeneity [104].

Strontium quantum gas microscope Implementing the quantum gas microscope is the last missing piece towards realizing our quantum simulator for light-matter interfaces. Most microscope experiments work with alkali atoms [27–32, 35, 36] while only two experiments use the alkaline-earth-like element ytterbium [33, 34]. Our system will be the first strontium quantum gas microscope. The microscope will enable us to spatially resolve atoms in light-matter quantum simulation and allow observing the atom-photon bound state [95]. Moreover, we can use the objective to focus a laser beam onto individual lattice sites to spatially manipulate the atoms.

In this thesis, we report on the progress of one of the most demanding tasks in setting up a quantum gas microscope experiment: the isolation of a single atomic layer [26]. Our microscope objective has a depth of focus of ~ 2 µm. Along the microscope's optical axis, we confine the atoms in an optical lattice with a lattice spacing of 532 nm. Hence, several lattice planes can be in focus or close to focus, preventing a unique assignment of a signal to its initial lattice layer. Therefore, we have to isolate a single atomic layer in the experiment's preparation stage. Because the buildup cavity limits the optical access, we can not implement a lattice with variable spacing to initially load only a single plane as done by other experiments [29, 32, 105]. We follow the approach of optically removing atoms in all planes but one using the magnetic field sensitive $^1S_0$-$^3P_2$ transition. We separate the lattice planes in frequency space by applying a magnetic field gradient and locally address an individual layer by shining in a laser beam at the corresponding $^1S_0$-$^3P_2$ resonance.

The $^1S_0$-$^3P_2$ transition is magnetic-quadrupole allowed and, in contrast to the famous clock transition, remains to be investigated in detail. The Takahashi group experimentally investigated this transition in Yb [106–109] and only very recently, the Schreck group measured the transition frequency for the first time in ^{87}Sr with an uncertainty

of 30 MHz [110]. Due to this little knowledge of the $^1S_0$-$^3P_2$ transition, we extensively investigate it in the scope of this thesis.

In our microscope experiment, we confine the atoms along all three spatial directions with a 3D optical lattice. After the isolation, we obtain a single lattice layer extended along the microscope's focal plane. We can spatially read out and manipulate the atomic state by focusing an optical trough the microscope objective. However, the diffraction-limited resolution results in cross-talk between adjacent lattice sites. Applying a magnetic field gradient along the plane and using the magnetic-field-sensitive $^1S_0$-$^3P_2$ transition enhances the addressing resolution beyond the diffraction limit. This addressing technique gives us another state-manipulation tool at hand relevant for most quantum simulation and quantum computation experiments using strontium atoms. For example, local addressing allows preparing spin impurities [111] or excited-state impurities and observing their dynamics.

Thesis outline

The main topic of this thesis is the first comprehensive study of the $^1S_0$-$^3P_2$ magnetic quadrupole transition in strontium with the aim of using it to prepare a single lattice plane in the focus of a microscope objective. This step is a major milestone towards realizing the first strontium quantum gas microscope experiment.

In Chapter 2, we discuss the basic properties of strontium, including the naturally occurring isotopes and the electronic level structure.

In Chapter 3, we study resonant light-matter interaction from first principles to obtain a quantitative description of atomic multipole transitions. These transitions differ significantly from the well-known electric dipole transitions. We discuss the selection rules of multipole transitions and explain the dependence of the transition amplitude on the light polarization and the light propagation direction.

In Chapter 4, we calculate the polarizabilities of the $^1S_0$ ground state and the lowest triplet states. We discuss their magic wavelengths and investigate tuning of the polarizability of the $^3P_1$ state and the $^3P_2$ state by adjusting their vector and tensor polarizabilities. We use this polarizability tuning to realize a vanishing differential ac Stark shift of the $^1S_0$-$^3P_1$ and $^1S_0$-$^3P_2$ transitions in an 1064 nm optical lattice. Furthermore, we find the conditions for realizing a 3D magic lattice for the $^1S_0$-$^3P_2$ transition with horizontal lattices at 914 nm and a vertical lattice at 1064 nm. At the end of the chapter, we calculate the tune-out wavelengths for the $^1S_0$, the $^3P_0$ and the $^3P_2$ states.

In Chapter 5, we discuss the experimental apparatus. We give an overview of the vacuum system, including the crossed cavity design. We explain our considerations regarding the magnetic field coils, which generate the bias fields and the field gradient used to isolate a single lattice layer. Moreover, we describe our various low- and high-power laser systems from which we derive the cooling and trapping beams. We also explain the upgraded transport setup combining an optical dipole trap with a tunable focus position and a running-wave lattice.

Chapter 6 is devoted to the experimental study of the $^1S_0$-$^3P_2$ magnetic quadrupole transition. We investigate the transition probability as a function of the probe beam polarization and propagation direction. For the magnetic-field-insensitive $^1S_0$-$^3P_2$ $\Delta m_J = 0$ transition, we engineer a Stark-shift-free optical lattice by adjusting the excited state's polarizability. In this magic lattice, we resolve the transition with a precision of 2 kHz. We measure the absolute $^1S_0$-$^3P_2$ transition frequency in ^{88}Sr and ^{87}Sr with three orders of magnitude reduced uncertainty compared to previous measurements. Furthermore, we achieve a magic lattice for the magnetic-field-sensitive $^1S_0$-$^3P_2$ $\Delta m_J = -1$ transition by adjusting the lattice polarization. As a proof-of-principle experiment, we demonstrate local-addressing using this transition.

In the last chapter, we conclude and give an outlook on the future directions of the experiment. We discuss possible applications of the $^1S_0$-$^3P_2$ magnetic quadrupole transition in quantum simulation, quantum computing, and metrology.

Publications

The following papers were published in the course of this PhD-thesis:

- State-dependent optical lattices for the strontium optical qubit.
  A. Heinz*, A. J. Park*, N. Šantić, **J. Trautmann**, S. G. Porsev, M. S. Safronova, I. Bloch, and S. Blatt. Physical Review Letters **124,** 203201 (2020).
  * *Equal contributions*

- Crossed optical cavities with large mode diameters.
  A. Heinz, **J. Trautmann**, N. Šantić, A. J. Park, I. Bloch, and S. Blatt. Optics Letters **46**, 250 (2021).

- Cavity-enhanced optical lattices for scaling neutral atom quantum technologies.
  A. J. Park, **J. Trautmann**, N. Šantić, V. Klüsener, A. Heinz, I. Bloch, and S. Blatt. PRX Quantum **3**, 030314 (2022).

- The $^1S_0$-$^3P_2$ magnetic quadrupole transition in neutral strontium.
  J. Trautmann, D. Yankelev, V. Klüsener, A. J. Park, I. Bloch, and S. Blatt. in preparation

Chapter 2

Strontium

In this Chapter, we discuss the properties of strontium, which is our element of choice to simulate open quantum systems and light-matter interfaces. Strontium is an alkaline-earth atom with two valence electrons.

The first Section discusses the different strontium isotopes and their natural abundances. Afterward, we explain the electronic level structure and summarize the properties of the transitions between electronic states that make strontium special.

2.1 Isotope abundances

Strontium has three naturally occurring bosonic isotopes (^{84}Sr, ^{86}Sr, ^{88}Sr) and one naturally occurring fermionic isotope (^{87}Sr). We list the isotope abundances and background scattering lengths in Tab. 2.1. In our experimental apparatus, we can cool the bosonic ^{88}Sr isotope with a nuclear spin of $I = 0$ or the fermionic ^{87}Sr isotope with a nuclear spin of $I = 9/2$. Here, the vanishing nuclear spin of the bosonic isotopes results in a vanishing hyperfine structure. Furthermore, we can see that ^{88}Sr is non-interacting due to its scattering length of $-2\,a_0$ which prevents evaporative cooling techniques [112].

				Scattering length $a(a_0)$			
Isotope	Abundance	Nuclear spin	Statistics	^{84}Sr	^{86}Sr	^{88}Sr	^{87}Sr
^{84}Sr	0.56 %	0	bosonic	123	32	1700	−57
^{86}Sr	9.86 %	0	bosonic	32	800	97	162
^{88}Sr	82.58 %	0	bosonic	1700	97	−2	55
^{87}Sr	7.00 %	9/2	fermionic	−57	162	55	96

Tab. 2.1 Abundance, nuclear spin and scattering length of the naturally occurring strontium isotopes. The background scattering lengths are given in units of the Bohr radius a_0. The data is taken from Ref. [113].

The experiments presented later in this thesis, mostly use the non-interacting ^{88}Sr due to its high abundance. The absence of hyperfine structure allows simpler cooling schemes compared to ^{87}Sr. Moreover, the low scattering length allows us to realize non-interacting bath particles analog to photons.

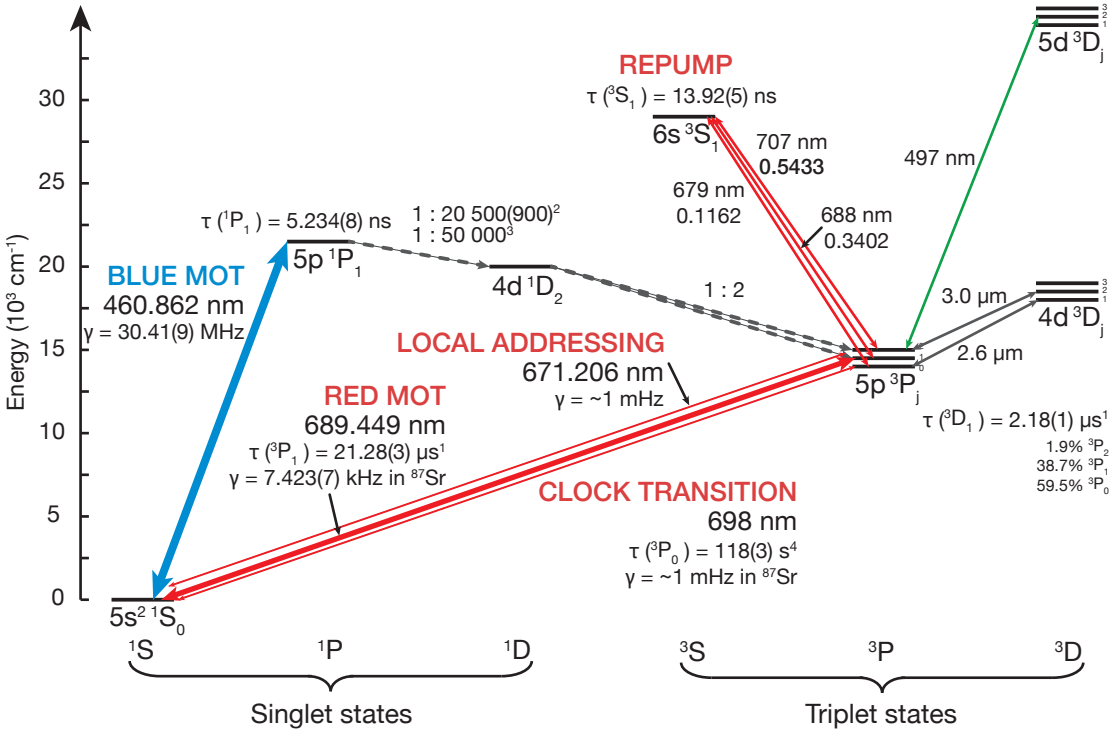

Fig. 2.1 Electronic level diagram of ^{88}Sr (adapted from Refs. [94, 93]). The diagram shows the transition that are relevant for this thesis and lists the corresponding lifetimes and branching ratios. The presented spectroscopic data is taken from Refs. [1] [115] [2] [77] [3] [116] [4] [49].

2.2 Level structure

The two valence electrons of alkaline-earth atoms result in an atomic level structure consisting of singlet and triplet states similar to helium [114]. For two electrons, the total spin can be either $S = 0$ or $S = 1$, corresponding to the singlet and triplet states, respectively. We show the energy level diagram of strontium in Fig. 2.1. The electronic structure offers a variety of broad transitions in the megahertz regime and narrow intercombination transitions between singlet and triplet states with linewidths reaching from the millihertz to the kilohertz regime.

The ^{1}S$_0$ ground state of strontium is a singlet state with vanishing angular momentum $J = 0$. Starting from the ground state, we can drive the ~ 30 MHz broad transition to the ^{1}P$_1$ state. Typically, we use this transition for processes that require large scattering rates or large momentum transfers, such as imaging, initial laser cooling, or slowing of atoms effusing from the oven [117].

The ground state can also be coupled to the ^{3}P$_J$ triplet states by narrow transitions. The strongest of these transitions is the ^{1}S$_0$-^{3}P$_1$ transition. It is a spin-forbidden electric dipole transition with a linewidth of ~ 7 kHz. This transition is weakly allowed due to spin-orbit-interaction-induced mixing of the ^{3}P$_1$ state with the ^{1}P$_1$ state. We use the ^{1}S$_0$-^{3}P$_1$ transition

for narrow-line laser cooling in a second stage of the magneto optical trap (MOT) [118] or for direct sideband cooling in an optical lattice to reach µK temperatures [119].

The metastable $^3P_0$ state has a lifetime of $118(3)$ s [49]. This state has a vanishing angular momentum $J = 0$ that makes the state insensitive to most environmental effects such as trapping light polarization and magnetic fields. The $^1S_0$ ground state and the $^3P_0$ state are connected by a doubly forbidden electric dipole transition. This transition is enabled by hyperfine interaction-induced mixing [71]. The interaction mixes the $^3P_0$ state with the $^3P_1$, $^3P_2$ and $^1P_1$ states. As the $^1S_0$-$^3P_0$ transition forms the basis of strontium optical lattice clocks, it has been thoroughly investigated [62, 51, 49, 56, 120–122] and is known as the clock transition. The bosonic isotopes do not experience the mixing due to the lack of hyperfine structure. However, this mixing can be induced by a strong external magnetic field [77, 78, 92, 123–126]. Remarkably, in the absence of state mixing, the clock transition is forbidden in all higher-order multipole transitions because it connects two states with an angular momentum of $J = 0$.

In contrast to the $^3P_0$ state, the $^3P_2$ state possesses a large magnetic moment of 2.1 G/cm, which allows controlling the energy of the excited states with magnetic fields [127]. This metastable state has a natural lifetime of hundreds of seconds [128]. The $^3P_2$ state's non-vanishing angular momentum of $J = 2$ enables engineering of the atomic polarizability in optical traps [77, 78, 119], extending the scope of experimental manipulation tools. The $^1S_0$-$^3P_2$ single-photon transition is magnetic-quadrupole allowed [129]. The quadrupole transition enables us to couple the states without a large external magnetic field or hyperfine mixing. In the fermionic isotope, the hyperfine mixing leads to an additional excitation branch via an electric dipole transition. The transitions to the Zeeman sublevels with $|m_J| > 0$ are magnetically sensitive, which we use for single-addressing within a magnetic field gradient [73, 130, 106, 107]

Hyperfine levels Since ^{87}Sr is relevant for many quantum computing and quantum simulation proposals, we discuss its hyperfine level structure shown in Fig. 2.2. The $^1S_0$ ground state and $^3P_0$ clock state have a single hyperfine level with $F = 9/2$ resulting in 10 magnetic substates (m_F), which are also called nuclear spin states in this context. Due to the vanishing angular momentum $J = 0$, the nuclear spin states are decoupled from the electron. The excited states with $J > 0$ split into multiple hyperfine states. Because the $^1S_0$-$^3P_1$ transition and the $^1S_0$-$^3P_2$ transition have narrow linewidths, one can resolve the hyperfine levels with laser spectroscopy.

Later in this thesis, we present spectroscopy data of the $^1S_0$-$^3P_2$ transition in ^{88}Sr and ^{87}Sr. In ^{87}Sr, we probe the $F' = 5/2$, $F' = 7/2$, $F' = 9/2$, and $F' = 11/2$ hyperfine levels. From the measurements we can extract the hyperfine splittings and can compare them with the literature values calculated from Ref. [131]. Furthermore, we can deduce the isotope shift between ^{88}Sr and ^{87}Sr of the $^1S_0$-$^3P_2$ transition of $\Delta^{88}_{87} = \nu(^{88}\text{Sr}) - \nu(^{87}\text{Sr}) = 62.93(6)$ MHz, which is the first direct isotope-shift measurement of this transition.

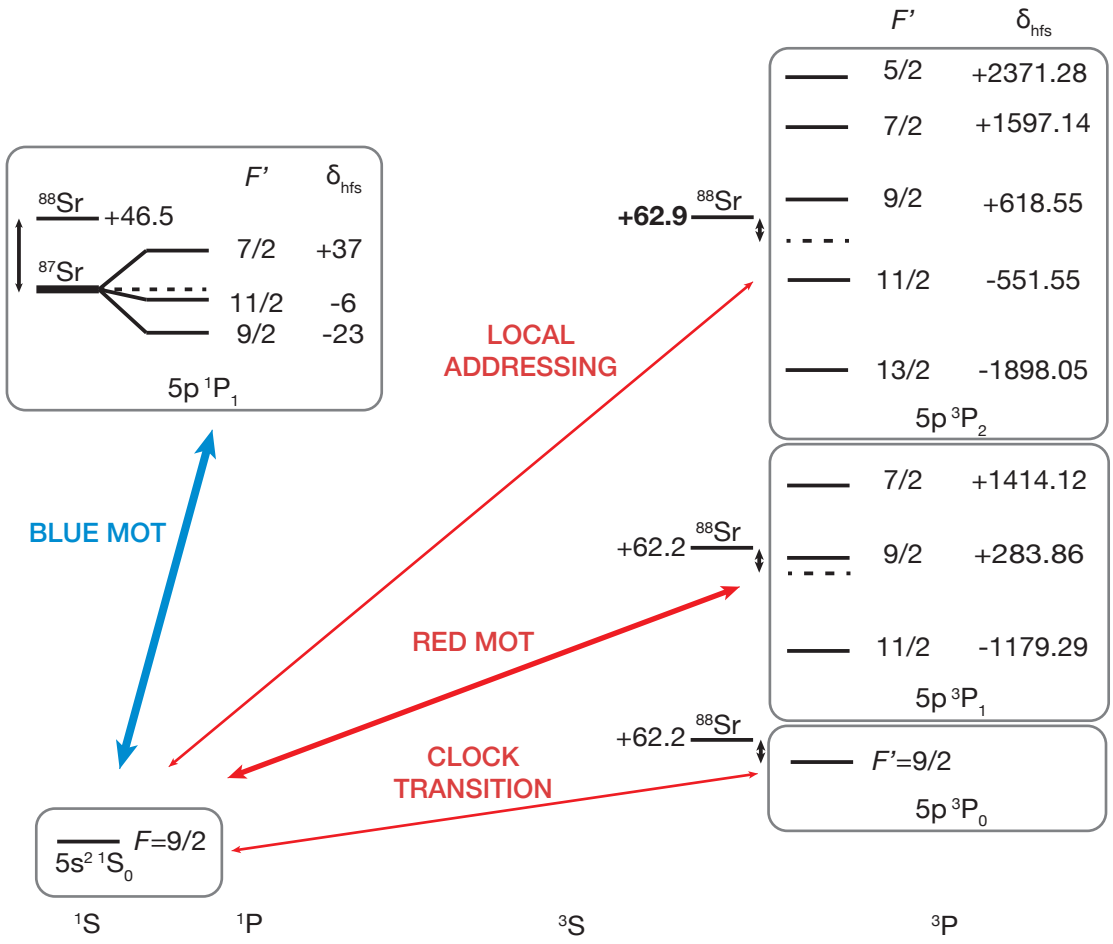

Fig. 2.2 ^{87}Sr hyperfine level structure (adapted from Refs. [93, 117]). The hyperfine splitting energies $\delta_{\mathrm{hfs}} = \Delta/(2\pi)$ are calculated with respect to a reference state assuming $I = 0$ and are given in MHz. The isotope shift of the ^{3}P$_2$ state is marked in bold since we measured the shift in the course of this thesis.

Conclusion

The experiments presented later in this thesis mostly use the non-interacting bosonic ^{88}Sr isotope. From the ^{1}S$_0$ ground state of strontium, one can reach the metastable ^{3}P$_0$ and ^{3}P$_2$ states using millihertz-wide optical transitions. The states and transitions offer various applications in metrology, quantum computing, and quantum simulation. To locally address atoms in our quantum simulation of light-matter interfaces, we use the magnetic-field-sensitive ^{1}S$_0$-^{3}P$_2$ magnetic quadrupole transition, which has not been studied before in detail. To understand the properties of this transition, we first build intuition by working through the general theory of multipole transitions in the next Chapter.

Chapter 3

Resonant light-matter interaction

The interaction of light and matter is one cornerstone of quantum optics and atomic physics. Understanding this interaction laid the foundation for developing modern technologies that nearly everybody comes across daily, like light-emitting diodes, solar cells, and lasers. The origin of the light-matter interaction is the coupling of electromagnetic fields to charge carriers in matter. We are especially interested in the coupling between light and atoms, whose charge carriers are their valence electrons.

If the light frequency is resonant with the energy splitting of electron levels inside the atom, the electron changes its state from one level to the other. This process is called an atomic transition. Driving atomic transitions is one of the main tools in quantum simulation, quantum computing, and metrology with neutral atoms.

Coherently driving optical atomic transition allows laser cooling, atomic state preparation, and state readout. The physical applications of a transition depend on properties like the selection rules and the coupling strength. Hence, understanding the transition's properties is the first step to later applications.

In this chapter, we introduce the light-matter interaction Hamiltonian in a semiclassical theory, where we describe the atom as a two-level system and treat the electromagnetic field classically. This Hamiltonian includes the interaction responsible for all atomic multipole transitions. Typically, only electric dipole transitions are considered. Here, we extend the discussion to higher-order electric and magnetic multipole transitions. The higher-order multipole transitions have remarkably different selection rules than the well-known electric dipole transitions. Moreover, the multipole transition amplitudes depend differently on beam polarization and beam propagation direction than we are used to from an daily work in the laboratory with electric dipole transitions.

We start this Chapter with the light-matter interaction Hamiltonian. To begin with something familiar to most readers, we derive the well-known electric dipole transition operator. In Sec. 3.2, we generate an understanding of multipole transitions. We calculate the multipole transition operators and derive selection rules for the corresponding transitions. In the last Section, we investigate the geometric dependence of multipole transitions, describing which polarization and which probe beam direction is required to drive the transition.

3.1 Light-matter interaction Hamiltonian

We start our discussion of the light-matter interaction by writing down the interaction Hamiltonian. The electromagnetic field of the light couples to matter via the interaction with charged particles inside the matter. For the light-atom interaction the coupling occurs between the light and the valence electrons of the atom. We describe the light field in terms of the electromagnetic vector potential $\mathbf{A}(\mathbf{r},t)$ and the scalar potential $\Phi(\mathbf{r},t)$. The result is the Hamiltonian [132, 133]

$$H = \frac{1}{2m_\mathrm{e}}\left[\mathbf{p} - e\mathbf{A}(\mathbf{r},t)\right]^2 + e\Phi(\mathbf{r},t) + V(\mathbf{r}), \tag{3.1}$$

where an electron of charge e and mass m_e interacts with the electromagnetic potentials. In our case, the electron is bound to the atom by the potential $V(\mathbf{r})$. Including the electron's spin $\mathbf{S}$, the interaction is governed by the minimal coupling Hamiltonian [132] plus the interaction between $\mathbf{S}$ and $\mathbf{A}(\mathbf{r},t)$, resulting in

$$H = \frac{\mathbf{p}^2}{2m_\mathrm{e}} + V(\mathbf{r}) - \frac{e}{m_\mathrm{e}}\mathbf{p}\cdot\mathbf{A}(\mathbf{r},t) + g_\mathrm{B}\mu_\mathrm{B}\mathbf{S}\cdot\left[\boldsymbol{\nabla}\times\mathbf{A}(\mathbf{r},t)\right] + e\Phi(\mathbf{r},t) + \frac{e^2}{2m_\mathrm{e}}A^2, \tag{3.2}$$

where $h = 2\pi\hbar$ is the Planck constant, g_B is the gyromagnetic factor, and $\mu_\mathrm{B} = e\hbar/(2m_\mathrm{e})$ is the Bohr magneton. The first two terms describe the bound electron, the next three terms characterize the interaction of the electron with the light field, and the last term corresponds to the ponderomotive potential which can be neglected because at typical laser powers it is only a small correction [114]. For simplicity we work through the following calculations assuming a single electron, but we can easily extent the formalism to many-electron systems [133, 134].

Before we take a closer look at the interaction, we recall briefly the basics of electrodynamics. We introduce the gauge transformation of the electromagnetic potentials, which will become important to calculate the electric multipole transition operator. The gauge transformation has the form

$$\mathbf{A}(\mathbf{r},t) \to \mathbf{A}'(\mathbf{r},t) = \mathbf{A}(\mathbf{r},t) + \boldsymbol{\nabla}\chi(\mathbf{r},t), \tag{3.3}$$

$$\Phi(\mathbf{r},t) \to \Phi'(\mathbf{r},t) = \Phi(\mathbf{r},t) - \frac{\partial\Phi(\mathbf{r},t)}{\partial t}, \tag{3.4}$$

where $\chi(\mathbf{r},t)$ is the gauge function. Using the gauge-dependent potentials $\mathbf{A}$ and Φ for the interaction Hamiltonian is the result of making the corresponding Schrödinger equation invariant to local phases of the electron wave function [135].

Instead of the potentials, we can also express the interaction in terms of the electromagnetic fields $\mathbf{E}(\mathbf{r},t)$ and $\mathbf{B}(\mathbf{r},t)$. The fields are gauge-independent and are given by

$$\mathbf{E}(\mathbf{r},t) = -\boldsymbol{\nabla}\Phi(\mathbf{r},t) - \frac{\partial\mathbf{A}(\mathbf{r},t)}{\partial t}, \tag{3.5}$$

$$\mathbf{B}(\mathbf{r},t) = \boldsymbol{\nabla}\times\mathbf{A}(\mathbf{r},t). \tag{3.6}$$

Calculating transition rates using the gauge-independent field or the gauge-dependent potential should give the same result. Generally speaking this argument means that a gauge transformation must not change the result of measurable quantities. To satisfy this requirement we have to keep in mind that a gauge transformation also transforms the wavefunctions by $\Psi(\mathbf{r},t) \to \Psi(\mathbf{r},t)\exp[i\chi(\mathbf{r},t)]$ [135]. Only if the potentials and the wavefunctions are transformed we obtain the correct result.

Above, we derived the light-matter interaction for general electromagnetic potentials. Now, we shift the focus towards experimentally relevant light fields. In our experiments, atoms interact with a laser beam which we approximate as a monochromatic plane wave described by

$$\mathbf{A}(\mathbf{r},t) = \hat{\boldsymbol{\epsilon}} A_0 \exp(i\mathbf{k}\cdot\mathbf{r} - i\omega t). \tag{3.7}$$

Here, ω is the oscillation frequency, $\mathbf{k}$ is the wave vector, $\hat{\boldsymbol{\epsilon}}$ is the polarization vector, and A_0 is the scalar amplitude of $\mathbf{A}(\mathbf{r},t)$. Here and in the following we mark unit vectors with a hat. To relate the vector potential to a specific electric field, we choose the *Coulomb* gauge, also known as the *radiation* or *transverse* gauge, defined by [136, 137]

$$\boldsymbol{\nabla}\cdot\mathbf{A}(\mathbf{r},t) = 0, \tag{3.8}$$

$$\Phi(\mathbf{r},t) = 0. \tag{3.9}$$

The first line implies that the momentum $\mathbf{p} = -i\hbar\boldsymbol{\nabla}$ and the vector potential $\mathbf{A}$ commute. Using this gauge, the electric field of the plane wave is given by

$$\mathbf{E}(\mathbf{r},t) = i\omega\hat{\boldsymbol{\epsilon}} E_0 \exp(i\mathbf{k}\cdot\mathbf{r} - i\omega t). \tag{3.10}$$

The electric field amplitude and the amplitude of the vector potential are related by $E_0 = \omega A_0$. We rewrite the first interaction term of Eq. (3.2) by replacing the vector potential with the electric field and obtain

$$\frac{e}{m_\mathrm{e}}\mathbf{p}\cdot\mathbf{A}(\mathbf{r},t) = i\frac{eE_0}{m_\mathrm{e}\omega}\mathbf{p}\cdot\hat{\boldsymbol{\epsilon}}\exp(i\mathbf{k}\cdot\mathbf{r})\exp(-i\omega t) \tag{3.11}$$

$$\approx i\frac{eE_0}{m_\mathrm{e}\omega}\mathbf{p}\cdot\hat{\boldsymbol{\epsilon}}\,(1 + i\mathbf{k}\cdot\mathbf{r} + \dots)\exp(-i\omega t). \tag{3.12}$$

In the second line, we approximated the exponential by its Taylor expansion for $\mathbf{k}\cdot\mathbf{r} \ll 1$. This condition is satisfied since the atom has a much smaller spatial extent than the wavelength $\lambda = \frac{c}{\nu} = 2\pi\frac{c}{\omega}$ which is the characteristic length scale of the light. If the electromagnetic field's oscillation frequency ω is resonant with the frequency $\omega_{ki} = \omega_k - \omega_i$ of the atomic transition $|i\rangle \to |k\rangle$, the field can drive this transition. The corresponding coupling is described by

$$i\frac{eE_0}{m_\mathrm{e}\omega_{ki}}\langle k|\mathbf{p}|i\rangle\cdot\hat{\boldsymbol{\epsilon}}\exp(-i\omega t), \tag{3.13}$$

where we only kept the first term of the expansion of the exponential compared to Eq. (3.12), which is known as the electric dipole approximation. In principle, we can use this expression to calculate the population dynamics of the states $|i\rangle$ and $|k\rangle$ with

the aid of time-dependent perturbation theory [138]. A resonant coupling results in the well-known Rabi oscillations [135]. However, here we are not interested in the time dynamics and instead refer to the discussion in Ref. [135, 114, 139].

The coupling strength of the transition is characterized by the matrix element

$$d_{ki} = \frac{1}{m_\mathrm{e}\omega_{ki}}\langle k|\mathbf{p}|i\rangle \cdot \hat{\boldsymbol{\epsilon}} = \frac{1}{\omega_{ki}}\langle k|\boldsymbol{v}|i\rangle \cdot \hat{\boldsymbol{\epsilon}}. \tag{3.14}$$

This form of the matrix element is known as the *velocity form* [137]. The associated *length form* [137] can be obtained by using the commutation relation of the momentum operator and the bare atomic Hamiltonian $[\mathbf{r}, H] = i\hbar/(m_\mathrm{e})\mathbf{p}$ [114] and the resulting relation $\langle k|\mathbf{p}|i\rangle = m_\mathrm{e}/(i\hbar)\omega_{ki}\langle k|\mathbf{r}|i\rangle$. Inserting this relation into Eq. (3.14) leads to

$$d_{ki} = \frac{1}{m_\mathrm{e}\omega_{ki}}\langle k|\mathbf{p}|i\rangle \cdot \hat{\boldsymbol{\epsilon}} = i\langle k|\mathbf{r}|i\rangle \cdot \hat{\boldsymbol{\epsilon}}. \tag{3.15}$$

We note that the length form of electric dipole operator can also be obtained by using the length gauge $\chi(\mathbf{r}, t) = -\mathbf{A}(\mathbf{r}, t) \cdot \mathbf{r}$. Rewriting the coupling in the length form leads to

$$-E_0\langle k|e\mathbf{r}|i\rangle \cdot \hat{\boldsymbol{\epsilon}} \exp(-i\omega t) = -E_0\langle k|\boldsymbol{d}|i\rangle \cdot \hat{\boldsymbol{\epsilon}} \exp(-i\omega t), \tag{3.16}$$

where we defined the electric dipole transition operator $\boldsymbol{d} = e\mathbf{r}$. We can see that the light-matter coupling can be expressed as the interaction between an electric dipole and the electric field. This is the reason why the approximation of $\exp(i\mathbf{k}\cdot\mathbf{r}) \approx 1$ is called the electric dipole approximation.

We derived the matrix element of an electric dipole transition from first principles of the light-matter interaction Hamiltonian. The matrix element are identical to the semi-classical description of the light-atom interaction where the electric dipole moment of the electron-nucleus pair interacts with the oscillating electric field [114]. The reader may ask why did we do this complicated derivation if the field-dipole interaction leads to the same result. The answer is that we can easily extend our derivation to multipole transitions which is not possible in the field-dipole interaction derivation.

3.2 Multipole transitions

In the previous Section, we derived the well-known electric dipole transitions by applying the electric dipole approximation to the electromagnetic potentials. The selection rules of electric dipole transitions allow a coupling between atomic states that differ in their angular momentum by $|\Delta J| = 0, 1$[114]. The change in angular momentum is the result of the absorption process where the atom acquires the photon's angular momentum. For an electric dipole transition, the photon's angular momentum is given by its spin of $s = 1$.

However, in experiments we can observe single-photon transitions that violate the electric dipole selection rules by connecting states with $|\Delta J| \geq 2$. These transitions are so-called multipole transitions and are already used in trapped ions for metrology applica-

tions [140, 141] and in quantum-computing research [63]. One example of a multipole transition in neutral atoms is the $^1S_0$-$^3P_2$ transition in bosonic alkaline-earth atoms [106, 142]. This transition in ^{88}Sr is of special interest for us since we would like to use it as an optical qubit and for local addressing. To guide these experiments, we first have to understand the selection rules of multipole transitions and transition amplitude's dependence on probe beam polarization and probe beam orientation.

Hence, we have to derive these dependencies from the interaction Hamiltonian. The first question the reader may ask is which part of the light-matter interaction Hamiltonian contains these transitions. Therefore, we revisit the interaction term $\mathbf{p} \cdot \mathbf{A}$ and take a closer look at the expansion of the plane wave for $\mathbf{k} \cdot \mathbf{r} \ll 1$

$$\mathbf{p} \cdot \mathbf{A}(\mathbf{r}, t) \propto \hat{\boldsymbol{\epsilon}} \cdot \mathbf{p} \exp(i\mathbf{k} \cdot \mathbf{r}) = \hat{\boldsymbol{\epsilon}} \cdot \mathbf{p} \left[1 + i\mathbf{k} \cdot \mathbf{r} - \frac{i}{2}(\mathbf{k} \cdot \mathbf{r})^2 + \cdots\right]. \tag{3.17}$$

We already saw that the first term is responsible for the electric dipole (E1) transitions. The multipole transitions occur from the higher-order terms, where the second term drives magnetic dipole (M1) and electric quadrupole (E2) transitions, the third term drives magnetic quadrupole (M2) and electric octupole (E3) transitions, and so on. Quadrupole (octupole) transitions couple atomic states with $|\Delta J| \leq 2$ ($|\Delta J| \leq 3$). The light field contributes additional angular momentum to satisfy the conservation of angular momentum.

The strength of the multipole transitions decreases from lower to higher order. Typically, only the lowest non-vanishing order is considered because it dominates the transition. Which transitions are non-vanishing is determined by the selection rules containing the conservation of angular momentum and the conservation of parity. Therefore, the angular momentum difference ΔJ, the parity of the atomic states, and the parity of the corresponding transition operator determine whether a specific multipole transition can occur [114]. For the $^1S_0$-$^3P_2$ transition the first non-vanishing contribution is the magnetic quadrupole. Typically, contributions from transitions of higher order than the dominant one are very small and can be neglected.

3.2.1 Multipole expansion of the plane wave

The magnetic dipole (M1) and the electric quadrupole (E2) transitions can be obtained by separating the interaction $\mathbf{p}(\mathbf{k} \cdot \mathbf{r})$ into the magnetic and the electric multipole transition operators as carried out in Ref. [114]. However, this approach is not very convenient and becomes relatively involved for higher-order multipoles [133]. Therefore, we choose a different method and expand the vector potential of the plane wave in terms of vector spherical harmonics, following Ref. [137]. By calculating the action of the operator $\mathbf{p}$ on the vector spherical harmonics, we can derive the multipole transition operators.

Before we start with the expansion, we construct the vector spherical harmonics $\mathbf{Y}_{KLq}$ by combining standard spherical harmonics $Y_L^q(\theta, \phi)$ with spherical basis vectors $\hat{\boldsymbol{e}}_p$ and

obtain

$$\mathbf{Y}_{KLq}(\theta,\phi) = (-1)^{K-q}\sqrt{2K+1}\sum_{p=-1}^{+1}\begin{pmatrix} K & 1 & L \\ -q & p & q-p \end{pmatrix} Y_L^q(\theta,\phi)\hat{\boldsymbol{e}}_p, \tag{3.18}$$

where the definition contains the Wigner 3-j symbols [137]. In many textbooks the (vector) spherical harmonics are labeled with JLM, whereas we use KLq to avoid confusion with the angular momentum associated with the atomic states. The spherical basis vectors are given by

$$\begin{aligned}\hat{\boldsymbol{e}}_{+1} &= -\frac{1}{\sqrt{2}}(\hat{\mathbf{x}} + i\hat{\mathbf{y}}),\\ \hat{\boldsymbol{e}}_0 &= \hat{\mathbf{z}},\\ \hat{\boldsymbol{e}}_{-1} &= \frac{1}{\sqrt{2}}(\hat{\mathbf{x}} - i\hat{\mathbf{y}}).\end{aligned}$$

The constructed vector spherical harmonics are a combination of angular momentum components, given by Y_L^q, and eigenfunctions of the spin operator for particles with $s = 1$. This combination makes these vectors ideal to describe light fields containing angular momentum and the photon spin.

The expansion of the vector potential of a plane wave in terms of the vector spherical harmonics $\mathbf{Y}_{KLq}$ is given by

$$\mathbf{A}(\mathbf{r}) = A_0\hat{\boldsymbol{\epsilon}}\exp(i\mathbf{k}\cdot\mathbf{r}) = A_0\sum_{KLq} A_{KLq}\mathbf{Y}_{KLq}(\mathbf{r}), \tag{3.19}$$

where $\hat{\boldsymbol{\epsilon}}$ is the polarization vector. For simplicity, we drop the explicit time dependence because it does not play a role in the following derivations. The expansion coefficients A_{KLq} can be calculated with the relation

$$A_{KLq} = \int_0^{\pi}\sin(\theta_r)\mathrm{d}\theta_r\int_0^{2\pi}\mathrm{d}\phi_r[\mathbf{Y}_{KLq}(\hat{\mathbf{r}}]\cdot\hat{\boldsymbol{\epsilon}})\exp(i\mathbf{k}\cdot\mathbf{r}). \tag{3.20}$$

To solve the integral we insert the well-known expansion of the plane wave in terms of spherical harmonics and spherical Bessel functions $j_{L'}(kr)$ [136]

$$\exp(i\mathbf{k}\cdot\mathbf{r}) = 4\pi\sum_{L'q'} i^{L'}j_{L'}(kr)Y_{L'}^{q'*}(\mathbf{k})Y_{L'}^{q'}(\mathbf{r}), \tag{3.21}$$

where we use the abbreviation $Y_L^q(\hat{\mathbf{r}}) \equiv Y_L^q(\theta_r, \phi_r)$ and $Y_L^q(\hat{\mathbf{k}}) \equiv Y_L^q(\theta_k, \phi_k)$. We obtain

$$A_{KLq} = 4\pi \sum_{L'q'} i^{L'} j_{L'}(kr) Y_{L'}^{q'*}(\hat{\mathbf{k}}) \int_0^\pi \sin(\theta_r) d\theta_r \int_0^{2\pi} d\phi (\mathbf{Y}_{KLq}(\mathbf{r}) \cdot \hat{\boldsymbol{\epsilon}}) Y_{L'}^{q'}(\hat{\mathbf{r}}) \tag{3.22}$$

$$= 4\pi \sum_{L'q'} \sum_{p=-1}^{+1} i^{L'} j_{L'}(kr) Y_{L'}^{q'}(\hat{\mathbf{k}}) (-1)^{K-q} \hat{\boldsymbol{e}}_p \cdot \hat{\boldsymbol{\epsilon}}_p \sqrt{2K+1} \times \begin{pmatrix} K & 1 & L \\ -q & p & q-p \end{pmatrix} \int d\Omega_r Y_{L'}^{q'*}(\hat{\mathbf{r}}) Y_L^q(\hat{\mathbf{r}}) \tag{3.23}$$

$$= 4\pi i^L j_L(kr) \mathbf{Y}_{KLq}(\mathbf{k}) \cdot \hat{\boldsymbol{\epsilon}}. \tag{3.24}$$

Due to the orthogonality of the spherical harmonics, the integral gives the Kronecker deltas $\delta_{L,L'}\delta_{q,q'}$, which collapse the sums over L' and q'. Including the spherical harmonics $Y_L^q(\hat{\mathbf{k}})$ in the sum over q results in the vector spherical harmonics $\mathbf{Y}_{KLq}(\mathbf{k})$. With the coefficients A_{KLq} we rewrite the expansion of the vector potential which is now given by

$$\mathbf{A}(\mathbf{r}) = 4\pi A_0 \sum_{KLq} i^L [\mathbf{Y}_{KLq}(\mathbf{k}] \cdot \hat{\boldsymbol{\epsilon}}) j_L(kr) \mathbf{Y}_{KLq}(\mathbf{r}). \tag{3.25}$$

In this expansion, the electric and magnetic contributions are not separated yet. To obtain a convenient separation we use a different set of vector spherical harmonics $\mathbf{Y}_{Kq}^{(\lambda)}$, defined by

$$\mathbf{Y}_{Kq}^{(-1)}(\hat{\mathbf{r}}) = \frac{\mathbf{r}}{r} Y_K^q(\hat{\mathbf{r}}), \tag{3.26}$$

$$\mathbf{Y}_{Kq}^{(0)}(\hat{\mathbf{r}}) = \frac{1}{\sqrt{K(K+1)}} \mathbf{L} Y_K^q(\hat{\mathbf{r}}), \tag{3.27}$$

$$\mathbf{Y}_{Kq}^{(1)}(\hat{\mathbf{r}}) = \frac{r}{\sqrt{K(K+1)}} \boldsymbol{\nabla} Y_K^q(\hat{\mathbf{r}}), \tag{3.28}$$

where $\mathbf{L}$ is the angular momentum operator. This new set of vectors and the old vectors $\mathbf{Y}_{KLq}(\mathbf{r})$ satisfy the following relations [137]

$$\mathbf{Y}_{KK-1q}(\hat{\mathbf{r}}) = \sqrt{\frac{K}{2K+1}} \mathbf{Y}_{Kq}^{(-1)}(\hat{\mathbf{r}}) + \sqrt{\frac{K+1}{2K+1}} \mathbf{Y}_{Kq}^{(1)}(\mathbf{r}), \tag{3.29}$$

$$\mathbf{Y}_{KKq}(\hat{\mathbf{r}}) = \mathbf{Y}_{Kq}^{(0)}(\mathbf{r}), \tag{3.30}$$

$$\mathbf{Y}_{KK+1q}(\hat{\mathbf{r}}) = -\sqrt{\frac{K+1}{2K+1}} \mathbf{Y}_{Kq}^{(-1)}(\hat{\mathbf{r}}) + \sqrt{\frac{K}{2K+1}} \mathbf{Y}_{Kq}^{(1)}(\mathbf{r}). \tag{3.31}$$

Using the $\mathbf{Y}_{Kq}^{(\lambda)}$ for the expansion results in

$$\mathbf{A}(\mathbf{r}) = 4\pi \sum_{Kq\lambda} i^{K-\lambda} (\mathbf{Y}_{Kq}^{(\lambda)}(\hat{\mathbf{k}}) \cdot \hat{\boldsymbol{\epsilon}}) \mathbf{a}_{Kq}^{(\lambda)}(\mathbf{r}). \tag{3.32}$$

We can see that the sum over L is replaced by the sum over λ. We introduced the functions $\mathbf{a}_{Kq}^{(\lambda)}(\mathbf{r})$ given by

$$\mathbf{a}_{Kq}^{(0)}(\mathbf{r}) = A_0 j_K(kr)\mathbf{Y}_{Kq}^{(0)}(\hat{\mathbf{r}}), \tag{3.33}$$

$$\mathbf{a}_{Kq}^{(1)}(\mathbf{r}) = A_0\sqrt{\frac{K+1}{2K+1}}j_{K-1}(kr)\mathbf{Y}_{KK-1q}(\mathbf{r}) - A_0\sqrt{\frac{K}{2K+1}}j_{K+1}(kr)\mathbf{Y}_{KK+1q}(\mathbf{r}). \tag{3.34}$$

Due to the fact that $\mathbf{Y}_{Kq}^{(-1)}(\mathbf{k}) = \mathbf{k}/kY_K^q(\hat{\mathbf{k}})$ is perpendicular to the polarization vector $\hat{\boldsymbol{\epsilon}}$, the terms with $\lambda = -1$ vanish and only $\lambda = 0$ and $\lambda = 1$ contribute to the multipole expansion. The terms with $\lambda = 0$ describe the magnetic contribution of the vector potential and the $\lambda = 1$ terms describe the electric contribution [137].

The expansion of the vector potential allows us to rewrite the interaction part of the full Hamiltonian in Eq.(3.2) in the Coulomb gauge to be

$$H_{\text{int}} = -\frac{e}{m_e}\mathbf{p}\cdot\mathbf{A}(\mathbf{r},t) + g_B\mu_B\mathbf{S}\cdot[\boldsymbol{\nabla}\times\mathbf{A}(\mathbf{r},t)] \tag{3.35}$$

$$= 4\pi\sum_{Kq\lambda} i^{K-\lambda}\underbrace{\left(\mathbf{Y}_{Kq}^{(\lambda)}(\hat{\mathbf{k}})\cdot\hat{\boldsymbol{\epsilon}}\right)}_{C_{Kq}^{(\lambda)}(\mathbf{k},\hat{\boldsymbol{\epsilon}})}\underbrace{\left[-\frac{e}{m_e}\mathbf{p}\cdot\mathbf{a}_{Kq}^{(\lambda)}(\mathbf{r}) + g_B\mu_B\mathbf{S}\cdot\left[\boldsymbol{\nabla}\times\mathbf{a}_{Kq}^{(\lambda)}(\mathbf{r})\right]\right]}_{H_{Kq}^{(\lambda)}}, \tag{3.36}$$

where λ takes the values 0 and 1, corresponding to magnetic and electric contributions, respectively. We can see that the expansion in the vector spherical harmonics enables us to separate the Hamiltonian into a geometric factor $C_{Kq}^{(0,1)}$ and an interaction component $H_{Kq}^{(\lambda)}$ that acts on the electronic wave functions of the involved atomic levels.

The multipole transition operators of the light-matter interaction in $H_{Kq}^{(\lambda)}$ can be obtained by calculating the tensor operator $\mathbf{p}\cdot\mathbf{a}_{Kq}^{(\lambda)}(\mathbf{r})$ which has rank K. We derive the electric transition operators in Sec. 3.2.2 and the magnetic transition operators in Sec. 3.2.3.

We note that the term $C_{Kq}^{(\lambda)}(\mathbf{k},\hat{\boldsymbol{\epsilon}})$ contains the full information about the light polarization and its propagation direction. Hence, these terms describe the spatial angular dependence of the multipole transition amplitude [114], which we also call absorption patterns in the following. Understanding the absorption patterns is necessary to know which polarization and laser beam orientation is required to probe a given multipole transition. Therefore, we take a closer look at the transition amplitude's angular dependence in Sec. 3.4.

3.2.2 Electric multipole transition operator

In this Section, we generate a better a better understanding of electric multipole transitions by deriving the associated transition operator from the interaction term $\mathbf{p}\cdot\mathbf{a}_{Kq}^{(1)}(\mathbf{r})$.

In Coulomb gauge, the electric interaction Hamiltonian is given by

$$H_{Kq}^{(\mathrm{el})} \equiv H_{Kq}^{(\lambda)} = -\frac{e}{m_\mathrm{e}} \mathbf{p} \cdot \mathbf{a}_{Kq}^{(1)}(\mathbf{r}). \tag{3.37}$$

For the electric transitions, the spin term does not contribute because the electric component of the vector potential $\mathbf{a}_{Kq}^{(1)}(\mathbf{r})$ does not couple to the spin $\mathbf{S}$ of the electron. Hence, the spin term is not part of the Hamiltonian. We begin the derivation of the transition operator by expressing $\mathbf{a}_{Kq}^{(1)}(\mathbf{r})$ in terms of the vector spherical harmonics $\mathbf{Y}_{Kq}^{(1)}(\mathbf{r})$. We insert Eq. (3.29) and Eq. (3.31) into Eq. (3.34) and find

$$\begin{aligned}
\mathbf{a}_{Kq}^{(1)}(\mathbf{r}) =& A_0 \frac{\sqrt{K(K+1)}}{2K+1} \mathbf{Y}_{Kq}^{(-1)}(\hat{\mathbf{r}}) \left[j_{K-1}(kr) + j_{K+1}(kr) \right] \\
&+ A_0 \frac{1}{2K+1} \mathbf{Y}_{Kq}^{(1)}(\hat{\mathbf{r}}) \left[(K+1) j_{K-1}(kr) - K j_{K+1}(kr) \right] && (3.38) \\
=& A_0 \left[\frac{j_K(kr)}{kr} + \frac{\partial j_K(kr)}{\partial (kr)} \right] \mathbf{Y}_{Kq}^{(1)}(\hat{\mathbf{r}}) + A_0 \sqrt{K(K+1)} \frac{j_K(kr)}{kr} \mathbf{Y}_{Kq}^{(-1)}(\mathbf{r}), && (3.39)
\end{aligned}$$

where we used the following identities of the spherical Bessel functions [137]

$$j_{K-1}(kr) = \frac{K+1}{kr} j_K(kr) + \frac{\partial j_K(kr)}{\partial (kr)}, \tag{3.40}$$

$$j_{K+1}(kr) = \frac{K}{kr} j_K(kr) - \frac{\partial j_K(kr)}{\partial (kr)}. \tag{3.41}$$

Because the atom has a much smaller spatial extent than the wavelength of the light, we have $kr \ll 1$. Using this relation to evaluate $\mathbf{p} \cdot \mathbf{a}_{Kq}^{(1)}(\mathbf{r})$, we obtain the electric multipole transition operator in the velocity form as carried out in Ref. [137]. We note that the calculation above is carried out in the Coulomb gauge and hence, we associate the corresponding gauge function with the velocity form. We can calculate the length form by using the gauge function

$$\chi_{Kq}(\mathbf{r}, t) = -\frac{1}{k} \sqrt{\frac{K+1}{K}} j_K(kr) Y_K^q(\hat{\mathbf{r}}) \exp(i\omega t). \tag{3.42}$$

To show the gauge transformation in a formally correct way, we include the time dependencies. The gauge transforms $\mathbf{a}_{Kq}^{(1)}(\mathbf{r}, t)$ and results in a non-vanishing vector potential

$\Phi(\mathbf{r},t)$,

$$\mathbf{a}^{(1)}_{Kq}(\mathbf{r},t) \to \mathbf{a}^{(1)}_{Kq}(\mathbf{r},t) + A_0 \boldsymbol{\nabla}\chi_{Kq}(\mathbf{r},t) \tag{3.43}$$

$$= -A_0 j_{K+1}(kr)\left[\mathbf{Y}^{(1)}_{Kq}(\mathbf{r},t) - \sqrt{\frac{K+1}{K}}\mathbf{Y}^{(-1)}_{Kq}(\mathbf{r},t)\right], \tag{3.44}$$

$$\Phi(\mathbf{r}) \to \Phi(\mathbf{r},t) + i\omega\Phi_0\chi_{Kq}(\boldsymbol{r},\boldsymbol{t}) \tag{3.45}$$

$$= 0 + i\omega\Phi_0\chi_{Kq}(\mathbf{r},t), \tag{3.46}$$

where Φ_0 is the amplitude of the scalar potential. Now, we neglect the time dependence again since it is not important for the further derivations. We note that a gauge transformation does not change the matrix elements of the corresponding operators. With the gauge above, the interaction Hamiltonian of Eq. (3.2) transforms into

$$H^{(\mathrm{el})}_{Kq} = -\frac{e}{m_\mathrm{e}}\mathbf{p}\cdot\mathbf{a}^{(1)}_{Kq}(\mathbf{r}) + \frac{e}{c}\Phi(\mathbf{r}) \tag{3.47}$$

$$= \frac{e}{m_\mathrm{e}}A_0\mathbf{p}\cdot\left(-j_{K+1}(kr)\left[\mathbf{Y}^{(1)}_{Kq}(\hat{\mathbf{r}}) - \sqrt{\frac{K+1}{K}}\mathbf{Y}^{(-1)}_{Kq}(\hat{\mathbf{r}})\right]\right)$$

$$+ i\frac{e}{c}\frac{\omega}{k}\Phi_0\sqrt{\frac{K+1}{K}}j_K(kr)Y^q_K(\hat{\mathbf{r}}). \tag{3.48}$$

The condition $kr \ll 1$ allows us to approximate the spherical Bessel function by $j_K(kr) \approx (kr)^K/[(2K+1)!!]$ [136]. We can see that the interaction from the vector potential is by orders in kr smaller than the interaction resulting from the scalar potential. Hence, we can neglect the vector potential component and the interaction Hamiltonian is given by

$$H^{(\mathrm{el})}_{Kq} \approx i\Phi_0\sqrt{\frac{K+1}{K}}\frac{(kr)^j}{(2K+1)!!}Y^q_K(\hat{\mathbf{r}}) \tag{3.49}$$

$$= i\Phi_0\sqrt{\frac{(2K+1)(K+1)}{4\pi K}}\frac{k^K}{(2K+1)!!}e\sqrt{\frac{4\pi}{(2K+1)}}r^K Y^q_K(\hat{\mathbf{r}}) \tag{3.50}$$

$$= i\Phi_0\sqrt{\frac{(2K+1)(K+1)}{4\pi K}}\frac{k^K}{(2K+1)!!}Q^{(\mathrm{el})}_{Kq}. \tag{3.51}$$

In the last line we defined the electric multipole transition operator $Q^{(\mathrm{el})}_{Kq}$ [134], which is a tensor operator of rank K. For $K=1$, the derived operator corresponds to the electric dipole transition operator defined in Eq. (3.16), which is given here in the spherical basis [114]

$$\hat{\mathbf{e}}_q\cdot\boldsymbol{d} = e\hat{\mathbf{e}}_q\cdot\mathbf{r} = e\sqrt{\frac{4\pi}{3}}rY^q_K(\hat{\mathbf{r}}) = Q^{(\mathrm{el})}_{1q},$$

where $\hat{\mathbf{e}}_q$ is a basis vector of the spherical basis.

The transition operator $H^{(\mathrm{el})}_{Kq}$ in Eq. (3.49) couples to the electron wave functions of the atomic states involved. Hence, the operator contains the selection rules of the corresponding transition. Using the parity operator $\mathcal{P}\Psi(\mathbf{r}) = \Psi(-\mathbf{r})$, we investigate the parity of $H^{(\mathrm{el})}_{Kq}$ and we obtain

$$\mathcal{P}H^{(\mathrm{el})}_{Kq} = \mathcal{P}[r^K Y^q_K(\hat{\mathbf{r}})] = |-\mathbf{r}|^K Y^q_K(-\hat{\mathbf{r}}) = r^K(-1)^K Y^q_K(\hat{\mathbf{r}}). \tag{3.52}$$

Hence, the electric multipole transition operator has a parity of $(-1)^K$. Due to the parity conservation law, electric dipole (E1) transitions connect states of different parity and electric quadrupole (E2) transitions states of equal parity, where the parity of an atomic state depends on the angular momentum L with $(-1)^L$. At the same time, this means that for E1 $\Delta L = \pm 1$ and for E2 $\Delta L = 0, \pm 2$.

The light field contains angular momentum K described by the spherical harmonic $Y^q_K(\hat{\mathbf{r}})$ resulting transition specific selection rules. We can obtain these selection rules by calculating the matrix element between the states of the transition. This matrix element depends on the radial $|\gamma\rangle$ and the angular $|J, m\rangle$ component of the electronic wave function [114]. Since $Q^{(\mathrm{el})}_{Kq}$ is an irreducible tensor operator of rank K, we can use the Wigner-Eckart theorem [114] to obtain [143, 144]

$$\langle \gamma', J', m'|Q^{(\mathrm{el})}_{Kq}|\gamma, J, m\rangle = (-1)^{J'-m'} \begin{pmatrix} J' & K & J \\ -m' & q & m \end{pmatrix} \langle \gamma', J'||Q^{(\mathrm{el})}_K||\gamma, J\rangle, \tag{3.53}$$

where $\langle \gamma', J'||Q^{(\mathrm{el})}_K||\gamma, J\rangle$ is the reduced matrix element. The Wigner $3j$-symbols are related to the Clebsch-Gordan coefficients described in Ref. [144]. The Wigner $3j$-symbols follow the triangle condition $|J' - K| \leq J \leq J' + K$ [133] and vanish otherwise. This condition results in the fact that dipole transitions ($K = 1$) cannot drive $J = 0 \nleftrightarrow J' = 0$ transitions and quadrupole transitions ($K = 2$) cannot drive $J = 0 \nleftrightarrow J' = 0, 1$ transitions, giving us additional selection rules.

Due to the conservation of angular momentum reflected by the Wigner $3j$-symbols, we find that $K \geq |\Delta J| = |J' - J|$. Furthermore, the projection of the angular momentum onto the quantization axis has to satisfy the condition $q = \Delta m = m' - m$. For electric dipole transitions, the angular momentum of the light field is given by the photon's spin, whereas for higher order multipole transitions, the field provides additional angular momentum.

Now, we briefly give explicit examples of one electric dipole and one electric quadrupole transition. In strontium, the $^1\mathrm{S}_0$-$^3\mathrm{P}_1$ transition is an electric dipole transition. The $^1\mathrm{S}_0$ state with $L = 0$ has even parity and angular momentum of $J = 0$. The excited $^3\mathrm{P}_1$ state with $L' = 1$ has odd parity and $J' = 1$. Therefore, the transition connects states of different parity and an angular momentum difference of $\Delta J = 1$. One example of an electric quadrupole transition is the $^2\mathrm{S}_{1/2}$-$^2\mathrm{D}_{5/2}$ transition in Ca^+ [145], where both states have odd parity and $\Delta J = 2$.

In this Section we have demonstrated how to obtain the electric multipole transition operator from our general interaction Hamiltonian and the expansion of the plane-wave

vector potential. We calculated the length form of the operator by applying the corresponding gauge transformation. We deduced the parity of the multipole operator and the maximum transfer of angular momentum transfer occurring during an electric multipole transition. By calculating the transition matrix element, we derived that the rank K of the transition operator has the meaning of the amount of angular momentum that can maximally be transferred during a transition.

3.2.3 Magnetic multipole transition operator

In the previous Section, we derived the electric multipole transition operator starting from the interaction Hamiltonian and the expansion of the plane wave. Now, we will generate a basic understanding of magnetic multipole transitions by deriving the corresponding transition operator. The light-matter interaction associated with the magnetic part of the vector potential is given by

$$H_{Kq}^{\mathrm{mg}} \equiv H_{Kq}^{(\lambda)} = -\frac{e}{m_{\mathrm{e}}}\mathbf{p}\cdot\mathbf{a}_{Kq}^{(0)}(\mathbf{r}) + g_{\mathrm{B}}\mu_{\mathrm{B}}\left[\boldsymbol{\nabla}\times\mathbf{a}_{Kq}^{(0)}(\mathbf{r})\right]\cdot\mathbf{S}, \tag{3.54}$$

where we again omit the time dependence and use the Coulomb gauge. The Hamiltonian consists of two terms. The first term contains the interaction between a charged particle and the magnetic components of the vector potential. This term has a form similar to the starting point of our derivation of the electric multipole transition operator. The second term can be seen as the electron spin $\mathbf{S}$ directly interacting with the magnetic field $\mathbf{B} = \boldsymbol{\nabla}\times\mathbf{A}$.

To obtain the magnetic multipole transition operator, we combine the two terms by calculating $\mathbf{p}\cdot\mathbf{a}_{Kq}^{(0)} = -i\hbar\boldsymbol{\nabla}\cdot\mathbf{a}_{Kq}^{(0)}$ and $\boldsymbol{\nabla}\times\mathbf{a}_{Kq}^{(0)}$. The functions $\mathbf{a}_{Kq}^{(0)}$ consist of the vector spherical harmonics and since they are defined in a spherical basis, it is convenient to also express our operators in a spherical basis. We use the following identities [136]

$$\mathbf{L} = \mathbf{r}\times\mathbf{p} = \frac{h}{i}\mathbf{r}\times\boldsymbol{\nabla}, \tag{3.55}$$

$$\boldsymbol{\nabla} = \frac{\mathbf{r}}{r}\frac{\partial}{\partial r} - \frac{i}{\hbar r^2}\mathbf{r}\times\mathbf{L}. \tag{3.56}$$

Because we want to combine both interaction terms, we bring the first one into a form closer to the spin-field interaction [134]

$$\mathbf{p}\cdot\mathbf{a}_{Kq}^{(0)} = -iA_0\hbar\left(\frac{\mathbf{r}}{r}\frac{\partial}{\partial r} - \frac{i}{\hbar r^2}\mathbf{r}\times\mathbf{L}\right)\cdot\left[j_K(kr)\mathbf{Y}_{Kq}^{(0)}(\hat{\mathbf{r}})\right] \tag{3.57}$$

$$= -i\hbar A_0\frac{\mathbf{r}}{r}\cdot\frac{\mathbf{L}}{\sqrt{K(K+1)}}Y_K^q(\hat{\mathbf{r}})\frac{\partial j_K(kr)}{\partial r} - A_0\frac{j_K(kr)}{r^2}(\mathbf{r}\times\mathbf{L})\cdot\mathbf{Y}_{Kq}^{(0)}(\hat{\mathbf{r}}) \tag{3.58}$$

$$= A_0\frac{1}{r^2}j_K(kr)\left[\mathbf{r}\times\mathbf{Y}_{Kq}^{(0)}(\hat{\mathbf{r}})\right]\cdot\mathbf{L}, \tag{3.59}$$

where we inserted the definition of the vector spherical harmonics $\mathbf{Y}_{Kq}^{(0)}(\hat{\mathbf{r}})$ from Eq. (3.27).

The first term of the second line vanishes because $\mathbf{r}$ and $\mathbf{L}$ are perpendicular, resulting in $\mathbf{r}\cdot\mathbf{L}=0$. The vector spherical harmonic $\mathbf{Y}^{(0)}_{Kq}\propto\mathbf{L}$ commutes with $\mathbf{L}$ and hence, we can use the permutation rules of the triple product to obtain the last line.

We obtained an expression for the first interaction term containing the angular momentum operator $\mathbf{L}$ and therefore, we try to group $\mathbf{L}$ with the spin operator $\mathbf{S}$. Before we can actually group the operators, we rewrite both interaction terms into forms similar to the electric multipole operator $Q^{(\mathrm{el})}_{Lq}$. We start with the interaction containing $\mathbf{L}$ and transform the expression into [134]

$$\frac{1}{r^2}j_K(kr)\left[\mathbf{r}\times\mathbf{Y}^{(0)}_{Kq}(\hat{\mathbf{r}})\right]=\frac{1}{r^2}j_K(kr)\left[\mathbf{r}\times\frac{\mathbf{L}}{\sqrt{K(K+1)}}Y^q_K(\hat{\mathbf{r}})\right] \tag{3.60}$$

$$=\frac{\hbar}{i}\frac{j_K(kr)}{r^2}(\mathbf{r}-r^2\boldsymbol{\nabla})\frac{1}{\sqrt{K(K+1)}}Y^q_K(\hat{\mathbf{r}}), \tag{3.61}$$

$$=\frac{\hbar}{i}\left(\frac{\partial j_K(kr)}{\partial r}\right)\frac{1}{\sqrt{K(K+1)}}\frac{\mathbf{r}}{r}Y^q_K(\hat{\mathbf{r}})-\frac{\hbar}{i}\frac{j_K(kr)}{\sqrt{K(K+1)}}\boldsymbol{\nabla}Y^q_K(\hat{\mathbf{r}}) \tag{3.62}$$

$$=-\frac{i\hbar}{\sqrt{K(K+1)}}\boldsymbol{\nabla}\left[j_K(kr)Y^q_K(\hat{\mathbf{r}})\right]. \tag{3.63}$$

The result allows us to bring the first term of $H^{(\mathrm{mg})}_{Kq}$ into the form

$$-\frac{e}{m_\mathrm{e}}\mathbf{p}\cdot\mathbf{a}^{(0)}_{Kq}(\mathbf{r})=i\frac{e\hbar}{m_\mathrm{e}}A_0\frac{1}{\sqrt{K(K+1)}}\boldsymbol{\nabla}\left[j_K(kr)Y^q_K(\hat{\mathbf{r}})\right]\cdot\mathbf{L}. \tag{3.64}$$

This term has a very similar shape as the electric multipole transition operator. We identify our result as the magnetic multipole transition operator for the light-matter interaction of a spinless charged particle. The next step is to calculate the spin-field interaction given by

$$\boldsymbol{\nabla}\times\mathbf{a}^{(0)}_{Kq}(\mathbf{r})=(\boldsymbol{\nabla}\times\mathbf{L})A_0\frac{j_K(kr)}{\sqrt{K(K+1)}}Y^q_K(\hat{\mathbf{r}}). \tag{3.65}$$

Using the identity $\boldsymbol{\nabla}\times\mathbf{L}=-i\mathbf{r}\boldsymbol{\nabla}^2+i\boldsymbol{\nabla}(\mathbf{r}\cdot\boldsymbol{\nabla}+1)$ [136], we can simplify the spin-field interaction to [134]

$$\boldsymbol{\nabla}\times\mathbf{a}^{(0)}_{Kq}(\mathbf{r})=-iA_0\mathbf{r}\boldsymbol{\nabla}^2\frac{j_K(kr)}{\sqrt{K(K+1)}}Y^q_K(\hat{\mathbf{r}})+A_0\boldsymbol{\nabla}(\mathbf{r}\cdot\boldsymbol{\nabla}+1)\frac{j_K(kr)}{\sqrt{K(K+1)}}Y^q_K(\hat{\mathbf{r}}) \tag{3.66}$$

$$=iA_0\sqrt{\frac{K+1}{K}}\boldsymbol{\nabla}\left[j_K(kr)Y^q_K(\hat{\mathbf{r}})\right]. \tag{3.67}$$

The first term of the first line vanishes because $\boldsymbol{\nabla}^2\mathbf{a}^{(0)}_{Kq}=0$ as one can easily prove [146].

We combine both interaction terms and the light-matter Hamiltonian becomes

$$\begin{aligned} H_{Kq}^{(\mathrm{mg})} =& i\frac{e\hbar}{2m_\mathrm{e}}A_0\frac{2}{\sqrt{K(K+1)}}\boldsymbol{\nabla}\left[j_K(kr)Y_K^q(\hat{\mathbf{r}})\right]\cdot\mathbf{L} \\ &+ ig_\mathrm{B}\mu_\mathrm{B}A_0\sqrt{\frac{K+1}{K}}\boldsymbol{\nabla}\left[j_K(kr)Y_K^q(\hat{\mathbf{r}})\right]\cdot\mathbf{S}. \end{aligned} \tag{3.68}$$

The spatial extent of the atom is much smaller than the wavelength of the light with $kr \ll 1$, leading to the approximation of the spherical Bessel function by [136]

$$j_K(kr) \approx (kr)^K/[(2K+1)!!]. \tag{3.69}$$

The approximation results in [129]

$$\begin{aligned} H_{Kq}^{(\mathrm{mg})} =& iA_0\sqrt{\frac{(2K+1)(K+1)}{4\pi K}}\frac{k^K}{(2K+1)!!}\mu_\mathrm{B}\sqrt{\frac{4\pi}{(2K+1)}} \\ &\times\boldsymbol{\nabla}\left[r^KY_K^q(\hat{\mathbf{r}})\right]\cdot\left(\frac{2}{K+1}\mathbf{L}+g_\mathrm{B}\mathbf{S}\right) \qquad (3.70) \\ =& iA_0\sqrt{\frac{(2K+1)(K+1)}{4\pi K}}\frac{k^K}{(2K+1)!!}Q_{Kq}^{(\mathrm{mg})}, \qquad (3.71) \end{aligned}$$

where we define the magnetic multipole transition operator $Q_{Kq}^{(\mathrm{mg})}$. For $K=1$, we obtain the magnetic dipole operator, which is similar to the magnetic dipole moment $\boldsymbol{q} = \mu_\mathrm{B}(\mathbf{L}+g_\mathrm{B}\mathbf{S})$ [114].

In analogy to the discussion of the electric multipole operator's parity in the previous Section, we can calculate the parity of the magnetic multipole operator

$$\mathcal{P}H_{Kq}^{(\mathrm{mg})} = \mathcal{P}\{(\boldsymbol{\nabla}\left[r^KY_K^q(\hat{\mathbf{r}})\right]\cdot[\mathbf{L}+\mathbf{S}]\} = (-1)^{K+1}H_{Kq}^{(\mathrm{mg})}. \tag{3.72}$$

The $\boldsymbol{\nabla}$ operator has odd parity, the spherical harmonics a parity of $(-1)^K$, and both the angular momentum operator $\mathbf{L}$ and spin operator $\mathbf{S}$ have even parity. Hence, magnetic dipole (M1) transitions can connect states of the same parity with $\Delta L = 0$ and magnetic quadrupole (M2) transitions of unequal parity with $\Delta L = \pm 1$. Similar to the electric transition, magnetic multipole transitions can connect states with a maximum difference in total electronic angular momentum $|\Delta J| = K$.

In analogy to the electric multipole transition operator, the magnetic multipole operator is also an irreducible tensor operator of rank K, resulting in [147]

$$\langle\gamma', J', m'|Q_{Kq}^{(\mathrm{mg})}|\gamma, J, m\rangle = (-1)^{J'-m'}\begin{pmatrix} J' & K & J \\ -m' & q & m \end{pmatrix}\langle\gamma', J'||Q_K^{(\mathrm{mg})}||\gamma, J\rangle, \tag{3.73}$$

where $\langle\gamma', J'||Q_K^{(\mathrm{mg})}||\gamma, J\rangle$ is the reduced matrix element. By comparing this equation to Eq. (3.53), we observe that electric and magnetic multipole transitions with equal K

and q possess the same Clebsch-Gordan coefficients and the same angular momentum selection rules.

Magnetic dipole transitions can be found in alkali atoms, connecting the hyperfine ground states. In strontium, the $^3P_2$ state decays predominately to the $^3P_1$ state via an M1 transition with $\Delta L = 0$ and $|\Delta J| = 1$. The $^1S_0$-$^3P_2$ transition is a magnetic quadrupole one with $\Delta L = 1$ and $|\Delta J| = 2$, where both state have even parity.

In this Section we obtained the magnetic multipole transition operator from the interaction Hamiltonian consisting of the minimal coupling Hamiltonian and a coupling of the vector potential to the electron spin $\mathbf{S}$. The multipole operator that we derived directly contains the angular momentum operator $\mathbf{L}$ and the spin operator $\mathbf{S}$. Therefore, the operator takes into account the interaction between a magnetic field and the electron spin, while the electric field does not couple to the spin. We note that the magnetic multipole operator is given in the velocity form because we used the Coulomb gauge in the derivation.

3.3 Relative transition strength of multipole transitions

In this section, we estimate the relative transition strength between electric and magnetic multipole transitions of the same rank K. Moreover, we compare the strength of electric and magnetic transitions.

The scattering rate of magnetic and electric multipole transitions is given by

$$\frac{\Gamma_{(\mathrm{mg})}}{\Gamma_{(\mathrm{el})}} = \frac{|H_{Kq}^{(\mathrm{mg})}|^2}{|H_{Kq}^{(\mathrm{el})}|^2} \propto \left(\frac{B_0 \mu_\mathrm{B} r^{K-1}}{E_0 e r^K}\right)^2, \tag{3.74}$$

where B_0 is the magnetic field amplitude and $E_0 = cB_0$ is the electric field amplitude. For atomic transitions we can approximate the radius $r \approx \frac{a_0}{Z_\mathrm{eff}}$, where $a_0 = \frac{\hbar}{m_\mathrm{e} c \alpha}$ is the Bohr radius, Z_eff the effective charge, and α the fine-structure constant. Inserting these relations into the equation above, we obtain

$$\frac{\Gamma_K^{(\mathrm{mg})}}{\Gamma_K^{(\mathrm{el})}} \propto \alpha^2 Z_\mathrm{eff}^2. \tag{3.75}$$

This relation shows that atomic magnetic multipole transition rates are suppressed by a factor of α^2 compared to electric transitions of the same K. Hence, electric quadrupole transitions are $\sim 10^5$ times stronger than magnetic quadrupole transitions.

We can also estimate the relative strength of electric or magnetic multipole transitions of different ranks. For example, we study the relative transition rates of electric transitions

$$\frac{\Gamma_{K+1}^{(\mathrm{el})}}{\Gamma_K^{(\mathrm{el})}} = \frac{|H_{K+1q}^{(\mathrm{el})}|^2}{|H_{Kq}^{(\mathrm{el})}|^2} = \left(\frac{E_0 k^{K+1} r^{K+1}}{E_0 k^K r^K}\right)^2 = (kr)^2. \tag{3.76}$$

For atomic transitions we can use $k = \frac{E}{\hbar c}$, where E is the energy splitting between the atomic levels of the transition. For estimates this energy is given by two times the Rydberg energy with $E = Z_{\text{eff}} \frac{m_e e^4}{4\epsilon_0^2 h^2}$ and we obtain

$$\frac{\Gamma_{K+1}^{(\text{el})}}{\Gamma_K^{(\text{el})}} \propto \left(\underbrace{\frac{m_e c}{\hbar} \alpha^2 Z_{\text{eff}}^2}_{k} \underbrace{\frac{\hbar}{m_e c \alpha Z_{\text{eff}}}}_{r} \right)^2 = \alpha^2 Z_{\text{eff}}^2. \tag{3.77}$$

From the derived relative transition rates, we observe that in atoms electric dipole transitions will always dominate the total transition strength if they are allowed by the selection rules. For nuclear transitions, the wavelength of emitted X-rays or γ-rays can become comparable to the size of the nucleus. Hence, the rates of quadrupole or octupole transitions can become comparable to dipole transitions [136]. Furthermore, nuclei can possess large magnetic moments resulting in a dominant higher order magnetic multipole transition.

3.4 Angular dependence of multipole transition amplitudes

In this Section, we discuss the transition amplitude's angular dependence [114] for electric and magnetic multipole transitions. In general, these geometric characteristics depend on the probe beam polarization and the beam propagation direction with respect to the atomic quantization axis. The angular dependence of multipole transitions is remarkably different from the one of the well-known electric dipole transitions.

We remember that the expansion of the vector potential in vector spherical harmonics $\mathbf{Y}_{Kq}^{(\lambda)}$ in Sec. 3.2 allowed us to separate the angular dependence of a transition from the transition operator

$$H_{\text{int}} = 4\pi \sum_{K,q,\lambda} i^{K-\lambda} \left[\mathbf{Y}_{Kq}^{(\lambda)}(\hat{\mathbf{k}}) \cdot \hat{\boldsymbol{\epsilon}} \right] H_{Kq}^{(\lambda)}. \tag{3.78}$$

Here, we can extend the equation describing a single electron to describing many electrons, since the polarization and wave vector do not depend on the electrons and only $H_{Kq}^{(\lambda)}$ is modified [134]. The transition operator $H_{Kq}^{(\lambda)}$ interacts with the electrons' wave functions describing the total transition strength and can be ignored for the discussion of the angular dependence.

This dependence is described by $C_{Kq}^{(\lambda)} = \mathbf{Y}_{Kq}^{(\lambda)}(\hat{\mathbf{k}}) \cdot \hat{\boldsymbol{\epsilon}}$. The transition amplitude is given by $A_{Kq} = |C_{Kq}^{(\lambda)}|^2$.

To simplify the calculations, we use the natural coordinate system shown in Fig. 3.1, based on a quantization along $\hat{\mathbf{z}}$ given by an external magnetic field $\mathbf{B}$, and the beam propagation direction $\hat{\mathbf{k}}$. This coordinate system allows us to describe the relevant vectors

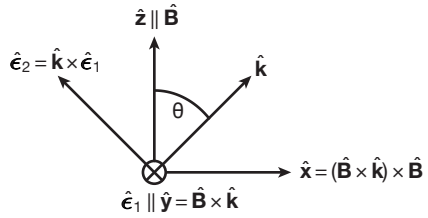

Fig. 3.1 Natural coordinate system to describe the angular dependence of atomic multipole transition amplitudes. The magnetic field $\mathbf{B}$ defines the quantization axis and atomic frame. The wave vector $\mathbf{k}$ is related to $\mathbf{B}$ by $\cos(\theta) = \hat{\mathbf{k}} \cdot \hat{\mathbf{B}}$, where a hat indicates a unit vector. We construct the polarization basis vectors $\hat{\boldsymbol{\epsilon}}_1 = \hat{\mathbf{B}} \times \hat{\mathbf{k}}$ and $\hat{\boldsymbol{\epsilon}}_2 = \hat{\mathbf{k}} \times \hat{\boldsymbol{\epsilon}}_1$.

using

$$\begin{aligned}
\hat{\mathbf{B}} &= \hat{\mathbf{z}}, \\
\hat{\mathbf{k}} &= \sin(\theta)\hat{\mathbf{x}} + \cos(\theta)\hat{\mathbf{z}}, \\
\hat{\boldsymbol{\epsilon}}_1 &= \hat{\mathbf{B}} \times \hat{\mathbf{k}} = \hat{\mathbf{y}}, \\
\hat{\boldsymbol{\epsilon}}_2 &= \hat{\mathbf{k}} \times \hat{\boldsymbol{\epsilon}}_1 = -\cos(\theta)\hat{\mathbf{x}} + \sin(\theta)\hat{\mathbf{z}}.
\end{aligned}$$

We construct the normalized Jones vectors $(\alpha, \beta)^\top$ [148] enabling the description of arbitrary polarizations $\hat{\boldsymbol{\epsilon}} = \alpha\hat{\boldsymbol{\epsilon}}_1 + \beta\hat{\boldsymbol{\epsilon}}_2$ with $|\alpha|^2 + |\beta|^2 = 1$. These polarizations are perpendicular to the wave vector $\hat{\mathbf{k}} \cdot \hat{\boldsymbol{\epsilon}} = 0$ due to our assumption of transverse fields for the plane wave expansion.

By choosing the natural coordinate system, $\hat{\mathbf{k}}$ is oriented in the xz-plane resulting in vanishing second argument of the (vector) spherical harmonics leading to $\mathbf{Y}^{(\lambda)}_{kq}(\hat{\mathbf{k}}) = \mathbf{Y}^{(\lambda)}_{kq}(\theta, \phi = 0)$. Then the interaction Hamiltonian is given by

$$\begin{aligned}
H_{\text{int}} =& 4\pi \sum_{K,q} i^{K+1} \sqrt{\frac{(2K+1)(K+1)}{4\pi K}} \frac{k^K}{(2K+1)!!} \\
&\times \left(\left[i\mathbf{Y}^{(1)}_{Kq}(\theta, 0) \cdot \hat{\boldsymbol{\epsilon}} \right] Q^{(\text{el})}_{Kq} + \left[\mathbf{Y}^{(0)}_{Kq}(\theta, 0) \cdot \hat{\boldsymbol{\epsilon}} \right] Q^{(\text{mg})}_{Kq} \right),
\end{aligned} \tag{3.79}$$

where the angular dependence of the corresponding multipole transition is given by $[\mathbf{Y}^{(\lambda)}_{Kq}(\theta, 0) \cdot \hat{\boldsymbol{\epsilon}}]^2$. Typically, the polarization $\hat{\boldsymbol{\epsilon}}$ is described in terms of the polarization basis vectors $\hat{\mathbf{e}}_{\pm 1}$ and $\hat{\mathbf{e}}_0$ corresponding to $\sigma^\pm$- and π-polarization in the atomic frame. To investigate the angular dependence, we decompose the vector spherical harmonics

using the same basis vectors, resulting in

$$\mathbf{Y}^{(1)}_{Kq}(\theta,0) = \sum_{\mu=-1}^{+1} \left[c^{(+)}_{\mu} Y^{q-\mu}_{K+1}(\theta,0) + c^{(-)}_{\mu} Y^{q-\mu}_{K-1}(\theta,0) \right] \hat{\mathbf{e}}_{\mu} \tag{3.80}$$

$$\mathbf{Y}^{(1)}_{Kq}(\theta,0) = \sum_{\mu=-1}^{+1} c^{(0)}_{\mu} Y^{q-\mu}_{K}(\theta,0) \hat{\mathbf{e}}_{\mu}, \tag{3.81}$$

where the coefficients $c^{(\pm,0)}_{\mu}$ weight the projections onto the individual basis vectors and can be obtained from the definition of the vector spherical harmonics. In the following, we will drop the arguments of the (vector) spherical harmonics for brevity.

From the expression above, we can observe the conservation of angular momentum during multipole transitions. The projection of the photon spin onto the quantization axis provides angular momentum of $m_s = 0, \pm 1$ according to the light polarization given by the basis vectors $\hat{\mathbf{e}}_{0,\pm}$, respectively. The light field can provide additional angular momentum $m_l = q, q \pm 1$ described by the spherical harmonics $Y^{q-\mu}_{K}$. Both angular momenta follow the relation $\Delta m = m' - m = m_s + m_l$ satisfying the conservation of angular momentum, where Δm is the difference between the Zeeman sublevels.

We can use the decomposition in Eq. (3.80) and in Eq. (3.81) to visualize the angular dependence of the vector spherical harmonics. This visualization will help us to gain first insight into the transition amplitude's angular dependence [114].

Before we show the visualization, we briefly discuss the emission patterns of multipole transitions. We can calculate these patterns by averaging over the all polarizations with equal contributions along the vectors $\hat{\mathbf{e}}_0$ and $\hat{\mathbf{e}}_{\pm}$. Hence, the emission patterns can be obtained from the decomposition by calculating the normalized strengths

$$P^{(\mathrm{el})}_{K,q} = \Big| \sum_{q=-1}^{+1} \left(c^{(+)}_{\mu} Y^{q-\mu}_{K+1} + c^{(-)}_{\mu} Y^{q-\mu}_{K-1} \right) \Big|^2 \tag{3.82}$$

$$P^{(\mathrm{mg})}_{K,q} = \Big| \sum_{\mu=-1}^{+1} c^{(0)}_{\mu} Y^{q-\mu}_{K} \Big|^2 \tag{3.83}$$

We note that the emission pattern is the coherent sum of the vector spherical harmonic's decomposition.

In the following Subsections, we present a visualization describing the angular dependence of dipole and quadrupole transition amplitudes. We show this visualization at the example of dipole transitions between states of $J = 0 \to J' = 1$ resulting in $\Delta J = K = 1$ and for quadrupole transition between states of $J = 0 \to J' = 2$ with $\Delta J = K = 2$. The visualization helps us to develop intuition about the geometric dependencies of the transitions. Moreover, our method can easily be adapted to higher-order multipole transitions. At the end of each Subsection, we show the transition amplitude's angular characteristics for a general linear polarization.

3.4.1 Electric dipole transition

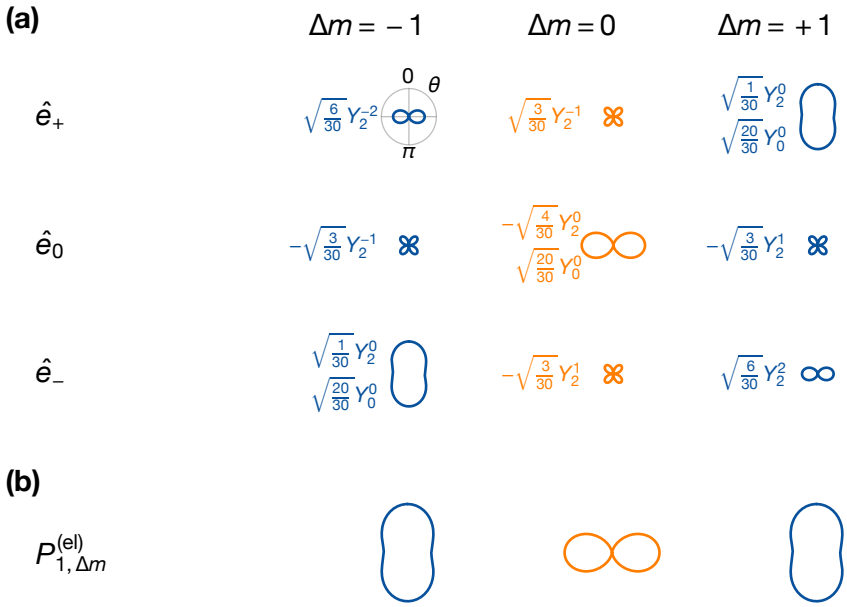

Fig. 3.2 (a) Visualization of the angular characteristics of the electric dipole transition's vector spherical harmonics describing transitions with a difference Δm between the Zeeman sublevels. Due to the choice of coordinate system, the second argument of the spherical harmonics vanish with $Y^q_{0,2}(\theta, 0)$. We decompose the vector spherical harmonics into contributions along the basis vectors $\hat{\mathbf{e}}_0$ and $\hat{\mathbf{e}}_\pm$ corresponding to the polarization π and $\sigma^\pm$ in the atomic frame. We note that this visualization contains also unphysical combinations of $\hat{\mathbf{k}}$ and $\hat{\boldsymbol{\epsilon}}$ with $\hat{\mathbf{k}} \cdot \hat{\boldsymbol{\epsilon}} \neq 0$ reflected by combinations of θ and the basis vectors. Δm describes the difference in Zeeman sublevels for an absorption of a photon. (b) Emission pattern of an electric dipole transition.

We study the geometric dependence of the electric dipole transition $(K = 1)$ with a difference of Δm between the Zeeman sublevels. Using the decomposition in Eq. (3.80), we show the angular dependence of the vector spherical harmonics in Fig. 3.2(a), describing the electric dipole transition. Due to the choice of the coordinate system with $\phi = 0$, all spherical harmonics are real, and we plot their value as a function of θ in polar coordinates.

This visualization may seem intuitively wrong since, we know that only $\hat{\mathbf{e}}_{+1}$ (corresponding to σ^+-polarized light) drives the $\Delta m = +1$ transition, while here also $\hat{\mathbf{e}}_0$ and $\hat{\mathbf{e}}_{-1}$ show non-vanishing contributions. The reason is that this visualization contains all combinations of $\hat{\mathbf{k}}$ and $\hat{\boldsymbol{\epsilon}}$ even if $\hat{\mathbf{k}} \cdot \hat{\boldsymbol{\epsilon}} \neq 0$, which may become relevant when the light field cannot be approximated as a plane wave like a beam focused through a high-numerical aperture objective.

We observe in the visualization of $\Delta m = 0$ for $\hat{\boldsymbol{e}}_0$ (π-polarization) that the spherical harmonic is vanishing for $\theta = 0$. This behavior agrees with the expectation since π-

polarization can never be achieved with $\hat{\mathbf{k}}$ being parallel to the quantization axis.

In Fig. 3.2(b) we show the emission patterns of the electric dipole transition calculated with Eq. (3.82). The patterns agree with the classical dipole patterns presented in Ref. [136].

As a sanity check, we calculate the electric dipole transition amplitude's angular dependence of the different $\Delta m = q = 0, \pm$ transitions for a general polarization $\hat{\boldsymbol{\epsilon}} = \alpha\hat{\boldsymbol{\epsilon}}_1 + \beta\hat{\boldsymbol{\epsilon}}_2$ with $|\alpha|^2 + |\beta|^2 = 1$ and the normalized Jones vectors $(\alpha, \beta)^\top$. Using this polarization, the transition amplitude is given by

$$\mathcal{A}_{1,0} \equiv (\mathbf{Y}_{1,0} \cdot \hat{\boldsymbol{\epsilon}})^2 = [\mathbf{Y}_{1,0} \cdot (\alpha\hat{\boldsymbol{\epsilon}}_1 + \beta\hat{\boldsymbol{\epsilon}}_2)]^2 = \frac{3}{8\pi}|\beta|^2 \sin^2\theta, \tag{3.84}$$

$$\begin{aligned}\mathcal{A}_{1,\pm1} &\equiv (\mathbf{Y}_{1,\pm1} \cdot \hat{\boldsymbol{\epsilon}})^2 = [\mathbf{Y}_{1,\pm1} \cdot (\alpha\hat{\boldsymbol{\epsilon}}_1 + \beta\hat{\boldsymbol{\epsilon}}_2)]^2 \\ &= \frac{3}{16\pi}\left(\alpha \pm i\beta\cos\theta\right)\left(\alpha^* \mp i\beta^*\cos\theta\right),\end{aligned} \tag{3.85}$$

We compare the results obtained with the general formalism to the results corresponding to calculating the transition amplitude using $\mathbf{d} \cdot \mathbf{E}$. We expect that only π-polarization in the atomic frame drives the $\Delta m = 0$ transition. We obtain the angular dependence by projecting the electric field $\hat{\boldsymbol{\epsilon}} E_0$ onto $\hat{\mathbf{e}}_0$ resulting in

$$\begin{aligned}\mathcal{A}_{1,0} &= \left([\alpha\hat{\boldsymbol{\epsilon}}_1 + \beta\hat{\boldsymbol{\epsilon}}_2] \cdot \hat{\mathbf{e}}_0 \left[-\sqrt{\frac{4}{30}}Y_2^0\left(\frac{\pi}{2}, 0\right) + \sqrt{\frac{20}{30}}Y_0^0\left(\frac{\pi}{2}, 0\right)\right]\right)^2 \\ &= \frac{3}{8\pi}|\beta|^2 \sin^2\theta.\end{aligned} \tag{3.86}$$

We note that pure π-polarization can only be obtained for $\theta = \pi/2$ and insert the decomposition of the vector spherical harmonic shown in Fig. 3.2(a). This result agrees with the one obtained above, demonstrating that our general formalism agrees with the physical intuition from $\mathbf{d} \cdot \mathbf{E}$.

For $\Delta m = \pm 1$, we can perform analogous calculations by projecting the electric field onto the basis vectors $\hat{\mathbf{e}}_\pm$, which correspond to $\sigma^\pm$-polarization. There, we use $\theta = 0$, since only for $\hat{\mathbf{k}} \parallel \hat{\mathbf{B}}$ we can obtain pure $\sigma^\pm$-polarization. The calculation gives us the expected result

$$\begin{aligned}\mathcal{A}_{1,\pm1} &= \left([\alpha\hat{\boldsymbol{\epsilon}}_1 + \beta\hat{\boldsymbol{\epsilon}}_2] \cdot \hat{\mathbf{e}}_{\pm1} \left[\sqrt{\frac{1}{30}}Y_2^0\left(0, 0\right) + \sqrt{\frac{20}{30}}Y_0^0\left(0, 0\right)\right]\right)^2 \\ &= \frac{3}{16\pi}\left(\alpha \pm i\beta\cos\theta\right)\left(\alpha^* \mp i\beta^*\cos\theta\right).\end{aligned} \tag{3.87}$$

Now, we calculate the transition amplitude's angular dependence using a linear polarization given by

$$\hat{\boldsymbol{\epsilon}}_{\text{lin}} = \sin(\rho)\hat{\boldsymbol{\epsilon}}_1 - \cos(\rho)\hat{\boldsymbol{\epsilon}}_2 = \sin(\rho)\hat{\mathbf{y}} + \cos(\rho)\left[-\cos(\theta)\hat{\mathbf{x}} + \sin(\theta)\hat{\mathbf{z}}\right]. \tag{3.88}$$

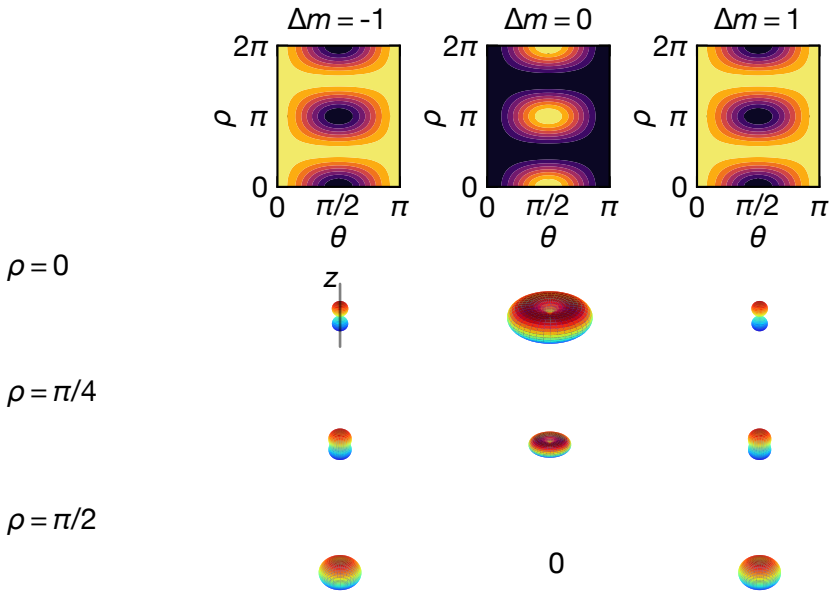

Fig. 3.3 Contour plot of the transition amplitude's angular dependence of the electric dipole transitions $[\mathbf{Y}^{(1)}_{1q}(\theta,0)\cdot\hat{\boldsymbol{\epsilon}}_{\mathrm{lin}}]^2$ with the linear polarization $\hat{\boldsymbol{\epsilon}}_{\mathrm{lin}}=\sin(\rho)\hat{\boldsymbol{\epsilon}}_1-\cos(\rho)\hat{\boldsymbol{\epsilon}}_2$ and $q=\Delta m$. In the first row, we show the angular characteristics as a function of θ and ρ in a contour plot, where the color from dark to light corresponding to a relative amplitude ranging from 0 to 1. In the second, third, and fourth row, we choose a specific ρ and present the corresponding transition amplitude in a 3D plot. Because the transition amplitude is an absolute value, phase factors vanish and the angular dependence is radially symmetric. The colors of the 3D plots are chosen for visibility and do not have a physical meaning.

We note that for $\rho=0$ the polarization is in the xz-plane and for $\rho=\pi/2$, the polarization is oriented along $\hat{\mathbf{y}}$. We show the transition amplitude's angular characteristics obtained from $\mathcal{A}^{(\mathrm{el})}_{1,q}=[\mathbf{Y}^{(1)}_{1q}(\theta,0)\cdot\hat{\boldsymbol{\epsilon}}_{\mathrm{lin}}]^2$ in the first row of Fig. 3.3. The colors encode the relative transition amplitude from 0 (dark) to 1 (bright).

We observe that where the $\Delta m=\pm1$ transition have an amplitude of 1, the $\Delta m=0$ transition's amplitude vanishes as a function of θ. This behavior is caused by the fact that the $\Delta m=\pm1$ ($\Delta m=0$) transitions are driven by $\sigma^{\pm}$-polarization (π-polarization) in the atomic frame, oriented perpendicular to each other. Furthermore, for $\rho=\pi/2$, the polarization is oriented along $\hat{\mathbf{y}}$ regardless of θ, corresponding to mixture of σ^+- and σ^--polarization with vanishing π-polarization. Therefore, the $\Delta m=\pm1$ transitions have a constant amplitude while the $\Delta m=0$ transition vanishes.

In the second, the third, and the fourth row of Fig. 3.3, we choose a specific ρ and show the transition amplitude in a 3D plot. Because the transition amplitude is given by $|\mathbf{Y}^{(\lambda)}_{Kq}\cdot\hat{\boldsymbol{\epsilon}}|^2$ the phase factor depending on ϕ vanishes resulting in radially symmetric transition amplitudes. These 3D plots are just a different visualization of the contour

plots for the chosen ρ. The $\Delta m = 0$ transition amplitude vanishes in the center, since for $\theta = 0$, we can not obtain a π-polarization with $\hat{\mathbf{k}} \cdot \hat{\epsilon}_{\text{lin}} = 0$. For $\rho = \pi/2$, we observe the discussed constant amplitudes of the $\Delta m = \pm 1$ transitions.

The presented formalism of calculating the angular dependence of the electric dipole transition agrees with our expectations. In the next Section, we will use this formalism to calculate the angular characteristics of magnetic dipole transitions.

3.4.2 Magnetic dipole transition

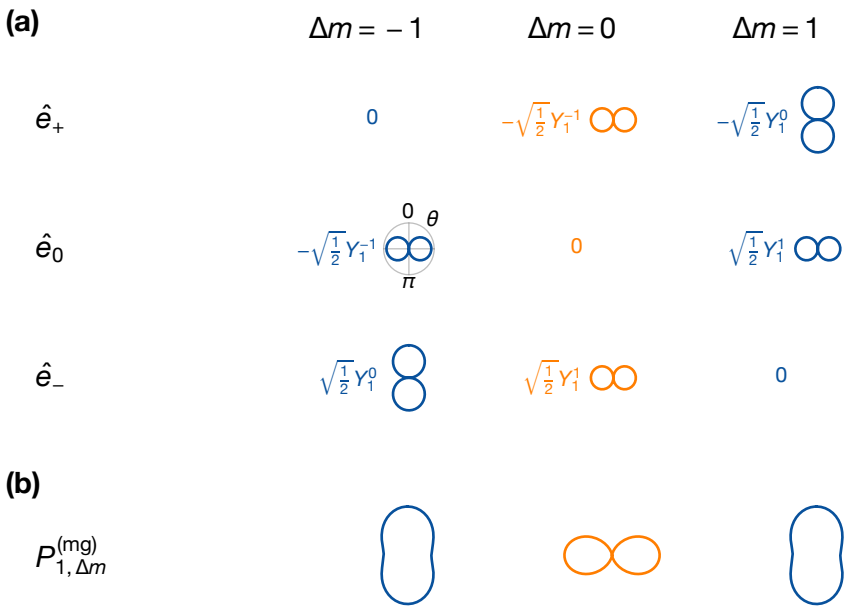

Fig. 3.4 (a) Visualization of the angular characteristics of the magnetic dipole transition's vector spherical harmonics describing transitions with a difference Δm between the Zeeman sublevels. Due to the choice of coordinate system, the second argument of the spherical harmonics vanish with $Y_1^q(\theta, 0)$. We decompose the vector spherical harmonics into contributions along the basis vectors $\hat{\mathbf{e}}_0$ and $\hat{\mathbf{e}}_\pm$ corresponding to the polarization π and $\sigma^\pm$ in the atomic frame. We note that this visualization contains also unphysical combinations of $\hat{\mathbf{k}}$ and $\hat{\epsilon}$ with $\hat{\mathbf{k}} \cdot \hat{\epsilon} \neq 0$ reflected by combinations of θ and the basis vectors. Δm describes the difference in Zeeman sublevels for an absorption of a photon. (b) Emission pattern of a magnetic dipole transition.

In analogy to the previous Section about the electric dipole transition, we now investigate the geometric dependence of the magnetic dipole transition $(K = 1)$. We show the visualization of the corresponding vector spherical harmonics in Fig. 3.4(a). Although the decomposition into vector spherical harmonics is different than the electric dipole transition ones, the emission patterns presented in Fig. 3.4(b) agree with the electric dipole's ones. The reason is that the emission patterns depend on the multipole order and not on whether a transition is of electric or magnetic nature.

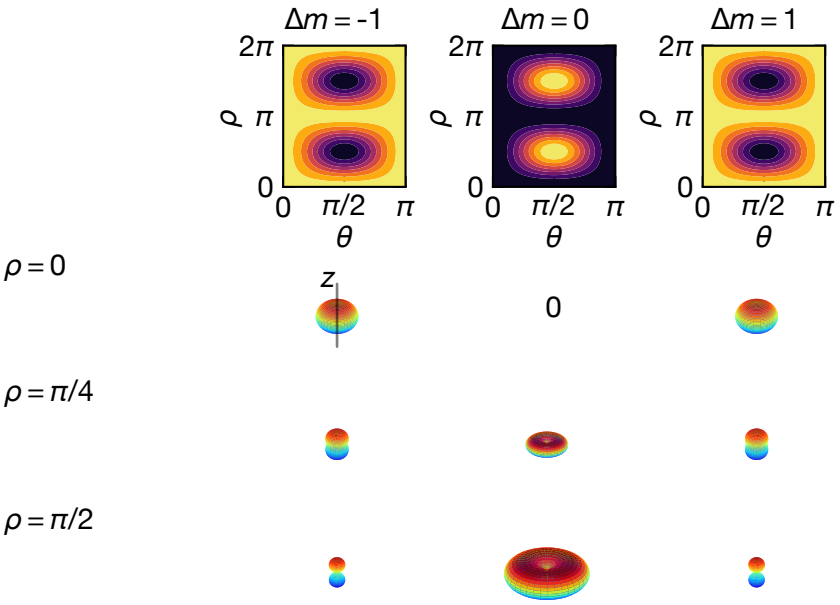

Fig. 3.5 Contour plot of the transition amplitude's angular dependence of the magnetic dipole transitions $[\mathbf{Y}_{1q}^{(0)}(\theta,0)\cdot\hat{\boldsymbol{\epsilon}}_{\mathrm{lin}}]^2$ with the linear polarization $\hat{\boldsymbol{\epsilon}}_{\mathrm{lin}}=\sin(\rho)\hat{\boldsymbol{\epsilon}}_1-\cos(\rho)\hat{\boldsymbol{\epsilon}}_2$ and $q=\Delta m$. In the first row, we show the angular characteristics as a function of θ and ρ in a contour plot, where the color from dark to light corresponding to a relative amplitude ranging from 0 to 1. In the second, third, and fourth row, we choose a specific ρ and present the corresponding transition amplitude in a 3D plot. Because the transition amplitude is an absolute value, phase factors vanish and the angular dependence is radially symmetric. The colors of the 3D plots are chosen for visibility and do not have a physical meaning.

We show the transition amplitude's angular characteristics obtained from $\mathcal{A}_{1,q}^{(\mathrm{mg})}=[\mathbf{Y}_{1q}^{(0)}(\theta,0)\cdot\hat{\boldsymbol{\epsilon}}_{\mathrm{lin}}]^2$ in Fig. 3.5. The colors of the contour plot in the first row encode the relative transition amplitude from 0 (dark) to 1 (light). Remarkably, the calculated angular dependence of the magnetic dipole transition amplitude agrees with electric dipole ones up to a phase shift of $\Delta\rho=\pi/2$. This phase shift makes perfect sense since the electric and the magnetic field are perpendicular to each other, corresponding to a phase shift of ρ.

3.4.3 Electric quadrupole transition

Now, we discuss the angular characteristics of the electric quadrupole transition amplitude. In Fig. 3.6(a), we present the visualization of the vector spherical harmonics decomposition in Eq. (3.80) with $K=\Delta J=2$. Since the component of the light field which is responsible for quadrupole transition can provide additional angular momentum of up to two quanta, transitions between Zeeman sublevels of $\Delta m=\pm 2$ become accessible.

We stress that this visualization does not describe the transition amplitude's angular

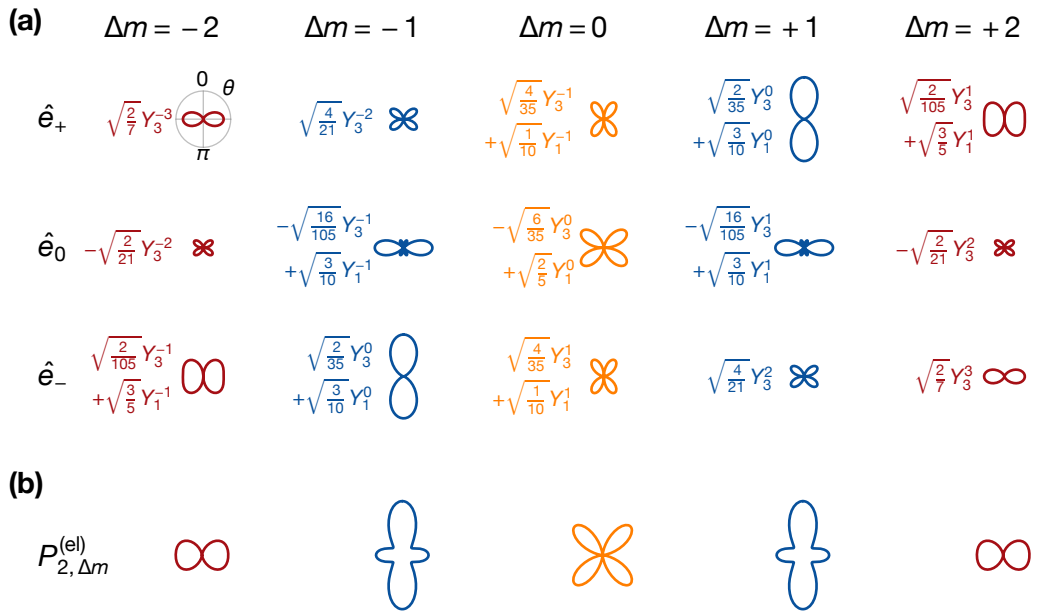

Fig. 3.6 (a) Visualization of the angular characteristics of the electric quadrupole transition's vector spherical harmonics describing transitions with a difference Δm between the Zeeman sublevels. Due to the choice of coordinate system, the second argument of the spherical harmonics vanish with $Y^q_{1,3}(\theta, 0)$. We decompose the vector spherical harmonics into contributions along the basis vectors $\hat{\mathbf{e}}_0$ and $\hat{\mathbf{e}}_\pm$ corresponding to the polarization π and $\sigma^\pm$ in the atomic frame. We note that this visualization contains also unphysical combinations of $\hat{\mathbf{k}}$ and $\hat{\epsilon}$ with $\hat{\mathbf{k}} \cdot \hat{\epsilon} \neq 0$ reflected by combinations of θ and the basis vectors. Δm describes the difference in Zeeman sublevels for an absorption of a photon. (b) Emission pattern of an electric quadrupole transition.

dependence since it contains also unphysical polarizations with $\hat{\boldsymbol{\epsilon}} \cdot \hat{\mathbf{k}} \neq 0$. However, we can still use it to obtain the angular characteristics. We find that the $\Delta m = \pm 2$ and $\Delta m = 0$ transitions vanish for the wave vector $\mathbf{k}$ being parallel to the magnetic field ($\theta = 0$), regardless of the polarization. Furthermore, we observe that the $\Delta m = 0$ transition also vanishes for $\theta = \pi/2$ and has a maximum transition strength for $\theta = \pi/4$. We cross-checked our calculations with the results of Ref. [149], which agree when we rotate our coordinate system into their system.

Using Eq. (3.82) we calculate the emission patterns of the electric quadrupole transition and show them in Fig. 3.6(b). We observe that these patterns are combinations of the decomposed spherical harmonics. The emission agrees with the one of classical quadrupole [136].

We show the electric quadrupole transition amplitude's angular characteristics obtained from $\mathcal{A}^{(\mathrm{el})}_{2,q} = [\mathbf{Y}^{(1)}_{2q}(\theta, 0) \cdot \hat{\boldsymbol{\epsilon}}_{\mathrm{lin}}]^2$ in Fig. 3.7. The colors of the contour plot in the first row encode the relative transition amplitude from 0 (dark) to 1 (light). As expected, the contour plots contain a different structure than the plot of the dipole transitions. We

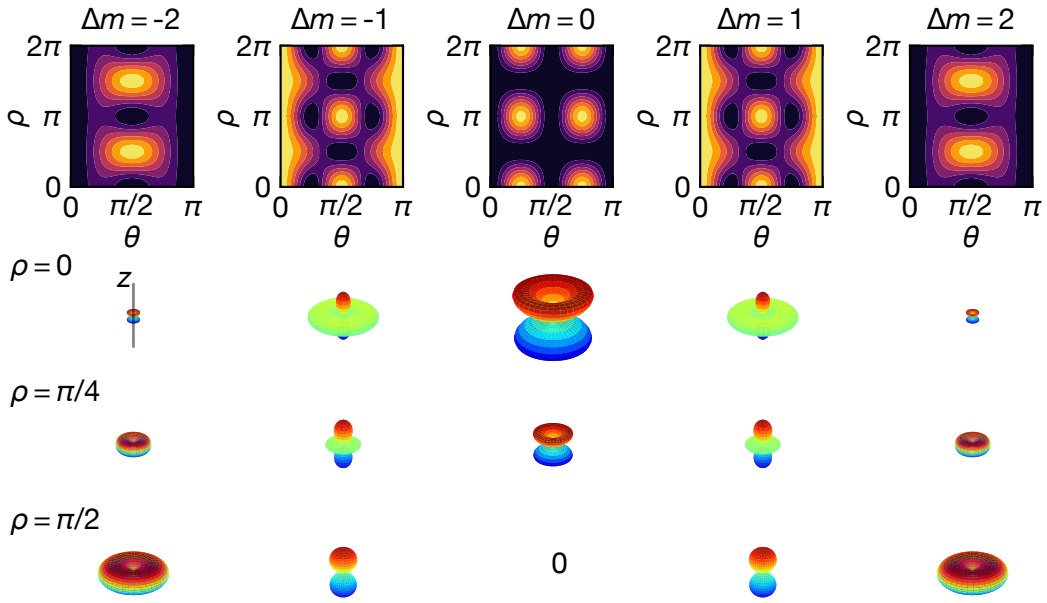

Fig. 3.7 Contour plot of the transition amplitude's angular dependence of the electric quadrupole transitions $[\mathbf{Y}^{(1)}_{2q}(\theta,0)\cdot\hat{\boldsymbol{\epsilon}}_{\mathrm{lin}}]^2$ with the linear polarization $\hat{\boldsymbol{\epsilon}}_{\mathrm{lin}}=\sin(\rho)\hat{\boldsymbol{\epsilon}}_1-\cos(\rho)\hat{\boldsymbol{\epsilon}}_2$ and $q=\Delta m$. In the first row, we show the angular characteristics as a function of θ and ρ in a contour plot, where the color from dark to light corresponding to a relative amplitude ranging from 0 to 1. In the second, third, and fourth row, we choose a specific ρ and present the corresponding transition amplitude in a 3D plot. Because the transition amplitude is an absolute value, phase factors vanish and the angular dependence is radially symmetric. The colors of the 3D plots are chosen for visibility and do not have a physical meaning.

find that the $\Delta m=\pm 2$ transitions vanish for $\theta=0$ and that the $\Delta m=0$ transition vanishes for $\theta=0$ and $\theta=\pi/2$. Both observations agree with the conclusion we draw from discussing the decomposition of the vector spherical harmonic in Fig. 3.6.

In the second, the third, and the fourth row of Fig. 3.7, we choose a specific ρ and show the transition amplitude in a 3D plot. The transition amplitude is an absolute value resulting in vanishing phase factors and a radial symmetry independent of phi. That the $\Delta m=0$ transition always vanishes for $\theta=0$ and $\theta=\pi/2$ shows that the electric quadrupole transition amplitude depends on the orientation of $\hat{\mathbf{k}}$ and the polarization. For $\rho=\pi/4$ and $\theta=\pi/2$, the polarization vector decomposes into a mixture of $\sigma^{\pm}$- and π-polarization in the atomic frame, but the transition amplitude still vanishes. Hence the quadrupole transition amplitude depends on θ and not exclusively on the polarization in the atomic frame as for dipole transitions.

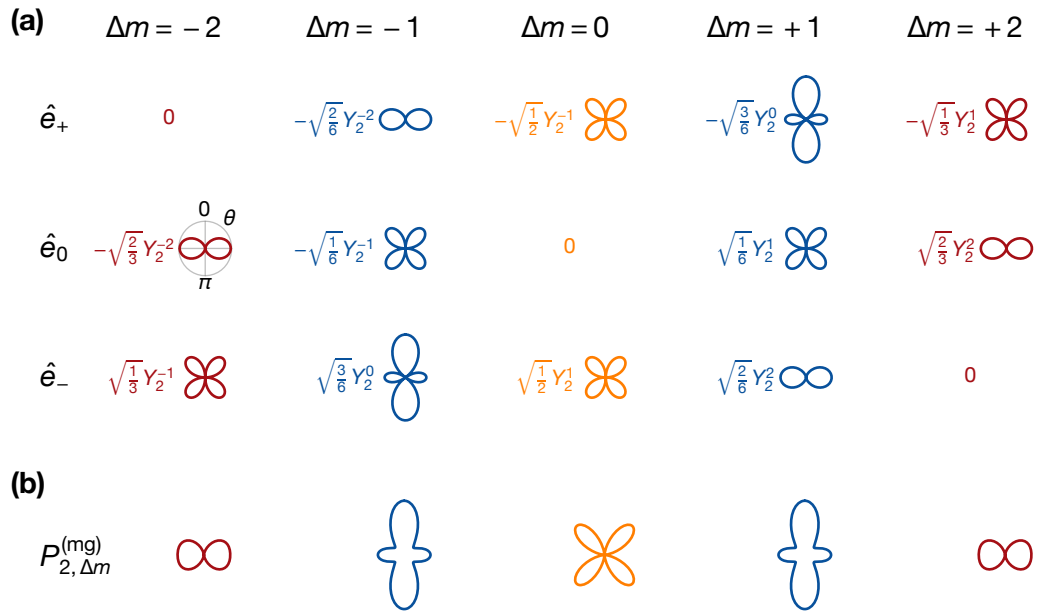

Fig. 3.8 (a) Visualization of the angular characteristics of the magnetic quadrupole transition's vector spherical harmonics describing transitions with a difference Δm between the Zeeman sublevels. Due to the choice of coordinate system, the second argument of the spherical harmonics vanish with $Y_2^q(\theta, 0)$. We decompose the vector spherical harmonics into contributions along the basis vectors $\hat{\mathbf{e}}_0$ and $\hat{\mathbf{e}}_\pm$ corresponding to the polarization π and $\sigma^\pm$ in the atomic frame. We note that this visualization contains also unphysical combinations of $\hat{\mathbf{k}}$ and $\hat{\epsilon}$ with $\hat{\mathbf{k}} \cdot \hat{\epsilon} \neq 0$ reflected by combinations of θ and the basis vectors. Δm describes the difference in Zeeman sublevels for an absorption of a photon. (b) Emission pattern of a magnetic quadrupole transition.

3.4.4 Magnetic quadrupole transition

Finally, we discuss the magnetic quadrupole transition amplitude's angular dependence. Magnetic quadrupole transitions are connecting states with $\Delta J = 2 = K$. We show the visualization of the decomposition of the vector spherical in Fig. 3.8(a). We find that the $\Delta m = \pm 2$ transition vanishes for $\theta = 0$. Moreover, the $\Delta m = 0$ transition can not be driven for $\theta = 0$ and $\theta = \pi/2$ regardless of the polarization.

The emission patterns are presented in Fig. 3.8(b), where we plot the transition amplitude as a function of θ. These patterns agree with the ones of classical electromagnetic quadrupoles [136].

In Fig. 3.7, we show the magnetic quadrupole transition amplitude's angular characteristics obtained from $\mathcal{A}_{2,q}^{(\mathrm{mg})} = [\mathbf{Y}_{2q}^{(0)}(\theta, 0) \cdot \hat{\boldsymbol{\epsilon}}_{\mathrm{lin}}]^2$. The colors of the contour plot in the first row encode the relative transition amplitude from 0 (dark) to 1 (light).

We observe that the angular characteristics of the magnetic quadrupole and electric quadrupole transition agree up to phase factor $\Delta\rho = \pi/2$, which can be explained by the

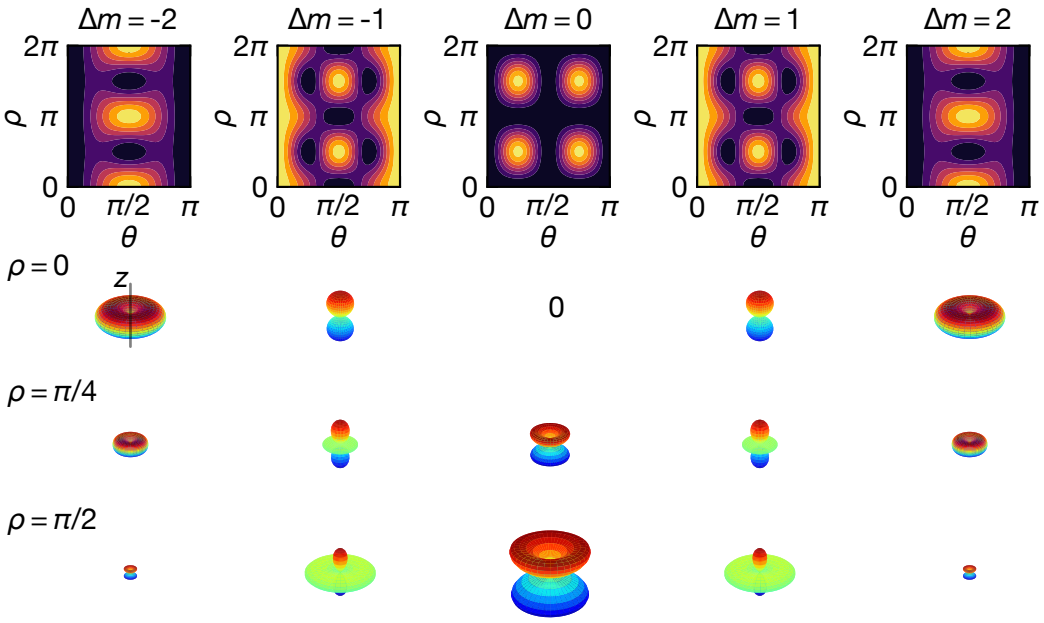

Fig. 3.9 Contour plot of the transition amplitude's angular dependence of the magnetic quadrupole transitions $[\mathbf{Y}^{(0)}_{2q}(\theta,0)\cdot\hat{\boldsymbol{\epsilon}}_{\mathrm{lin}}]^2$ with the linear polarization $\hat{\boldsymbol{\epsilon}}_{\mathrm{lin}}=\sin(\rho)\hat{\boldsymbol{\epsilon}}_1-\cos(\rho)\hat{\boldsymbol{\epsilon}}_2$ and $q=\Delta m$. In the first row, we show the angular characteristics as a function of θ and ρ in a contour plot, where the color from dark to light corresponding to a relative amplitude ranging from 0 to 1. In the second, third, and fourth row, we choose a specific ρ and present the corresponding transition amplitude in a 3D plot. Because the transition amplitude is an absolute value, phase factors vanish and the angular dependence is radially symmetric. The colors of the 3D plots are chosen for visibility and do not have a physical meaning.

perpendicular orientation of the electric and magnetic field.

Using the equations we derived, we can calculate the angular dependence of the $^1S_0$-$^3P_2$ magnetic quadrupole transition. The understanding we obtained enables us to choose probe beam polarizations and probe orientations and to investigate the transition experimentally. We present the corresponding experimental results in Chapter. 6.

Conclusion

In this Chapter we discussed the light-matter interaction in the context of a monochromatic plane wave driving multipole transitions in atoms. We started with the interaction Hamiltonian and expanded the electromagnetic potentials, describing the light, to derive the multipole transition operators. We summarize our findings by inserting the calculated

expressions into the full Hamiltonian of bound electrons interacting with light,

$$\begin{aligned} H =& \frac{\mathbf{p}}{2m_\mathrm{e}} + V(\mathbf{r}) + 4\pi A_0 \sum_{Kq} i^{K+1} \sqrt{\frac{(2K+1)(K+1)}{4\pi K}} \frac{k^K}{(2K+1)!!} \\ & \times \Bigg[\left(\mathbf{Y}^{(1)}_{Kq}(\mathbf{k}) \cdot \hat{\boldsymbol{\epsilon}} \right) e \sqrt{\frac{4\pi}{(2K+1)}} r^K Y^q_K(\hat{\mathbf{r}}) \\ & + \left(\mathbf{Y}^{(0)}_{Kq}(\mathbf{k}) \cdot \hat{\boldsymbol{\epsilon}} \right) \mu_\mathrm{B} \sqrt{\frac{4\pi}{(2K+1)}} \boldsymbol{\nabla} \left[r^K Y^q_K(\hat{\mathbf{r}}) \right] \cdot \left(\frac{2}{K+1} \mathbf{L} + g_\mathrm{B} \mathbf{S} \right) \Bigg]. \end{aligned} \tag{3.89}$$

The derivations allowed us to separate the geometric dependence of a transition from the multipole transition operator describing the atomic physics. The electric and magnetic transition operator has a parity of $(-1)^K$ and $(-1)^{K+1}$, respectively, with the transition rank K. In addition to the photon's spin, the light field can provide angular momentum to satisfy the conservation of angular momentum. Following the the rule of parity conservation, we can deduce the states a multipole transition couples. We summarize the selection rules for transitions between the atomic states $|i\rangle$ and $|k\rangle$ in Tab. 3.1.

		Angular momentum		
	State parity	J	m	Example
E1	$\mathcal{P}_i = -\mathcal{P}_k$	$\Delta J = 0, \pm 1 \;\; (0 \nleftrightarrow 0)$	$\Delta m = 0, \pm 1$	$^1\mathrm{S}_0$-$^1\mathrm{P}_1$
M1	$\mathcal{P}_i = \mathcal{P}_k$	$\Delta J = 0, \pm 1 \;\; (0 \nleftrightarrow 0)$	$\Delta m = 0, \pm 1$	$^3\mathrm{P}_1$-$^3\mathrm{P}_2$
E2	$\mathcal{P}_i = \mathcal{P}_k$	$\Delta J = 0, \pm 1, \pm 2 \;\; (0 \nleftrightarrow 0, 1)$	$\Delta m = 0, \pm 1, \pm 2$	$^2\mathrm{S}_{1/2}$-$^2\mathrm{D}_{5/2}$
M2	$\mathcal{P}_i = -\mathcal{P}_k$	$\Delta J = 0, \pm 1, \pm 2 \;\; (0 \nleftrightarrow 0, 1)$	$\Delta m = 0, \pm 1, \pm 2$	$^1\mathrm{S}_0$-$^3\mathrm{P}_2$

Tab. 3.1 Summary of the selection rules of multipole transitions derived from the multipole transition operators. Dipole transitions with $J = 0 \nleftrightarrow J' = 0$ are forbidden due to the triangle condition of the Wigner $3j$-symbols that result from calculating the angular part of the transition matrix element. [133]. For quadrupole transitions, $(J = 0 \nleftrightarrow J' = 0, 1)$ is forbidden following the same argument. The combination of parity and the angular momentum selection rules also enforce selection rules concerning the electron's angular momentum L, which are not shown here.

In the last part of this Chapter, we calculated the transition amplitude's angular dependence given by $(\mathbf{Y}^{(\lambda)}_{Kq}(\mathbf{k}) \cdot \hat{\boldsymbol{\epsilon}})^2$ of the electric and magnetic dipole and quadrupole transitions. We decomposed the vector spherical harmonics $\mathbf{Y}^{(\lambda)}_{Kq}$ into the polarization basis vectors and visualized the angular characteristics. Additionally, we showed the transition amplitude's angular dependence of a general linear polarization. We observed that the quadrupole transition amplitude depends on the probe beam orientation and polarization. We find that the transition amplitude's angular dependence of electric and magnetic multipole transitions (for a linear polarization) only differ by a phase factor of

$\pi/2$, which can be explained by the perpendicular orientation of the electric and magnetic fields. In addition, we calculated the emission patterns of electromagnetic dipole and quadrupole transitions. The patterns agree with the ones of classical dipoles and quadrupoles.

Now, we have the theoretical background to study the $^1S_0$-$^3P_2$ magnetic quadrupole transition in neutral strontium and make this transition accessible for applications in neutral-atom quantum technologies.

Chapter 4

Dynamical Stark shift

MANIPULATING atoms with light is a foundational technique in atomic physics and in ultracold atom experiments. Resonant laser light drives transitions between atomic states enabling cooling, imaging, and state preparation of the atomic ensemble [143]. But not only resonant radiation has effects on the atoms, also off-resonant light fields do. Off-resonant electromagnetic fields perturb the energies of the atomic states, which can be used to trap the atoms in optical fields [150]. Because the energies are shifted by the oscillating electromagnetic field, this light shift is called *dynamical Stark shift* or also *ac-Stark shift*.

Nowadays, optical traps have developed into standard tools in quantum simulation [20, 22], quantum computation [67, 69] and metrology [54, 50] with neutral atoms. However, the light shift used in optical traps can shift an atomic transition frequency by typically several hundreds of kilohertz. Hence, understanding and controlling this shift becomes especially important for transitions with a linewidth below the megahertz scale, for example the singlet to triplet transitions in alkaline-earth atoms like Sr [119]. The frequency shift is given by the differential light shift between the states of the transition. Because the light shift of the individual states depends on the wavelength of the trapping light and the light polarization, one can achieve a situation in which the differential light shift vanishes – the so-called *magic* condition. The concept of magic optical traps is used in optical lattice clocks for metrology applications [56]. Due to the recent development of using alkaline-earth atoms for quantum simulations and quantum computation, magic traps are becoming more important in these fields.

In Sec. 4.1 of this Chapter, we will discuss the basic models of the light shift and its application to trap neutral atoms in optical fields. We give a brief introduction to optical dipole traps and optical lattices. The light shift and the depth of these optical traps depends on the dynamical polarizability of the atomic state. Hence, we explain how to calculate the polarizability of an atomic state in Sec. 4.2. In Sec. 4.3, we use the concepts we derived to calculate the polarizability of the $^1S_0$ ground state and the metastable ^3P_J triplet states of neutral strontium. In addition, we show how the magic condition can be achieved for the transitions between the ground state and these excited states. At the end of this Chapter, we calculate the tune-out wavelength of strontium enabling the realization of state-dependent optical lattices.

4.1 Optical dipole potential

The derivations in this Section mostly summarize the discussions in Ref. [150]. The interaction of an atom with an off-resonant oscillating electromagnetic field can be understood in a semiclassical picture as the interaction between an induced dipole moment $\mathbf{d}$ and the electric field $\mathbf{E}$. The dipole moment oscillates at the driving frequency ω of the electric field

$$\mathbf{E}(\mathbf{r},t) = \hat{\boldsymbol{\epsilon}}\, E(\mathbf{r}) \exp(-i\omega t) + c.c.,$$
$$\mathbf{d}(\mathbf{r},t) = \hat{\boldsymbol{\epsilon}}\, d(\mathbf{r}) \exp(-i\omega t) + c.c.,$$

where $\hat{\boldsymbol{\epsilon}}$ is the polarization vector and c.c. is the complex conjugate. The amplitude d of the dipole moment is related to the electric field amplitude E by [114]

$$d(\mathbf{r}) = \alpha(\omega) E(\mathbf{r}). \tag{4.1}$$

Here, we introduced the complex polarizability α, which depends on the frequency ω. For now, we treat α as a known scalar quantity. Later in this section we will calculate the polarizability of a two-level system and in Sec. 4.2 the polarizabiliy of a multilevel atom.

The potential energy due to the interaction of the electric field with the induced dipole moment, can be obtained by calculating the time average

$$U_{\mathrm{dip}}(\mathbf{r}) = -\frac{1}{2}\frac{1}{T}\int_0^T \mathbf{d}(\mathbf{r},\tau)\cdot\mathbf{E}(\mathbf{r},\tau)\mathrm{d}\tau = -\frac{1}{2}\,\mathrm{Re}(\alpha)|E(\mathbf{r})|^2, \tag{4.2}$$
$$U_{\mathrm{dip}}(\mathbf{r}) = -\frac{1}{2\varepsilon_0 c}\,\mathrm{Re}(\alpha) I(\mathbf{r}). \tag{4.3}$$

In the second line, we express the potential as a function of the light intensity $I(\mathbf{r})$, where c is the speed of light and ε_0 is the vacuum permittivity. The factor $1/2$ reflects that the dipole is an induced dipole and not a permanent one. We see that the atom's potential energy is proportional to the real part of the polarizability as well as to the light intensity.

The corresponding dipole force is given by the gradient of the potential energy

$$\mathbf{F}_{\mathrm{dip}} = -\boldsymbol{\nabla} U_{\mathrm{dip}}(\mathbf{r}) = \frac{1}{2\varepsilon_0 c}\,\mathrm{Re}(\alpha)\boldsymbol{\nabla} I(\mathbf{r}). \tag{4.4}$$

This dipole force is conservative and hence, can be used to confine atoms in the maximum (minimum) of the light intensity for $\mathrm{Re}(\alpha) > 0$ ($\mathrm{Re}(\alpha) < 0$).

Before we discuss the traps resulting from the dipole potential, let's have a look at another effect resulting from the light-atom interaction. This effect is the scattering of photons by the atom. The associated scattering rate Γ_{sc} is given by the absorbed power

P_{abs} per photon [150]

$$\Gamma_{\mathrm{sc}} = \frac{P_{\mathrm{abs}}}{\hbar\omega} = \frac{1}{\hbar\omega}\frac{1}{T}\int_0^T \left[\frac{\partial}{\partial\tau}\mathbf{d}(\mathbf{r},\tau)\right]\cdot\mathbf{E}(\mathbf{r},\tau)d\tau \tag{4.5}$$

$$= \frac{1}{\hbar\varepsilon_0 c}\,\mathrm{Im}(\alpha)I(\mathbf{r}). \tag{4.6}$$

This scattering can lead to heating of the atoms confined in an optical trap due to the photon recoil. The heating results in decoherence of the atomic state and therefore, has to be taken into account during the design of these traps.

To obtain insight into the relation between the dipole potential and the scattering rate, we use a simplified model to describe the atom and its transitions. We assume that the atom can be described by a perfect two-level system. We describe the atom as a Lorentz-oscillator, where the electron is elastically bound to the core with the oscillation frequency ω_0, which corresponds to the atomic transition frequency. This simple classical model allows us to derive several properties of the atom related to transitions. Using this model, the polarizability $\alpha(\omega)$ is given by [150]

$$\alpha(\omega) = 6\pi\varepsilon_0 c^3 \frac{\Gamma}{\omega_0^2\left(\omega_0^2-\omega^2-i\Gamma\frac{\omega^3}{\omega_0^2}\right)}, \tag{4.7}$$

where Γ is the spontaneous decay rate of the excited state. By substituting Eq. (4.7) into the equation of the dipole potential [Eq. (4.3)], we obtain

$$U_{\mathrm{dip}}(\mathbf{r}) = -\frac{6\pi c^2}{2}\frac{\Gamma(\omega_0^2-\omega^2)\omega_0^2}{(\omega_0^2-\omega^2)^2\omega_0^4+\omega^6\Gamma^2}I(\mathbf{r}) = -\frac{3\pi c^2}{2}\frac{1}{\omega_0^3}\frac{2\Gamma\omega_0}{\omega_0^2-\omega^2+\frac{\omega^6}{\omega_0^4}\Gamma^2}I(\mathbf{r}) \tag{4.8}$$

$$\approx -\frac{3\pi c^2}{2\omega_0^3}\left(\frac{\Gamma}{\omega_0-\omega}+\frac{\Gamma}{\omega_0+\omega}\right)I(\mathbf{r}), \tag{4.9}$$

where we can neglect the last term in the denominator of Eq. (4.8) for far off-resonant light fields. In analogy, the scattering rate (Eq. 4.6) becomes

$$\Gamma_{\mathrm{sc}} = \frac{6\pi c^2}{\hbar}\frac{\omega^3\Gamma^2}{(\omega_0^2-\omega^2)^2\omega_0^4+\omega^6\Gamma^2}I(\mathbf{r}) = \frac{3\pi c^2}{2\hbar\omega_0^3}\left(\frac{\omega}{\omega_0}\right)^3\frac{4\Gamma^2\omega_0^2}{(\omega_0^2-\omega^2)^2+\frac{\omega^6}{\omega_0^4}\Gamma^2}I(\mathbf{r}) \tag{4.10}$$

$$\approx \frac{3\pi c^2}{2\hbar\omega_0^3}\left(\frac{\omega}{\omega_0}\right)^3\left(\frac{\Gamma}{\omega_0-\omega}+\frac{\Gamma}{\omega_0+\omega}\right)^2 I(\mathbf{r}). \tag{4.11}$$

We define the detuning $\Delta = \omega_0 - \omega$ and use the rotating wave approximation [114]. This

approximation allows us to drop the terms of $\Gamma/(\omega_0+\omega)$ and to set $\omega_0 \approx \omega$, resulting in

$$U_{\mathrm{dip}}(\mathbf{r}) = -\frac{3\pi c^2}{2\omega_0^3}\frac{\Gamma}{\Delta}I(\mathbf{r}), \tag{4.12}$$

$$\Gamma_{\mathrm{sc}} = \frac{3\pi c^2}{2\hbar\omega_0^3}\left(\frac{\Gamma}{\Delta}\right)^2 I(\mathbf{r}). \tag{4.13}$$

Although we simplified the atom with a classical model, the derived equations contain the basic principles of the light-atom interaction for far off-resonant laser fields. We can see that atoms are trapped in the intensity maxima for *red-detuned* light ($\Delta < 0$) and in the minima for *blue-detuned* light ($\Delta > 0$).

The dipole potential scales with I/Δ, whereas the scattering rate scales with I/Δ^2. To obtain a deep trapping potential, we should use a high intensity and to reduce the scattering rate we should use a large detuning. Typically, the scattering is not the dominant heating source in optical traps. The dominant heating source of these traps is usually parametric heating caused by intensity noise [151]. However, to prepare quantum many-body states with very low entropy [152, 153] or when atoms are confined in extremely deep optical potentials [154] the scattering has to be considered.

Above, we covered the basic concepts of the optical dipole potential. Now, we discuss two specific traps generated by laser beams that use the optical dipole force to confine the atoms in space. First, we elaborate on the optical dipole trap and second, on the optical lattice. Both of these traps are used in the experiments presented in this thesis.

4.1.1 Optical dipole trap

Confining atoms in a light field requires a restoring force along all spatial directions given by the intensity gradient. The most simple optical dipole trap is realized with a red-detuned, focused Gaussian beam. The intensity profile of a Gaussian beam propagating along the z-axis is described by [148]

$$I(r,z) = I_0\left(\frac{w_0}{w(z)}\right)^2 \exp\left(-\frac{2r^2}{w(z)^2}\right), \tag{4.14}$$

where w_0 is the waist at the focus of the beam. I_0 is the peak intensity defined by $I_0 = (2P)/(\pi w_0^2)$ with the beam power P. The beam waist $w(z)$ changes along the propagation direction given by

$$w(z) = w_0\sqrt{1+\left(\frac{z}{z_{\mathrm{R}}}\right)^2}, \tag{4.15}$$

where $z_{\mathrm{R}} = (\pi w_0^2)/\lambda$ is the Rayleigh range which depends on the wavelength λ. We can see that the intensity of the beam decreases radially, resulting in a restoring force towards the beam center. By moving along the z-direction away from the focus, the beam waist becomes larger and the intensity decreases. Therefore, the atoms located inside the red-detuned beam experience a force towards the focus. The result is a conservative trapping

potential along all spatial directions with a potential depth of

$$U_0 = -\frac{1}{2\varepsilon_0 c}\,\mathrm{Re}(\alpha)\frac{2P}{\pi w_0^2}. \tag{4.16}$$

If the temperature T of the trapped atoms is much smaller than the potential depth ($k_\mathrm{B}T \ll U_0$), the atoms are confined radially in a region of $\Delta r \ll w_0$ and axially in a region of $\Delta z \ll z_\mathrm{R}$. Under this condition, we can approximate the potential by a harmonic oscillator of the form

$$U(r,z) \approx -U_0\left[1-\left(\frac{r}{w_0}\right)^2-\left(\frac{z}{z_\mathrm{R}}\right)^2\right]. \tag{4.17}$$

Within this harmonic approximation, we can calculate the radial trap frequency $\nu_r = \omega_r/(2\pi)$ with

$$\frac{1}{2}m\omega_r^2 r^2 = 2U_0\left(\frac{r}{w_0}\right)^2 \tag{4.18}$$

$$\Leftrightarrow \omega_r = \sqrt{\frac{4U_0}{mw_0^2}} \tag{4.19}$$

an the axial trap frequency $\nu_z = \omega_z/(2\pi)$ with

$$\omega_z = \sqrt{\frac{2U_0}{mz_\mathrm{R}^2}}. \tag{4.20}$$

Typically, one realizes optical dipole traps with $\omega_0 < z_\mathrm{R}$. Hence, the trapped atoms experience much steeper radial confinement than axial.

4.1.2 Optical lattice

In an optical lattice trap, atoms are confined inside the intensity pattern of a standing light wave. The optical lattice is created by overlapping a retro-reflected propagating laser beam. Here, we approximate the laser beam with a plane wave. The resulting intensity pattern is given by

$$I(z) = \frac{1}{2}c\varepsilon_0|E_0\exp(-ikz-i\omega t)+E_0\exp(+ikx-i\omega t)|^2 = 4I_0\cos^2(kz), \tag{4.21}$$

with $k = 2\pi/\lambda$. The factor of 4 is the result of the interference between the beam and its retro-reflection. The intensity pattern leads to a periodic trapping potential of periodicity $\lambda/2$ along the propagation direction. Similar to the dipole trap, each lattice well can be approximated by a harmonic potential of the form

$$U(z) = -U_0\cos^2(kz) \approx -U_0[1-k^2x^2], \tag{4.22}$$

where the trap depth is given by $U_0 = 2\,\mathrm{Re}(\alpha) I_0/(c\varepsilon_0)$. The trap frequency of the optical lattice can be calculated with

$$2\pi\nu_z = \omega_z = \sqrt{\frac{2U_0k^2}{m}} = \sqrt{\frac{4U_0E_{\mathrm{rec}}}{\hbar^2}}. \tag{4.23}$$

We define the recoil energy as $E_{\mathrm{rec}} = \hbar^2k^2/(2m) = h\nu_{\mathrm{rec}}$. Using the recoil frequency ν_{rec} we can relate the trap frequency to the trap depth by $\nu_t/\nu_{\mathrm{rec}} = \sqrt{4U_0/E_{\mathrm{rec}}}$.

In reality, optical lattices are created with Gaussian beams and not plane waves. The finite extent of the Gaussian beams results in a Gaussian envelope of the potential depth along the radial direction. The radial trap frequency is given by Eq. (4.19). This envelope leads to a radial harmonic confinement on top of the lattice, which limits the number of usable lattice sites for quantum simulation, quantum computation, and optical lattice clocks [104].

4.2 Theory of atomic polarizability

In this Section we discuss how to calculate the atomic polarizability of a multilevel atom. In the further content of this thesis, the term polarizability α refers to the real part of the complex polarizability. The following results are based on the explanations given in Ref. [155, 156, 86] and on our work carried out in Ref. [104, 92, 142].

In general, the polarizability α is a tensor of rank 2 resulting from the Stark shift interaction Hamiltonian [155]. We can decompose the tensor into three irreducible parts: scalar α_{S}, vector α_{V}, tensor α_{T} polarizability [157]. For the atomic state $|i\rangle$ the total polarizability is given

$$\alpha^i = \alpha^i_{\mathrm{S}} + \alpha^i_{\mathrm{V}} + \alpha^i_{\mathrm{T}}. \tag{4.24}$$

Each of these term describes the interaction of the valence electrons with the light field. Additionally, the scalar polarizability contains the interaction with electrons on lower atomic orbits, the core electrons.

In Sec. 4.1 we discussed the polarizability of a two-level system in terms of the interaction between an induced electric dipole moment and the electric field. Besides this interpretation, we can understand the polarizability as the coupling of the electric field, oscillating at the frequency ω, to the atomic states' multipole transitions contributing in second order. In the previous Chapter 3, we derived that electric diopole transitions are dominate in terms of transitions strength and we can neglect contributions from higher order multipole transitions. We can calculate the interaction with second-order perturbation theory [114]. The scalar polarizability of the atomic state $|i\rangle$ with the angular

momentum J is given by [156, 86]

$$\alpha_{\mathrm{S}}^{i} = \frac{1}{3(2J+1)} \frac{1}{\hbar} \sum_{k} |\langle k|d|i\rangle|^2 \,\mathrm{Re}\left(\frac{1}{\omega_{ki} - \omega - i\frac{\Gamma_{ki}}{2}} + \frac{1}{\omega_{ki} + \omega + i\frac{\Gamma_{ki}}{2}} \right) \tag{4.25}$$

$$= \frac{1}{3(2J+1)} \frac{2}{\hbar} \sum_{k} \frac{|\langle k|d|i\rangle|^2 \omega_{ki}}{\omega_{ki}^2 - \omega^2}, \tag{4.26}$$

where ω_{ki} is the transition frequency between the states $|i\rangle$ and $|k\rangle$ with the partial linewidth Γ_{ik}. To obtain the second line, we neglect the last term of the denominator of Eq. (4.25) which is valid for large detunings. The sum is carried out over all electric dipole transitions connecting the states $|i\rangle$ and $|k\rangle$. The coupling strength of the transitions is described by the dipole matrix element $\langle k|d|i\rangle$. The coupling strengths and the detunings determine the contributions of the individual states $|k\rangle$ to the polarizability. Hence, transitions with small detunings and large matrix elements contribute heavily to the polarizability of the state $|i\rangle$. If the frequency of the electric field is approaching the transition frequency, the polarizability will diverge. For $\omega > \omega_{ki}$, the transition has a negative polarizability contribution to the sum.

We note that the frequency dependency is very similar to the dependency of our simplified polarizability model in Sec. 4.1. Furthermore, we can see that the scalar polarizability is independent of the light polarization and hence, independent of the orientation of the electric field with respect to the quantization axis of the atom.

The light-matter interaction determining the vector polarizability α_{V}^{i} has the character of a vector. Hence, α_{V}^{i} depends on the orientation of the electric field characterized by the polarization vector $\hat{\boldsymbol{\epsilon}}$. We describe the vector in a Cartesian coordinate system $\{\hat{\mathbf{x}}, \hat{\mathbf{y}}, \hat{\mathbf{z}}\}$ with the quantization axis orientated along the z-direction, defined by a strong external magnetic field. The polarization is given by its components along the basis vectors with $\hat{\boldsymbol{\epsilon}} = \epsilon_x \hat{\mathbf{x}} + \epsilon_y \hat{\mathbf{y}} + \epsilon_z \hat{\mathbf{z}}$. For the vector polarizability we have to include the projection of the angular momentum J_i along the quantization axis, described by the quantum number m_i. With these definitions, the vector polarizability can be calculated [155],

$$\alpha_{\mathrm{V}}^{i} = \frac{m_i}{2J_i} \alpha_{\mathrm{V}}^{\prime i} 2\,\mathrm{Im}(\epsilon_x^* \epsilon_y). \tag{4.27}$$

We define the bare vector polarizability $\alpha_{\mathrm{V}}^{\prime i}$, which is independent of $\hat{\boldsymbol{\epsilon}}$ and m_i

$$\begin{aligned} \alpha_{\mathrm{V}}^{\prime i} = &- \sqrt{\frac{6J_i}{(J_i+1)(2J_i+1)}} \sum_{k} (-1)^{J_i + J_k + 1} \begin{Bmatrix} 1 & 1 & 1 \\ J_i & J_k & J_i \end{Bmatrix} \\ &\times \frac{|\langle k|d|i\rangle|^2}{\hbar} \left(\frac{1}{\omega_{ki} - \omega} - \frac{1}{\omega_{ki} + \omega} \right). \end{aligned} \tag{4.28}$$

This expression contains the Wigner 6-j symbols and depends on the angular momentum J_k of the state $|k\rangle$. We note that α_{V}^{i} vanishes for light polarized along the quantization axis. A beam propagating along the quantization axis has a polarization oriented in the

xy-plane and can be described in terms of the ellipticity angle γ [158, 77],

$$\hat{\boldsymbol{\epsilon}} = \cos(\gamma)\hat{\mathbf{x}} + i\sin(\gamma)\hat{\mathbf{y}}. \tag{4.29}$$

For $\gamma = 0$ the light is linearly polarized and for $\gamma = \pi/4$ the light has circular polarization. Since the beam propagates parallel to the quantization axis, we only have one definite axis determining the geometry. Hence, the vector polarizability is radially symmetric around the z-axis and α_{V}^{i} does not depend on the choice of $\hat{\mathbf{x}}$ and $\hat{\mathbf{y}}$. With this polarization we obtain

$$2\,\mathrm{Im}(\epsilon_x^* \epsilon_y) = \sin(2\gamma). \tag{4.30}$$

We can see that α_{V}^{i} vanishes for light polarized linearly in the plane perpendicular to the quantization axis. Moreover, the vector polarizability vanishes for atomic states with $m_i = 0$. Since α_{V}^{i} depends on the polarization ellipticity, we can use γ to tune the total polarizability of a specific atomic state [77].

The interaction determining tensor polarizability has the character of a tensor. The tensor polarizability α_{T}^{i} is given by [155]

$$\alpha_{\mathrm{T}}^{i} = \frac{3m_i^2 - J_i(J_i+1)}{2J_i(2J_i-1)} \alpha_{\mathrm{T}}^{\prime i} \left(3|\epsilon_z|^2 - 1\right) \tag{4.31}$$

We define the bare tensor polarizability $\alpha_{\mathrm{T}}^{\prime i}$, which is independent of $\hat{\boldsymbol{\epsilon}}$ and m_i,

$$\begin{aligned} \alpha_{\mathrm{T}}^{\prime i} = &- \sqrt{\frac{10J_i(2J_i-1)}{3(J_i+1)(2J_i+1)(2J_i+3)}} \sum_k (-1)^{J_i+J_k} \\ &\times \begin{Bmatrix} 1 & 2 & 1 \\ J_i & J_k & J_i \end{Bmatrix} \frac{2}{\hbar} \frac{|\langle k|d|i\rangle|^2 \omega_{ki}}{\omega_{ki}^2 - \omega^2}. \end{aligned} \tag{4.32}$$

For a linear polarization, we can simplify the polarization dependency with

$$\left(3|\epsilon_z|^2 - 1\right) = 3\cos^2(\beta) - 1, \tag{4.33}$$

This means that we can tune the tensor polarizability by adjusting the polarization relative to the quantization axis. Either we can rotate the polarization or we fix the polarization in the beam frame and rotate the quantization axis defined by a magnetic field [119]. Later, we will show how to transform between beam frame and atomic frame.

With the equations above, we have the tools to calculate the polarizability of a state of a multilevel atom. However, the accuracy of the calculations strongly depends on the precise knowledge of the dipole matrix elements. It is possible to extract these matrix elements from experimentally available lifetimes. However, calculating exact branching ratios can become very difficult since for high $|J, m\rangle$ states the LS-coupling is not a good approximation anymore. Hence, the results of our own calculations are often only valid as a rough estimate. It is better to take measured dipole matrix elements from available databases [159] or from atomic-structure theory calculations if experimental data is not

available.

The calculations above are valid for the atomic fine-structure states in the absence of nuclear spin, for example, in the bosonic isotopes of neutral strontium. However, the equation can easily be extended to describe the polarizability of the hyperfine levels [155, 92].

4.2.1 Transformation from beam frame to atomic frame

We have seen that the vector and tensor polarizabilities depend on the light polarization in the atomic frame defined by the quantization axis. In our case, we define the quantization axis by applying a strong external magnetic field. For the daily work in the laboratory it is more convenient to describe the beam polarization in the beam frame. Therefore, we will show how to transform any polarization from the beam frame into the atomic frame.

In the beam frame, the propagation direction $\hat{\mathbf{k}}$ defines the z-axis. The basis vectors, the polarization vector $\hat{\boldsymbol{\epsilon}}$, and the magnetic field vector $\hat{\mathbf{B}}$ are given by

$$\begin{aligned}
\hat{\mathbf{e}}_{\mathrm{b},1} &= \hat{\mathbf{x}},\\
\hat{\mathbf{e}}_{\mathrm{b},2} &= \hat{\mathbf{y}},\\
\hat{\mathbf{e}}_{\mathrm{b},3} &= \hat{\mathbf{z}} = \hat{\mathbf{k}},\\
\hat{\boldsymbol{\epsilon}}_{\mathrm{b}} &= \cos(\phi)\hat{\mathbf{x}} + \sin(\phi)\hat{\mathbf{y}},\\
\hat{\mathbf{B}}_{\mathrm{b}} &= \sin(\theta)\hat{\mathbf{x}} + \cos(\theta)\hat{\mathbf{z}}.
\end{aligned}$$

With these definitions the basis vectors of the atomic frame are given by

$$\begin{aligned}
\hat{\mathbf{e}}_3 &= \sin(\theta)\hat{\mathbf{x}} + \cos(\theta)\hat{\mathbf{z}},\\
\hat{\mathbf{e}}_2 &= \hat{\mathbf{y}},\\
\hat{\mathbf{e}}_1 &= \boldsymbol{e}_3 \times \boldsymbol{e}_2 = -\cos(\theta)\hat{\mathbf{x}} + \sin(\theta)\hat{\mathbf{z}}.
\end{aligned}$$

The matrix T transforming from the atomic into the beam frame is simply

$$T = \begin{pmatrix} -\cos(\theta) & 0 & \sin(\theta) \\ 0 & 1 & 0 \\ \sin(\theta) & 0 & \cos(\theta) \end{pmatrix} = T^{-1} \tag{4.34}$$

and hence, T also describes the transformation from the beam frame into the atomic frame. This allows us to describe the light polarization in the convenient beam frame and for calculations transform the polarization into the atomic frame with

$$\hat{\boldsymbol{\epsilon}} = T\hat{\boldsymbol{\epsilon}}_b. \tag{4.35}$$

4.3 Atomic polarizability of strontium

In this Section, we calculate the atomic polarizabilities of the states $^1S_0$, $^3P_0$, $^3P_1$, and $^3P_2$ of neutral ^{88}Sr. We use the calculations to obtain the magic wavelengths of the corresponding transitions, which are of high relevance for several applications. At these wavelength the differential polarizability vanishes resulting in Stark-shift-free optical traps. The magic wavelength of the $^1S_0$-$^3P_0$ transition is a key ingredient for building neutral strontium optical lattice clocks for metrology research [56]. An optical dipole trap or an optical lattice at the magic wavelength of the $^1S_0$-$^3P_1$ transition allows very efficient laser cooling on this narrow-line transition. Using the magnetic field sensitive $^1S_0$-$^3P_2$ transition for local addressing in an optical lattice within a magnetic field gradient requires a magic lattice. The results of our calculations are presented in Sec. 4.3.1, Sec. 4.3.2, and Sec. 4.3.3.

In the previous Section, we already mentioned the tunability of the vector and tensor polarizability. We use this tunability and calculate the configuration to obtain a 3D magic lattice for the $^1S_0$-$^3P_1$ transition and for the $^1S_0$-$^3P_2$ transition at our lattice wavelengths of 914 nm and 1064 nm.

In the last part of this Section, we focus on the tune-out wavelengths [92]. At the tune-out wavelength the polarizability of an atomic state vanishes. This condition is of high interest to generate highly state-dependent optical lattices which can be used in simulations of open quantum systems [99, 100] and in proposed quantum computing schemes [74].

4.3.1 $^1S_0$ and $^3P_0$ polarizabilities

We use the formalism carried out in Sec. 4.2 to calculate the polarizability of the $5s5p$ $^1S_0$ state and the $5s5p$ $^3P_0$ state. In Tab. 4.1 we list the relevant transitions and their contributions to the polarizability at a wavelength of 813 nm. The transition energies ΔE can be converted into transition frequencies with $\omega_{ki} = \Delta E/\hbar$. The listed matrix elements are the result of atomic structure calculations provided by Marianna Safronova. The energies (matrix elements) are carefully checked against precision measurements in optical lattice clocks resulting in typical uncertainties of 0.5% (0.8 %), respectively.

We can see that the dominant contribution to the polarizability of the $^1S_0$ state is given by the $^1S_0$-$5s5p$ $^1P_1$ transition. This high contribution is the result of the matrix element beeing one order of magnitude larger than the other matrix elements. For the polarizability of the $^3P_0$ state, the largest contribution arises from the $^3P_0$-$5s6s$ $^3S_1$ transition. The reason is that this transition has the smallest detuning to the light.

The contribution of states that are not listed explicitely are summarized in *Other*, which depends on the wavelength. This contribution is difficult to calculate but can be determined from the comparison to experimentally measured polarizabilities.

In Fig. 4.1 we plot the polarizability of the $^1S_0$ state and the $^3P_0$ state of ^{88}Sr as a function of the wavelength. Because both states have a vanishing angular momentum, only the scalar polarizability contributes, while the vector and tensor polarizabilities vanish.

k	ΔE (cm^{-1})	$\langle k\|d\|i\rangle$ (a.u.)	α_S^i (a.u.)
		$i = 5s5p\,^1\mathrm{S}_0$	
$5s5p\,^3\mathrm{P}_1$	14504	0.1510	0.82
$5s5p\,^1\mathrm{P}_1$	21698	5.248	273.66
$5s6p\,^3\mathrm{P}_1$	33868	0.034	0.01
$5s6p\,^1\mathrm{P}_1$	34098	0.282	0.39
Other			5.8
Core			5.3
Total			286.0(1.3)
		$i = 5s5p\,^3\mathrm{P}_0$	
$5s4d\,^3\mathrm{D}_1$	3842	2.671	−29.37
$5s6s\,^3\mathrm{S}_1$	14721	1.968	127.53
$5s5d\,^3\mathrm{D}_1$	20689	2.450	65.66
$5p^2\,^3\mathrm{P}_1$	21083	2.605	71.39
$5s7s\,^3\mathrm{S}_1$	23107	0.515	2.34
Other			42.1
Core			5.6
Total			285.2(2.6)

Tab. 4.1 Contributions to the scalar polarizability α_S of the states $5s5p\,^1\mathrm{S}_0$ and $5s5p\,^3\mathrm{P}_0$ in ^{88}Sr at 813 nm. Because both states have an angular momentum of $J = 0$, the vector and tensor polarizabilities vanish. The transition energies ΔE are listed in cm^{-1} and the reduced electric-dipole matrix elements $\langle k|d|i\rangle$ in atomic units. The energies and matrix elements are taken from Refs. [160] and Ref. [156, 161]. *Other* refers to contributions from states which are not listed explicitly and *Core* to the core polarizability. Uncertainties for individual contributions are the result from propagating uncertainties in the matrix elements and are not shown here [161].

Hence, the total polarizabilities do not depend on the light polarization and they only depend on the wavelength. We extract a magic wavelength with equal polarizabilities at 813(1) nm. Our calculated value is in agreement with the experimentally used magic wavelength for ^{88}Sr of 813.43 nm [125]. This is not surprising since the atomic structure calculation are fine-tuned to reproduce this value.

4.3.2 $^3\mathrm{P}_1$ polarizability

In Tab. 4.2 we list the relevant transitions to calculate the polarizability of the $5s5p\ ^3\mathrm{P}_1$ state. We can see that more transitions are contributing compared to the $^3\mathrm{P}_0$ state. The reason is that the $^3\mathrm{P}_1$ state is connected to more states via electric dipole transitions than the $^3\mathrm{P}_0$ state. Because the $^3\mathrm{P}_1$ state has an angular momentum of $J_i = 1$, it has non-vanishing vector and tensor polarizabilities.

We show the polarizabilities of the $^3\mathrm{P}_1$ state and the $^1\mathrm{S}_0$ state of ^{88}Sr as a function of

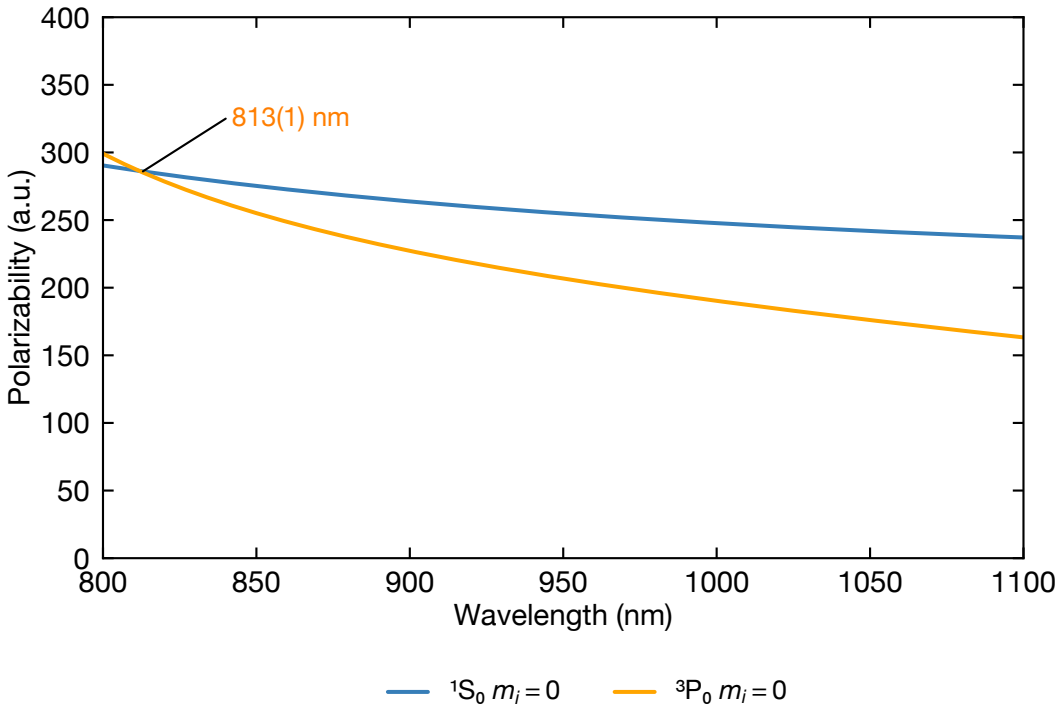

Fig. 4.1 Polarizability of the $^1S_0$ and the $^3P_0$ state of ^{88}Sr as a function of the wavelength. Both states have $J = 0$ and hence, have vanishing contribution from the vector and tensor polarizability. The polarizabilities of the states only depend on the wavelength of the light. We marked the magic wavelength at $813(1)$ nm.

the wavelength and the light polarization in Fig. 4.2. The Zeeman sublevels (m-states) of the $^3P_1$ state differ in their polarizability and depend on the light polarization $\hat{\epsilon}$.

For a linear polarization along the quantization axis ($\hat{\epsilon} = \hat{e}_0$), the vector polarizability vanishes. Hence, for π-polarization, the difference between the m-states is given by the tensor polarizability. We note that for $\hat{\epsilon} = \hat{e}_{\pm 1}$ the polarizability of the $m_i = 0$ state is equal to the polarizability of the state $m = 1$ for $\hat{\epsilon} = \hat{e}_0$. The reason for this is that the difference in the factor $(3m_i^2 - J_i(J_i+1))/(2J_i(2J_i-1))$ of the tensor polarizability (Eq. 4.31) is compensated by the term $(3\sin^2(\theta) - 1)/2$, with $\theta = 0$ ($\theta = \pi$) for π-polarization ($\sigma^{\pm}$-polarization), respectively. For the $m_i = 0$ state, this applies for all polarizations in the xy-plane.

For the $m_i = \pm 1$ states, the degeneracy between σ^+- and σ^--polarization is lifted by the vector polarizability. By changing the ellipticity angle, the region between σ^+- and σ^--polarization becomes accessible.

Furthermore, we extract the magic wavelength for the $^1S_0$-$^3P_1$ $\Delta m = \pm 1$ transition to be $914(1)$ nm for π-polarized trap light. Operating a lattice at this wavelength enables efficient direct sideband cooling with uniform cooling frequency over the entire sample trapped in an optical lattice.

k	ΔE (cm^{-1})	$\langle k\|d\|i\rangle$ (a.u.)	$\alpha^i_{S,k}$ (a.u.)	$\alpha'^i_{V,k}$ (a.u.)	$\alpha'^i_{T,k}$ (a.u.)
			$i = 5s^2\ {}^1\mathrm{S}_0$		
$5s5p\ {}^3\mathrm{P}_1$	14504	0.397	0.53		
$5s5p\ {}^1\mathrm{P}_1$	21698	5.248	249.04		
$5s6p\ {}^3\mathrm{P}_1$	33868	0.034	0.01		
$5s6p\ {}^1\mathrm{P}_1$	34098	0.282	0.38		
Other			5.8		
Core			5.3		
Total			261.1(1.2)	0	0
			$i = 5s5p\ {}^3\mathrm{P}_1$		
$5s^2\ {}^1\mathrm{S}_0$	−14505	0.151	−0.18	−0.40	0.18
$5s4d\ {}^3\mathrm{D}_1$	3655	2.318	−9.00	40.44	−4.50
$5s4d\ {}^3\mathrm{D}_2$	3714	4.013	−27.55	−121.71	2.75
$5s4d\ {}^1\mathrm{D}_2$	5645	0.190	−0.11	−0.33	0.01
$5s6s\ {}^3\mathrm{S}_1$	14534	3.435	91.37	−103.16	45.68
$5s6s\ {}^1\mathrm{S}_0$	16087	0.045	0.01	−0.02	−0.01
$5s5d\ {}^1\mathrm{D}_2$	20223	0.061	0.01	0.01	0.00
$5s5d\ {}^3\mathrm{D}_1$	20503	2.005	13.37	−10.70	6.69
$5s5d\ {}^3\mathrm{D}_2$	20518	3.671	44.76	35.80	−4.48
$5p^2\ {}^3\mathrm{P}_0$	20689	2.658	23.12	−36.68	−23.12
$5p^2\ {}^3\mathrm{P}_1$	20896	2.363	17.96	−14.10	8.98
$5p^2\ {}^3\mathrm{P}_2$	21170	2.867	25.84	20.03	−2.58
$5p^2\ {}^1\mathrm{D}_2$	22457	0.228	0.14	0.11	−0.01
$5p^2\ {}^1\mathrm{S}_0$	22656	0.291	0.24	−0.34	−0.245
$5s7s\ {}^3\mathrm{S}_1$	22920	0.921	2.34	−1.67	1.17
Other			42.2		
Core			5.6		
Total			230.1(1.9)	−192.7	30.5(7)

Tab. 4.2 Contributions to the scalar α^i_{S}, the bare vector α'^i_{V} and the bare tensor polarizability α'^i_{T} of the states $5s^2\ {}^1\mathrm{S}_0$ and $5s5p\ {}^3\mathrm{P}_1$ of ^{88}Sr at 914 nm. The transition energies ΔE are shown in cm^{-1}, the reduced electric-dipole matrix elements $\langle i|d|k\rangle$ and polarizabilities are listed in atomic units. The energies and matrix elements are taken from Ref. [160] and Refs. [156, 161]. Here, *Other* refers to contributions to the scalar polarizability from states which are not listed explicitly and *Core* to the core polarizability. Uncertainties for individual contributions are the result from propagating uncertainties in the matrix elements and are not shown here [161].

4.3.3 $^3\mathrm{P}_2$ polarizability

We list the relevant transitions and their contributions to the polarizability of the $5s5p\ {}^3\mathrm{P}_2$ state at a wavelength of 1064 nm in Tab. 4.3. Due to its angular momentum of $J_i = 2$, the $^3\mathrm{P}_2$ state has non-vanishing vector and tensor polarizability. The wavelength of 1064 nm

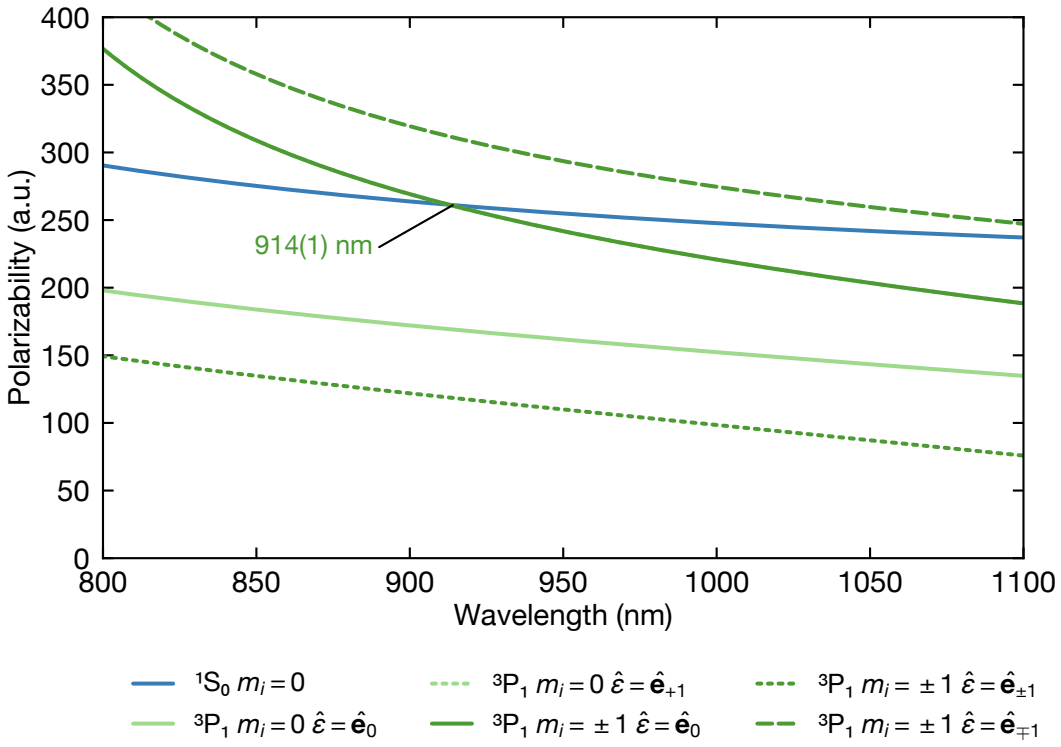

Fig. 4.2 Polarizability of the $^1S_0$ and the $^3P_1$ state as a function of the wavelength at for various polarizations $\hat{\epsilon}$. The polarization is defined with respect to the quantization axis, where $\hat{\epsilon} = \hat{\mathrm{e}}_0$ is along the quantization axis. $\hat{\mathrm{e}}_{\pm 1}$ are the circular polarizations in the plane perpendicular to the quantization axis. In a π-polarized light field, the $^1S_0$-$^3P_1$ $\Delta m = 1$ transition is magic at 914 nm. The states $m_i = 0$ for $\hat{\epsilon} = \hat{\mathrm{e}}^{\pm}$ and $m_i = 1$ for $\hat{\epsilon} = \hat{\mathrm{e}}_0$ have the same polarizability.

is of interest because commercial high-power fiber amplifiers with powers of up to several tens of Watts are available for this wavelength. The high power enables the generation of large and deep optical potentials.

In Fig. 4.3 we show the polarizability of the Zeeman sublevels (m-states) of the $^3P_2$ state of ^{88}Sr as a function of the wavelength and for various light polarizations. With a linear polarization along the quantiization axis ($\hat{\epsilon} = \hat{\mathrm{e}}_0$ the $^1S_0$-$^3P_2$ $\Delta m = 0$ transition is magic at $1081(1)$ nm and the $^1S_0$-$^3P_2$ $\Delta m = \pm 1$ transition is magic at $994(1)$ nm.

By changing the ellipticity of a beam polarized in the plane perdendicular to the quantization axis, the polarizability can be tuned between the extreme cases of σ^+- and σ^--polarization. This tuning allows to obtain a magic condition for the magnetic field sensitive $^1S_0$-$^3P_2$ $\Delta m = \pm 1$ transition in a setup where the lattice propagation direction is along the quantization axis. This case is extremely relevant for us because we want to use the $^1S_0$-$^3P_2$ $\Delta m = \pm 1$ transition for local addressing within a magnetic field gradient.

k	ΔE (cm^{-1})	$\langle k\|d\|i\rangle$ (a.u.)	$\alpha^i_{S,k}$(a.u.)	$\alpha'^i_{V,k}$ (a.u.)	$\alpha'^i_{T,k}$ (a.u.)
			$i = 5s^2\ {}^1\mathrm{S}_0$		
$5s5p\ {}^3\mathrm{P}_1$	14504	0.397	0.40		
$5s5p\ {}^1\mathrm{P}_1$	21698	5.248	228.61		
$5s6p\ {}^3\mathrm{P}_1$	33868	0.034	0.01		
$5s6p\ {}^1\mathrm{P}_1$	34098	0.282	0.37		
Other			5.8		
Core			5.3		
Total			240.5(1.1)	0	0
			$i = 5s5p\ {}^3\mathrm{P}_2$		
$5s4d\ {}^3\mathrm{D}_1$	3260	0.6021	−0.45	3.85	0.45
$5s4d\ {}^3\mathrm{D}_2$	3320	2.331	−6.83	19.33	−6.83
$5s4d\ {}^3\mathrm{D}_3$	3421	5.530	−39.95	−219.52	11.41
$5s4d\ {}^1\mathrm{D}_2$	5251	0.102	−0.03	0.05	−0.03
$5s6s\ {}^3\mathrm{S}_1$	14140	4.521	75.78	−151.10	−75.78
$5s5d\ {}^1\mathrm{D}_2$	19829	0.365	0.25	−0.12	0.25
$5s5d\ {}^3\mathrm{D}_1$	20108	0.460	0.39	−0.55	−0.39
$5s5d\ {}^3\mathrm{D}_2$	20123	1.956	7.12	−3.32	7.12
$5s5d\ {}^3\mathrm{D}_3$	20146	4.994	46.30	43.20	−13.23
$5p^2\ {}^3\mathrm{P}_1$	20502	2.992	16.18	−22.25	−16.18
$5p^2\ {}^3\mathrm{P}_2$	20776	5.119	46.41	−21.00	46.41
$5p^2\ {}^1\mathrm{D}_2$	22062	0.682	0.75	−0.32	0.75
$5s7s\ {}^3\mathrm{S}_1$	22526	1.264	2.51	−3.15	−2.51
Other			43.1		0.3
Core			5.6		
Total			197.1(2.0)	−354.9	−48.6(1.2)

Tab. 4.3 Contributions to the scalar α^i_{S}, the bare vector α'^i_{V} and the bare tensor polarizability α'^i_{T} of the states $5s^2\ {}^1\mathrm{S}_0$ and $5s5p\ {}^3\mathrm{P}_2$ of ^{88}Sr at 1064 nm. The transition energies ΔE are shown in cm^{-1}, the reduced electric-dipole matrix elements $\langle i|d|k\rangle$ and polarizabilities are listed in atomic units. The energies and matrix elements are taken from Ref. [160] and Refs. [156, 161]. Here, *Other* refers to contributions to the scalar polarizability from states which are not listed explicitly and *Core* to the core polarizability. Uncertainties for individual contributions are the result from propagating uncertainties in the matrix elements and are not shown here [161].

4.3.4 Magic 3D lattice for ^{3}P$_1$ and ^{3}P$_2$

In the previous Sections, we extracted the magic wavelengths for the ^{1}S$_0$-^{3}P$_J$ transitions of ^{88}Sr. Here, we explain how the vector and tensor polarizabilities of the ^{3}P$_1$ $m_i = \pm 1$ and ^{3}P$_2$ $m_i = 0, \pm 1$ states can be tuned to obtain a magic condition while keeping the wavelength fixed. We derive the required parameters at the example of a 1064 nm optical lattice propagating along the z-axis. At the end of the section, we apply these techniques

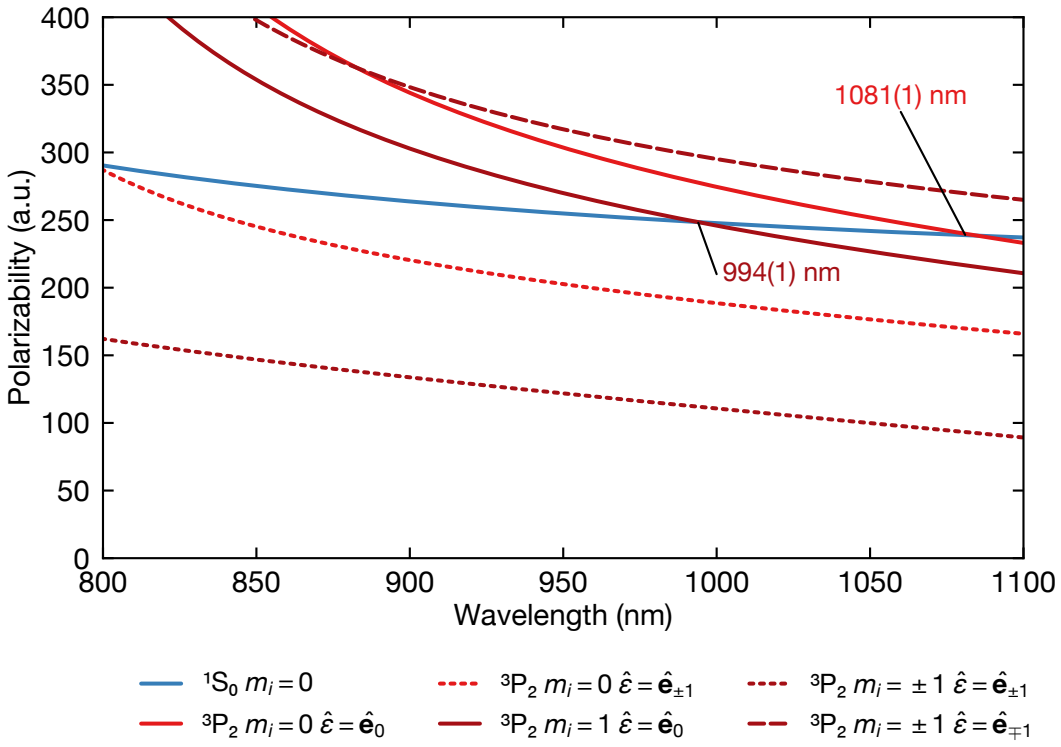

Fig. 4.3 Polarizability of the $^1S_0$ and $^3P_2$ $m_i = 0, \pm 1$ state as a function of the wavelength at for various polarizations $\hat{\epsilon}$. The polarization is defined with respect to the quantization axis, where $\hat{\epsilon} = \hat{\mathbf{e}}_0$ is along the quantization axis. $\hat{\mathbf{e}}_{\pm 1}$ correspond to the circular polarizations in the plane perpendicular to the quantization axis. In a π polarized light field, the $^1S_0$-$^3P_2$ $\Delta m = 0$ transition is magic at 1081 nm and the $^1S_0$-$^3P_2$ $\Delta m = \pm 1$ transition at 994 nm.

to our 3D optical lattice setup composed of a vertical 1064 nm lattice and horizontal lattices with a wavelength of 914 nm.

In Sec. 4.2, we derived that the tensor polarizability depends on the angle β between the polarization and the quantization axis. Here, we tune the tensor polarizability by tilting the magnetic field that defines the quantization axis by an angle θ and keep the trapping light propagation direction fixed. Tilting the magnetic field changes the light polarization given by $\hat{\epsilon} = -\cos(\theta)\hat{\mathbf{x}} + \sin(\theta)\hat{\mathbf{z}}$ in the atomic frame. For this special polarization, we obtain the relation $\beta = \theta - \pi/2$. In Fig. 4.4(a), we plot the polarizabilities of the $^1S_0$, $^3P_1$ and $^3P_2$ states as a function of θ. The polarizabilities are calculated at a fixed wavelength of 1064 nm. Because the $^1S_0$ state has only a scalar polarizability component, α does not depend on θ. The polarizabilities of the triplet states follow a sinusoidal modulation in θ [see Eq. (4.31)]. However, only the $^3P_2$ $m_i = 0$ state has a modulation amplitude large enough to cross the polarizability of the $^1S_0$ state. With this state it is possible to obtain a magic condition for the $^1S_0$-$^3P_2$ $\Delta m = 0$ transition by tilting the magnetic field. The magic condition is reached at an angle of $\theta = 0.409\,\pi$.

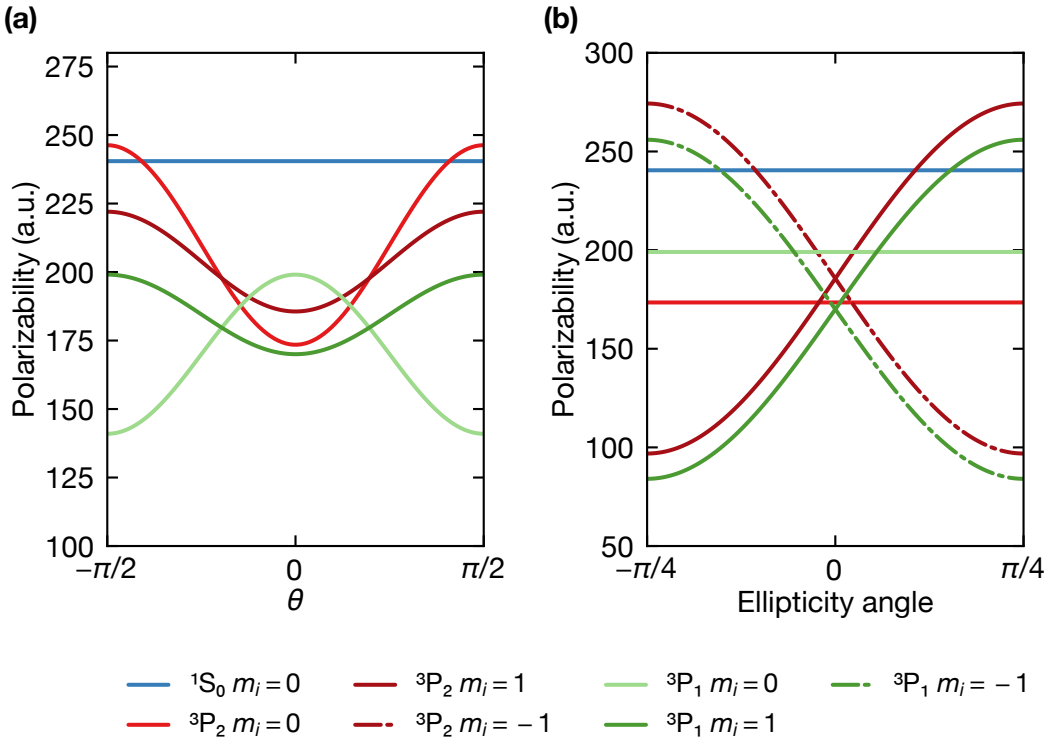

Fig. 4.4 Tuning the polarizability of the $^3P_0$ and the $^3P_2$ state by using the vector and the tensor polarizability at an example wavelength of 1064 nm. (a) We assume a quantization axis along z and a linear polarization $\hat{\epsilon} = -\cos(\theta)\hat{\mathbf{x}} + \sin(\theta)\hat{\mathbf{z}}$. By adjusting the angle θ between quantization axis and beam propagation direction, we change the tensor component of the polarizability. Since $^1S_0$ has only a scalar polarizability component, the polarizability is constant. (b) The total polarizability can also be tuned by changing the vector polarizability. We assume elliptical polarization $\hat{\epsilon} = \cos(\gamma)\hat{\mathbf{x}} + i\sin(\gamma)\hat{\mathbf{y}}$, where γ is the ellipticity angle.

We can also adjust the vector polarizability to obtain magic conditions. For the light polarization $\hat{\epsilon} = \cos(\gamma)\hat{\mathbf{x}} + i\sin(\gamma)\hat{\mathbf{y}}$, the vector polarizability depends on the ellipticity angle γ [see Eq. (4.27)]. We plot the polarizability of the $^1S_0$, $^3P_0$, $^3P_1$, and $^3P_2$ states as a function of the ellipticity angle at a wavelength of 1064 nm in Fig. 4.4(b). The $m = 0$ states have vanishing vector polarizability and therefore, their polarizability is constant with respect to γ. The polarizabilities of the $m = \pm 1$ states follow the derived $\sin(2\gamma)$ modulation. Since the amplitude of the vector polarizability is larger than the tensor polarizability, we can obtain magic conditions for the $^1S_0$-$^3P_1$ $\Delta m = \pm 1$ transition at $\gamma = \pm 0.153\,\pi$ and the $^1S_0$-$^3P_2$ $\Delta m = \pm 1$ transition at $\gamma = \pm 1.08\,\pi$.

We have shown that we can obtain a magic condition for the $^1S_0$-$^3P_2$ $\Delta m = 0$ transition in a 1064 nm vertical lattice by tilting the magnetic field. Furthermore, it is possible to make the lattice magic for the $^1S_0$-$^3P_1$ $\Delta m = \pm 1$ transition and for the $^1S_0$-$^3P_2$ $\Delta m = \pm 1$ transition by tuning the ellipticity of the lattice polarization. The tilting and the ellipticity

can easily be adjusted during an experimental sequence and enable magic lattices for these transitions using the same laser setup.

In our experiment, we use a 3D optical lattice setup composed of a vertical 1064 nm lattice and two 914 nm horizontal lattices. During the cooling of our atomic sample, the 3D lattice should be magic for one of the $^1S_0$-$^3P_1$ $\Delta m = \pm 1$ transitions. After the cooling, the lattices should be magic for the $^1S_0$-$^3P_1$ $\Delta m = \pm 1$ transition for applications like spatial addressing. To obtain these conditions we can adjust the angle θ and we can tune the polarizations' ellipticity γ. We plot the relevant polarizabilties as a function of γ in Fig. 4.5. In the left column, we present the polarizabilties in the 1064 nm lattice oriented along the z-direction with a polarization of $\hat{\boldsymbol{\epsilon}}_{z,\mathrm{lat}} = \cos(\gamma)\hat{\mathbf{x}} + i\sin(\gamma)\hat{\mathbf{y}}$ in the beam frame. The right column corresponds to a 914 nm lattice with a propagation direction along the x-axis and a polarization of $\hat{\boldsymbol{\epsilon}}_{x,\mathrm{lat}} = i\sin(\gamma)\hat{\mathbf{y}} + \cos(\gamma)\hat{\mathbf{z}}$ in the beam frame. The angle θ is encoded in the rows of the figure.

We can see that for $\theta = 0$ and $\theta = \pi/4$ the 3D lattice can be magic for the $^1S_0$-$^3P_1$ $\Delta m = \pm 1$ transition as well as for the $^1S_0$-$^3P_2$ $\Delta m = \pm 1$ transition. Furthermore, at $\theta = \pi/4$ both states of the $^3P_0$-$^3P_2$ fine-structure qubit [76] can have equal polarizability. However, it is not possible to obtain a magic 3D lattice for the $^1S_0$-$^3P_2$ $\Delta m = 0$ transition.

We find that for a 914 nm horizontal lattice with a quantization axis along the z-direction, the tensor shift offers enough tunability to obtain a magic condition for the $^1S_0$-$^3P_2$ $\Delta m = \pm 1$ transition. A horizontal lattice propagating along $\hat{\mathbf{x}}$ has a polarization in the yz-plane. By rotating a linear polarization with a half-wave plate, we can adjust the angle between the quantization axis and polarization, enabling us to tune the tensor polarizability. This method is analog to rotating the quantization axis. We plot the polarizability as a function of the polarization angle in Fig. 4.6. A polarization angle of 0 corresponds to a linear polarization along the z-axis. This tuning method allows us to realize a 3D magic lattice with a quantization axis along the z-direction. For the vertical 1064 nm lattice, we achieve a magic condition by tuning the ellipticity angle. We make the horizontal 914 nm lattice magic by adjusting the polarization angle with a half-wave plate.

In this Section, we outlined that the tunability of the vector and the tensor polarizabilites offer the tools to obtain magic conditions at non-magic wavelengths. We can use these tools to create magic lattices for the $^1S_0$-$^3P_1$ $\Delta m = \pm 1$ transition and for the $^1S_0$-$^3P_1$ $\Delta m = \pm 1$ transition.

4.3.5 Tune-out wavelengths for strontium

State-dependent lattices are highly relevant for the implementation of novel quantum simulation [96–100] and quantum computation schemes [74, 72, 73]. In strontium, state-dependent lattices can be realized for the optical qubits $^1S_0$-$^3P_0$ and $^1S_0$-$^3P_2$ by using tune-out wavelengths [92]. At the tune-out wavelength the polarizability of one state vanishes while the other state has a finite polarizability. Hence, one state can move around freely while the other state is tightly trapped.

In Fig. 4.7 we calculate the tune-out wavelengths for the states $^1S_0$, $^3P_0$ and $^3P_2$ in

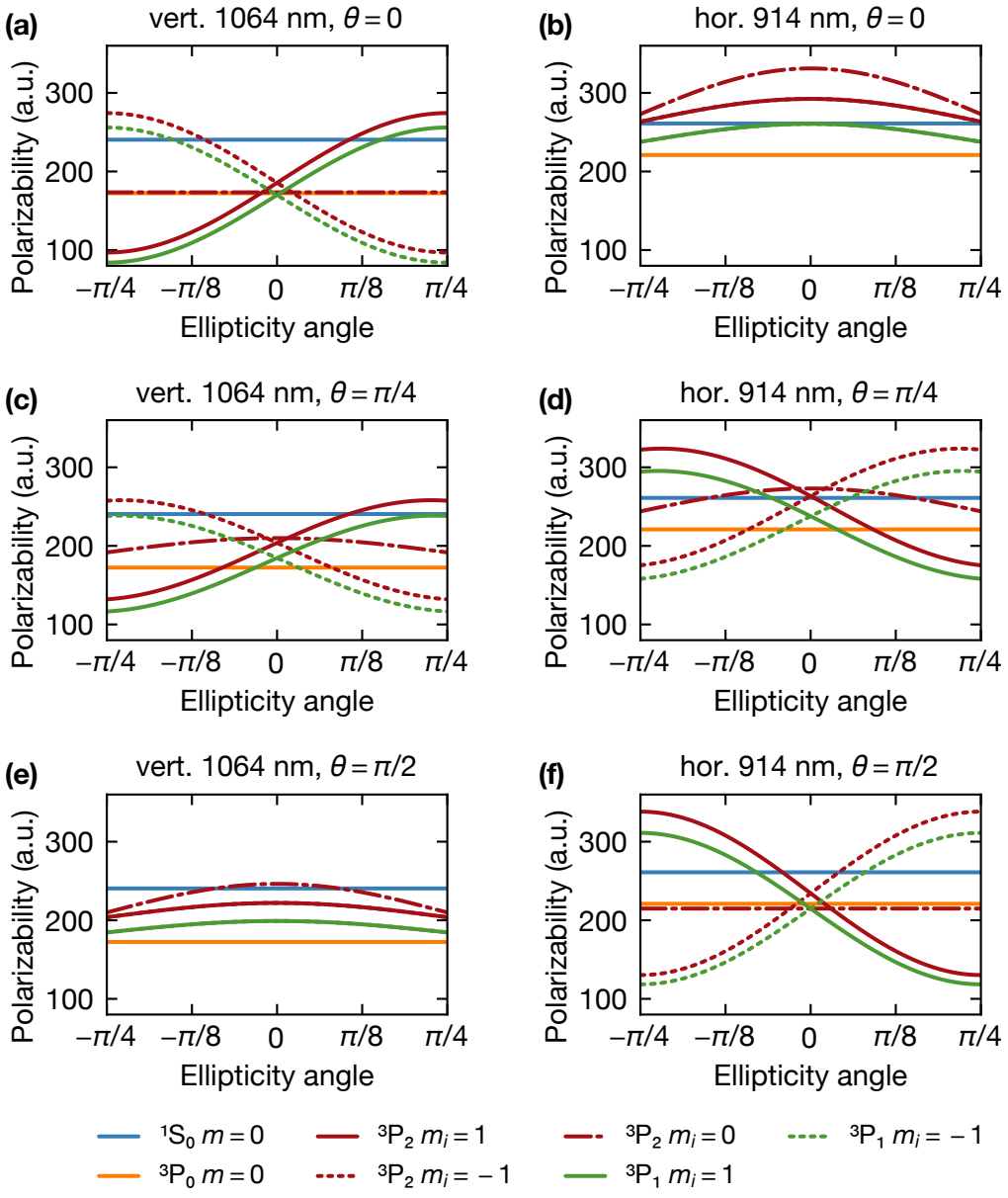

Fig. 4.5 Achieving a magic 3D optical lattice in our experimental setup with 1064 nm vertical and 914 nm horizontal lattices by tilting the quantization axis and by using elliptical polarizations. We plot the polarization of the $^1S_0$, the $^3P_0$, the $^3P_1$ $m_i = \pm 1$, and the $^3P_2$ $m_i = 0, \pm 1$ states as function of the ellipticity for various angles θ between quantization axis and vertical lattice propagation direction. In the left column we show the polarizability in the 1064 nm vertical lattice and in the right column the polarizability in the horizontal 914 nm lattices.

^{88}Sr. The tune-out wavelengths occur at frequencies close to atomic resonances. At the

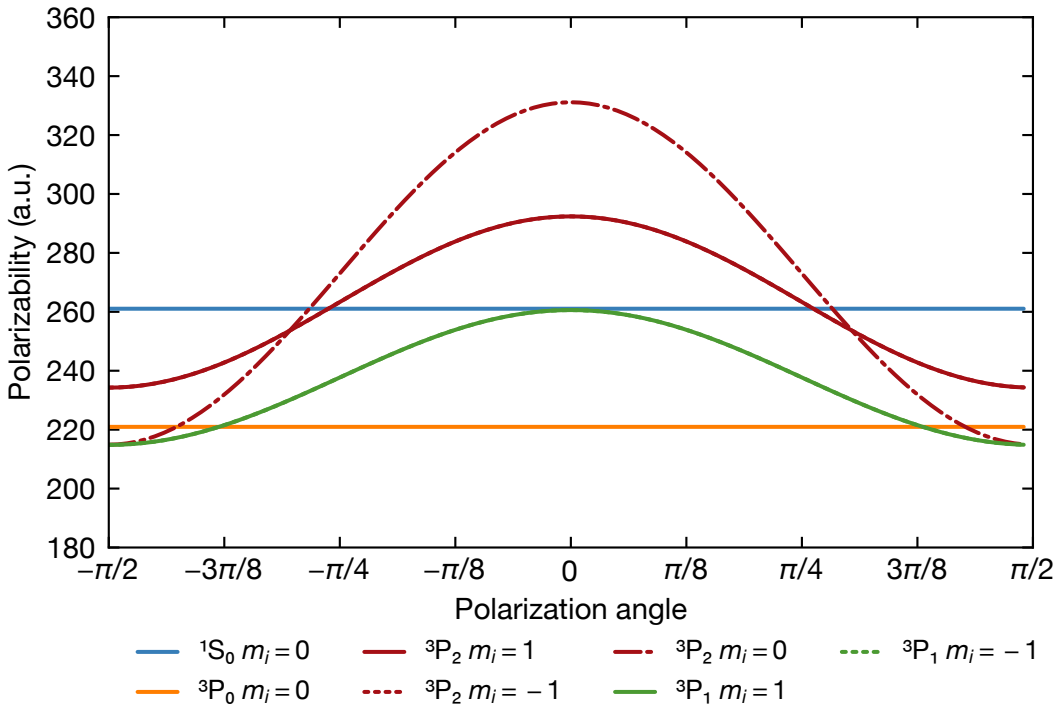

Fig. 4.6 Polarization of a horizontal 914 nm lattice and a quantization axis along the z-direction. We adjust the tensor polarizability by tuning the angle between quantization axis and polarization. This angle can be tuned using a half-wave plate to rotate a linear polarization. A polarization angle of 0 corresponds a polarization along the quantization axis.

resonances, the polarizabilities diverge and hence, the polarizabilities change their sign. The tuneout wavelengths are $689.25(5)$ nm for $^1S_0$, $679(2)$ nm for $^3P_2$, and $631(2)$ nm for $^3P_0$. In Ref. [92], we experimentally measured the $^1S_0$ tune-out wavelength and obtained $689.22222(1)$ nm, which agrees with our calculations.

In the figure, the resonances of the $^3P_1$-$^3S_1$ transition at 679 nm, the $^1S_0$-$^3P_1$ transitions at 689.449 nm, and the $^3P_2$-$^3S_1$ transition at 707 nm are nicely visible. The $^1S_0$-$^3P_1$ resonance is much narrower due to its orders of magnitudes smaller dipole-matrix element.

Independent control over the trapping potentials of the $^1S_0$-$^3P_0$ qubit can be achieved by operating one optical lattice at the ground state tune-out wavelength of $689.22222(1)$ nm and another lattice at the $^3P_0$ tune-out wavelength of $631(2)$ nm. At the tune-out of the $^1S_0$ ($^3P_0$) state, the $^3P_0$ ($^1S_0$) state has a positive polarizability resulting in trapping of this state in the intensity maxima of the lattice.

Independent potentials for the $^1S_0$-$^3P_2$ qubit can be achieved by using the $^1S_0$ tune-out wavelength and the $^3P_2$ tune-out wavelength at $679(2)$ nm. We note that at 689 nm the $^3P_2$ state has a negative polarizability resulting in $^3P_2$ atoms being trapped in the intensity minima of the lattice. This setup allows the realization of a state-dependent lattice with a similar structure as an anti-magic lattice[74] with applications for the simulation of

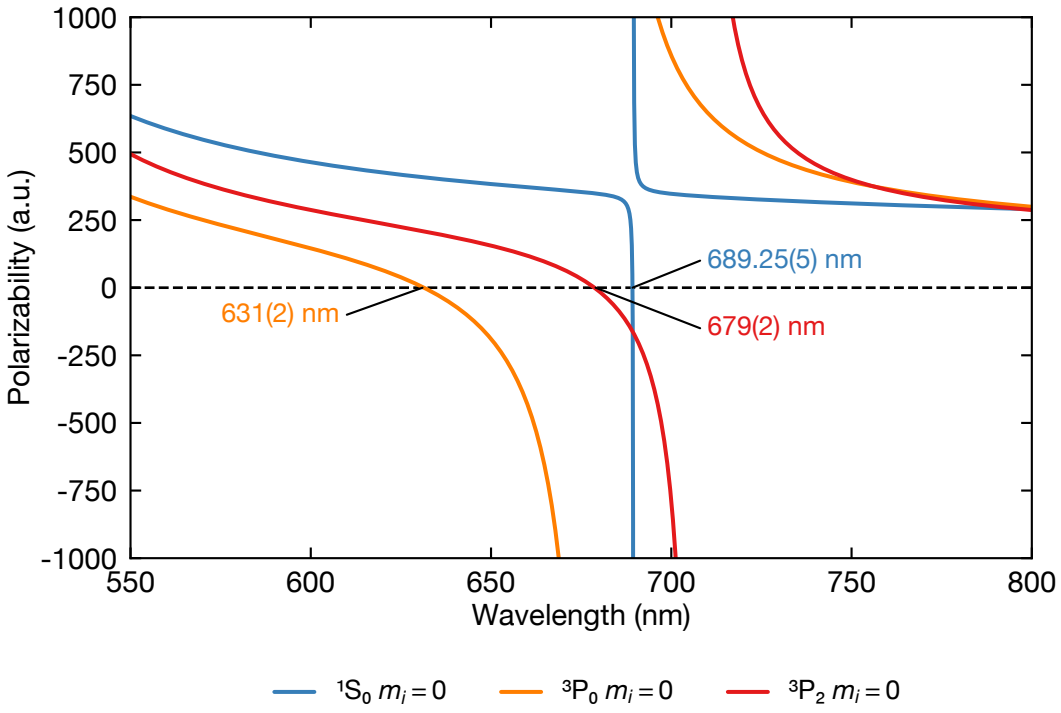

Fig. 4.7 Tune-out wavelength for the $^1S_0$, $^3P_0$ and $^3P_2$ states. We refer to the term tuneout when the polarizability of the corresponding state vanishes. The polarizabilities diverge at the wavelength corresponding to the resonances of the $^1S_0$-$^3P_1$, $^3P_0$-$^3S_1$, and $^3P_2$-$^3S_1$ transitions.

artificial gauge fields [162].

Conclusion

In this Chapter, we outlined the interaction between far off-resonant light and atoms. We used a semi-classical model to derive the polarizability of a two-level system and calculated the optical dipole potential. The associated dipole force allows trapping of atoms inside laser beams as used in optical dipole traps or optical lattices. Furthermore, we calculated the polarizability of the ground state and metastable triplet states of ^{88}Sr. The calculations allowed us to extract the magic wavelength of the singlet- to triplet-state transitions. Moreover, we elaborated on adjusting the vector and tensor polarizabilities to achieve magic conditions even at non-magic wavelengths. Finally, we discussed the tune-out wavelength of the $^1S_0$-$^3P_0$ and the $^1S_0$-$^3P_2$ qubit.

Our calculations have been verified by our own precision measurements presented in Refs. [92, 104] and in Cha. 6 of this thesis.

Chapter 5

Experimental apparatus

The quantum systems that we can study in the lab are tied to the capabilities of our experimental apparatus. Constructing new and unique experiments often requires new technical developments to overcome the limitations of already existing systems. One such technical innovation is our crossed-cavity assembly which increases the system size of state-of-the-art quantum simulators by an order of magnitude to 200×200 usable lattice sites. We aim to extend the detection and control capabilities of ultracold strontium atoms by installing a high numerical-aperture imaging system to realize the first strontium quantum gas microscope worldwide. Constructing a microscope experiment with a new atomic species requires adapting and modifying existing techniques to suit the properties of the chosen species. One major challenge of microscope experiments is isolating a single layer of atoms in the optical lattice in the focus of the microscope.

In this Chapter, we describe the construction of our experimental apparatus, overcoming the technical challenges to realize a strontium quantum gas microscope with 200×200 usable lattice sites. In Sec. 5.1, we introduce our vacuum system and the in-vacuum crossed-cavity assembly. In Sec. 5.2, we explain the design considerations for the magnetic fields. These fields are used during the isolation of a single plane and require careful stabilization schemes. We discuss our laser setups for cooling and trapping of the strontium atoms in Sec. 5.3. Finally, we describe our optical transport in Sec. 5.4, which combines a focus-tunable optical dipole tap and a travelling-wave lattice. This transport setup allows us to transport atoms ten times faster than with our previously used transport scheme.

5.1 Vacuum system

Setting up new ultracold atoms experiments requires a careful design of the vacuum system since it can only modified by rebuilding the whole experiment. The key features of our experimental apparatus are the in-vacuum crossed cavities generating the large optical lattices and the microscope objective installed during the writing of this thesis. We use two vacuum chambers spatially separating the preparation of ultracold strontium atoms from the quantum simulation under the microscope. These chambers are the so-called “main chamber” and the “science chamber”, respectively.

A render of our complete vacuum system is shown in Fig. 5.1. In Sec. 5.1.1, we discuss the part of the vacuum system used for the preparation of ultracold strontium atoms. This part includes the oven, the transverse cooling region, the Zeeman slower, and the main

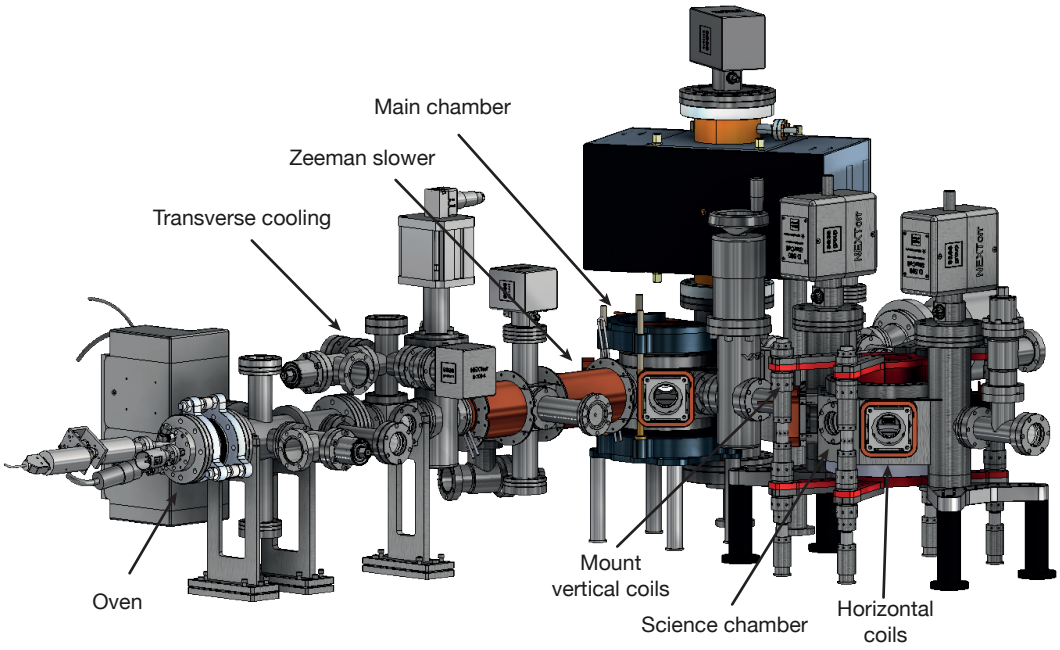

Fig. 5.1 Render of the vacuum system of our strontium apparatus.

chamber. In Sec. 5.1.2, we focus on the science chamber including the crossed cavities. The content of Sec. 5.1.1 and Sec. 5.1.2 was already well-described in the theses of André Heinz [94] and Annie Jihyun Park [93] and we briefly summarize the main ideas here.

5.1.1 Main chamber

Oven All ultracold atoms experiments start with acquiring atoms in the gas phase. Due to the high melting point of strontium (777 °C at standard pressure), we heat up strontium in an oven to 500 °C, resulting in atoms leaving the solid phase and becoming gaseous. In our experiment, we use a commercial oven (CREATEC) to heat solid chunks of naturally abundant strontium at $\sim 10^{-8}$ mbar. The hot gas of strontium atoms leaves the oven through a nozzle forming a collimated atomic beam [94].

Heating the oven to higher temperatures results in a higher atomic flux reducing the loading times of the magneto optical trap (MOT). Running the oven at 50 °C higher increases the atomic flux in the main chamber by a factor of 3 [93]. However, higher oven temperatures reduce the oven's lifetime and require to reload the oven more often. Therefore, we run the oven at 500 °C when working with ^{88}Sr and increase the temperature to 550 °C when working with ^{87}Sr to partially compensate for the lower abundance.

A differential pumping tube between the oven and the rest of the vacuum systems allows reaching a lower pressure in the main chamber.

Transverse cooling In addition to the atomic flux, the collimation of the atomic beam determines the efficiency of the Zeeman slower [143] and the loading of the magneto-optical trap (MOT) [143]. We collimate the atomic beam after the differential pumping tube using molasses cooling [143] on the blue transition along the transverse directions of the atomic beam. The cooling reduces the transverse velocities increasing the overlap of the Zeeman slower beam and the atomic beam. The increased overlap results in a higher Zeeman slower efficiency. This higher efficiency allows for shorter MOT loading times, where the transverse cooling reduces the loading time by a factor of $\sim 2-3$ [93].

Zeeman slower Our Zeeman slower is about ~ 40 cm long and uses a configurable "Bitter-coil-like" design [94] generating the magnetic field gradient. In our setup, we slow down the lower tail of the longitudinal velocity distribution resulting in a new peak of the distribution at ~ 30 m/s which is the capture velocity of the blue MOT. The light for the Zeeman slower enters the vacuum system at the very end of the chamber through a viewport.

Main chamber In this chamber, we finally capture and cool the atoms using the blue MOT. In this part of the vacuum system, we measure a magnetic trap lifetime of atoms in the $^3P_2$ state of $51(2)$ s [94].

Before we appended our vacuum system with the science chamber, we also performed experiments in the main chamber. For example, we acquired the data presented in Ref. [118] and Ref. [92] in the main chamber.

5.1.2 Science chamber

The main chamber and the science chamber are connected by a bellows and a pneumatic valve. The bellows relieves possible mechanical stress between the two chambers. By closing the valve, we can isolate the chambers, for example during the reloading of the oven.

The science chamber is a custom-manufactured steel chamber in the shape of an octagon [92]. To ensure a ultra-high-vacuum environment, we use two ion and two non-evaporative-getter (NEG) pumps reaching a pressure of $\sim 3 \times 10^{-11}$ mbar. In Fig. 5.2 we show a render of the science chamber. On the top and bottom of the chamber, we install viewports shaped like buckets, the so-called bucket windows. These windows have a glass diameter of 75 mm providing sufficient optical access to install the microscope objective from the top. The science chamber also houses the crossed cavities in which we generate our horizontal lattices. In the horizontal direction, six additional viewports provide optical access, and we use four of the seven viewports for the cavity lattices.

To enable manipulating the atoms trapped inside the cavity with magnetic fields, we install several sets of magnetic field coils around the science chamber. To generate horizontal magnetic fields, we place two pairs of square-shaped coils at the horizontal viewport where the cavity beams enter, see Fig. 5.1. We insert round coils into the bucket

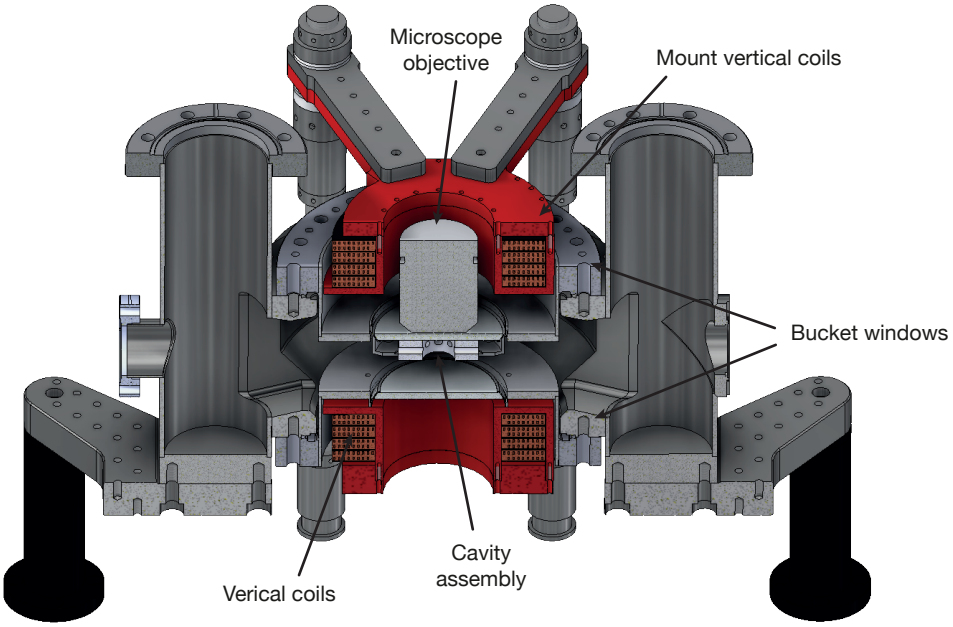

Fig. 5.2 Render of the science chamber including the cavity assembly, the vertical coils, and the microscope objective.

windows creating vertical magnetic field gradients and bias fields. We designed a mounting structure, enabling us to align the tip-tilt of the magnetic field to the planes of the optical lattice. In Sec. 5.2, we will discuss the properties of the magnetic fields in detail.

Crossed cavities

The crossed cavities are unique features of our experimental apparatus. The cavity assembly consists of an octagon-shaped spacer out of ultra-low expansion (ULE) glass and two mirror sets. Each mirror set is composed of one flat mirror and one curved mirror, which has a radius of curvature of $\sim$10 m. The mirrors are optically contacted onto the cavity spacer forming two cavities that overlap in the center of the spacer. We designed a mechanical assembly that allows us to position the mirrors with the help of an interferometer [94] before contacting. This positioning enables us to optically contact the mirror with interferometric precision achieving an overlap of the two cavity modes of 99 % [103].

After constructing the cavity, we mount the assembly to the bucket window using a cage system [103]. A render of this structure is shown in Fig. 5.3(a). The spacer rests inside the cage with a distance of 100 µm to the glass of the viewport. The cage was the only tested mounting structure that preserved the overlap of the cavity modes during several bakeout tests.

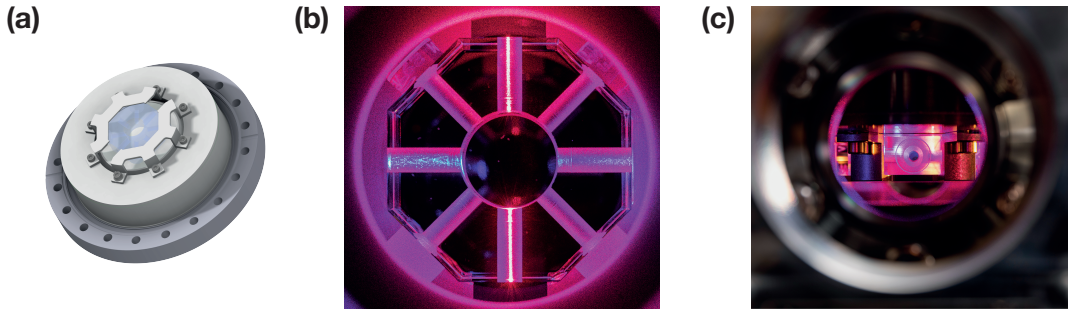

Fig. 5.3 (a). Render of the crossed cavities mounted to the top viewport. Adapted from Ref. [104]. (b) Photo of the crossed cavities from the top. To illuminate the cavities we scatter a red and a blue laser beam at the cavity spacer. (c) Photo of the illuminated cavity spacer through one of the horizontal viewports. (Photos ©Axel Griesch).

In Figs. 5.3(b) and (c), we present artistic photos of the cavity inside the vacuum chamber through the top bucket window and through one of the horizontal viewports, respectively. In panel (c), we are facing one of the cavity mirrors. We can see the mirror mask as a filled blue circle. Moreover, we can see parts of the cage mount. To illuminate the assembly, we scattered a red and a blue laser beam at the bores of the cavity spacer.

We characterize the power buildup inside the cavity by measuring the input power, the transmitted power, and the cavity finesse. We find that the cavity enhances the light intensity at the $^1S_0$-$^3P_0$ magic wavelength of 813 nm by a factor of $161(5)$ and at the $^1S_0$-$^3P_1$ magic wavelength of 914 nm by a factor of $1132(13)$. A reader interested in the details of the cavity characterization can find more information in Ref. [94] and Ref. [103].

A careful characterization of the optical lattices generated inside the cavity using atoms is the subject of Ref. [104]. In this publication, we experimentally confirmed a cavity mode waist of $489(8)$ µm agreeing with our expectations of a large and homogeneous lattice potential.

5.2 Magnetic fields

For our experiment, we require the ability to apply bias magnetic fields along all spatial directions and a strong magnetic field gradient along the vertical direction at the position of the atoms inside the cavities. The magnetic fields are especially relevant for the isolation of a single lattice plane and the local addressing. To isolate a single plane we apply the magnetic field gradient resulting in a lattice layer dependent shift of the $^1S_0$-$^3P_2$ resonance frequency due to the Zeeman effect. Each layer has a different resonance frequency enabling addressing of individual layers using the magnetic-field-sensitive $^1S_0$-$^3P_2$ transition. Coils in an anti-Helmholtz configuration generate a quadrupole magnetic field with a strong vertical gradient. To compensate the gradient curvature, we apply a bias field of $\sim 80 - 150$ G in the vertical direction and use a horizontal bias field of $\sim 5 - 10$ G to align the gradient field horizontally.

We installed large coils outside the optical table to compensate Earth's magnetic field and the field of the ion pumps. At the long side of the table the coils have dimensions of 1.9×1.3 m and at the short side 1.4×1.3 m with ~ 50 windings each. Using a current of a few Amperes the coils generate a field of $\sim 1 - 2$ G which is sufficient to compensate the environmental magnetic fields.

Now, we take a closer look at our coil designs and the magnetic field stabilization of the vertical bias field. We begin by briefly discussing the horizontal coils. Afterward, we focus on the coils generating the gradient and the vertical bias field. In addition, we explain a scheme to stabilize a current of $\sim 150 - 200$ A running through the vertical bias field coils to a relative field stability of $\sim 3 \times 10^{-5}$.

5.2.1 Horizontal magnetic fields

The horizontal coils are square-shaped with inner dimension of 76×76 mm. They consist of 15 turns of hollow-core wire. We use hollow-core wire to enable water cooling while running high electrical currents. For water-cooling, we connect the coils to a chiller providing a pressure of 3.5 bar resulting in a sufficient water flow through the coils. We monitor the water flow through each coil using a flow meter read out via a microcontroller. Currently, we do not use this possibility but are planning to integrate the monitoring capability into an interlock system.

Coils installed on opposite viewports are connected in series and form a coil pair. We connect each pair to two switching power supplies[1]. In our setup, running currents of more than ~ 70 A requires voltages higher than 15 V. Hence, we connect the supplies in series, providing up to 30 V and 100 A. We can run the coils with a maximum at 100 A at ~ 20 V, corresponding to heat deposit of 2 kW requiring water cooling to remove the heat.

With the spacing of 268 mm between the coils, we can only generate fields of 89 mG/A with a single coil pair. Hence, we can apply along one horizontal direction a magnetic field up to 8.9 G. The power supplies offer relative current stability of 9×10^{-5} resulting in magnetic field stability of 0.8 mG at full load. As we will see in the next Chapter, this stability is better than the vertical field stability. Therefore, we do not actively stabilize the horizontal fields.

5.2.2 Vertical magnetic fields

We require large magnetic fields along the vertical direction for two reasons: (i) spatially translating the zero of the field gradient for isolating a single lattice layer and (ii) inducing the $^1S_0$-$^3P_0$ clock transition in ^{88}Sr [123]. Isolating a single plane puts more stringent constraints on the field strength and the field stability than inducing the clock transition. Therefore, we will focus our discussion on using the vertical magnetic fields for the layer isolation.

[1] Delta Elektronika SM15-100

First, we explain the design of our coil mount. Afterward, we calculate the fields generated by the coils and briefly discuss our considerations regarding water-cooling.

Coil mount The mounting structure of the coils is shown in Fig. 5.2. To maximize the magnetic field at the position of the atoms, we place the coils as close as possible to the atoms. For that purpose, we design a coil mount that allows us to insert the coils inside the bucket windows without connecting them mechanically to the vacuum chamber. The coils are clamped inside custom holders manufactured from PEEK which we insert into the bucket windows. We connect these holders with the optical table via four rods of stainless steel. The complete coils mount looks like a spider with four legs. The rods consist of several components with left and right handed threads enabling us to individually adjust the height of the coil holders. In addition, we can control the tip-tilt of the holders. These degrees of freedom allow us to align the vertical magnetic field to the planes of the optical lattice.

Inside each holder, we clamp four individual coils with 2×9 turns. We use hollow-core wire with outer dimensions of 3×4 mm to wind the coils. After their winding, the coils are encased with epoxy to maintain their form. We connect the two axially inner and two axially outer coils, where we use the inner ones to generate a magnetic field gradient and the outer ones for a bias field.

The innermost layer of the top and bottom coils have a distance of 47.5 mm to the position of the atoms. The coil holders have an inner diameter of 69 mm providing sufficient space to insert the microscope objective with its diameter of 49 mm.

Magnetic field We calculate the magnetic field gradient and the bias field that we can generate with our vertical coils. These calculations form the basis to discuss the parameters of the magnetic field necessary to isolate a single lattice layer using the $^1S_0$-$^3P_2$ transition.

We simplify a coil with N number of turns by a wire loop in the xy-plane with radius R. Running a current NI through the loop generates a radial magnetic field B_ρ and a perpendicular axial field B_z given by [163]

$$B_\rho(\rho, z) = \frac{\mu_0 N I}{2\pi} \frac{z}{\rho\sqrt{(\rho+R)^2+z^2}} \left(\frac{R^2+\rho^2+z^2}{(R-\rho)^2+z^2} E(m) + K(m) \right), \tag{5.1}$$

$$B_z(\rho, z) = \frac{\mu_0 N I}{2\pi} \frac{1}{\sqrt{(\rho+R)^2+z^2}} \left(\frac{R^2-\rho^2-z^2}{(R-\rho)^2+z^2} E(m) + K(m) \right), \tag{5.2}$$

where $m = 4R\rho/[(R+\rho)^2+z^2]$. We use a cylindrical coordinate system. Here, $K(m)$ and $E(m)$ are the complete elliptic integral of first and second kind, respectively. These

integrals are defined by

$$K(m) = \int_0^{\pi/2} \frac{\mathrm{d}\phi}{\sqrt{1 - m^2 \sin^2 \phi}} \tag{5.3}$$

$$E(m) = \int_0^{\pi/2} \mathrm{d}\phi \sqrt{1 - m^2 \sin^2 \phi} \tag{5.4}$$

One can obtain the values of these integrals using software libraries such as "scipy", enabling fast computations of magnetic fields. We can calculate the radial and the axial magnetic field of a coil pair spaced by a distance d with

$$B_\rho^{(\mathrm{tot})}(\rho, z) = B_\rho(\rho, z + d/2) + B_\rho(\rho, z - d/2), \tag{5.5}$$

$$B_z^{(\mathrm{tot})}(\rho, z) = B_z(\rho, z + d/2) + B_z(\rho, z - d/2). \tag{5.6}$$

To calculate the magnetic field of anti-Helmholtz coils, we insert a negative current into the equation describing one of the coils.

We use the equations derived above to calculate the magnetic fields generated by our configuration, which connects two coil pairs in series to produce a gradient and the other two to supply a bias field. Because the coils have a finite radial and axial extent, we calculate the fields using the following dimensions

$$\begin{aligned} R &= 53 \text{ mm}, \\ d^{(\mathrm{gradient})}/2 &= \pm 51.5 \text{ mm}, \pm 59.5 \text{ mm}, \\ d^{(\mathrm{bias})}/2 &= \pm 67.5 \text{ mm}, \pm 75.5 \text{ mm}, \end{aligned}$$

where R is the averaged radius and d is the averaged axial spacing of the coils.

In Fig. 5.4(a) we show the calculated bias magnetic field with a strength of 1.78 G/A at the position of the atoms. The anti-Helmholtz coils produce a quadrupole magnetic field as shown in Fig. 5.4(b). This field possesses a vertical gradient [Fig. 5.4(c)] of 0.8 G/(A cm). With a lattice spacing of 532 nm and a Zeeman shift of 2.1 MHz/G for the $^3\mathrm{P}_2$ $m_J = 1$ state, the vertical gradient separates neighboring lattice layers in frequency by 89 Hz/A for ^{88}Sr. We can run a current of 280 A through the gradient coils, resulting a frequency splitting of 24 kHz, which we can easily resolve using the ultranarrow $^1\mathrm{S}_0$-$^3\mathrm{P}_2$ transition.

Let us study the vector magnetic field shown in Fig. 5.4(b) in more detail. In the center between the coils, the orientation of the magnetic field changes drastically over a small spatial region. The reason for this behavior is the quadrupole nature of the field which consists of vertical gradient and a half-as-strong horizontal gradient shown in Fig. 5.4(d). Hence, the horizontal gradients lead to circles of equal magnetic field strength, preventing a uniform atomic resonance frequency over the extent of a lattice layer. Away from the center, the radii of these circles increase, resulting in more homogeneous resonance frequency over a single layer. We can access such a less-curved field region by applying

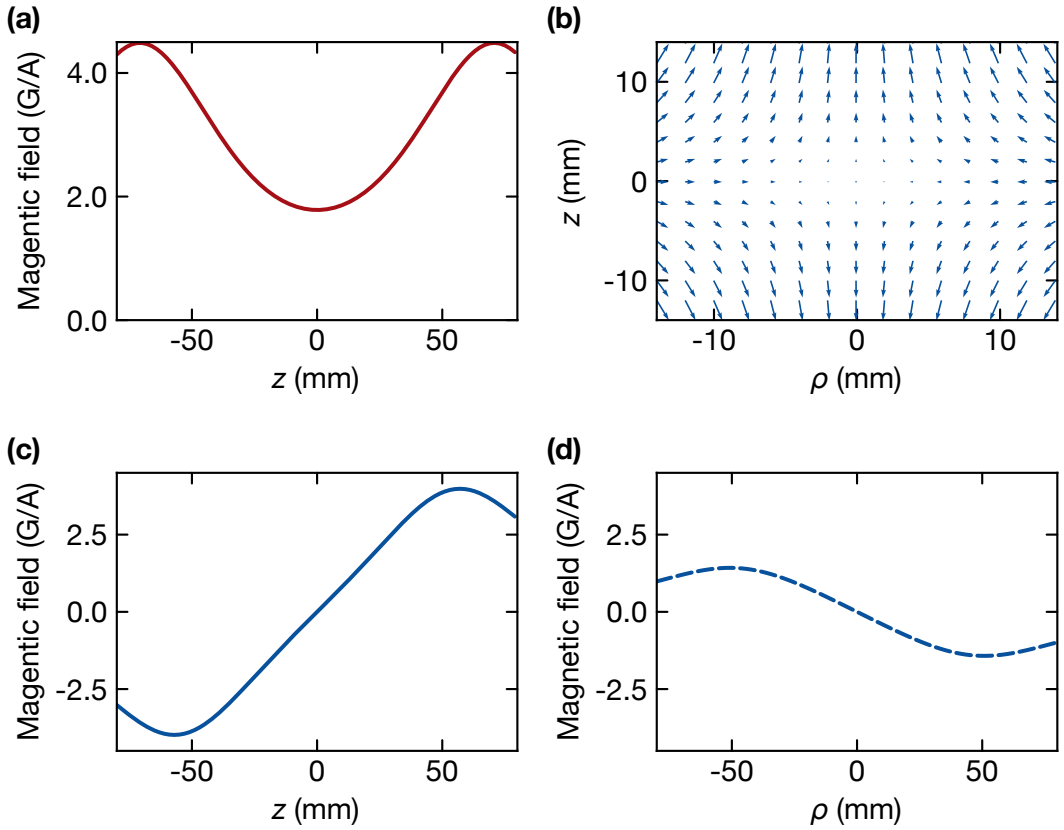

Fig. 5.4 Calculated vertical magnetic fields. (a) Calculated bias magnetic field along the vertical direction. (b) Vector plot of the magnetic field produced by the gradient coils. (c) Magnetic field along the vertical direction produced by the gradient coils. (d) Horizontal magnetic field in the plane of the atoms produced by the gradient coils.

a bias magnetic field, which is equivalent to moving the zero-position of the gradient. In such a region, we can isolate a single layer.

We investigate the frequency shift of several neighboring lattice layers when we simultaneously apply a gradient of 224 G/cm ($\cong 280$ A) and bias field of variable strength. Along the radial direction, we allow a variation of the resonance frequency of 8 kHz over a single layer. This frequency band corresponds to a third of the frequency spacing between neighboring layers. In Fig. 5.5, we plot the resonance frequency shift of the $^1S_0$-$^3P_2$ $\Delta m = 1$ transition as a function of the radial position ρ. We observe that the layer below the central one is at some radial distance in resonance with the frequency interval of the central layer. If this crossing region occurs inside the spatial extent of the atomic cloud, we can not isolate a single layer. The region inside our frequency interval increases as we increase the bias magnetic field. Assuming a cloud size of ~ 150 µm, we require a bias field larger than ~ 150 G to move the crossing region sufficiently far away from the position of the atoms.

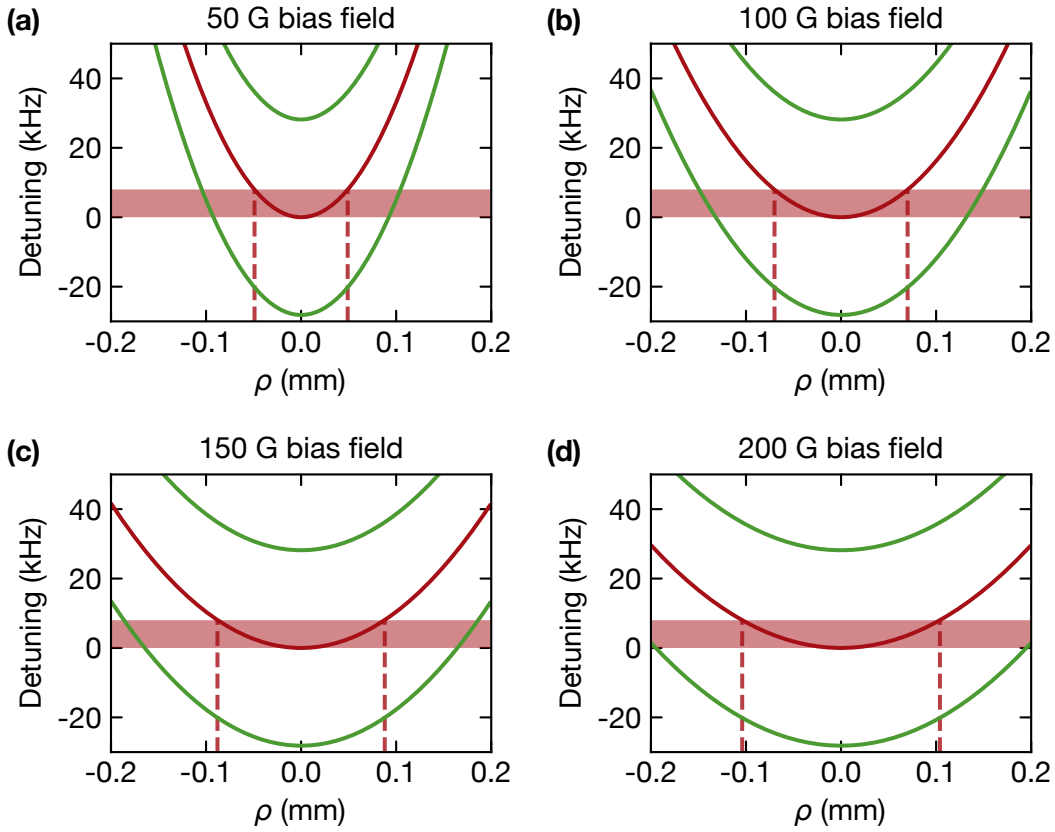

Fig. 5.5 $^1S_0$-$^3P_2$ resonance frequency detuning of individual optical lattice planes, where the central layer is red and its neighboring layers are green. We apply a gradient of 224 G/cm and a bias field of variable strength. The red-shaded area corresponds to a frequency interval of 8 kHz. The dashed, vertical lines indicate the size of the isolated layer. To move the region in which the central layer is resonant with a neighboring one outside the spatial extent of the atomic cloud (radius of ~ 150 µm), we have to apply a bias field larger than 150 G.

By running a current of ~ 85 A through our bias field coils, we can generate such a field. To limit magnetic field noise induced broadening of the $^1S_0$-$^3P_2$ transition to several kilohertz, we have to stabilize the magnetic field to a relative stability in the lower 10^{-5} regime. Before we explain our stabilization scheme in Sec. 5.2.3, we briefly discuss our considerations regarding water-cooling the coils.

Water cooling We briefly discuss how we dimension water flow and pressure to cool the science chamber coils generating the vertical magnetic fields. We base our estimates on the parameters used to cool the MOT coils and scale them accordingly.

To generate the magnetic fields of the blue MOT, we run a current of 200 A at a voltage of 30 V through 6 coils. The corresponding electric power results in a heat deposit of 1 kW per coil. We cool these coils by running water through the hollow core of the wire

with an input pressure of 4.5 bar. The resulting water flow rate is sufficient to remove the deposited heat. In analogy to Ohm's law $U = RI$, the flow rate Q is given by

$$Q = \frac{\Delta P}{R_{\mathrm{hyd}}}, \tag{5.7}$$

where R_{hyd} is the hydrodynamic resistance and ΔP is the pressure drop. To calculate the flow rate of the MOT coils, we first calculate the hydrodynamic resistance of the wire's rectangular hollow core given by [164]

$$\frac{1}{R_{\mathrm{hyd}}} = \frac{h^3 w}{12\eta L}\left[1 - \sum_{n,\mathrm{odd}} \frac{192h}{n^5\pi^5 w}\tanh\left(n\pi\frac{w}{2h}\right)\right], \tag{5.8}$$

$$R_{\mathrm{hyd}} = 0.86 \times 10^{11}\ \mathrm{Pa\,s/m^3}, \tag{5.9}$$

where $w = 2$ mm is the core width, $h = 1$ mm is the core height, $L = 9.8$ m is the length of the coil wire and $\eta = 1$ mPa s is the viscosity of water. This equation assumes $w > h$. With the hydrodynamic resistance and the pressure drop of $\Delta P = 4.5$ bar, we obtain a flow rate of 0.31 l/min.

Assuming that the cooling power scales linearly with the flow rate, we can estimate the flow required to cool the science chamber gradient coils, through which we run the highest current. To generate the gradient we use a current of 280 A at a voltage of ≈ 40 V, resulting in a deposited power of 11.2 kW. This deposited power means that each of the four coils experiences a deposited heat of 2.8 kW. The deposited heat is a factor of 2.8 higher than in the MOT coils resulting in a required flow rate of 2.8×0.31 l/min $= 0.87$ l/min. Each gradient coil has a wire length of $L = 9.9$ m with the same hollow core dimensions as the MOT coils resulting in comparable hydrodynamic resistance of 0.87×10^{11} Pa s/m^3. Hence, to achieve comparable temperature stability of the coils, we have to apply a pressure of ≈ 13 bar.

As a compromise between the chiller's cooling power, output flow rate, and output pressure, we decided on a commercial chiller with an output pressure of 10 bar. While running the coils during the experimental sequence, we observe that the temperature of the coils increases, but in an acceptable regime of a few degrees Kelvin.

5.2.3 Current stabilization

In this Section, we discuss our current stabilization scheme for the bias field. The stability of the bias field is relevant during the isolation of a single lattice layer, where we apply a magnetic field gradient and a bias field and locally address atoms using the field-sensitive ^{1}S$_0$-^{3}P$_2$ $\Delta m_J = \pm 1$ transitions. The applied gradient splits the resonance frequency of neighboring layers by 24 kHz. As an upper bound, we can allow a broadening of the linewidth up to 12 kHz corresponding to a relative field stability of $\sim 4 \times 10^{-5}$.

Our feedback loop to stabilize the current running through the bias field coils is shown in Fig. 5.6. Our stabilization is based on measuring the current with a Hall-probe and

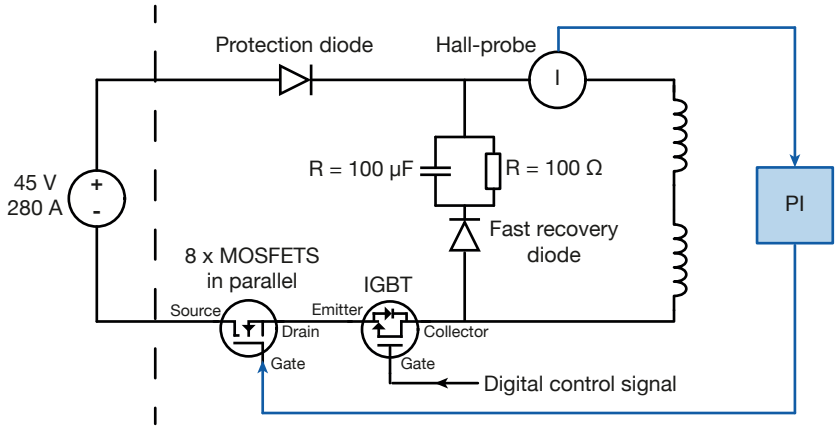

Fig. 5.6 Schematic of the current stabilization circuit for the science chamber offset coils. A commercial Hall-probe measures the current flowing through the coils. The probe signal is used to feed back to eight MOSFETS connected in parallel. We are able to switch off the current within ~ 150 µs using an IGBT and a quarter-wave circuit. The dashed line indicates a separation between two rooms.

using 8 metal–oxide–semiconductor field-effect transistors (MOSFETs) connected in parallel as actuators. We use a commercial Hall-probe (LEM 400-S ultrastab) to measure currents up to 400 A. A home-built electronics board converts the transducer output current into a voltage which we feed into a proportional-integral (PI) controller. The PI controller acts on the gates of the MOSFETs to regulate the current. We modified the PI controller to linearize the MOSFETs' transfer function.

To enable fast current switch-offs, the circuit in Fig. 5.6 contains an additional insulated gate bipolar transistor (IGBT) and a so-called quarter-wave circuit. When we open the IGBT, the current stops flowing and the coils and the capacitor form an LC-circuit. A fast recovery diode stops the oscillations of the circuit after a quarter of the oscillation period enabling a switch-off within 150 µs. The capacitor is discharged via a resistor connected in parallel. However, eddy currents in the vacuum chamber and bucket windows increase the settling time of the magnetic field by an order of magnitude.

To avoid acoustic noise of the power supplies in the lab, we place them inside a separate room. The supplies are connected to the stabilization circuit via cooper cables with a cross-section of 35 mm^2.

We quantify the magnetic field stability out-of-loop using a fluxgate sensor. We find a relative stability of 3.5×10^{-5} corresponding to a broadening of the $^1S_0$-$^3P_2$ transition to a linewidth of 11 kHz. This broadening is sufficiently small for isolating a single layer. We believe that electronic noise in our current read-out circuit and the PI controller limits the stability. To further improve the stability, one can think about adding a slow feedback system that measures the magnetic field directly and then servoing on currents of tens of milliampere.

5.3 Laser systems

Cooling and trapping strontium requires several lasers at different wavelengths. In the following, we briefly explain the steps required to prepare a cloud of ultracold strontium and a detailed explanation can be found in the Refs. [93, 94]. The first steps are slowing down the atoms emitted from the oven and trapping them in a magneto optical trap (MOT) [165]. These two steps use laser cooling on the $^1S_0$-$^1P_1$ transition with a wavelength of 461 nm. From the $^1P_1$ state the atoms decay via the $^1D_2$ state to the $^3P_2$ state, which is metastable. We optically pump the atoms back to the $^1S_0$ ground state by driving the $^3P_2$-$^3S_1$ transition at 707 nm. From the $^3S_1$ state, the atoms can decay to all ^3P_J states. Atoms that end up in the $^3P_0$ state are pumped again to the $^3S_1$ state with the corresponding transition at 679 nm. Atoms in the $^3P_1$ state decay quickly to the $^1S_0$ state. After the blue MOT stage, the atoms have a temperature of ~ 1 mK. To cool the atoms further, we apply a red MOT [166] on the $^1S_0$-$^3P_1$ transition at 689 nm. With this cooling stage, we reach a temperature of $1 - 2$ µK [118]. A detailed description of the experimental parameters, such as frequency detuning, beam size, etc., can be found in Refs. [93, 94].

From the discussion above, we see that preparing strontium atoms at ultracold temperatures requires four different lasers at wavelengths of 461 nm, 679 nm, 689 nm, and 707 nm. To drive the $^1S_0$-$^3P_2$ transition, used for local addressing, we need an additional laser at 671 nm. Fortunately, all these wavelengths can be derived from diode lasers. Our diode laser systems use a single frequency-stabilized master laser and several injection-locked laser diodes to amplify the power [94].

Transporting and trapping of atoms with light requires lasers with high output powers, such as solid-state lasers or fiber-based amplifiers. For our optical transport and the vertical lattice, we use three Yb-doped fiber amplifiers with output powers of $30 - 40$ W at a wavelength of 1064 nm. Such high-power beam paths require careful design considerations to avoid thermal-lensing effects [154].

We create our horizontal lattices inside our crossed buildup cavities at the $^1S_0$-$^3P_0$ magic wavelength of 813 nm or at the $^1S_0$-$^3P_1$ magic wavelength of 914 nm. We derive the laser light from a Ti:sapphire laser which we frequency stabilize to the cavities. Trapping atoms in optical cavities is challenging due to the cavity's frequency-noise to amplitude-noise conversion that compromises the trap lifetime [167]. We overcome this challenge by carefully adjusting the feedback loop of the frequency stabilization.

In the following, we only briefly discuss the blue and the red laser systems, since Refs. [93, 94] contain detailed information about these setups. We focus on the $^3P_2$ laser setup, the high-power 1064 nm laser systems and the frequency stabilization of the Ti:sapphire laser to our crossed cavities.

5.3.1 Blue laser system

We use our blue laser system to derive the 461 nm beams required for various cooling stages, including the Zeeman slower and the blue MOT. In addition, the laser setup provides the probe beams for imaging on the $^1S_0$-$^1P_1$ transition. The system consists of one

commercial diode laser (Toptica DL Pro) and several home-built injection-locked laser diodes. We frequency-stabilize the diode laser to a spectroscopy cell [117] using a frequency transfer modulation technique [168]. Using a double-pass acousto-optic modulator (AOM) to compensate for the isotope shift, we can stabilize the laser frequency to the $^1S_0$-$^1P_1$ atomic resonance of ^{88}Sr or ^{87}Sr.

We split the laser beam into multiple beam paths for frequency stabilization, imaging, the transverse cooling of the atomic beam after the oven, Zeeman slower, and blue MOT beams. If required, we shift the light frequency using AOMs. Since each beam of the transverse cooling, the Zeeman slower, and the blue MOT requires several milliwatts of power, we use injection locks to amplify the laser power. A schematic of the beam paths can be found in Ref. [94].

5.3.2 Red laser system

The red laser system consists of a frequency-stabilized diode laser (Toptica DL Pro) and one injection lock. Since the $^1S_0$-$^3P_1$ transition has a natural linewidth of $\sim$7 kHz, the red laser frequency has to be orders-of-magnitude more stable than the blue laser frequency.

We stabilize the red laser frequency to an ultrastable high-finesse reference cavity using the Pound-Drever-Hall (PDH) technique [169]. The cavity has a finesse of $280,000$ at 689 nm, providing a cavity linewidth of 5.4 kHz. To maintain a stable resonance frequency, we place the cavity under vacuum, including two temperature-isolating copper heat shields. Additionally, we stabilize the temperature of the chamber to the cavity's zero-crossing temperature [170]. We generate the frequency sidebands for the PDH scheme using a fiber-based electro-optic modulator (EOM). A high-bandwidth PID controller (Toptica FALC) servos on the laser current and laser cavity piezo and narrows the linewidth to the Hertz regime.

We amplify the laser power with the help of an injection-lock module. After the amplification, we split the beam into several beam paths and shift their frequencies with AOMs if required. A detailed description of the red laser system is given in Ref. [93].

5.3.3 Repump laser system

To repump the atoms during the blue MOT stage, we use two diode lasers (Toptica DL Pro) operating at 679 nm and 707 nm. We do not actively stabilize the laser frequency and keep them free-running. To adjust the frequencies to the $^3P_0$-$^3S_1$ and the $^3P_2$-$^3S_1$ repump transitions, we optimize the laser frequency to maximize the blue MOT fluorescence signal. For the fermionic isotope ^{87}Sr, the $^3P_2$ level splits into several hyperfine states, and we modulate the 707 nm laser frequency by scanning the laser cavity piezo.

5.3.4 $^3P_2$ laser systems

To drive the $^1S_0$-$^3P_2$ transition at 671 nm, we use a laser system based on a frequency-stabilized external cavity diode laser (ECDL) and an injection-locked laser diode. A schematic of the setup is shown in Fig. 5.7.

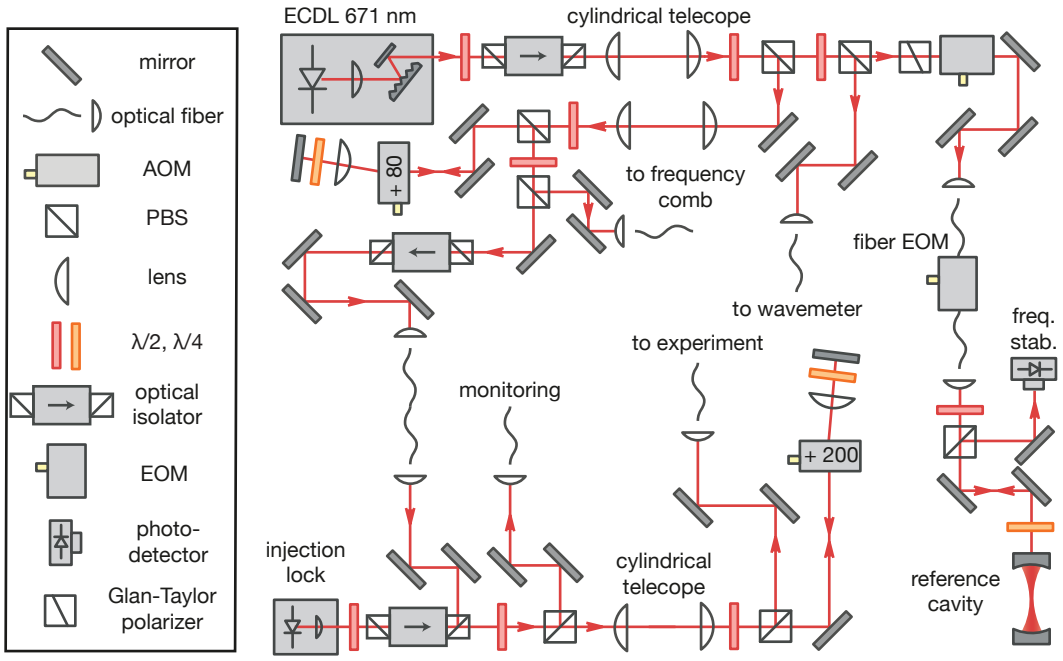

Fig. 5.7 Schematic of the $^3P_2$ laser system including injection lock and reference cavity. To drive the $^1S_0$-$^3P_2$ at 671 nm, we use a home-built external cavity diode laser (ECDL) frequency stabilizized to a reference cavity using the PDH technique. We amplify the laser power with an injection locked diode resulting in ≈ 26 mW power at the atoms. We can use a frequency comb to measure the absolute laser frequency.

We frequency-stabilize the laser using the dual sideband locking technique [171], where a fiber-EOM and an additional home-built EOM generate the sidebands. This technique allows us to stabilize the laser at arbitrary frequencies even if the desired laser frequency and the cavity resonance are several hundreds of megahertz detuned from each other.

The reference cavity is placed in a similar environment as the reference cavity of the red laser system [170]. We use a high-bandwidth PID controller (Toptica FALC) to servo on the laser current and the laser cavity piezo resulting in a laser linewidth of about 1 kHz. The laser linewidth at 671 nm is limited by the cavity finesse of $20,000$. Using a cavity with a higher finesse will immediately allow us to reduce the laser linewidth to a few hertz. Such a cavity is already ordered and will be installed soon.

We amplify the laser power using a home-built injection lock resulting in ~ 26 mW of usable laser power at the atoms. Reference. [93] gives a detailed description of our injection lock design. A double-pass AOM after the injection lock enables us to scan the laser frequency over a few megahertz. Since we found that the master laser frequency becomes unstable once we seed the injection lock, we installed an additional optical isolator between the injection lock and the ECDL to prevent optical feedback.

A fiber connecting the $^3P_2$ laser with a frequency comb allows us to measure the laser's

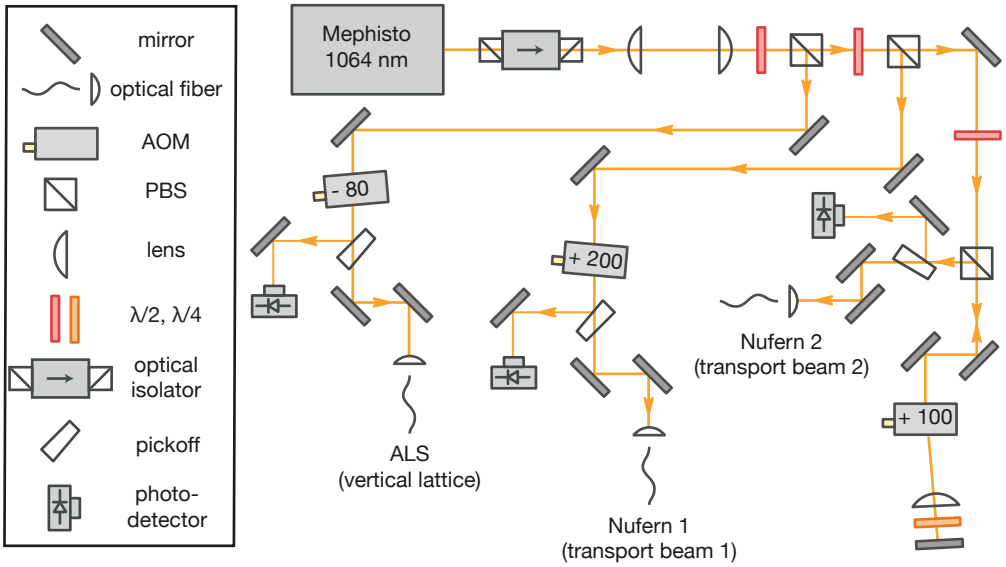

Fig. 5.8 Schematic of the laser setup to seed the high-power Yb-doped fiber amplifiers generating the transport and vertical lattice beams. We use acousto-optic modulators (AOMs) to shift the frequencies of the individual beams. Before we couple the beams into fiber, their powers are monitored with photodetectors.

absolute frequency. We highly appreciated being able to measure the laser frequency with the comb during the spectroscopy measurements of the $^1S_0$-$^3P_2$ transition presented in Ch. 6.

5.3.5 High-power laser system

Here, we describe our optical setup of the high-power 1064 nm laser beams. A nonplanar ring oscillator laser seeds high-power Yb-doped fiber amplifiers deriving beams with powers of $30 - 40$ W. We use two beams to realize an optical transport and one beam to generate the vertical lattice.

The optical setup of the seed laser is shown in Fig. 5.8. The seed light is generated by a commercial low-noise nonplanar ring oscillator laser (Coherent Mephisto) with $\sim$1.2 W output power. We split the laser beam into three beam paths, where we use two beams for the optical transport of atoms and one beam for the vertical lattice. We shift the frequency of the transport (vertical lattice) beams by $+200$ MHz (-80 MHz) using acousto-optic modulators (AOMs). After the AOMs, we monitor the laser power using photodetectors. We couple the beams into optical fibers, seeding the fiber amplifiers.

We transport our atoms from the main chamber into the science chamber using a travelling-wave optical lattice (see Sec. 5.4 for further details). Such a lattice requires two phase-coherent beams with a variable frequency difference. Since we generate both transport beams from a single seed laser, they are naturally phase-coherent. We use an AOM in double-pass configuration to sweep the frequency of one beam, while the fre-

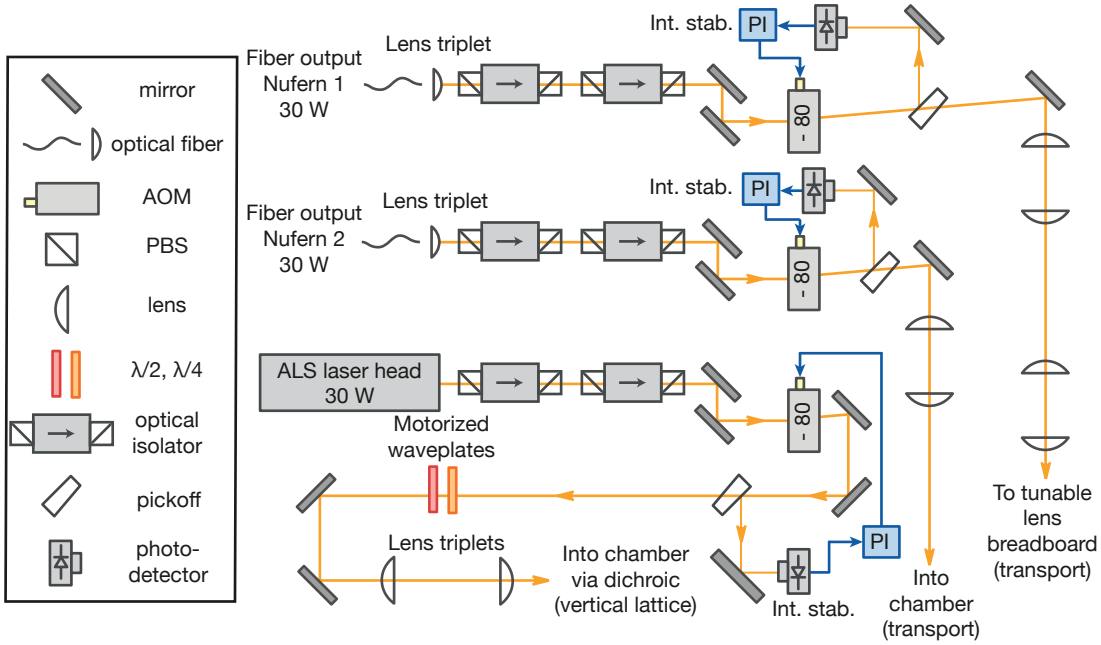

Fig. 5.9 Schematic of transport and vertical lattice laser path. We stabilize the laser intensity with a PI control loop acting on the individual AOMs. The light polarization of the lattice beam can be controlled via a motorized half-wave plate and a quarter-wave plate.

quency of the other beam is fixed. The double-pass configuration allows us to sweep the frequency within a bandwidth of ~ 5 MHz, while the fiber-coupled laser power varies by $10\,\%$, which is sufficiently small for the amplifiers to provide constant output powers.

During the characterization of the atom transport, we observed that the phase noise and the phase coherence of the radio frequency signals, that seeds the AOMs is crucial to achieve a high transport efficiency. Hence, we use a dual-channel arbitrary function generator[2] as a radio-frequency source for the AOMs.

We use the third beam path to seed the amplifier generating the vertical lattice beam. To avoid interference between the lattice and the transport beams, we detune the lattice by -280 MHz from the transport frequency.

The high-power beams are derived from Yb-doped fiber amplifiers. We depict a schematic of the beam path in Fig. 5.9. The design follows the considerations of Ref. [154] to build the setup as stable as possible. In the beam path, we use fused-silica optics to minimize thermal lensing effects that result in beam pointing and focus instabilities.

We generate the transport beams with amplifiers from Nufern and the lattice beam with an amplifier from ALS[3]. The Nufern amplifiers have output fibers which we mount in custom-manufactured fiber chucks. We ensure high beam qualities by collimating

[2] Tektronix AFG3252C
[3] Azurlight Systems 1064 nm 50 W

the beams with air-spaced fused silica lens triplets[4]. The lattice beam is emitted from the ALS laser head as a collimated beam. To avoid damaging back-reflections into the amplifiers, we equip each beam path with two isolators providing 60 dB isolation in total. We replaced the cube beam splitters of the isolators with half-wave plates and fused-silica Brewster polarizers because the cubes are susceptible to thermal lensing. We prevent thermal drifting of the isolator crystals by water-cooling them.

We stabilize the beam intensity using shear-mode AOMs[5] as actuators, which we water-cool. We measure the beam power with InGasAs photodetectors and use the detector signal as an input for the control loop. After the AOMs, each beam has maximum available laser power of about 20 W.

Using a motorized half-wave and a quarter-wave plate, we can control the lattice polarization during the experimental sequence. We adjust the lattice waist and focus with a telescope. Because the available space to set up the telescope was very limited, we also used air-spaced fused-silica lens triplets.

5.3.6 Ti:Sapphire laser

The final laser system we discuss is the Ti:Sapphire laser. The laser can produce light at the $^1S_0$-$^3P_0$ magic wavelength of 813 nm or at the $^1S_0$-$^3P_1$ magic wavelength of 914 nm. We pump the Ti:Sapphire laser (M2 SolsTis) with 18 W of 532 nm light derived from a solid-state laser (Verdi V18). We split the light emitted from the Ti:Sapphire laser into two beam paths. Each path is coupled into one arm of our crossed cavities generating the horizontal optical lattice. Here, we focus on the technical details of stabilizing the frequency of the individual beam paths onto the cavity resonance. The reader interested in the optical setup may look at Ref. [94] for further details.

Using optical cavities to generate traps for neutral atoms is technically challenging. The reason is that cavities convert frequency noise into intensity noise [167] reducing the trap lifetime via parametric heating [151]. If we frequency-stabilize the laser to the resonance of one cavity arm directly, we can not turn off the cavity lattice without unlocking the laser which results in mode hops. Hence, we develop the more complicated, but at the same time more robust, stabilization scheme shown in Fig. 5.10.

We frequency-stabilize the Ti:Sapphire laser to the resonance of a transfer cavity using the PDH technique. The feedback loop acts on the slow piezo and the fast piezo of the laser cavity to control the frequency. The purpose of the transfer cavity is to keep the laser frequency constant in the range of tens to hundreds of kilohertz. Hence, the stabilization can be relatively loose. Using this additional cavity as a prestabilization stage, we can turn off or ramp the power of the cavity lattices without disturbing the laser.

The transfer cavity has a finesse of 5000 at 914 nm. One mirror of the transfer cavity is glued onto a piezo stack, to actively control the cavity length. We stabilize the cavity length to the frequency of the several-hertz-wide clock diode laser using the PDH technique. We obtain this narrow laser by frequency-stabilizing it to a reference cavity with

[4] Optosigma HFTLSQ-30-40PF1
[5] Gooch & Housego I-FS080-2S2G-3-LV1

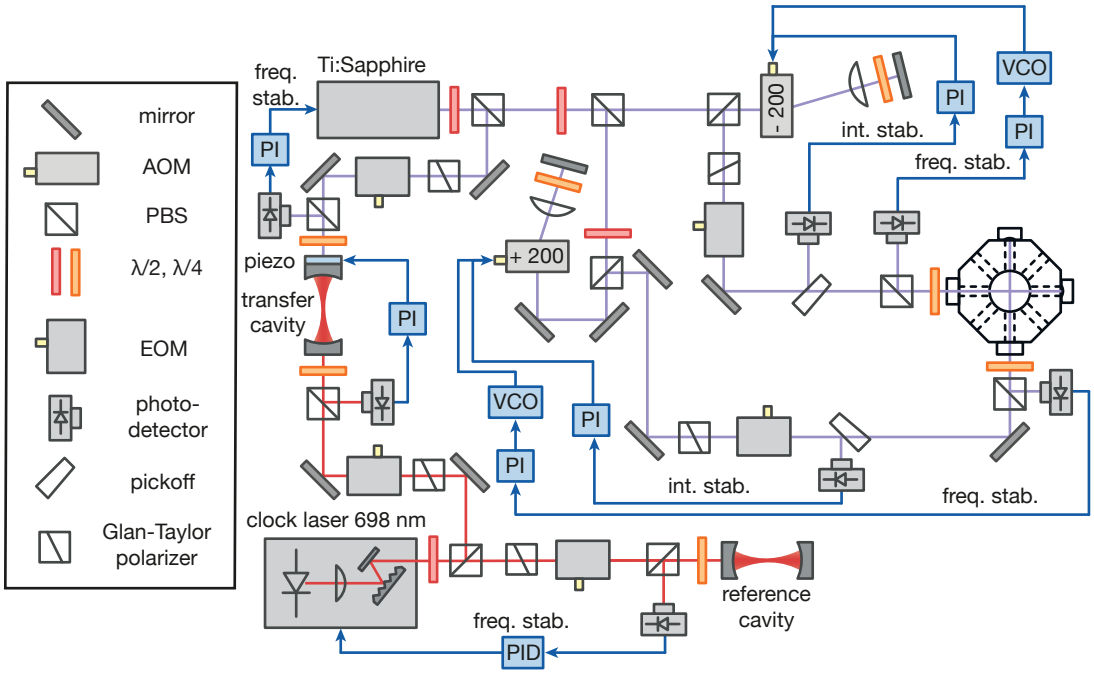

Fig. 5.10 Schematic of the Ti:Sapphire laser system including the frequency stabilization to the crossed cavities. A frequency stabilized diode laser at 698 nm, the so-called clock laser, is used to stabilize the length of a transfer cavity. We use the transfer cavity to stabilize the Ti:Sapphire laser frequency. The two Ti:Sapphire beam paths are stabilized to the resonances of the crossed cavities using double-pass AOMs. All frequency stabilizations are based on the PDH technique. In addition, we stabilize the intensity of the cavity arms.

a finesse of $280,000$.

We stabilize the two beams to the crossed cavities' resonances using double-pass AOMs as the actuators. A PI controller uses the cavity reflection as an input signal and actively controls a voltage-controlled oscillator (VCO). We use the VCO as a frequency source for the double-pass AOM closing the control loop.

Additionally, we stabilize the intensities of the cavity beam paths. A photodetector measures the beam intensity. The photovoltage serves as an input for another PI controller servoing on the amplitude of the rf signal seeding the AOM.

Our stabilization scheme allows us to control the power inside the crossed cavities independently from each other without disturbing the Ti:Sapphire laser frequency. By carefully adjusting the PI parameters, we can obtain a trap lifetime of $59(2)$ s [104] demonstrating that we can overcome the challenge of frequency noise to amplitude noise conversion.

5.4 Optical transport

We have separated our vacuum system into the main chamber and the science chamber. However, this design requires transporting the atoms from the MOT to the overlap region of the crossed cavities over a distance of 55 cm. Transporting a sample of ultracold atoms increases the cycle time of the experiment as well as the complexity of the experimental sequence. Hence, a transport should be fast and reliable.

Typically, one transports atoms by translating the potential minimum of magnetic or optical traps. Several experiments use a magnetic transport by translating a coil pair [172, 173] or sequentially running current through overlapping coils [174] realizing a reliable transport over large distances. At the same time, magnetic traps can provide deep potentials combined with large trap volumes and passive stability. However, moving a coil pair or installing several coil pairs along the transport path requires a lot of space around the chamber, which reduces the optical access. In addition, magnetic transport can only be used for atoms with sufficiently large magnetic moments, which is not the case for the $^1S_0$ ground state of strontium.

However, an optical transport scheme can instead be used for every polarizable atom. For this transport scheme, one confines the atoms in an optical dipole trap and dynamically moves the beam's focus position by mechanically moving a lens on a linear translation stage [175]. A more compact design uses a focus-tunable lens [176] to translate the focus of an optical dipole trap transporting the atoms. Our experiments described in Ref. [104, 93] successfully used such a scheme. The disadvantage of using stale beam optical dipole potentials is the small longitudinal confinement that limits the maximum transport velocity. This limitation resulted in transport durations of 7 s in our previous experiments.

One can realize an optical transport on much faster timescales using a travelling-wave lattice [177, 178]. The travelling-wave lattice is generated by two overlapped, counter-propagating laser beams that are detuned in frequency which results in a lattice with moving nodes. The velocity of the nodes depends linearly on the frequency difference. The lattice traps the atoms tightly along the longitudinal direction enabling atomic transport over tens of centimeters in tens of milliseconds [178].

To reduce the transport duration, we also incorporated a travelling-wave lattice. The small size of the cavity bores and the long transport distance restrict us to lattice beam waists of ~ 450 µm. For smaller waists, the beams diverge significantly over the transport distance and deposit their power on the cavity which leads to expansion of the cavity. However, we do not have strong-enough laser sources to confine atoms against gravity in such a lattice. Therefore, we choose a hybrid approach which combines an optical dipole trap with a moving focus and a travelling-wave lattice [179].

We begin this Section by deriving the basic formulas describing the travelling-wave lattice. Afterward, we calculate the beam parameters required to trap atoms against gravity. Finally, we discuss our transport setup and characterize it.

5.4.1 Moving Lattice

To understand the basic principles of the travelling-wave lattice, we derive the describing equations. We begin by calculating the intensity pattern of two overlapping Gaussian laser beams propagating along the x-axis with wave vectors $\boldsymbol{k}_1$ and $\boldsymbol{k}_2$, respectively. The corresponding electric fields oscillate with the angular frequencies ω_1 and ω_2. The resulting intensity pattern is given by

$$I(\boldsymbol{x},t) = \frac{1}{2}c\varepsilon_0|E_1\exp(i\boldsymbol{k}_1\cdot\boldsymbol{x}-i\omega_1 t)+E_2\exp(-i\boldsymbol{k}_2\cdot\boldsymbol{x}-i\omega_2 t)|^2, \tag{5.10}$$

$$= \frac{1}{2}c\varepsilon_0\left(E_1^2+E_2^2+2E_1E_2\cos\left[(\boldsymbol{k}_1+\boldsymbol{k}_2)\cdot\boldsymbol{x}-(\omega_1-\omega_2)t\right]\right), \tag{5.11}$$

where ε_0 the electric permittivity, and E_i is the electric field amplitude. We introduce the detuning $\Delta\omega = \omega_1 - \omega_2$, which is typically in the regime of tens of Megahertz. For these frequency differences, we can approximate the wave vectors by $\boldsymbol{k} = \boldsymbol{k}_1 \approx -\boldsymbol{k}_2$. With this approximation the intensity pattern is given by

$$I(\boldsymbol{x},t) \approx \frac{1}{2}c\varepsilon_0\left(E_1^2+E_2^2+2E_1E_2\cos\left[2\boldsymbol{k}\cdot\boldsymbol{x}-\Delta\omega t\right]\right). \tag{5.12}$$

The first and the second term result in an intensity offset. The third term generates a standing wave pattern with an oscillating phase. The nodes of the standing wave have a spacing of $\lambda/2$. The oscillating phase results in an effective movement of the nodes with a velocity of $v = \Delta\omega/(2k) = \lambda\Delta\nu/2$, where $\nu = \omega/(2\pi)$ is the oscillation frequency of the electromagnetic field.

In Cha. 4, we derived that the potential energy of atoms in a light field is proportional to the light intensity. Using Eq. (4.3) the intensity pattern above generates an optical potential given by

$$U_{\mathrm{latt}}(\boldsymbol{x},t) \propto -\frac{1}{2\varepsilon_0 c}\alpha\sqrt{I_1 I_2}\cos(2\boldsymbol{k}\cdot\boldsymbol{x}-\Delta\omega t), \tag{5.13}$$

where α is the polarizability and $I_i = 1/2\varepsilon_0 c|E_i|^2$ is the peak intensity of the corresponding light field. The dipole potential has the form of a travelling-wave lattice. By sweeping the frequency difference we can use the lattice to transport the atoms.

By sweeping the frequency difference, an atom of mass m experiences an acceleration a_{latt} corresponding to a force of

$$F = ma_{\mathrm{latt}} = m\frac{\partial v}{\partial t} = m\frac{\lambda}{2}\frac{\partial\Delta\nu}{\partial t}. \tag{5.14}$$

To confine the atoms in the lattice while accelerating them, the trapping force has to be larger than the accelerating force. For a deep optical lattice, we can approximate the atoms as classical particles. The restoring force of the lattice potential can then be

calculated using Eq. (4.4), and we obtain

$$F_{\mathrm{latt}} = -\boldsymbol{\nabla} U_{\mathrm{latt}}(\boldsymbol{x}, t) = -U_0 2k \sin(2\boldsymbol{k} \cdot \boldsymbol{x} - \Delta\omega t), \tag{5.15}$$

where $U_0 = 1/(2\varepsilon_0 c)\alpha\sqrt{I_1 I_2}$ is the trap depth. At the maximum of the restoring force we obtain the condition

$$m a_{\mathrm{latt}} < 2U_0 k. \tag{5.16}$$

If this condition is satisfied, we can transport the atoms without losing them from the trap. The reader may ask what happens for a shallow optical lattice, where we have to treat the atoms as quantum mechanical particles. In this scenario, the accelerating force induces Bloch oscillations. To not lose the atoms, the acceleration has to be small enough to prevent the excitation to higher bands of the optical lattice. A detailed discussion is beyond the scope of this thesis but can be found in Ref. [180].

In this Section, we derived the basic equations describing the transport of atoms in a travelling-wave lattice. In the next Section, we discuss the beam parameters required to confine the atoms against gravity.

5.4.2 Gravity

While the lattice confines the atoms in the longitudinal direction very tightly, the radial potential is less tight. To transport atoms in the horizontal direction, the radial confinement has to be sufficiently strong to trap the atoms against gravity. Typically, one uses Gaussian beams with a static focus position to generate the travelling-wave lattice. At the focus position, the waist is small enough to generate a strong radial potential. However, over transport distances of several tens of centimeters, the waist of the beams expands which decreases the radial confinement. Depending on the initial waist and power, the confinement may be so weak that it can not trap the atoms against the gravitational force anymore. In this Section, we discuss the required transport beam parameters. Our experiment is special because our parameters are constrained by the crossed cavities and the long transport distance. Therefore, we cannot use a non-diverging Bessel beam [178] and are restricted to Gaussian beams.

The radial confinement increases with decreasing beam waist. However, a Gaussian beam with small waist diverges strongly over our transport distance of 55 cm. The waist w along the transport direction x is given by

$$w(x) = w_0 \sqrt{1 + \left(\frac{x}{z_{\mathrm{R}}}\right)^2}, \tag{5.17}$$

where w_0 is the waist at the focus and $z_{\mathrm{R}} = (\pi w_0^2)/\lambda$ is the Rayleigh range which depends on the wavelength λ. We assume that the beam is focused in the center between the MOT and the crossed cavities.

In Fig. 5.11(a), we plot the waist of a 1064 nm beam as function of x for various w_0. We can see that beams with $w_0 \sim 300$ µm or larger have a relatively constant waist over

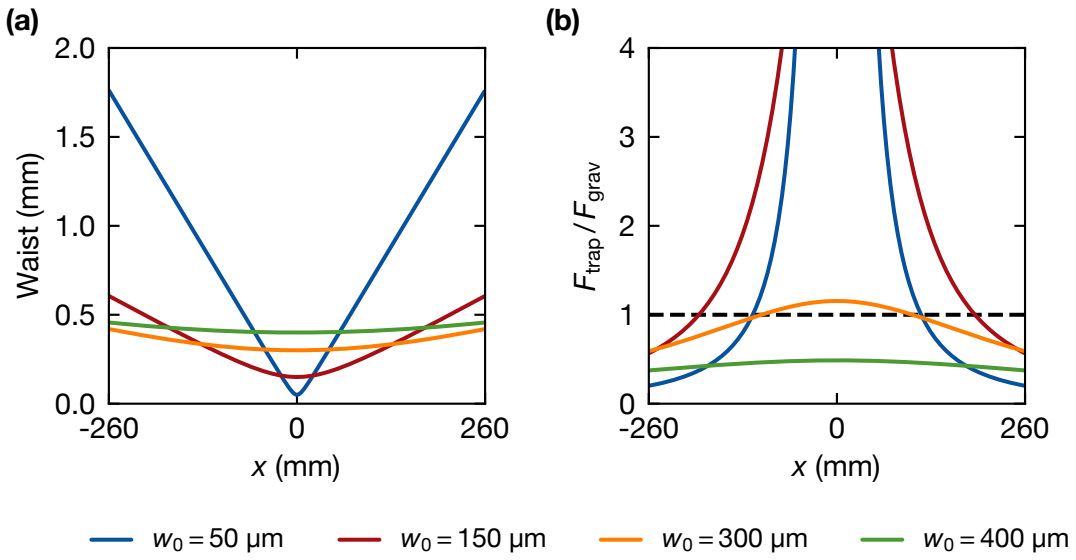

Fig. 5.11 (a) Waist of a Gaussian beam as a function of propagation distance for various waist sizes w_0. We place the beam focus at half the transport distance. (b) We use two counter-propagating 1064 nm beams with an individual power of 20 W and the waists of panel (a) to generate a travelling-wave lattice. We plot the force of the radial confinement as a function of the transport position. We normalize the force to gravity. The horizontal line shows were the confinement is sufficiency strong to trap the atoms against gravity.

the transport distance. However, we have to calculate whether our laser powers of 20 W per beam provide sufficient confinement to trap atoms against gravity.

To simplify the calculation, we assume that the beams forming the moving lattice have equal power and equal waist. The resulting radial intensity profile of the overlapping beams is given by

$$I(r) = 4I_0 \left(\frac{w_0}{w(x)}\right)^2 \exp\left(-\frac{2r^2}{w(x)^2}\right), \tag{5.18}$$

where $I_0 = (2P)/(\pi w_0^2)$ is the peak intensity. The factor of 4 takes into account the constructive interference of the beams. Using Eq. (4.3) and Eq. (4.4) the radial trapping force is given by

$$F_r(x) = \frac{\partial}{\partial r}\frac{1}{2\varepsilon_0 c}\alpha I(r) \tag{5.19}$$

$$= -8I_0 \left(\frac{w_0}{w(x)^3}\right)^2 \frac{\alpha r}{\varepsilon_0 c} \exp\left(-\frac{2r^2}{w(x)^2}\right). \tag{5.20}$$

The maximum confining force is given at $r = w(x)/2$ with

$$F_{\text{trap}} = -\frac{4}{c\varepsilon_0}\frac{w_0}{w(x)^2}\alpha\frac{2P}{\sqrt{e}\pi w_0^2}. \tag{5.21}$$

For $|F_{\text{trap}}| > F_{\text{grav}} = mg$, we can confine atoms in the lattice against gravity with $g = 9.81\ \text{m/s}^2$.

We assume that we generate a travelling-wave lattice using two counter-propagating 1064 nm beams with a power of 20 W and the beam waists shown in Fig. 5.11(b). We calculate the resulting radial confinement force F_{trap} and plot the force as function of the transport position in Fig. 5.11(b). We normalize the magnitude of the confinement force to the gravitational force F_{grav}. We can see that the confinement of a lattice with focus waists up to $w_0 \sim 300$ µm can trap atoms against gravity close to the focus position. However, the expansion of the beam at the start or end position of the transport prevents holding atoms there. This behavior shows that with our available laser power we cannot transport the atoms using a travelling-wave lattice generated by two Gaussian beams.

Our solution is to generate a travelling-wave lattice from one beam with a waist of 50 µm, but tunable focus position, and a counter-propagating beam with a more or less constant waist over the transport distance. We achieve the tunability of the focus position by sending the beam through a focus-tunable lens. The small waist results in a strong confinement against gravity, while the travelling-wave lattice allows for a fast transport. In the next Section, we discuss our transport scheme in detail and characterize it.

5.4.3 Setup

Due to our long transport distance of 55 cm and limited available laser power, we can not hold the atoms against gravity with a travelling-wave lattice generated by two Gaussian beams with a static focus position. Our transport scheme combines a travelling-wave lattice with a focus-tunable lens similar to the transport characterized in Ref. [179].

A schematic of our atomic transport is shown in Fig. 5.12. The beam with a tunable focus has a waist of 50 µm and a power of 6 W, generating a radial confinement sufficiently strong to trap atoms against gravity. The interference between this beam and a focus-fixed counter-propagating beam results in a travelling-wave lattice when detuning their frequencies. The focus-fixed beam has a waist of ~ 420 µm and a power of 30 W. To transport the atoms we synchronously translate the focus position and the lattice.

We transport the atoms over the distance of 55 cm in 600 ms using a linear frequency sweep. We ramp up the frequency of the focus-fixed beam by 1.624718 MHz in 300 ms using an AOM and afterward, ramp the frequency down again in the same duration. The linear frequency change results in a constant acceleration and an s-shaped position ramp. The frequency difference corresponds to a maximum lattice velocity of 0.86 m/s. The total transport time is one order of magnitude shorter than our previously used scheme and reduces the experimental cycle time significantly.

Staring at the position of the MOT, we load $\sim 7 - 9 \times 10^6$ atoms into the transport lattice and we obtain $\sim 3 \times 10^6$ atoms in the science chamber. These atom numbers cor-

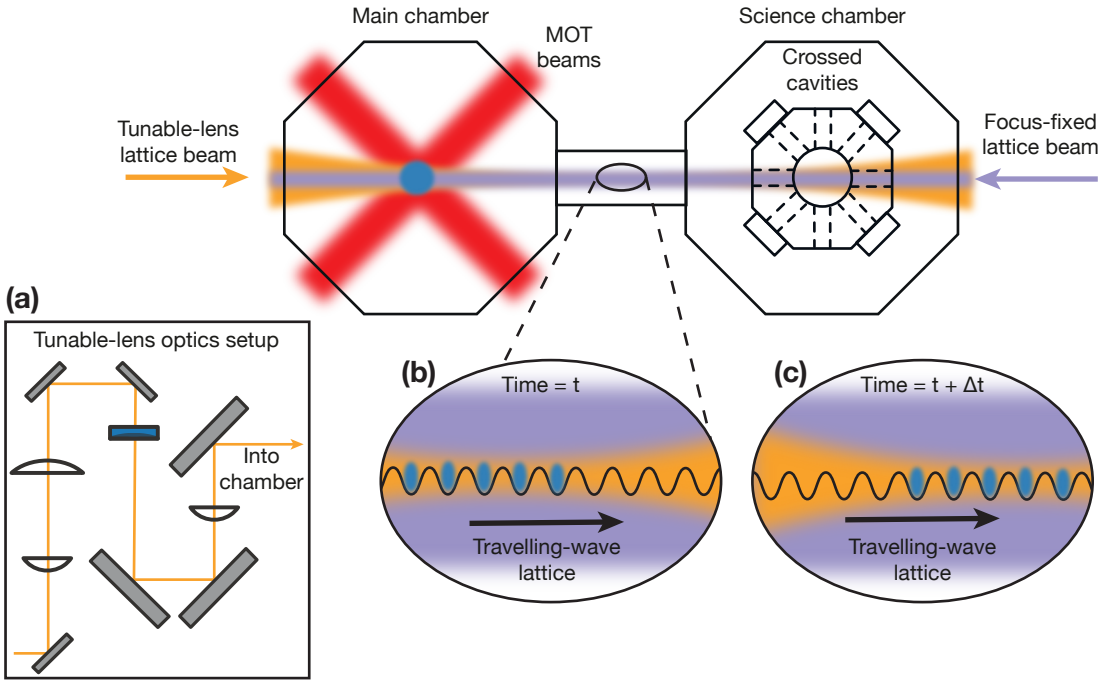

Fig. 5.12 Schematic of the transport setup. We combine a beam with a tunable focus position and a focus-fixed beam to generate a travelling-wave lattice. The focus-tunable beam has a waist of 50 µm and provides sufficient radial confinement to trap the atoms against gravity. The interference of this beam and the focus-fixed counter-propagating beam form a travelling-wave lattice. The MOT beams are shown in red, and the strontium atoms are shown in blue. Inset (a) is a schematic of the optics setup generating the focus tunable beam. In insets (b) and (c), atoms are trapped in the travelling-wave lattice. The lattice moves towards the cavity assembly in the science chamber.

respond to a transport efficiency of $32 - 42\,\%$. We believe that our transport efficiency is limited by how synchronously we move the focus and the lattice. After careful optimization, Ref. [179] reported a transport efficiency of $50\,\%$ which we can probably also reach following their optimization procedure.

We characterize the temperature of the atoms after transport via time of flight expansion. We suddenly release the atoms from the trap mapping momentum distribution into spatial distributions. A Gaussian cloud of atoms expands according to their temperature T given by [25]

$$\sigma(t,T) = \sqrt{\sigma_0^2 + \left(\frac{k_B T}{m}\right)^2 t^2}, \tag{5.22}$$

where k_B is the Boltzmann constant, and σ_0 is the initial cloud size. We extract the temperature of the atoms by fitting the measured cloud size as a function of the time-of-flight (TOF) t. In Fig. 5.13 we plot the cloud sizes along all three spatial directions with the corresponding fits. Compared to a temperature of $\sim 1 - 2$ µK in the MOT, the

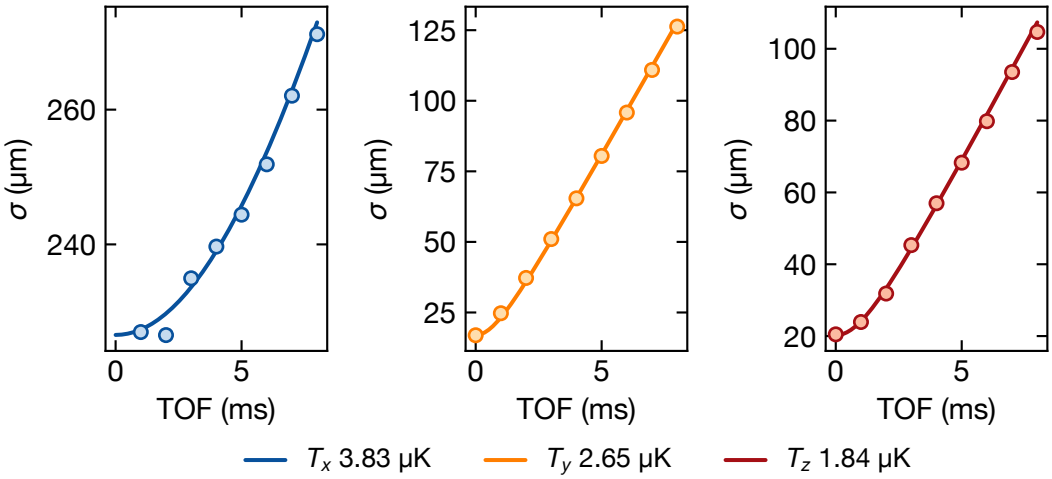

Fig. 5.13 Temperature along all three spatial directions measured via time of flight (TOF). We release the atoms from the transport lattice in the science chamber and take absorption images of the cloud after TOF. From the images we extract the cloud size σ and we fit the size as a function of the expansion time.

transport heats the atoms slightly along the horizontal direction. This small heating is no problem since we can easily cool the atoms again using the red $^1S_0$-$^3P_1$ transition. The transport does not change the vertical temperature.

In this Section, we discussed our new transport scheme reducing the transport time by one order of magnitude compared to our previously used transport scheme. The measured temperatures show minimal heating, which we can easily remove by cooling on the red transition.

Chapter 6

The $^1S_0$-$^3P_2$ magnetic quadrupole transition in neutral strontium

In this Chapter, we investigate the $^1S_0$-$^3P_2$ magnetic quadrupole transition in neutral strontium. This transition possesses a natural linewidth on the millihertz level similar to the famous $^1S_0$-$^3P_0$ electric dipole clock transition [56, 120–122, 51, 62, 49]. While the $^3P_0$ state is insensitive to magnetic fields, the potential energy of the $^3P_2$ state can be tuned using these fields [127]. This tunability opens up new opportunities for quantum computing and quantum simulation [73, 130].

Magnetic-field-sensitive transitions can be used to locally control and manipulate the electronic state of atoms trapped in individual sites of an optical lattice within a magnetic field gradient [111]. The magnetic field gradient splits the transition resonance frequency of neighboring lattice sites due to the Zeeman effect. If the splitting is larger than the transition linewidth, one can drive the transition on a given lattice site without influencing atoms on neighboring sites. This technique is called local addressing.

We can also use local addressing to isolate a single two-dimensional (2D) layer within a three-dimensional (3D) optical lattice in the focus of the quantum gas microscope objective [26, 107]. Without this isolation, we cannot be certain when assigning detected atoms to a single lattice layer. Removing all atoms from unwanted layers is called "slicing" and is a technically demanding task [26] since it requires highly stable optical setups and large magnetic fields with relative stability on the $\sim 10^{-5}$ level. Using the $^1S_0$-$^3P_2$ transition for local addressing increases the complexity in terms of atomic physics because it requires understanding and probing magnetic quadrupole transitions. In Ch. 3, we developed a theoretical understanding of multipole transitions, which helps us to experimentally investigate the magnetic quadrupole transition. Furthermore the $^1S_0$-$^3P_2$ absolute transition frequency has only been measured very recently in ^{87}Sr with an uncertainty of 30 MHz. [110]. In this Chapter, we overcome these challenges and our results will enable future experiments to easily incorporate the magnetic quadrupole transition for various applications.

Since the $^1S_0$ state and the $^3P_2$ state are separated in energy by optical frequencies, they can experience very different ac Stark shifts caused by the same light field. Their differential Stark shift results in light-shift-broadened transition lines. Using the $^1S_0$-$^3P_2$ transition to isolate a single layer requires the broadening to be smaller than the splitting between neighboring lattice layers. Therefore, we implement the polarizability tuning techniques discussed in Cha. 4 in our experiment.

Using these techniques, we achieve a magic lattice for the magnetic-field-insensitive

$^1S_0$-$^3P_2$ $\Delta m_J = 0$ transition which possesses applications as an optical qubit. In addition, we measure the absolute transition frequency in ^{88}Sr with an uncertainty of 5 kHz. We can also engineer a magic lattice for the magnetic-field-sensitive $^1S_0$-$^3P_2$ $\Delta m_J = -1$ transition. Within this Stark-shift-free lattice, we demonstrate local addressing, paving the way to isolate a single lattice layer and to prepare a 2D system in the microscope's focus.

At the beginning of the Chapter, we explain our experimental setup and the preparation of ultracold strontium atoms in the optical lattice. In this lattice, we experimentally investigate the transition probability of the magnetic quadrupole transition as a function of the angle between the quantization axis and the wave vector of the probe beam (Sec. 6.2). Afterwards, we use the tensor polarizability of the $^3P_2$ $m_J = 0$ state to engineer a magic lattice for the $^1S_0$-$^3P_2$ $\Delta m_J = 0$. In Sec. 6.3, we probe this transition with high resolution in the magic lattice, enabling us to observe the motional lattice sidebands. In Sec. 6.4, we measure the absolute frequency of the $^1S_0$-$^3P_2$ transition in ^{88}Sr and ^{87}Sr. Thereafter, we apply our knowledge of tuning the vector polarizability to generate a magic lattice for the $^1S_0$-$^3P_2$ $\Delta m_J = -1$ transition (Sec. 6.5), which we use in Sec. 6.6 to demonstrate local addressing. The content of this Chapter is based on the experimental data presented in Ref. [142].

6.1 Sample preparation

The experiment begins by cooling a hot beam of Sr atoms in a fast and robust two-stage magneto optical trap to reach ultracold temperatures of $1 - 2$ µK [118]. We optically transport the atomic sample into the science chamber by combing a focus-tunable dipole trap and a running-wave lattice, as discussed in Sec. 5.4. From the transport, we adiabatically load the atoms into a one dimensional (1D) vertical optical lattice perpendicular to the cavity-enhanced lattices.

A schematic of the experimental setup is shown in Fig. 6.1(a). We generate the optical lattice by retro-reflecting a 1064 nm beam focused to a waist of ~ 140 µm at the position of the atoms. For a typical beam power of 5 W, the lattice has a trap depth of ~ 30 µK and an axial trap frequency of ~ 70 kHz. We can dynamically adjust the lattice polarization using motorized half-wave and quarter-wave plates. The adjustable lattice polarization allows tuning the vector light shift of the excited $^3P_2$ state, as we will see later in this chapter.

We measure the number of ground state atoms in the science chamber using absorption imaging. A 461 nm probe beam propagating along the x-axis illuminates the atomic cloud. The probe beam has a frequency resonant with the $^1S_0$-$^1P_1$ transition, and hence, ground state atoms absorb the light. We image the resulting shadow on a CCD camera and extract the atom number from the image.

Using the horizontal and vertical coils, we can apply magnetic fields in all spatial directions. We choose a coil configuration that enables us to tilt the magnetic field $\mathbf{B}$ the xz-plane. The tilt is described by the angle θ between $\mathbf{B}$ and the z-axis. For $\theta = 0$, the field points along the $-z$-axis which lets us compensate the background magnetic field of the ion pumps.

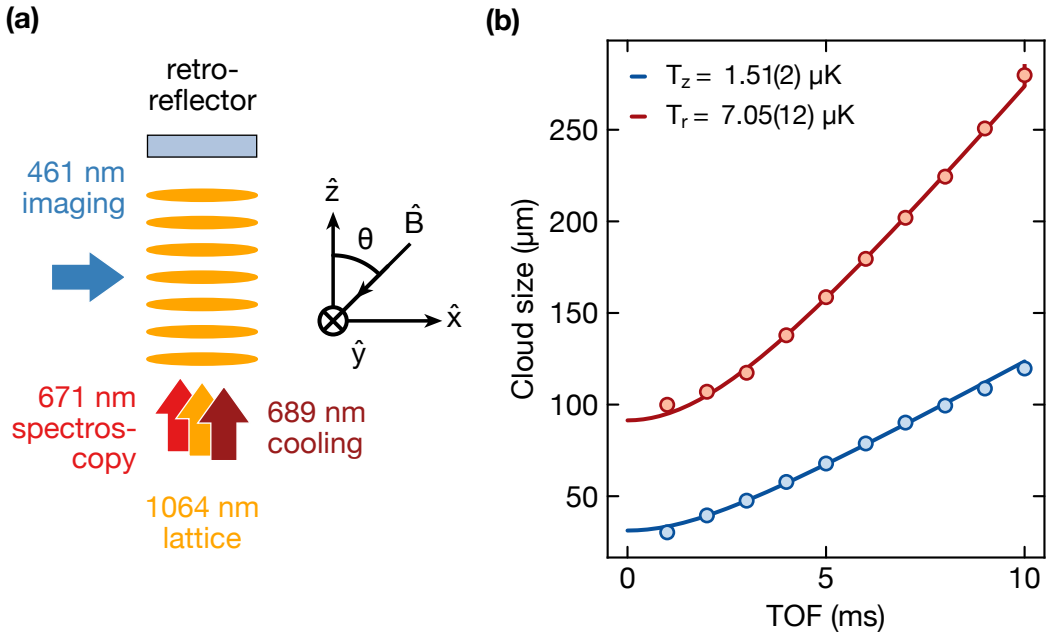

Fig. 6.1 (a) Schematic of our experimental setup to study the $^1S_0$-$^3P_2$ transition. We generate a vertical lattice by retro-reflecting a 1064 nm laser beam. We use a beam at 689 nm propagating along the z-direction to cool the atoms on the $^1S_0$-$^3P_1$ transition via direct sideband cooling. We use a 671 nm beam to probe the $^1S_0$-$^3P_2$ transition. From the side, we shine in a blue 461 nm beam for absorption imaging. We can apply a strong magnetic field in the xz-plane tilted by an angle θ from the z-axis. (b) Axial T_z and radial temperatures T_r in the vertical lattice measured using time of flight (TOF) expansion.

We use a 689 nm beam aligned collinearly with the vertical lattice beam to cool the atoms on the $^1S_0$-$^3P_1$ transition. Because the transition linewidth of 7.4 kHz is much smaller than the trap frequency of 70 kHz, we can cool the atoms into the axial vibrational ground state of the lattice using direct sideband cooling [104]. We define the quantization axis by applying a magnetic field of 1 G pointing along the $-z$-axis. The magnetic field splits the Zeeman sublevels. To optimize the cooling efficiency, we use an elliptically polarized lattice with an ellipticity angle $\gamma = 0.17\,\pi$. This ellipticity results in a magic lattice for the $^1S_0$-$^3P_1$ $\Delta m_J = -1$ cooling transition.

After cooling, we measure the axial (radial) temperatures T_z (T_r) in the vertical lattice using time of flight (TOF) expansion. We plot the cloud size as a function of the TOF in Fig. 6.1(b). We extract an axial temperature of 1.5 μK and a radial temperature of 7.1 μK. Due to the axial sideband cooling, the axial temperature is much lower than the radial one. In the vertical lattice, the atoms are radially hotter than in the transport lattice. We attribute the heating to an imperfect transfer of atoms from the transport into the lattice. Using additional horizontal lattices will enable us to cool the radial direction with direct sideband cooling as well. For the spectroscopy of the $^1S_0$-$^3P_2$ transition, additional cooling

is not required since the radial temperature has a negligible effect on the spectroscopic resolution if the probe beam is well-aligned with the lattice axis.

We probe the $^1S_0$-$^3P_2$ transition by interrogating the atoms with a 671 nm laser beam propagating parallel to the vertical lattice. The beam is focused to a $1/e^2$ waist of ~ 450 µm at the position of the atoms with a typical power of 25.8 mW. To measure the absolute laser frequency, we beat a few mW of laser light with a commercial frequency comb. We measure the beat frequency with a counter and average about 1000 counts to extract the beat frequency.

We study the magnetic quadrupole transition using loss spectroscopy. We excite the atoms into the $^3P_2$ state, where they are lost from the lattice via inelastic collisions [104, 109, 122, 124, 181, 182]. Therefore, a resonant excitation results in a reduction of ground state atoms, which we measure using absorption imaging.

6.2 Probing the magnetic quadrupole transition

In Ch. 3, we derived a theoretical model of the magnetic quadrupole transition probability as a function of the probe polarization $\hat{\boldsymbol{\epsilon}}$ and the orientation of the probe beam wave vector $\hat{\mathbf{k}}$. Here, we experimentally investigate this dependence at the example of $^1S_0$-$^3P_2$ magnetic quadrupole transition in strontium.

For the first time, we investigate the M2 absorption pattern with a simple experimental procedure. We record spectra of the $^1S_0$-$^3P_2$ transition to all Zeeman sublevels m_J as a function of the angle θ between the probe wave vector and the quantization axis. A schematic of the setup is shown in Fig. 6.2(a). We use a fixed linear lattice polarization $\hat{\boldsymbol{\epsilon}}_\mathrm{l}$. We apply a magnetic field of 1 G, which we can tilt by an angle θ with respect to $\hat{\mathbf{k}}$, defining the quantization axis. The field splits the adjacent m_J states by 2.1 MHz as illustrated in Fig. 6.2(b).

We interrogate the atoms with a probe beam polarization $\hat{\boldsymbol{\epsilon}} \approx 1/\sqrt{2}(0.68, 0.18, 0)^\top$. This polarization has components perpendicular to the plane in which we can orient the magnetic field. This configuration allows driving the $^1S_0$-$^3P_2$ transition to all Zeeman sublevels m_J. We can calculate the corresponding absorption patterns using the derivations of Ch. 3. We plot the transition probability as a function of θ in a polar coordinate system in Fig. 6.2(c). The transition probability depends on θ since the decomposition of $\hat{\boldsymbol{\epsilon}}$ in the atomic frame changes. Because we orient the quantization axis in the xz-plane, the major polarization component along the x-axis transforms into a π-polarization in the atomic frame as θ approaches $\pi/2$. The $^1S_0$-$^3P_2$ $\Delta m_J = 0$ transition can not be driven with pure π-polarization and only the small amount of $\sigma^\pm$-polarized light contributes to the transition amplitude resulting in a 10 times smaller transition probability as for the other Zeeman states. According to Eq. (3.73) all the transitions have equal Clebsch-Gordan coefficients.

To experimentally study the magnetic quadrupole transition, we interrogate the atoms for 500 ms and afterward measure the number of remaining ground state atoms. We probe all m_J states for various angles θ. The recorded spectra are shown in Fig. 6.2(d). In the first row, the probe beam and the quantization axis are aligned parallel ($\theta = 0$).

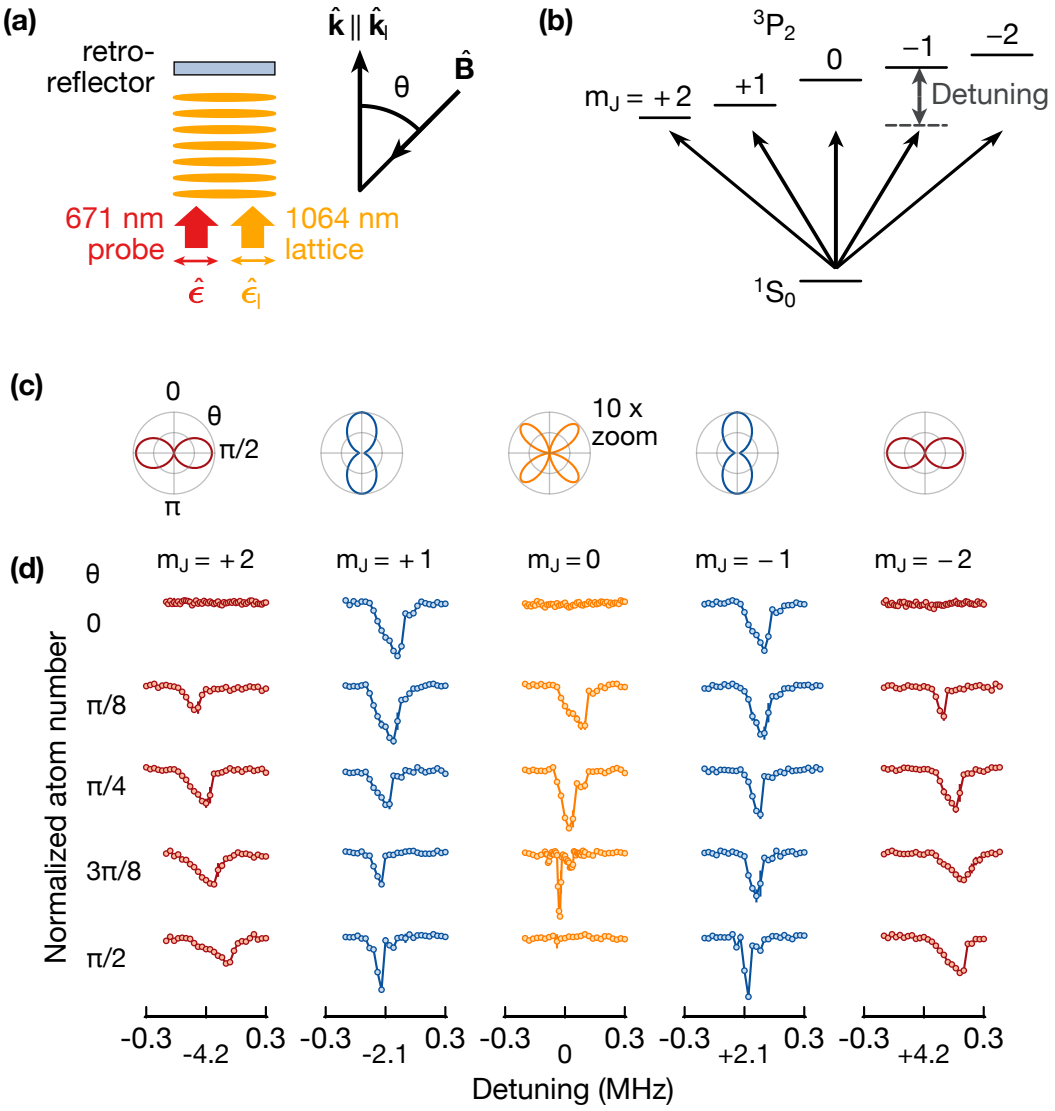

Fig. 6.2 The figure is adapted from Ref. [142]. (a) Schematic of the setup used to probe the $^1S_0$-$^3P_2$ absorption pattern. (b) Zeeman sublevel structure of the $^1S_0$ and the $^3P_2$ state split by a magnetic field. (c) With the probe beam polarization $\hat{\epsilon} \approx 1/\sqrt{2}(0.68, 0.18, 0)^\top$ we calculate the expected absorption pattern. (d) We apply a magnetic field and record the spectra of the $^1S_0$-$^3P_2$ transition for all possible m_J-states as a function of θ. The line strength of the measured spectra follows the calculated pattern of (c), but the spectra are broadened according to the differential light shifts of the $^1S_0$ and the $^3P_2$ m_J states.

Here, we can drive the $\Delta m_J = \pm 1$ transitions, similar to what one would expect for an electric dipole (E1) transition. For $\theta > 0$, the $m_J = \pm 2$ transitions appear. Remarkably, we can drive the $\Delta m_J = \pm 1$ transitions for all θ. If the transition were an E1 transition, we

would expect that the $\Delta m_J = \pm 1$ transitions would vanish, and that only the $\Delta m_J = 0$ transition can be driven as we approach $\theta = \pi/2$. However, we can drive the $\Delta m_J = 0$ transition for $\theta \neq 0$ and $\theta \neq \pi/2$ as we already expected from the absorption pattern calculations. We conclude that the strengths of the recorded spectra qualitatively agree with the calculated transition probabilities.

Two effects prevent us from performing a more quantitative analysis of the amplitudes of the spectra. First, we are using interrogation times and probe beam powers optimized to drive the $\Delta m_J = 0$ transition which results in a plateau of the depleted atom number of the other states. Hence, the amplitudes of the $m_J \neq 0$ spectra reach a finite value. Second, we observe that the lines broaden and shift as a function of θ, caused by a varying ac Stark shift of the optical lattice as θ changes.

The lines broaden and shift because the $^1S_0$ and $^3P_2$ states have different polarizabilities at the lattice wavelength of 1064 nm. According to the derivations in Chapter 4, the polarizability α of an electronic state with angular momentum J in the Zeeman sublevel m_J is given by

$$\alpha^i = \alpha^i_{\mathrm{S}} + \frac{m_J}{2J}\alpha'^i_{\mathrm{V}}\sin(2\gamma) + \frac{m_J^2 - J(J+1)}{2J(2J-1)}\alpha'^i_{\mathrm{T}}\frac{3\cos(\theta-\pi/2)-1}{2}, \tag{6.1}$$

where α_{S} is the scalar, α'_{V} is the vector, and α'_{T} is the tensor polarizability. We describe the lattice polarization using the ellipticity angle γ [158, 77]. A linearly polarized lattice with $\gamma = 0$ results in a vanishing vector polarizability. The $^1S_0$ ground state only depends on the scalar polarizability since the vector and the tensor light shifts vanish due to $J = 0$ and $m_J = 0$. The polarizability of the $^3P_2$ state depends on θ via the tensor component which allows us to adjust the differential polarizability of $^1S_0$-$^3P_2$ transition.

In the fourth row of Fig. 6.2(d), we observe a narrow linewidth of the transition to the $m_J = 0$ state as the result of the vanishing differential polarizability. Hence, by tilting the quantization axis, we can make the 1064 nm optical lattice magic for the $^1S_0$-$^3P_2$ $\Delta m_J = 0$ transition. Furthermore, we observe the motional sidebands of the lattice, which we will discuss in detail in the next Section.

Because we understand magnetic quadrupole transitions and atomic polarizabilities, we can drive the $^1S_0$-$^3P_2$ $\Delta m_J = 0$ transition in a Stark-shift-free optical lattice. This transition is insensitive to magnetic fields and has an ultranarrow linewidth. These are excellent properties required to use the transition as an optical qubit in quantum computing with neutral strontium. In the next Section, we further investigate the $^1S_0$-$^3P_2$ $\Delta m_J = 0$ transition by probing it with higher frequency-resolution.

6.3 Magnetic-field-insensitive quadrupole transition

In this Section, we investigate the magnetic-field-insensitive $^1S_0$-$^3P_2$ $\Delta m_J = 0$ magnetic quadrupole transition in a linearly polarized optical lattice of vanishing differential ac Stark shift. We achieve the magic condition by tilting the magnetic field by $\theta = 0.41\,\pi$. To maximize the transition probability to the $^3P_2$ $m_J = 0$ state, we use a probe beam

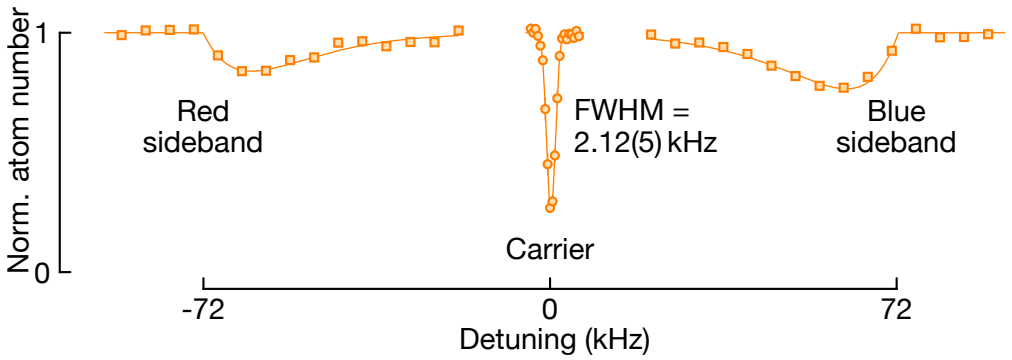

Fig. 6.3 Sideband spectrum of the $^1S_0$-$^3P_2$ $\Delta m_J = 0$ transition in a Stark-shift-free optical lattice. We use a probe beam polarization $\hat{\epsilon} = 1/\sqrt{2}(1,1,0)^\top$ and interrogate the carrier (dots) for 35 ms. We achieve a magic condition for the linear polarized 1064 nm optical lattice by tilting the quantization axis by $\theta = 0.41\,\pi$. We observe the motional red and blue sideband (square) of the lattice. The sidebands are probed with ten times longer interrogating times to compensate the suppression of their amplitude in the Lamb-Dicke regime with a Lamb-Dicke parameter of $\eta = 0.26$. This figure is taken from Ref. [142].

polarization $\hat{\epsilon} = 1/\sqrt{2}(1,1,0)^\top$ and interrogate the carrier for 35 ms.

The resulting spectrum is shown in Fig. 6.3. The carrier has a symmetric lineshape, and we fit it with a Gaussian. We extract a full-width-at-half-maximum (FWHM) linewidth of $2.12(5)$ kHz. We believe that the laser linewidth limits the frequency resolution. In the near future, we will frequency stabilize the 671 nm laser to a new cavity with a finesse of $\sim 200,000$, where we expect a laser linewidth of a few Hertz. With the much more narrow laser, we hope to resolve the carrier with an even higher resolution. We note that carrier spectroscopy in a deep optical lattice is free of motional effects [183] as well as recoil-free [184], enabling the observation of a linewidth on the kHz level and much smaller.

The measured linewidth is one order of magnitude smaller than the axial trap frequency ν_t enabling us to resolve the motional sidebands of the optical lattice as shown in Fig. 6.3. These sidebands are transitions between the resolved vibrational states of the lattice that are spaced in energy by $h\nu_\mathrm{t}$. The blue sideband drives a transition to a higher vibrational state and therefore heats the atoms. The red sideband transition removes one vibrational excitation, lowering the atoms' temperature. The relative strength between the red and the blue sideband contains the full information about the atomic sample's temperature [185]. Here, we intentionally probe a hot sample to amplify the red sideband. Later, we show a spectrum of a cooled cloud, where the red sideband is nearly vanishing. Since the amplitude of the sidebands is suppressed by $\eta^2 = \nu_\mathrm{rec}/\nu_\mathrm{t}$ [119, 183], where $\eta = 0.26$ is the Lamb-Dicke parameter, and ν_rec is the recoil frequency of the probe beam, we probe the sidebands with 10 times longer interrogation times.

Sideband theory To explain the model used to fit the motional sidebands, we briefly discuss the theoretical background of the sidebands. We assume a tight axial confinement such that the atoms is localized in single lattice site and we can approximate the trap as a 1D harmonic oscillator potential. We base the following discussion on the explanations given in Ref. [186].

A single atom at the position x experiences the probe beam's electric field oscillating with frequency $\omega = 2\pi\nu$ given by

$$E(x,t) = E_0 \sin(kx - \omega t), \tag{6.2}$$

where E_0 is the electric field amplitude, $k = 2\pi/\lambda$ is the wave number and t is the time. The atom is confined in the 1D harmonic oscillator and oscillates in space with the trap frequency ν_t. We describe the position of the atom inside the trap with

$$x(t) = x_0 \sin(2\pi\nu_\mathrm{t} t + \phi_0), \tag{6.3}$$

where x_0 is the oscillation amplitude and ϕ_0 is a phase factor. We choose $\phi_0 = 0$ and insert the atomic motion into the equation of the electric field, obtaining

$$E(x,t) = E_0 \sin[kx_0 \sin(2\pi\nu_\mathrm{t} t) - 2\pi\nu t]. \tag{6.4}$$

This expression is equivalent to a frequency modulated signal, where kx_0 is the modulation index. We can substitute the amplitude x_0 with the harmonic oscillator length $\sqrt{\hbar/(2m\nu_\mathrm{t})}$. Using the recoil energy $E_\mathrm{rec} = \hbar^2k^2/(2m) = h\nu_\mathrm{rec}$ we can rewrite the modulation index into

$$\eta = \sqrt{\frac{E_\mathrm{rec}}{\hbar\nu_\mathrm{t}}} = \sqrt{\frac{\nu_\mathrm{rec}}{\nu_\mathrm{t}}}. \tag{6.5}$$

Having the modulation index at hand, we express the electric field as a series of Bessel functions of first kind

$$E(x,t) = E_0 \sum_n J_n(\eta) \sin[2\pi(\nu \pm n\nu_\mathrm{t})t], \tag{6.6}$$

where $\nu = \omega/(2\pi)$ and n is the order of the sideband. Hence, the spectrum of the electric field consists of one carrier frequency ν and sidebands at $\nu \pm i\nu_\mathrm{t}$.

When we interrogate the atoms with the probe light, the intensity couples to an atomic transition of Lorentzian lineshape. We can describe the resulting spectrum by the function

$$F(\nu) = a \sum_i^n J_i^2(\eta) \frac{1}{(\nu - \nu_{ik} \pm i\nu_\mathrm{t})^2 + (\Gamma/2)^2}, \tag{6.7}$$

where a is the amplitude, ν_{ki} is the transition frequency, and Γ is the linewidth. The derived function F agrees with the recorded spectrum in Fig. 6.3, describing the frequencies and the amplitude of the sidebands. However, we observe asymmetric broadening of the sidebands caused by the radial motion of the atoms in the lattice, which we neglected so

far.

At finite temperatures, the atoms experience a reduced light intensity of the trap away from the center. The reduced intensity results in smaller axial confinement and hence, a reduced axial trap frequency. Probing these spatially dependent trap frequencies causes asymmetric broadening. We can describe the resulting lineshape by [77, 183, 187]

$$f(\nu) = a(\nu - \nu_\mathrm{t}) \exp[-b(\nu - \nu_\mathrm{t})]\Theta(\nu - \nu_\mathrm{t}), \tag{6.8}$$

where a is the amplitude, b is a parameter describing the width of the sideband, and Θ is the Heaviside function. We use this lineshape to fit the sidebands in Fig. 6.3.

The measured amplitudes of the sidebands are related to the temperature of the sample by [185, 187]

$$T \approx \frac{\hbar\omega_\mathrm{t}}{k_\mathrm{B}} \frac{1}{\ln(a_\mathrm{blue}/a_\mathrm{red})}, \tag{6.9}$$

where $\omega_\mathrm{t} = \nu_\mathrm{t}/(2\pi)$, k_B is the Boltzmann constant and a_blue (a_red) is the amplitude of the blue (red) sideband. For the spectrum shown in Fig. 6.3, we extract a temperature of 9.2 µK.

In conclusion, we realized a 1064 nm magic lattice for the magnetic-field-insensitive $^1S_0$-$^3P_2$ $\Delta m_J = 0$ transition. In this magic lattice, we can accurately model the observed line shapes. The demonstrated control and understanding of the $^1S_0$-$^3P_2$ $\Delta m_J = 0$ magnetic quadrupole transition paves the way to use this transition as an optical qubit for quantum computing with neutral strontium atoms.

6.4 Absolute transition frequency in ^{88}Sr and ^{87}Sr

Although the $^1S_0$-$^3P_2$ transition has many applications for quantum simulation and quantum computing, its absolute transition frequency was measured only very recently in ^{87}Sr with an uncertainty of 30 MHz [110]. Here, we will present measurements of the absolute transition frequency in ^{88}Sr and ^{87}Sr with three to four orders of magnitude improved uncertainty. The measurements allow us to extract the isotope-shift of this transition.

^{88}Sr

In ^{88}Sr, we probe the magnetic field insensitive $^1S_0$-$^3P_2$ $\Delta m_J = 0$ transition in the magic lattice as presented in Fig. 6.3. We set the laser frequency to the carrier position and beat the laser light with a commercial frequency comb. We measure the beat frequency using a counter. By averaging about ~ 1000 counts, we obtain a statistical uncertainty of the beat frequency of 22 Hz. The fit of the carrier frequency has an uncertainty of 27 Hz. We add the errors quadratically, resulting in a total statistical uncertainty of 35 Hz.

To estimate the uncertainties caused by density shifts, we perform additional measurements with atom numbers reduced by one order of magnitude. From these measurements, we conclude that density shifts are negligible.

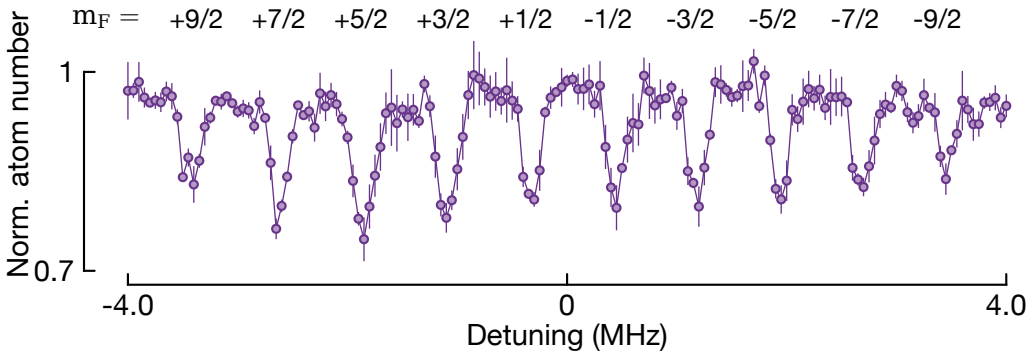

Fig. 6.4 Spectrum of the $^1S_0$-$^3P_2$ $F = 9/2$ transition in ^{87}Sr. We apply a magnetic field of 3 G to split the m_F Zeeman sublevels. This figure is taken from Ref. [142].

Due to the insensitivity of the $^1S_0$-$^3P_2$ $\Delta m_J = 0$ transition to magnetic fields, field fluctuations can only influence the magic condition leading to light shifts. Taking into account residual light shifts, we use a conservative bound of 2.5 times the measured FWHM, resulting in a systematic uncertainty of 5 kHz.

We add the estimated uncertainties and deduce an absolute frequency of the $^1S_0$-$^3P_2$ $\Delta m_J = 0$ transition in ^{88}Sr of $(446,647,242,704 \pm 0.04_{\text{stat}} \pm 5_{\text{sys}})$ kHz, where we combine the estimated uncertainties.

^{87}Sr

In ^{87}Sr, the $^1S_0$-$^3P_2$ $F = 7/2, 9/2, 11/2$ transitions are electric-dipole-allowed due to the hyperfine interaction induced state mixing [110] and at the same time magnetic-quadrupole-allowed. In principle, we could distinguish the multipole transition order by measuring the transition amplitude's geometric dependence or by trying to drive an $\Delta m_F = \pm 2$ transition after spin polarizing the atomic sample. However, we leave this task as an open question to be investigated in future experiments.

Measuring the ^{87}Sr transition frequency is more involved than for ^{88}Sr. The reason is that due to the hyperfine structure of ^{87}Sr all Zeeman subselevels are magnetically sensitive. In Fig. 6.4, we show a spectrum of the $^1S_0$-$^3P_2$ $F = 9/2$ transition. To split the different m_F Zeeman sublevels we apply a magnetic field of 3 G. We can observe the lines of all m_F states with varying width and amplitude. The lines are broadened due to the differential ac Stark shift. Note that for the presented measurements, we did not operate at magic conditions. In principle, it is possible to generate a 1064 nm magic lattice using the developed light shift tuning techniques.

In Fig. 6.5(a), we show the recorded spectra of the magnetic quadrupole transition to the $^3P_2$ $F = 9/2$ $m_F = \pm 9/2$ states. We fit the lines using the asymmetric broadened lineshape we introduced in Eq. (6.8) in the context of the motional sidebands. By averaging the frequencies of two m_F states with opposite signs, we obtain the magnetic-field-insensitive transition frequency.

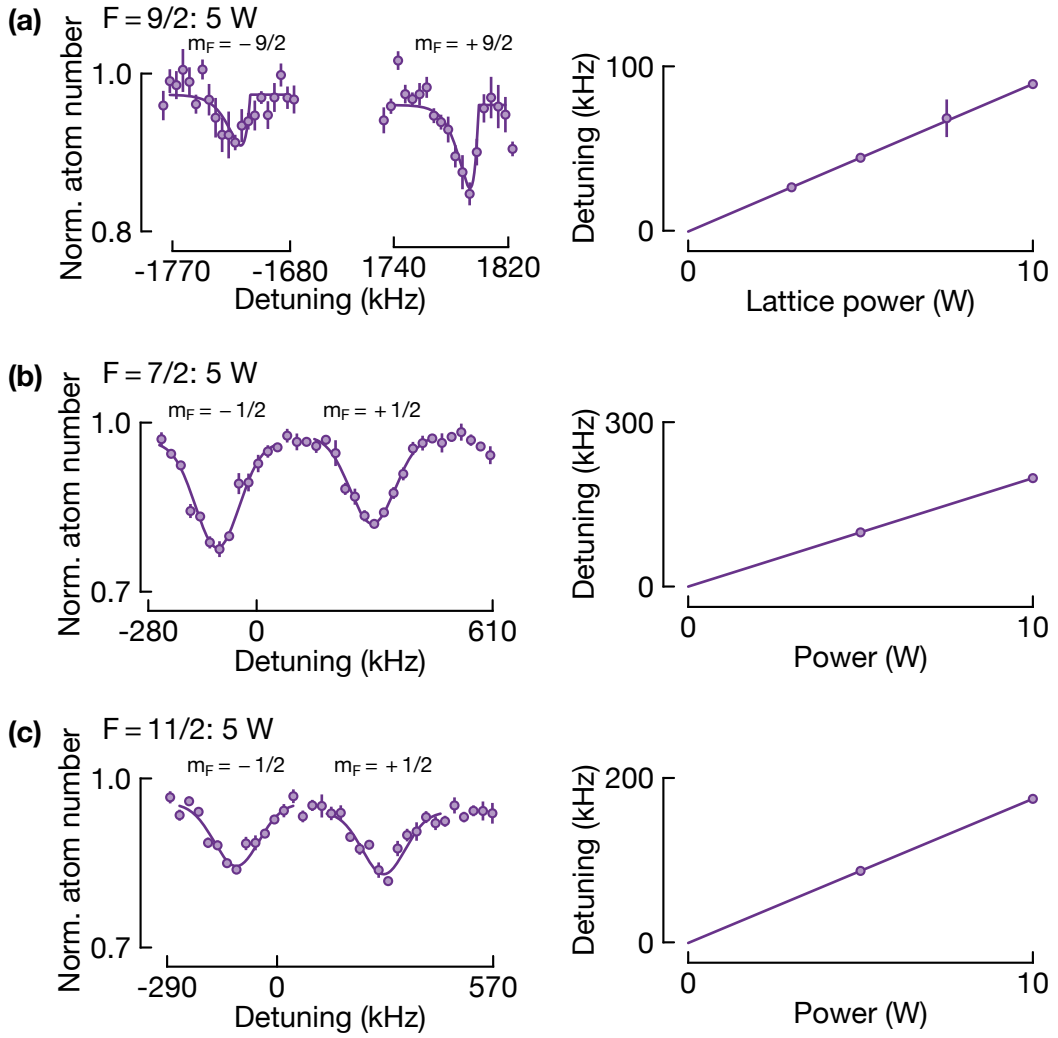

Fig. 6.5 Spectra of the $^1S_0$-$^3P_2$ $F = 9/2$, $F = 7/2$, and $F = 11/2$ transitions in ^{87}Sr to determine the absolute transition frequency. (a) (left) Transition to the excited $F = 9/2$ $m_F = \pm 9/2$ states. We fit the lines using the asymmetric broadened lineshapes derived in Eq. (6.8) and average the line centers to obtain the magnetic-field-insensitive transition frequency. (right) Averaged frequencies plotted as a function of the lattice power and linear fit to extract the Stark-shift-free frequency. (b) and (c) Spectra of the $F = 7/2$ and $F = 11/2$ transitions fitted with Gaussian lineshapes. Averaged frequencies are interpolated to the Stark-shift-free frequency. This figure is adapted from Ref. [142].

Because the lattice is not free of ac Stark shifts, we probe the transition for several lattice powers. We plot the extracted frequencies as a function of the power in Fig. 6.5(a) and fit the data with a linear function enabling us to estimate the ac Stark shift. The fitted intercept corresponds to the Stark-shift-free transition frequency. We obtain a statistical frequency uncertainty of 5 kHz.

In an additional set of measurements, we vary the atomic density in the lattice and extract the transition frequency enabling us to estimate the density shift. We observe shifts up to 40 kHz which are the result the two orders-of-magnitude larger scattering length of ^{87}Sr than ^{88}Sr. We use a conservative upper bound of 60 kHz as a systematic uncertainty caused by density shifts.

Using an optical frequency comb, we measure the $^1S_0$-$^3P_2$ $F = 9/2$ transition frequency of $(446,647,798,423 \pm 5_{\text{stat}} \pm 60_{\text{sys}})$ kHz in ^{87}Sr.

To measure the frequency of the transitions to the $F = 7/2$ and $F = 11/2$ states, we follow the procedure for the $F = 9/2$ state. However, we fit the spectra of the $m_F = \pm 1/2$ states in Fig. 6.5(b) and (c) using a Gaussian lineshape. We only measure the frequency for two lattice powers, resulting in a larger statistical uncertainty attributed to the ac Stark shift. We summarize the transition frequencies in Tab. 6.1. In addition we can extract the hyperfine state energies which agree with the literature values within the errorbars [131].

Isotope	Transition	ν
^{88}Sr	$^1S_0$-$^3P_2$	$446,647,242,704(5)$ kHz
^{87}Sr	$^1S_0$-$^3P_2$ $F = 9/2$	$446,647,798,423(60)$ kHz
^{87}Sr	$^1S_0$-$^3P_2$ $F = 7/2$	$446,648,776,833(80)$ kHz
^{87}Sr	$^1S_0$-$^3P_2$ $F = 11/2$	$446,646,628,232(80)$ kHz

Tab. 6.1 Summary of the $^1S_0$-$^3P_2$ absolute transition frequencies measured in the context of this thesis. The uncertainties contains both statistical and systematic errors.

Isotope shift

The energy of the $F = 9/2$ manifold lies 618.65 MHz [131] above the $^1S_0$-$^3P_2$ line's center of gravity resulting in an ^{88}Sr-^{87}Sr isotope-shift of $\Delta_{87}^{88} = \nu(^{88}\text{Sr}) - \nu(^{87}\text{Sr}) = 62.93(6)$ MHz. We can confirm this isotope-shift by comparing the probe beam frequency shifts of subsequent measurements for the two isotopes.

Transition	$\Delta_{87}^{88} = \nu(^{88}\text{Sr}) - \nu(^{87}\text{Sr})$	Reference
$^1S_0$-$^3P_1$	$62.19(1)$ MHz	[188]
$^3P_1$-$5s5d$ $^3D_2$	$30.2(6)$ MHz	[189, 190]
$^1S_0$-$^3P_2$	$62.93(6)$ MHz	This work
$^3P_2$- $5s5d$ $^3D_2$	$17(2)$ MHz	[191]

Tab. 6.2 Comparison of the measured isotope-shift with the existing data. By adding the measured shifts, we observe a discrepancy of about 13 MHz.

In Tab. 6.2, we compare the measured to existing data. By adding the ^{1}S$_0$-^{3}P$_1$ shift with the ^{3}P$_1$-$5s5d$ ^{3}D$_2$ shift and adding the ^{1}S$_0$-^{3}P$_2$ shift with the ^{3}P$_2$- $5s5d$ ^{3}D$_2$ shift, we observe a discrepancy of about 13 MHz. We believe that this discrepancy is caused by a systematic effect in one of the frequency measurements of the transitions to $5s5d$ ^{3}D$_2$ state, calling for further investigations.

6.5 Magnetic-field-sensitive quadrupole transition

Our procedure to isolate a single lattice layer requires a magnetic field gradient and a magnetic-field-sensitive transition. We use the magnetic-field-sensitive ^{1}S$_0$-^{3}P$_2$ $\Delta m_J = -1$ transition, which we investigate in this Section. Addressing the individual layers requires the transition linewidth to be smaller than the frequency spacing of the layers. Therefore, we engineer a Stark-shift-free lattice by tuning the lattice polarization to adjust the polarizability of the ^{3}P$_2$ $m_J = -1$ state.

A schematic of the experimental setup is shown in Fig. 6.6(a). We use an elliptical probe polarization, similar to Sec. 6.2, and a static magnetic field oriented along the $-z$-direction. We use an elliptically polarized lattice of $\hat{\boldsymbol{\epsilon}}_l = \hat{\mathbf{x}}\cos(\gamma) + i\hat{\mathbf{y}}\sin(\gamma)$, where γ is the ellipticity angle [158, 77]. Because the polarizability of the ^{3}P$_2$ m_J state depends on the lattice polarization $\propto \sin(2\gamma)$, we tune the differential ac Stark shift by adjusting γ.

In Fig. 6.6(b), we show example spectra of the ^{1}S$_0$-^{3}P$_2$ $\Delta m_J = -1$ transition in a lattice with $\gamma = 0.17\,\pi$ for two lattice powers. We observe that the lines are asymmetrically broadened by the light shift and that the carrier frequency moves. We fit the lines using the asymmetric lineshape function of Eq. (6.8).

In Fig. 6.6(c), we present spectra in a nearly Stark-shift-free lattice at $\gamma = 0.09\,\pi$. The lines are symmetric and barely move as a function of the lattice power. We find that these lineshapes are best described by Gaussians.

For several ellipticity angles, we record transition spectra as a function of the lattice power and extract the carrier frequencies. We plot the carrier frequencies as a function of the power in Fig. 6.6(d) and fit the data with a common linear offset. As expected, the carrier frequencies depend linearly on the lattice power. From the fitted slope, we can extract the Stark shift.

We plot the extracted light shift coefficients as a function of the ellipticity angle in Fig. 6.6(e). To obtain the magic ellipticity angle γ_0, where the lattice is free of Stark-shifts, we fit the data with $\kappa = a_0(\sin(2\gamma) - \sin(2\gamma_0))$, where a_0 is the amplitude. We find $\gamma_0 = 0.106(3)\,\pi$, which is in excellent agreement with the theoretical expectation $0.108\,\pi$ calculated in Ch. 4.

Now, we use the ^{1}S$_0$-^{3}P$_2$ $\Delta m_J = -1$ transition in this Stark-shift-free lattice to characterize our cooling by recording sideband spectra. In Fig. 6.7(a) and (b), we show sideband spectra of a hot and a cold atomic sample, respectively. The hot sample has a temperature of 10.4 µK, estimated from the sideband amplitudes, and is obtained by not cooling the atoms after loading them to the lattice. The cold sample has a temperature of 1.8 µK being a typical temperature after direct sideband cooling. This temperature corresponds to a vibrational ground state fraction of 84 %.

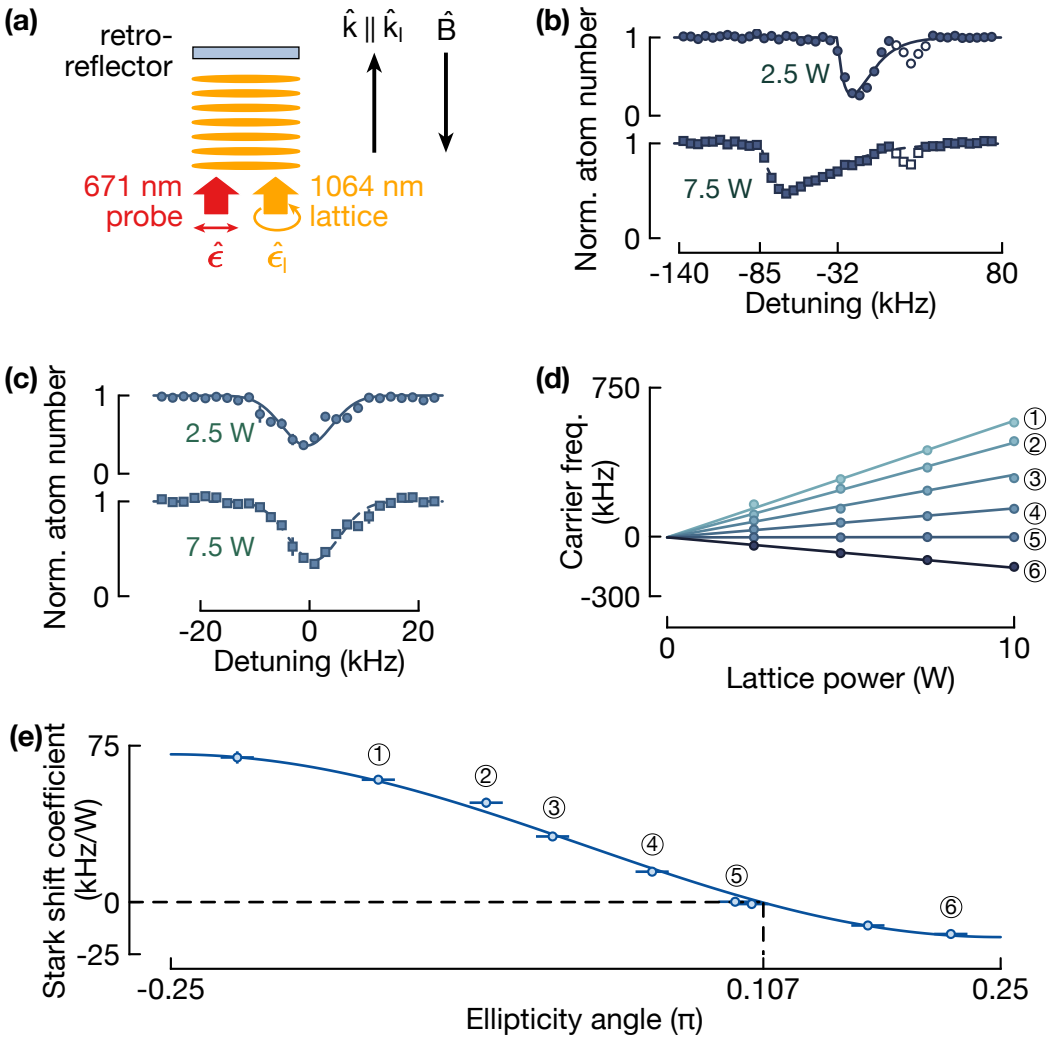

Fig. 6.6 Magic lattice ellipticity angle for $^1S_0$-$^3P_2$ $\Delta m_J = -1$ transition. (a) Schematic of the setup. (b) Transition line in an optical lattice of elliptical polarization with ellipticity angle $\gamma = 0.17\,\pi$. We use lattice powers of 2.5 W (dots) and 7.5 W (squares). The sidebands (open markers) are not fitted. (c) Spectrum in a lattice of $\gamma = 0.09\,\pi$ polarization and a powers of 2.5 W (dots) and 7.5 W (squares). (d) For various ellipticity angles, we plot the carrier frequency as a function of the lattice power. The data is fitted with a common offset. (e) Stark shifts coefficient extracted from the slopes in (d) plotted as function of the ellipticity angle γ. We fit the stark shift coefficient with $\kappa = a_0(\sin(2\gamma) - \sin(2\gamma_0))$ and obtain the magic ellipticity angle of $\gamma_0 = 0.106(3)\,\pi$. This figure is adapted from Ref. [142].

We fit the carrier in Fig. 6.7(b) and extract a full-width-at-half-maximum (FWHM) of $10.8(2)$ kHz, which is roughly 5 times larger than the carrier FWHM of the $^1S_0$-$^3P_2$ $\Delta m_J = 0$ transition. The broadening is caused by fluctuations of the magnetic field on

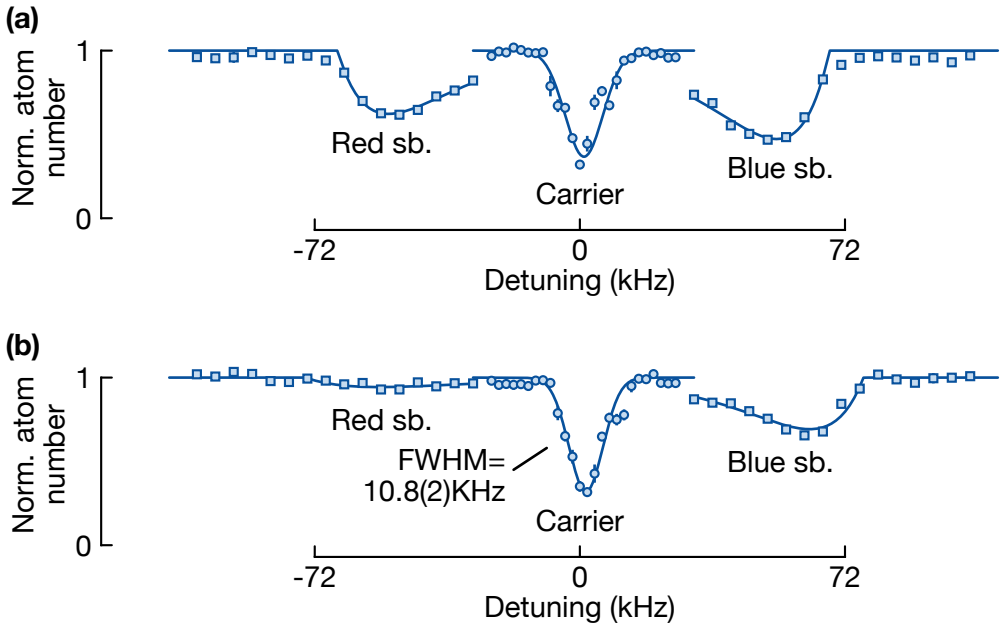

Fig. 6.7 Sideband spectrum of the $^1S_0$-$^3P_2$ $\Delta m_J = -1$ transition a Stark-shift-free lattice. We probe the sidebands (squares) with 10 times longer interrogation times than the carrier (dots). (a) Spectrum of a hot sample with a temperature of 10.4 µK. (b) Cold sample with a temperature of 1.8 µK, corresponding to vibrational ground state fraction of $84\,\%$. Fig. (b) is adapted from Ref. [142]

the 2 mG level.

The experiments in this section demonstrate that we can engineer a Stark-shift-free optical lattice for the magnetic-field-sensitive $^1S_0$-$^3P_2$ $\Delta m_J = -1$ transition. Moreover, we obtain a FWHM linewidth of $10.8(2)$ kHz being sufficiently small for local addressing.

6.6 Local addressing

In this Section, we demonstrate local addressing using the magnetic-field-sensitive $^1S_0$-$^3P_2$ $\Delta m_J = -1$ quadrupole transition in a Stark-shift-free optical lattice. To engineer the magic condition, we use an elliptical lattice polarization of γ_0, see the previous Section for details.

A schematic of the setup is shown in Fig. 6.8(a). Before loading the atoms to the lattice, we compress them spatially using a tightly focused elliptical light sheet. This light sheet is focused at the position of the atoms with a $1/e^2$ waist of ~ 15 µm (~ 300 µm) along the z-axis (horizontal axis) with a typical power of 40 W, resulting in an optical dipole trap with a vertical trap frequency of 2.2 kHz. We measured the trap frequency via parametric heating by modulating the light intensity [151].

We cool the atoms inside the light sheet via Doppler-cooling on the $^1S_0$-$^3P_1$ $\Delta m_J =$

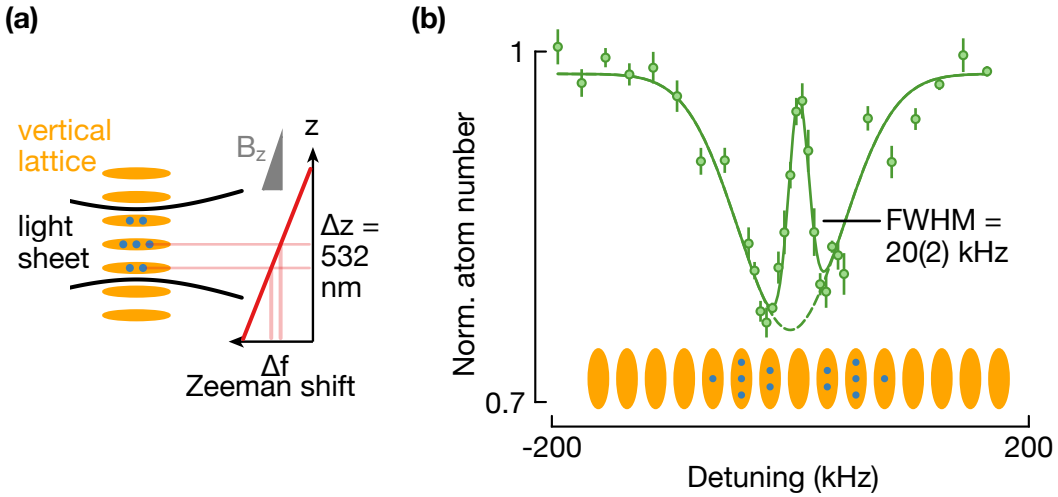

Fig. 6.8 Local addressing in a Stark-shift-free optical lattice using the $^1S_0$-$^3P_2$ $\Delta m_J = -1$ transition. (a) Setup for local addressing with exaggerated dimensions for visibility. We compress the atomic cloud using a light sheet. With a magnetic field gradient of 215 G/cm we split neighboring lattice sites by 24 kHz on the $^1S_0$-$^3P_2$ $\Delta m_J = -1$ transition. (b) Local addressing in 1D optical lattice using the $^1S_0$-$^3P_2$ transition in a magnetic field gradient. Atoms in the layer that is resonant with the detuning of preparation pulse are depleted resulting in a depletion dip of the atomic cloud (lattice sites frequency separation is approximately to scale). The spectrum without the dip is fitted with a Gaussian (dashed line). This figure and caption is taken from Ref. [142].

-1 transition. To increase the cooling efficiency, we engineer a vanishing differential light shift for that transition. We rotate the magnetic field along the sheet propagation direction and use circular beam polarization to achieve a vanishing differential shift. After cooling, we obtain a sample temperature of ~ 0.6 µK and adiabatically load the atoms into the lattice. Using this compression via the light sheet, we typically populate 6-8 layers of the optical lattice. Without the compression stage, the atoms spread over 20 layers.

Once the atoms are loaded to the lattice, we cool them again via direct sideband cooling along the vertical direction. We apply a vertical magnetic field gradient of 215 G/cm and a bias magnetic field of 80 G along the $-z$-direction. This gradient splits the resonance frequency of the $^1S_0$-$^3P_2$ $\Delta m_J = -1$ transition of neighboring lattice layers by 24 kHz as depicted in Fig. 6.8(a). We use the bias magnetic field to spatially translate the zero of the field gradient reducing the gradient curvature at the position of the atoms.

We expose the atomic sample to a first pulse. Atoms trapped in the lattice layer resonant with the probe pulse are excited to the $^3P_2$ state and are lost via inelastic collisions. Because the transition linewidth is smaller than the frequency spacing of neighboring layers, the pulse does not influence atoms in other layers. After the first pulse, we apply a second pulse and record the spectrum as shown in Fig. 6.8(b). At the detuning of the first pulse, we observe a depletion dip of the atomic cloud, demonstrating local addressing in the lattice.

We characterize the spatial resolution corresponding to the depletion dip in the spectrum using the Rayleigh criterion. We adapt the Rayleigh criterion $\sin(\theta) = \lambda/d$ to the diffraction of light at a slit [192]. We consider two diffracted light beams, where after the slit, the intensity profile of each beam is described by a $\mathrm{sinc}^2(x)$ function. If the maximum of one is located in the first minimum of the other profile, the summed intensity drops to $81\ \%$ between the peaks. Adapting this criterion to two Gaussian peaks, the depletion dip's FWHM of $20(2)$ kHz corresponds to a spatial resolution of $494(40)$ µm. This resolution should be sufficient to isolate a single lattice layer as soon as we install a more stable retro-reflector.

In this Section, we demonstrated local addressing using the ultranarrow ^{1}S$_0$-^{3}P$_2$ magnetic quadrupole transition. This technique required to engineer a Stark-shift-free optical lattice. Our experiments pave the way to prepare a single layer of ultracold strontium atoms in the focus of a high-resolution imaging system to realize the first strontium quantum gas microscope.

Conclusion

In this Chapter we presented narrow-line spectroscopy of the ^{1}S$_0$-^{3}P$_2$ magnetic quadrupole transition in optical lattice paving the way for applications of this transition in quantum simulation and quantum computing.

We experimentally investigated the absorption pattern of the quadrupole transition and found qualitative agreement with the expected pattern, which is significantly different than the pattern of an electric dipole (E1) transition. For a quantization axis perpendicular to the probe propagation, we can drive the $\Delta m_J = \pm 1, \pm 2$ transition, which is impossible for an E1 transition.

We adjusted the polarizability of the ^{3}P$_2$ $m_J = 0$ state by tilting the quantization axis with respect to the lattice polarization to engineer a Stark-shift-lattice for the magnetic-field-insensitive ^{1}S$_0$-^{3}P$_2$ $\Delta m_J = 0$ transition. In this lattice, we performed Doppler-free spectroscopy and achieve a kilohertz resolution of the line. The magnetic-field-insensitive transition provides an optical qubit for quantum computing.

Tuning the polarizability of the ^{3}P$_2$ $m_J = -1$ state by adjusting the lattice polarization enabled us to realize a magic lattice for the magnetic-field-sensitive ^{1}S$_0$-^{3}P$_2$ $\Delta m_J = -1$ transition. Using this transition we demonstrated local-addressing in the optical lattice within a magnetic field gradient. The demonstrated addressing will allow us to control and manipulate the atomic sample on the level of single atoms and single qubits in an optical lattice.

Chapter 7

Conclusion and Outlook

Conclusion

This thesis reported on the first local addressing of strontium atoms on the $^1S_0$-$^3P_2$ magnetic quadrupole transition in an optical lattice presented. This demonstration is the first crucial step towards single-particle control of strontium under a quantum gas microscope. In the near future, we will use this local addressing to isolate a single layer of the optical lattice in the focus of the microscope. Recently, our team used the techniques developed during the work described in this thesis to isolate a few lattice layers and obtained first site-resolved images of strontium atoms under the microscope.

Magnetic quadrupole transitions are fundamentally different than electric dipole transitions in terms of their selection rules, angular momentum, and the transition amplitude's dependence on probe beam polarization and propagation direction. Therefore, we theoretically investigated multipole transitions starting from a fundamental description of light-matter interaction in Ch. 3. We derived selection rules and found that the driving light can provide additional angular momentum apart from the spin of the photons. In addition, we calculated the transition-amplitude-dependence on the probe beam orientation and polarization. This new understanding supported an experimental investigation of the $^1S_0$-$^3P_2$ transition including its geometric dependence, which agreed well with our theoretical models.

Local addressing required suppressing line broadening effects caused by the trapping potential's light shifts. We engineered a Stark-shift-free optical lattice by adjusting the excited $^3P_2$ state's polarizability using an elliptical lattice polarization. On the way to this result, we were also able to achieve a vanishing differential light shift for the magnetic-field-insensitive $^1S_0$-$^3P_2$ $\Delta m_J = 0$ transition by tilting the quantization axis with respect to the lattice in Ch. 6. This light-shift-free lattice allowed us to resolve the $^1S_0$-$^3P_2$ $\Delta m_J = 0$ transition with a full-width-at-half-maximum linewidth of $\sim$2 kHz. Finally, we measure the absolute transition frequency with an improvement of three orders of magnitude compared to previously reported values.

The presented results pave the way to realize the first strontium quantum gas microscope. With this microscope, we will be able to perform a quantum simulation of light-matter interfaces. Beyond these specific quantum simulations, our detailed investigation of the $^1S_0$-$^3P_2$ magnetic quadrupole transition enables various applications of this transition in more general quantum simulation and quantum computing. We will discuss these aspects in the following.

Outlook

Beyond the practical use of the $^1S_0$-$^3P_2$ transition to isolate a single layer in the focus of the microscope, this transition can have general applications in quantum technology using ultracold strontium atoms. Due to their minute-scale lifetime and their insensitivity to magnetic fields, the $^1S_0$ and the $^3P_2$ $\Delta m_J = 0$ states can serve as an optical qubit for neutral atom quantum computing. Using the magnetic-field-sensitive $^1S_0$-$^3P_2$ $\Delta m_J = \pm 1$ transition can enable local manipulation of the atom's electronic state in-plane of an isolated lattice layer. In the following, we will discuss these applications in more detail and present further examples.

The magnetic-field-insensitive $^1S_0$-$^3P_2$ $\Delta m_J = 0$ transition provides an optical qubit for quantum computation. Using the metastable $^3P_2$ state, one can implement Rydberg-mediated two-qubit gates via a single photon process already demonstrated in Yb [68]. In strontium, these gates were recently realized using the $^3P_0$ clock state [69, 70]. We see two advantages in using the $^1S_0$-$^3P_2$ qubit instead of the $^1S_0$-$^3P_0$ clock qubit. First, in ^{88}Sr we can drive the $^1S_0$-$^3P_2$ transition without applying a strong magnetic field, which is required to open the $^1S_0$-$^3P_0$ transition in the bosonic isotopes. Second, one can engineer the polarizability of the $^3P_2$ state, allowing the realization of Stark-shift-free optical traps at convenient wavelengths such as 1064 nm.

The magnetic-field-sensitive $^1S_0$-$^3P_2$ $\Delta m_J = \pm 1$ transitions enable local addressing within a magnetic field gradient demonstrated in this thesis. The addressing allows us to manipulate and control atoms on the level of single lattice sites or tweezer arrays for quantum computing and quantum simulation [74, 72, 111]. Beyond isolating a single lattice layer, we can also use the transition to spatially manipulate atoms in-plane by exploiting a horizontal magnetic field gradient.

Besides the discussed optical qubits, alkaline earth atoms can be used to encode the fine structure qubit between $^3P_1$ and $^3P_2$ $m_J = 0$ [76] that recently became of major interest for quantum computing. The $^3P_0$ state is insensitive to most environmental effects ideally suited for information storage. The magnetic-field-sensitive $^3P_2$ $m_J = \pm 1$ states enable local manipulation and readout. In addition, one can implement Rydberg-mediated two-qubit gates from both states. The developed techniques, such as engineering the $^3P_2$ state's profitability and driving the $^1S_0$-$^3P_2$ transition, offer tools to investigate this fine structure qubit.

The availability of two ultranarrow transitions allows the construction of an optical lattice clock that sequentially interrogates each of the transitions. The sequential operation enables one to directly compare the ratios of the transition frequencies and search for variations of the fine-structure constant α. However, the $^1S_0$-$^3P_0$ and the $^1S_0$-$^3P_2$ transition in neutral strontium depend only weakly on α [193]. Typically, optical transitions depend on α via relativistic corrections that scale with $(Z\alpha)^2$, where Z is the nuclear charge [194]. Hence, the $^1S_0$-$^3P_0$ and $^1S_0$-$^3P_2$ transitiosn in neutral ytterbium is better suited for these experiments than strontium [59]. Relativistic many-body amplitude calculations showed that comparing the clock transition and an electric quadrupole transition in neutral ytterbium possesses the highest relative sensitivity to α variations [59, 195].

In the scope of this thesis, inelastic $^3P_2$-$^3P_2$ collisions and too low probe beam powers prevented driving Rabi oscillations on the $^1S_0$-$^3P_2$ transition. We can prevent these collisions in a sparsely filled 3D optical lattice. Stabilizing the laser to a reference cavity with higher finesse will enable us to reduce the laser linewidth to the low Hertz regime, which makes it possible to observe Rabi flopping for small Rabi frequencies.

By probing the $^1S_0$-$^3P_2$ transition in a magic 3D lattice while applying a bias magnetic field, we can also search for magnetic Feshbach resonances between the ground and the excited state as already observed in ytterbium [108]. If one can resolve such a resonance with a factor of 3 improved resolution compared to Ref. [108], one could obtain a more than 10 times higher elastic to inelastic scattering rate. For this estimation, we assumed that the $^3P_0$ and $^3P_2$ inelastic losses are comparable between ytterbium and strontium [124, 122, 181].

In the future, improving the probe laser linewidth to the mHz regime may enable us to resolve the quadrupole-quadrupole interaction of atoms in the $^3P_2$ state on neighboring lattice sites. This interaction results in frequency shifts of tens of mHz for spacings of $\sim$500 nm [196]. The quadrupole-quadrupole interaction potential is given by [197]

$$V^{qq} \propto \frac{1}{r^5}(35\cos^4\theta - 30\cos^2\theta + 3), \tag{7.1}$$

where θ is the angle between the quadrupole orientation and the interatomic axis. This interaction possesses a different anisotropy than the dipole-dipole interaction $V^{dd} \propto 1/r^3(1-\cos\theta)$ between atoms in the $^3P_0$ state and allows tuning the interaction from attractive to repulsive. If the quadrupole interactions dominate the energy scales of the system, they can give rise to a rich phase diagram [196, 197].

Another potential project could be to drive the $^1S_0$-$^3P_2$ transition using beams that carry orbital angular momentum as demonstrated for an electric quadrupole transition in trapped ions [145, 149]. There, the structure of the Gaussian vortex beam enhanced the transition probability.

Probing the ultranarrow transitions under a quantum gas microscope combines sub-hertz frequency resolution with sub-micron spatial resolution acting as a multiaxis sensor of field gradients [62]. Applying this idea to the magnetic-field-sensitive $^1S_0$-$^3P_2$ $\Delta m_J = 1$ transition, one can realize such a sensor of magnetic field gradients with a resolution on the mG/cm level.

The local addressing demonstrated in this thesis was one of the major technical challenges toward isolating a single optical lattice layer in the focus of the microscope. Once we achieve single site resolution, the large systems size and new experimental capabilities will allow us to study open quantum systems in new ways.

For these simulations of open quantum systems, we will use ultracold strontium atoms to realize artificial emitters that can decay via a matter-wave emission [99]. We will generate a large, two-dimensional, state-dependent lattice by coupling individual lattice sites with clock laser light, slightly detuned from the $^1S_0$ tune-out wavelength into our crossed cavities. In these lattices, the $^3P_0$ excited state (e) is tightly trapped, while the $^1S_0$ ground state (g) experiences a very shallow potential such that atoms in g can tunnel

in the lattice. In this system, the e-g decay results in the emission of a matter-wave in analogy to the emission of radiation from a physical emitter. Using the quantum gas microscope, we will be able to observe the matter-wave emission in real space and in a time-resolved way.

The advantage of this simulation is that one can tune the parameters of the open system. The state-dependent lattice imposes a band structure on the atoms in analogy to photonic crystals [198]. By varying the lattice depth, one can adjust the band structure and the corresponding dispersion relation of the matter-wave. Furthermore, one can control the coupling to the vacuum by tuning the laser frequency that drives the e-g transition. This tuning will allow us to couple an emitter into the band gap resulting in a bound state that is exponentially localized. Such a bound state has been realized in photonic crystals [199] and an open quantum system simulator in 1D measuring observables in momentum space [99]. Our experimental platform will enable us to study this bound state in a 2D system and image this state in real space. In the long-term, in these 2D systems, one can use the interactions between bound states to realize subradiant states with strongly enhanced lifetimes [98] with applications for metrology and quantum computing.

Using alkaline earth atoms for metrology applications has a long-standing history resulting in optical lattice clocks with outstanding precision [57, 58]. The techniques developed for optical clocks laid the basis for using alkaline earth atoms for quantum simulation and, very recently, also for quantum computing. Similarly, manipulation and controlling methods for quantum simulations, such as state-dependent lattices [92], optical buildup cavities [103, 104], or local addressing on the $^1S_0$-$^3P_2$ [142] transition, may boost developments in quantum computing with alkaline earth atoms [72, 74, 73] and vice versa. In the near future, both platforms will co-exist [200], and the interplay between these platforms will enable realizing proposed applications that range from chemistry [2, 201] to solving optimization problems [202] and artificial intelligence [203, 204].

Appendix A

Time-of-flight expansion from a deep optical lattice

In this Section we derive an analytic expression for the expansion of a thermal cloud suddenly released from a harmonic trap when the energy-scale of the temperature is comparable to or smaller than the trap frequency.

We start with a single harmonic oscillator state and calculate its free space time evolution. The corresponding Schrödinger equation in momentum space is given by

$$i\hbar\partial_t\Psi(p) = \hat{H}\Psi(p) = \frac{p^2}{2m}\Psi(p), \tag{A.1}$$

where $\Psi(p)$ is the momentum space wave function, p is the momentum, m the mass of the wave packet, and t is the time.This differential equation is solved by

$$\Psi(p,t) = \exp\Big(-i\frac{p^2}{2m\hbar}t\Big)\Psi(p,t=0). \tag{A.2}$$

Here we can see that in momentum-space the time propagator is simply a multiplication by a quadratic phase factor. The momentum-space wave function $\Psi(p)$ is the Fourier transform of the real-space wave function φ and vice versa. By solving the harmonic oscillator Schrödinger equation in dimensionless symmetric coordinates one can show that $\Psi(p)$ can be obtained from $\varphi(x)$ by the substitutions

$$\begin{aligned} x &\to p \\ m\omega &\to 1/(m\omega), \end{aligned}$$

where ω is the harmonic oscillator frequency. This means that the initial momentum-space wave function has the form of a harmonic oscillator state. The procedure to calculate the expansion is then to multiply the initial momentum-space harmonic oscillator state by the quadratic phase factor and afterwards to calculate the real-space wave function by the inverse Fourier transformation. We then see that this procedure is exactly the same as calculating the diffraction of a Hermite-Gaussian beam in optics. Adjusting the equations of a Hermite-Gaussian mode to the n-th real-space Harmonic oscillator wave function at $t = 0$,we obtain

$$\varphi_n(t=0) = \frac{1}{2^n n!}\Big(\frac{m\omega}{\pi\hbar}\Big)^{1/4}\exp\Big(-\frac{m\omega x^2}{2\hbar}\Big)H_n\Big(\sqrt{\frac{m\omega}{\hbar}}x\Big), \tag{A.3}$$

where H_n is the Hermite polynomial of the order n. The associated waist at $t = 0$ is defined as $w_0 = \sqrt{2\hbar/(m\omega)}$. In analogy to a Gaussian beam, the waist scales with $w(t) = w_0\sqrt{1+\omega^2 t^2}$.

We model the thermal atomic cloud expanding from the harmonic trap as a thermal mixture of harmonic oscillator states at temperature T

$$n(x) \equiv \frac{1}{N}\sum_{n=0}^{N} \exp\Big[-\frac{\hbar\omega}{k_B T}\Big(n+\frac{1}{2}\Big)\Big]|\varphi_n(x)|^2. \tag{A.4}$$

Here, N is a cutoff due to the finite depth of the trap. We insert the explicit form of φ_n and include the waist scaling to obtain

$$\begin{aligned} n(x) = \frac{1}{N}\Big(\frac{m\omega}{\pi\hbar}\Big)^{1/2}\frac{w_0^2}{w(t)^2}\exp\Big(-\frac{2x^2}{w(t)^2}\Big) \\ \times\sum_{n=0}^{N}\exp\Big(-\frac{\hbar\omega}{k_B T}n\Big)\frac{1}{2^n n!}H_n^2\Big(\frac{\sqrt{2}x}{w(t)}\Big). \end{aligned} \tag{A.5}$$

For deep traps we can let $N \to \infty$ with the result

$$\begin{aligned} n(x) = \Big(\frac{m\omega}{\pi\hbar}\Big)^{1/4}\frac{w_0^2}{w(t)^2}\tanh\Big(\frac{\hbar\omega}{2k_B T}\Big) \\ \exp\Big[-\frac{2x^2}{w(t)^2}\tanh\Big(\frac{\hbar\omega}{2k_B T}\Big)\Big]. \end{aligned} \tag{A.6}$$

From the equation above we can conclude that the fitted $1/e^2$ waist of the cloud is given by

$$w(t,T) = \frac{\sqrt{\frac{2\hbar}{m\omega}}\sqrt{1+\omega^2 t^2}}{\sqrt{\tanh\Big(\frac{\hbar\omega}{2k_B T}\Big)}}. \tag{A.7}$$

For the case of $k_B T \ll \hbar\omega/2$, we approach $\tanh\Big(\frac{\hbar\omega}{2k_B T}\Big) \approx 1$.

For $k_B T \gg \hbar\omega/2$, we approximate $\tanh\left(\frac{\hbar\omega}{2k_B T}\right) \approx \sqrt{\frac{2k_B T}{\hbar\omega}}$. We convert the waist into $\sigma = w/4$ of a Gaussian to obtain the standard expression.

$$\sigma(t,T) = \sigma_0\sqrt{\frac{2k_B T}{\hbar\omega}}\sqrt{1+\omega^2 t^2} = \sqrt{\frac{2\hbar}{m\omega}\frac{1}{4}\frac{2k_B T}{\hbar\omega}}\sqrt{1+\omega^2 t^2} = \sqrt{\sigma_0^2 + \frac{k_B T}{m}t^2} \tag{A.8}$$

The calculations above are for the case of the expansion from a single harmonic trap and are valid for all temperature regimes. Nevertheless, it can be easily extended to a cloud of atoms expanding from individual harmonic confinements, e.g. in an optical lattice. If the atomic cloud has a Gaussian shape with waist w', the total expansion is

given by the convolution of two Gaussians, leading to

$$w'(t,T) = \sqrt{w_0'^2 + w(t,T)^2}. \tag{A.9}$$

We can see that the expression for the whole cloud just changes the initial cloud size, but the expansion itself is not changed.

References

[1] Lee, P. A., N. Nagaosa, and X.-G. Wen. *Doping a Mott insulator: Physics of high-temperature superconductivity*, Rev. Mod. Phys. **78**, 17–85 (2006). DOI: 10.1103/RevModPhys.78.17.

[2] Cao, Y., J. Romero, J. P. Olson, M. Degroote, P. D. Johnson, M. Kieferová, I. D. Kivlichan, T. Menke, B. Peropadre, N. P. Sawaya, *et al. Quantum chemistry in the age of quantum computing*, Chemical Reviews **119**., 10856–10915 (2019). DOI: 10.1021/acs.chemrev.8b00803.

[3] Zinner, N. T. and A. S. Jensen. *Comparing and contrasting nuclei and cold atomic gases*, Journal of Physics G: Nuclear and Particle Physics **40**., 053101 (2013). DOI: 10.1088/0954-3899/40/5/053101.

[4] Feynman, R. P. *Simulating physics with computers*, International Journal of Theoretical Physics **21**., 467–488 (1982). DOI: 10.1007/BF02650179.

[5] Manin, Y. I. *Computable and Non-Computable*, Sovetskoe Radio (1980).

[6] Phillips, W. D. *Nobel Lecture: Laser cooling and trapping of neutral atoms*, Rev. Mod. Phys. **70**, 721–741 (1998). DOI: 10.1103/RevModPhys.70.721.

[7] Cohen-Tannoudji, C. N. *Nobel Lecture: Manipulating atoms with photons*, Rev. Mod. Phys. **70**, 707–719 (1998). DOI: 10.1103/RevModPhys.70.707.

[8] Chu, S. *Nobel Lecture: The manipulation of neutral particles*, Rev. Mod. Phys. **70**, 685–706 (1998). DOI: 10.1103/RevModPhys.70.685.

[9] Georgescu, I. M., S. Ashhab, and F. Nori. *Quantum simulation*, Rev. Mod. Phys. **86**, 153–185 (2014). DOI: 10.1103/RevModPhys.86.153.

[10] Anderson, M. H., J. R. Ensher, M. R. Matthews, C. E. Wieman, and E. A. Cornell. *Observation of Bose-Einstein condensation in a dilute atomic vapor*, science **269**., 198–201 (1995). DOI: 10.1126/science.269.5221.198.

[11] Davis, K. B., M. .-.-O. Mewes, M. R. Andrews, N. J. van Druten, D. S. Durfee, D. M. Kurn, and W. Ketterle. *Bose-Einstein Condensation in a Gas of Sodium Atoms*, Phys. Rev. Lett. **75**, 3969–3973 (1995). DOI: 10.1103/PhysRevLett.75.3969.

[12] DeMarco, B. and D. S. Jin. *Onset of Fermi degeneracy in a trapped atomic gas*, science **285**., 1703–1706 (1999). DOI: 10.1126/science.285.5434.1703.

[13] Chin, C., R. Grimm, P. Julienne, and E. Tiesinga. *Feshbach resonances in ultracold gases*, Rev. Mod. Phys. **82**, 1225–1286 (2010). DOI: 10.1103/RevModPhys.82.1225.

[14] Cornish, S. L., N. R. Claussen, J. L. Roberts, E. A. Cornell, and C. E. Wieman. *Stable ^{85}Rb Bose-Einstein Condensates with Widely Tunable Interactions*, Phys. Rev. Lett. **85**, 1795–1798 (2000). DOI: 10.1103/PhysRevLett.85.1795.

[15] Bourdel, T., J. Cubizolles, L. Khaykovich, K. M. F. Magalhães, S. J. J. M. F. Kokkelmans, G. V. Shlyapnikov, and C. Salomon. *Measurement of the Interaction Energy near a Feshbach Resonance in a ^{6}Li Fermi Gas*, Phys. Rev. Lett. **91**, 020402 (2003). DOI: 10.1103/PhysRevLett.91.020402.

[16] Bartenstein, M., A. Altmeyer, S. Riedl, S. Jochim, C. Chin, J. H. Denschlag, and R. Grimm. *Collective Excitations of a Degenerate Gas at the BEC-BCS Crossover*, Phys. Rev. Lett. **92**, 203201 (2004). DOI: 10.1103/PhysRevLett.92.203201.

[17] Regal, C. A., M. Greiner, and D. S. Jin. *Observation of Resonance Condensation of Fermionic Atom Pairs*, Phys. Rev. Lett. **92**, 040403 (2004). DOI: 10.1103/PhysRevLett.92.040403.

[18] Zwierlein, M. W., C. A. Stan, C. H. Schunck, S. M. F. Raupach, A. J. Kerman, and W. Ketterle. *Condensation of Pairs of Fermionic Atoms near a Feshbach Resonance*, Phys. Rev. Lett. **92**, 120403 (2004). DOI: 10.1103/PhysRevLett.92.120403.

[19] Inguscio, M., S. Stringari, and C. Wieman. *Bose-Einstein condensation in atomic gases*. Vol. 140. IOS Press, 1999.

[20] Bloch, I., J. Dalibard, and W. Zwerger. *Many-body physics with ultracold gases*, Rev. Mod. Phys. **80**, 885–964 (July 2008). DOI: 10.1103/RevModPhys.80.885.

[21] Greiner, M., O. Mandel, T. Esslinger, T. W. Hänsch, and I. Bloch. *Quantum phase transition from a superfluid to a Mott insulator in a gas of ultracold atoms*, nature **415**., 39–44 (2002). DOI: 10.1038/415039a.

[22] Bloch, I., J. Dalibard, and S. Nascimbène. *Quantum simulations with ultracold quantum gases*, Nature Physics **8**, 267 (2012). DOI: 10.1038/nphys2259.

[23] Bloch, I. *Ultracold quantum gases in optical lattices*, Nature physics **1**., 23–30 (2005). DOI: 10.1038/nphys138.

[24] Esslinger, T. *Fermi-Hubbard Physics with Atoms in an Optical Lattice*, Annual Review of Condensed Matter Physics **1**., 129–152 (2010). DOI: 10.1146/annurev-conmatphys-070909-104059.

[25] Ketterle, W., D. S. Durfee, and D. M. Stamper-Kurn. *Making, probing and understanding Bose-Einstein condensates*, (1999). DOI: 10.48550/ARXIV.COND-MAT/9904034.

[26] Gross, C. and W. S. Bakr. *Quantum gas microscopy for single atom and spin detection*, Nature Physics **17**., 1316–1323 (2021). DOI: 10.1038/s41567-021-01370-5.

[27] Bakr, W. S., J. I. Gillen, A. Peng, S. Fölling, and M. Greiner. *A quantum gas microscope for detecting single atoms in a Hubbard-regime optical lattice*, Nature **462**., 74–77 (2009). DOI: 10.1038/nature08482.

[28] Sherson, J. F., C. Weitenberg, M. Endres, M. Cheneau, I. Bloch, and S. Kuhr. *Single-atom-resolved fluorescence imaging of an atomic Mott insulator*, Nature **467**., 68–72 (2010). DOI: 10.1038/nature09378.

[29] Parsons, M. F., F. Huber, A. Mazurenko, C. S. Chiu, W. Setiawan, K. Wooley-Brown, S. Blatt, and M. Greiner. *Site-Resolved Imaging of Fermionic* ^{6}Li *in an Optical Lattice*, Phys. Rev. Lett. **114**, 213002 (2015). DOI: 10.1103/PhysRevLett.114.213002.

[30] Haller, E., J. Hudson, A. Kelly, D. A. Cotta, B. Peaudecerf, G. D. Bruce, and S. Kuhr. *Single-atom imaging of fermions in a quantum-gas microscope*, Nature Physics **11**., 738–742 (2015). DOI: 10.1038/nphys3403.

[31] Cheuk, L. W., M. A. Nichols, M. Okan, T. Gersdorf, V. V. Ramasesh, W. S. Bakr, T. Lompe, and M. W. Zwierlein. *Quantum-Gas Microscope for Fermionic Atoms*, Phys. Rev. Lett. **114**, 193001 (2015). DOI: 10.1103/PhysRevLett.114.193001.

[32] Omran, A., M. Boll, T. A. Hilker, K. Kleinlein, G. Salomon, I. Bloch, and C. Gross. *Microscopic Observation of Pauli Blocking in Degenerate Fermionic Lattice Gases*, Phys. Rev. Lett. **115**, 263001 (2015). DOI: 10.1103/PhysRevLett.115.263001. URL: https://link.aps.org/doi/10.1103/PhysRevLett.115.263001.

[33] Miranda, M., R. Inoue, Y. Okuyama, A. Nakamoto, and M. Kozuma. *Site-resolved imaging of ytterbium atoms in a two-dimensional optical lattice*, Phys. Rev. A **91**, 063414 (2015). DOI: 10.1103/PhysRevA.91.063414.

[34] Yamamoto, R., J. Kobayashi, T. Kuno, K. Kato, and Y. Takahashi. *An ytterbium quantum gas microscope with narrow-line laser cooling*, New Journal of Physics **18**., 023016 (2016). DOI: 10.1088/1367-2630/18/2/023016.

[35] Yang, J., L. Liu, J. Mongkolkiattichai, and P. Schauss. *Site-Resolved Imaging of Ultracold Fermions in a Triangular-Lattice Quantum Gas Microscope*, PRX Quantum **2**, 020344 (2021). DOI: 10.1103/PRXQuantum.2.020344.

[36] Kwon, K., K. Kim, J. Hur, S. Huh, and J.-y. Choi. *Site-resolved imaging of a bosonic Mott insulator of* ^{7}Li *atoms*, Phys. Rev. A **105**, 033323 (2022). DOI: 10.1103/PhysRevA.105.033323.

[37] Jaksch, D., C. Bruder, J. I. Cirac, C. W. Gardiner, and P. Zoller. *Cold Bosonic Atoms in Optical Lattices*, Phys. Rev. Lett. **81**, 3108–3111 (1998). DOI: 10.1103/PhysRevLett.81.3108.

[38] Jaksch, D. and P. Zoller. *The cold atom Hubbard toolbox*, Annals of physics **315**., 52–79 (2005). DOI: 0.1016/j.aop.2004.09.010.

[39] Cheneau, M., P. Barmettler, D. Poletti, M. Endres, P. Schauß, T. Fukuhara, C. Gross, I. Bloch, C. Kollath, and S. Kuhr. *Light-cone-like spreading of correlations in a quantum many-body system*, Nature **481**., 484–487 (2012). DOI: 10.1038/nature10748.

[40] Fukuhara, T., A. Kantian, M. Endres, M. Cheneau, P. Schauß, S. Hild, D. Bellem, U. Schollwöck, T. Giamarchi, C. Gross, *et al. Quantum dynamics of a mobile spin impurity*, Nature Physics **9**., 235–241 (2013). DOI: 10.1038/nphys2561.

[41] Islam, R., R. Ma, P. M. Preiss, M. Eric Tai, A. Lukin, M. Rispoli, and M. Greiner. *Measuring entanglement entropy in a quantum many-body system*, Nature **528**., 77–83 (2015). DOI: 10.1038/nature15750.

[42] Boll, M., T. A. Hilker, G. Salomon, A. Omran, J. Nespolo, L. Pollet, I. Bloch, and C. Gross. *Spin-and density-resolved microscopy of antiferromagnetic correlations in Fermi-Hubbard chains*, Science **353**., 1257–1260 (2016). DOI: 10.1126/science.aag1635.

[43] Mazurenko, A., C. S. Chiu, G. Ji, M. F. Parsons, M. Kanász-Nagy, R. Schmidt, F. Grusdt, E. Demler, D. Greif, and M. Greiner. *A cold-atom Fermi-Hubbard antiferromagnet*, Nature **545**., 462–466 (2017). DOI: 10.1038/nature22362.

[44] Vijayan, J., P. Sompet, G. Salomon, J. Koepsell, S. Hirthe, A. Bohrdt, F. Grusdt, I. Bloch, and C. Gross. *Time-resolved observation of spin-charge deconfinement in fermionic Hubbard chains*, Science **367**., 186–189 (2020). DOI: 10.1126/science.aay2354.

[45] Rubio-Abadal, A., M. Ippoliti, S. Hollerith, D. Wei, J. Rui, S. L. Sondhi, V. Khemani, C. Gross, and I. Bloch. *Floquet Prethermalization in a Bose-Hubbard System*, Phys. Rev. X **10**, 021044 (2020). DOI: 10.1103/PhysRevX.10.021044.

[46] Rui, J., D. Wei, A. Rubio-Abadal, S. Hollerith, J. Zeiher, D. M. Stamper-Kurn, C. Gross, and I. Bloch. *A subradiant optical mirror formed by a single structured atomic layer*, Nature **583**., 369–374 (2020). DOI: 10.1038/s41586-020-2463-x.

[47] Sompet, P., S. Hirthe, D. Bourgund, T. Chalopin, J. Bibo, J. Koepsell, P. Bojović, R. Verresen, F. Pollmann, G. Salomon, *et al. Realizing the symmetry-protected Haldane phase in Fermi-Hubbard ladders*, Nature, 1–5 (2022). DOI: 10.1038/s41586-022-04688-z.

[48] Wei, D., A. Rubio-Abadal, B. Ye, F. Machado, J. Kemp, K. Srakaew, S. Hollerith, J. Rui, S. Gopalakrishnan, N. Y. Yao, *et al. Quantum gas microscopy of Kardar-Parisi-Zhang superdiffusion*, Science **376**., 716–720 (2022). DOI: 10.1126/science.abk2397.

[49] Muniz, J. A., D. J. Young, J. R. K. Cline, and J. K. Thompson. *Cavity-QED measurements of the ^{87}Sr millihertz optical clock transition and determination of its natural linewidth*, Phys. Rev. Research **3**, 023152 (2021). DOI: 10.1103/PhysRevResearch.3.023152.

[50] Young, A. W., W. J. Eckner, W. R. Milner, D. Kedar, M. A. Norcia, E. Oelker, N. Schine, J. Ye, and A. M. Kaufman. *Half-minute-scale atomic coherence and high relative stability in a tweezer clock*, Nature **588**., 408–413 (2020). DOI: 10.1038/s41586-020-3009-y.

[51] Campbell, S. L., R. Hutson, G. Marti, A. Goban, N. Darkwah Oppong, R. McNally, L. Sonderhouse, J. Robinson, W. Zhang, B. Bloom, *et al. A Fermi-degenerate three-dimensional optical lattice clock*, Science **358**., 90–94 (2017). DOI: 10.1126/science.aam5538.

[52] Udem, T., J. Reichert, R. Holzwarth, and T. W. Hänsch. *Absolute Optical Frequency Measurement of the Cesium D_1 Line with a Mode-Locked Laser*, Phys. Rev. Lett. **82**, 3568–3571 (1999). DOI: 10.1103/PhysRevLett.82.3568.

[53] Jones, D. J., S. A. Diddams, J. K. Ranka, A. Stentz, R. S. Windeler, J. L. Hall, and S. T. Cundiff. *Carrier-envelope phase control of femtosecond mode-locked lasers and direct optical frequency synthesis*, Science **288**., 635–639 (2000). DOI: 10.1126/science.288.5466.635.

[54] Oelker, E., R. Hutson, C. Kennedy, L. Sonderhouse, T. Bothwell, A. Goban, D. Kedar, C. Sanner, J. Robinson, G. Marti, *et al. Demonstration of 4.8× 10- 17 stability at 1 s for two independent optical clocks*, Nature Photonics **13**., 714–719 (2019). DOI: 10.1038/s41566-019-0493-4.

[55] McGrew, W., X. Zhang, R. Fasano, S. Schäffer, K. Beloy, D. Nicolodi, R. Brown, N. Hinkley, G. Milani, M. Schioppo, *et al. Atomic clock performance enabling geodesy below the centimetre level*, Nature **564**., 87–90 (2018). DOI: 10.1038/s41586-018-0738-2.

[56] Takamoto, M., F.-L. Hong, R. Higashi, and H. Katori. *An optical lattice clock*, Nature **435**., 321–324 (2005). DOI: 10.1038/nature03541.

[57] Bothwell, T., C. J. Kennedy, A. Aeppli, D. Kedar, J. M. Robinson, E. Oelker, A. Staron, and J. Ye. *Resolving the gravitational redshift across a millimetre-scale atomic sample*, Nature **602**., 420–424 (2022). DOI: 10.1038/s41586-021-04349-7.

[58] Zheng, X., J. Dolde, V. Lochab, B. N. Merriman, H. Li, and S. Kolkowitz. *Differential clock comparisons with a multiplexed optical lattice clock*, Nature **602**., 425–430 (2022). DOI: 10.1038/s41586-021-04344-y.

[59] Safronova, M. S., D. Budker, D. DeMille, D. F. J. Kimball, A. Derevianko, and C. W. Clark. *Search for new physics with atoms and molecules*, Rev. Mod. Phys. **90**, 025008 (2018). DOI: 10.1103/RevModPhys.90.025008.

[60] Zhang, X., M. Bishof, S. L. Bromley, C. V. Kraus, M. S. Safronova, P. Zoller, A. M. Rey, and J. Ye. *Spectroscopic observation of SU(N)-symmetric interactions in Sr orbital magnetism*, science **345**., 1467–1473 (2014). DOI: 10.1126/science.1254978.

[61] Sonderhouse, L., C. Sanner, R. B. Hutson, A. Goban, T. Bilitewski, L. Yan, W. R. Milner, A. M. Rey, and J. Ye. *Thermodynamics of a deeply degenerate SU(N)-symmetric Fermi gas*, Nature Physics **16**., 1216–1221 (2020). DOI: 10.1038/s41567-020-0986-6.

[62] Marti, G. E., R. B. Hutson, A. Goban, S. L. Campbell, N. Poli, and J. Ye. *Imaging Optical Frequencies with* $100\ \mu\mathrm{Hz}$ *Precision and* $1.1\ \mu\mathrm{m}$ *Resolution*, Phys. Rev. Lett. **120**, 103201 (2018). DOI: 10.1103/PhysRevLett.120.103201.

[63] Blatt, R., H. Häffner, C. Roos, C. Becher, and F. Schmidt-Kaler. *Ion trap quantum computing with Ca+ ions*, Quantum Information Processing **3**., 61–73 (2004). DOI: 10.1007/s11128-004-3105-1.

[64] Blinov, B. B., D. Leibfried, C. Monroe, and D. J. Wineland. *Quantum computing with trapped ion hyperfine qubits*, Quantum Information Processing **3**., 45–59 (2004). DOI: 10.1007/s11128-004-9417-3.

[65] Stock, R., N. S. Babcock, M. G. Raizen, and B. C. Sanders. *Entanglement of group-II-like atoms with fast measurement for quantum information processing*, Phys. Rev. A **78**, 022301 (2008). DOI: 10.1103/PhysRevA.78.022301.

[66] Häffner, H., C. F. Roos, and R. Blatt. *Quantum computing with trapped ions*, Physics reports **469**., 155–203 (2008). DOI: 10.1016/j.physrep.2008.09.003.

[67] Bluvstein, D., H. Levine, G. Semeghini, T. T. Wang, S. Ebadi, M. Kalinowski, A. Keesling, N. Maskara, H. Pichler, M. Greiner, *et al. A quantum processor based on coherent transport of entangled atom arrays*, Nature **604**., 451–456 (2022). DOI: 10.1038/s41586-022-04592-6.

[68] Okuno, D., Y. Nakamura, T. Kusano, Y. Takasu, N. Takei, H. Konishi, and Y. Takahashi. *High-resolution spectroscopy and single-photon Rydberg excitation of reconfigurable ytterbium atom tweezer arrays utilizing a metastable state*, arXiv:2204.07995 (2022). DOI: 10.48550/ARXIV.2204.07995.

[69] Madjarov, I. S., J. P. Covey, A. L. Shaw, J. Choi, A. Kale, A. Cooper, H. Pichler, V. Schkolnik, J. R. Williams, and M. Endres. *High-fidelity entanglement and detection of alkaline-earth Rydberg atoms*, Nature Physics **16**., 857–861 (2020). DOI: 10.1038/s41567-020-0903-z.

[70] Schine, N., A. W. Young, W. J. Eckner, M. J. Martin, and A. M. Kaufman. *Long-lived Bell states in an array of optical clock qubits*, (2021). DOI: 10.48550/ARXIV.2111.14653.

[71] Boyd, M. M., T. Zelevinsky, A. D. Ludlow, S. Blatt, T. Zanon-Willette, S. M. Foreman, and J. Ye. *Nuclear spin effects in optical lattice clocks*, Phys. Rev. A **76**, 022510 (2007). DOI: 10.1103/PhysRevA.76.022510.

[72] Daley, A. J. *Quantum computing and quantum simulation with group-II atoms*, Quantum Information Processing **10**., 865–884 (2011). DOI: 10.1007/s11128-011-0293-3.

[73] Daley, A. J., M. M. Boyd, J. Ye, and P. Zoller. *Quantum Computing with Alkaline-Earth-Metal Atoms*, Phys. Rev. Lett. **101**, 170504 (2008). DOI: 10.1103/PhysRevLett.101.170504.

[74] Daley, A. J., J. Ye, and P. Zoller. *State-dependent lattices for quantum computing with alkaline-earth-metal atoms*, The European Physical Journal D **65**., 207–217 (2011). DOI: 10.1140/epjd/e2011-20095-2.

[75] Gorshkov, A. V., A. M. Rey, A. J. Daley, M. M. Boyd, J. Ye, P. Zoller, and M. D. Lukin. *Alkaline-Earth-Metal Atoms as Few-Qubit Quantum Registers*, Phys. Rev. Lett. **102**, 110503 (2009). DOI: 10.1103/PhysRevLett.102.110503.

[76] Pagano, A., S. Weber, D. Jaschke, T. Pfau, F. Meinert, S. Montangero, and H. P. Büchler. *Error budgeting for a controlled-phase gate with strontium-88 Rydberg atoms*, Phys. Rev. Research **4**, 033019 (2022). DOI: 10.1103/PhysRevResearch.4.033019.

[77] Cooper, A., J. P. Covey, I. S. Madjarov, S. G. Porsev, M. S. Safronova, and M. Endres. *Alkaline-Earth Atoms in Optical Tweezers*, Phys. Rev. X **8**, 041055 (2018). DOI: 10.1103/PhysRevX.8.041055.

[78] Norcia, M. A., A. W. Young, and A. M. Kaufman. *Microscopic Control and Detection of Ultracold Strontium in Optical-Tweezer Arrays*, Phys. Rev. X **8**, 041054 (2018). DOI: 10.1103/PhysRevX.8.041054.

[79] Saskin, S., J. T. Wilson, B. Grinkemeyer, and J. D. Thompson. *Narrow-Line Cooling and Imaging of Ytterbium Atoms in an Optical Tweezer Array*, Phys. Rev. Lett. **122**, 143002 (2019). DOI: 10.1103/PhysRevLett.122.143002.

[80] Jenkins, A., J. W. Lis, A. Senoo, W. F. McGrew, and A. M. Kaufman. *Ytterbium Nuclear-Spin Qubits in an Optical Tweezer Array*, Phys. Rev. X **12**, 021027 (2022). DOI: 10.1103/PhysRevX.12.021027.

[81] Barnes, K., P. Battaglino, B. J. Bloom, K. Cassella, R. Coxe, N. Crisosto, J. P. King, S. S. Kondov, K. Kotru, S. C. Larsen, *et al. Assembly and coherent control of a register of nuclear spin qubits*, Nature Communications **13**., 1–10 (2022). DOI: 10.1038/s41467-022-29977-z.

[82] Kaufman, A. M. and K.-K. Ni. *Quantum science with optical tweezer arrays of ultracold atoms and molecules*, Nature Physics **17**., 1324–1333 (2021). DOI: 10.1038/s41567-021-01357-2.

[83] Ebadi, S., T. T. Wang, H. Levine, A. Keesling, G. Semeghini, A. Omran, D. Bluvstein, R. Samajdar, H. Pichler, W. W. Ho, *et al. Quantum phases of matter on a 256-atom programmable quantum simulator*, Nature **595**., 227–232 (2021). DOI: 10.1038/s41586-021-03582-4.

[84] Scholl, P., M. Schuler, H. J. Williams, A. A. Eberharter, D. Barredo, K.-N. Schymik, V. Lienhard, L.-P. Henry, T. C. Lang, T. Lahaye, *et al. Quantum simulation of 2D antiferromagnets with hundreds of Rydberg atoms*, Nature **595**., 233–238 (2021). DOI: 10.1038/s41586-021-03585-1.

[85] Young, A. W., W. J. Eckner, N. Schine, A. M. Childs, and A. M. Kaufman. *Tweezer-programmable 2D quantum walks in a Hubbard-regime lattice*, (2022). DOI: 10.48550/ARXIV.2202.01204.

[86] Safronova, M., Z. Zuhrianda, U. Safronova, and C. W. Clark. *Extracting transition rates from zero-polarizability spectroscopy*, Physical Review A **92.**, 040501 (2015). DOI: 10.1103/PhysRevA.92.040501.

[87] Cazalilla, M. A. and A. M. Rey. *Ultracold Fermi gases with emergent SU(N) symmetry*, Reports on Progress in Physics **77.**, 124401 (2014). DOI: 10.1088/0034-4885/77/12/124401.

[88] Gorshkov, A. V., M. Hermele, V. Gurarie, C. Xu, P. S. Julienne, J. Ye, P. Zoller, E. Demler, M. D. Lukin, and A. Rey. *Two-orbital SU(N) magnetism with ultracold alkaline-earth atoms*, Nature physics **6.**, 289–295 (2010). DOI: 10.1038/nphys1535.

[89] Ozawa, H., S. Taie, Y. Takasu, and Y. Takahashi. *Antiferromagnetic Spin Correlation of* SU($\mathcal{N}$) *Fermi Gas in an Optical Superlattice*, Phys. Rev. Lett. **121**, 225303 (2018). DOI: 10.1103/PhysRevLett.121.225303.

[90] Taie, S., E. Ibarra-García-Padilla, N. Nishizawa, Y. Takasu, Y. Kuno, H.-T. Wei, R. T. Scalettar, K. R. A. Hazzard, and Y. Takahashi. *Observation of antiferromagnetic correlations in an ultracold SU(N) Hubbard model*, (2020). DOI: 10.48550/ARXIV.2010.07730.

[91] Sonderhouse, L., C. Sanner, R. B. Hutson, A. Goban, T. Bilitewski, L. Yan, W. R. Milner, A. M. Rey, and J. Ye. *Thermodynamics of a deeply degenerate SU(N)-symmetric Fermi gas*, Nature Physics **16.**, 1216–1221 (2020). DOI: 10.1038/s41567-020-0986-6.

[92] Heinz, A., A. J. Park, Šanti ć, J. Trautmann, S. G. Porsev, M. S. Safronova, I. Bloch, and S. Blatt. *State-Dependent Optical Lattices for the Strontium Optical Qubit*, Phys. Rev. Lett. **124**, 203201 (2020). DOI: 10.1103/PhysRevLett.124.203201.

[93] Park, A. J. "Towards Quantum Simulations with Strontium in Cavity-enhanced Optical Lattices". PhD thesis. Ludwig Maximilians Universität München, 2021.

[94] Heinz, A. "Ultracold Strontium in State-Dependent Optical Lattices". PhD thesis. Ludwig Maximilians Universität München, 2020.

[95] Vega, I. de, D. Porras, and J. Ignacio Cirac. *Matter-Wave Emission in Optical Lattices: Single Particle and Collective Effects*, Phys. Rev. Lett. **101**, 260404 (2008). DOI: 10.1103/PhysRevLett.101.260404.

[96] González-Tudela, A. and J. I. Cirac. *Markovian and non-Markovian dynamics of quantum emitters coupled to two-dimensional structured reservoirs*, Phys. Rev. A **96**, 043811 (2017). DOI: 10.1103/PhysRevA.96.043811.

[97] González-Tudela, A. and J. I. Cirac. *Quantum Emitters in Two-Dimensional Structured Reservoirs in the Nonperturbative Regime*, Phys. Rev. Lett. **119**, 143602 (2017). DOI: 10.1103/PhysRevLett.119.143602.

[98] González-Tudela, A., C.-L. Hung, D. E. Chang, J. I. Cirac, and H. Kimble. *Subwavelength vacuum lattices and atom–atom interactions in two-dimensional photonic crystals*, Nature Photonics **9**., 320–325 (2015). DOI: 10.1038/nphoton.2015.54.

[99] Krinner, L., M. Stewart, A. Pazmino, J. Kwon, and D. Schneble. *Spontaneous emission of matter waves from a tunable open quantum system*, Nature **559**., 589–592 (2018). DOI: 10.1038/s41586-018-0348-z.

[100] Kwon, J., Y. Kim, A. Lanuza, and D. Schneble. *Formation of matter-wave polaritons in an optical lattice*, Nature Physics, 1–5 (2022). DOI: 10.1038/s41567-022-01565-4.

[101] Greif, D., M. F. Parsons, A. Mazurenko, C. S. Chiu, S. Blatt, F. Huber, G. Ji, and M. Greiner. *Site-resolved imaging of a fermionic Mott insulator*, Science **351**., 953–957 (2016). DOI: 10.1126/science.aad9041.

[102] Srakaew, K., P. Weckesser, S. Hollerith, D. Wei, D. Adler, I. Bloch, and J. Zeiher. *A subwavelength atomic array switched by a single Rydberg atom*, (2022). DOI: 10.48550/ARXIV.2207.09383.

[103] Heinz, A., J. Trautmann, N. Šantić, A. J. Park, I. Bloch, and S. Blatt. *Crossed optical cavities with large mode diameters*, Opt. Lett. **46**., 250–253 (2021). DOI: 10.1364/OL.414076.

[104] Park, A. J., J. Trautmann, Šanti ć, V. Klüsener, A. Heinz, I. Bloch, and S. Blatt. *Cavity-Enhanced Optical Lattices for Scaling Neutral Atom Quantum Technologies to Higher Qubit Numbers*, PRX Quantum **3**, 030314 (2022). DOI: 10.1103/PRXQuantum.3.030314.

[105] Brown, P. T., D. Mitra, E. Guardado-Sanchez, P. Schauß, S. S. Kondov, E. Khatami, T. Paiva, N. Trivedi, D. A. Huse, and W. S. Bakr. *Spin-imbalance in a 2D Fermi-Hubbard system*, Science **357**., 1385–1388 (2017). DOI: 10.1126/science.aam7838.

[106] Kato, S., K. Shibata, R. Yamamoto, Y. Yoshikawa, and Y. Takahashi. *Optical magnetic resonance imaging with an ultra-narrow optical transition*, Applied Physics B **108**., 31–38 (2012). DOI: 10.1007/s00340-012-4893-0.

[107] Shibata, K., R. Yamamoto, Y. Seki, and Y. Takahashi. *Optical spectral imaging of a single layer of a quantum gas with an ultranarrow optical transition*, Phys. Rev. A **89**, 031601 (2014). DOI: 10.1103/PhysRevA.89.031601.

[108] Kato, S., S. Sugawa, K. Shibata, R. Yamamoto, and Y. Takahashi. *Control of Resonant Interaction between Electronic Ground and Excited States*, Phys. Rev. Lett. **110**, 173201 (2013). DOI: 10.1103/PhysRevLett.110.173201.

[109] Yamaguchi, A., S. Uetake, D. Hashimoto, J. M. Doyle, and Y. Takahashi. *Inelastic Collisions in Optically Trapped Ultracold Metastable Ytterbium*, Phys. Rev. Lett. **101**, 233002 (2008). DOI: 10.1103/PhysRevLett.101.233002.

[110] Onishchenko, O., S. Pyatchenkov, A. Urech, C. C. Chen, S. Bennetts, G. A. Siviloglou, and F. Schreck. *Frequency of the ultranarrow $^1\mathrm{S}_0$ - $^3\mathrm{P}_2$ transition in ^{87}Sr*, Physical Review A **99**., 1–8 (2019). DOI: 10.1103/PhysRevA.99.052503.

[111] Weitenberg, C., M. Endres, J. F. Sherson, M. Cheneau, P. Schauß, T. Fukuhara, I. Bloch, and S. Kuhr. *Single-spin addressing in an atomic Mott insulator*, Nature **471**., 319–324 (2011). DOI: 10.1038/nature09827.

[112] Ketterle, W. and N. Van Druten. *Evaporative cooling of trapped atoms*, *Advances in atomic, molecular, and optical physics*. Vol. 37. Elsevier, 1996, pp. 181–236. DOI: 10.1016/S1049-250X(08)60101-9.

[113] Stellmer, S., R. Grimm, and F. Schreck. *Production of quantum-degenerate strontium gases*, Phys. Rev. A **87**, 013611 (2013). DOI: 10.1103/PhysRevA.87.013611.

[114] Hertel, I. V. and C.-P. Schulz. *Atoms, molecules and optical physics*. Springer, 2014.

[115] Nicholson, T. L., S. Campbell, R. Hutson, G. E. Marti, B. Bloom, R. L. McNally, W. Zhang, M. Barrett, M. S. Safronova, G. Strouse, *et al. Systematic evaluation of an atomic clock at 2$\times 10^{-18}$ total uncertainty*, Nature communications **6**., 1–8 (2015). DOI: 10.1038/ncomms7896.

[116] Xu, X., T. H. Loftus, J. L. Hall, A. Gallagher, and J. Ye. *Cooling and trapping of atomic strontium*, JOSA B **20**., 968–976 (2003). DOI: 10.1364/JOSAB.20.000968.

[117] Stellmer, S. "Degenerate quantum gases of strontium". PhD thesis. Universität Innsbruck, 2013.

[118] Snigirev, S., A. J. Park, A. Heinz, I. Bloch, and S. Blatt. *Fast and dense magneto-optical traps for strontium*, Phys. Rev. A **99**, 063421 (2019). DOI: 10.1103/PhysRevA.99.063421.

[119] Ido, T. and H. Katori. *Recoil-Free Spectroscopy of Neutral Sr Atoms in the Lamb-Dicke Regime*, Phys. Rev. Lett. **91**, 053001 (2003). DOI: 10.1103/PhysRevLett.91.053001.

[120] Brusch, A., R. Le Targat, X. Baillard, M. Fouché, and P. Lemonde. *Hyperpolarizability Effects in a Sr Optical Lattice Clock*, Phys. Rev. Lett. **96**, 103003 (2006). DOI: 10.1103/PhysRevLett.96.103003.

[121] Ludlow, A. D., M. M. Boyd, T. Zelevinsky, S. M. Foreman, S. Blatt, M. Notcutt, T. Ido, and J. Ye. *Systematic Study of the $^{87}\mathrm{Sr}$ Clock Transition in an Optical Lattice*, Phys. Rev. Lett. **96**, 033003 (2006). DOI: 10.1103/PhysRevLett.96.033003.

[122] Bishof, M., M. J. Martin, M. D. Swallows, C. Benko, Y. Lin, G. Quéméner, A. M. Rey, and J. Ye. *Inelastic collisions and density-dependent excitation suppression in a ^{87}Sr optical lattice clock*, Phys. Rev. A **84**, 052716 (2011). DOI: 10.1103/PhysRevA.84.052716.

[123] Taichenachev, A. V., V. I. Yudin, C. W. Oates, C. W. Hoyt, Z. W. Barber, and L. Hollberg. *Magnetic Field-Induced Spectroscopy of Forbidden Optical Transitions with Application to Lattice-Based Optical Atomic Clocks*, Phys. Rev. Lett. **96**, 083001 (2006). DOI: 10.1103/PhysRevLett.96.083001.

[124] Lisdat, C., J. S. R. V. Winfred, T. Middelmann, F. Riehle, and U. Sterr. *Collisional Losses, Decoherence, and Frequency Shifts in Optical Lattice Clocks with Bosons*, Phys. Rev. Lett. **103**, 090801 (2009). DOI: 10.1103/PhysRevLett.103.090801.

[125] Akatsuka, T., M. Takamoto, and H. Katori. *Three-dimensional optical lattice clock with bosonic* ^{88}Sr *atoms*, Phys. Rev. A **81**, 023402 (2010). DOI: 10.1103/PhysRevA.81.023402.

[126] Koller, S. B., J. Grotti, S. Vogt, A. Al-Masoudi, S. Dörscher, S. Häfner, U. Sterr, and C. Lisdat. *Transportable Optical Lattice Clock with* 7×10^{-17} *Uncertainty*, Physical Review Letters **118**, 073601 (2017).

[127] Schäfer, F., T. Fukuhara, S. Sugawa, Y. Takasu, and Y. Takahashi. *Tools for quantum simulation with ultracold atoms in optical lattices*, Nature Reviews Physics **2**., 411–425 (2020). DOI: 10.1038/s42254-020-0195-3.

[128] Yasuda, M. and H. Katori. *Lifetime measurement of the* ^{3}P$_2$ *metastable state of strontium atoms*, Physical Review Letters **92**, 153004 (2004). DOI: 10.1103/PhysRevLett.92.153004.

[129] Garstang, R. H. *Magnetic Quadrupole Line Intensities*, Astrophysical Journal **148**, 579 (1967). DOI: 10.1086/149179.

[130] Shibata, K., S. Kato, A. Yamaguchi, S. Uetake, and Y. Takahashi. *A scalable quantum computer with ultranarrow optical transition of ultracold neutral atoms in an optical lattice*, Applied Physics B **97**., 753–758 (2009). DOI: 10.1007/s00340-009-3696-4.

[131] Heider, S. M. and G. O. Brink. *Hyperfine structure of* ^{87}Sr *in the* $^3P_2$ *metastable state*, Phys. Rev. A **16**, 1371–1374 (1977). DOI: 10.1103/PhysRevA.16.1371.

[132] Lamb, W. E., R. R. Schlicher, and M. O. Scully. *Matter-field interaction in atomic physics and quantum optics*, Phys. Rev. A **36**, 2763–2772 (1987). DOI: 10.1103/PhysRevA.36.2763.

[133] Sobelman, I. I. *Atomic spectra and radiative transitions*. Vol. 12. Springer Science & Business Media, 2012.

[134] Mizushima, M. $\Delta S = \pm 1$ *Magnetic Multipole Radiative Transitions*, Phys. Rev. **134**, A883–A888 (1964). DOI: 10.1103/PhysRev.134.A883.

[135] Scully, M. O. and M. S. Zubairy. *Quantum optics*. American Association of Physics Teachers, 1999.

[136] Jackson, J. D. *Classical electrodynamics*. American Association of Physics Teachers, 1999.

[137] Johnson, W. R. *Atomic structure theory*. Springer, 2007.

[138] Sakurai, J. J. and E. D. Commins. *Modern quantum mechanics, revised edition*. American Association of Physics Teachers, 1995.

[139] Loudon, R. *The quantum theory of light*. OUP Oxford, 2000.

[140] Godun, R. M., P. B. R. Nisbet-Jones, J. M. Jones, S. A. King, L. A. M. Johnson, H. S. Margolis, K. Szymaniec, S. N. Lea, K. Bongs, and P. Gill. *Frequency Ratio of Two Optical Clock Transitions in* $^{171}\mathrm{Yb}^{+}$ *and Constraints on the Time Variation of Fundamental Constants*, Phys. Rev. Lett. **113**, 210801 (2014). DOI: 10.1103/PhysRevLett.113.210801.

[141] Lange, R., A. A. Peshkov, N. Huntemann, C. Tamm, A. Surzhykov, and E. Peik. *Lifetime of the* $^2F_{7/2}$ *Level in* Yb^{+} *for Spontaneous Emission of Electric Octupole Radiation*, Phys. Rev. Lett. **127**, 213001 (2021). DOI: 10.1103/PhysRevLett.127.213001.

[142] Trautmann, J., D. Yankelev, V. Klüsener, A. J. Park, I. Bloch, and S. Blatt. *The* $^1S_0$-$^3P_2$ *magnetic quadrupole transition in neutral strontium*, In preparation (2022).

[143] Metcalf, H. J. and P. Van der Straten. *Laser cooling and trapping*. Springer, 1999. DOI: 10.1007/978-1-4612-1470-0.

[144] Auzinsh, M., D. Budker, and S. Rochester. *Optically polarized atoms: understanding light-atom interactions*. Oxford University Press, 2010.

[145] Schmiegelow, C. T., J. Schulz, H. Kaufmann, T. Ruster, U. G. Poschinger, and F. Schmidt-Kaler. *Transfer of optical orbital angular momentum to a bound electron*, Nature communications **7**., 1–6 (2016). DOI: 10.1038/ncomms12998.

[146] Barrera, R. G., G. A. Estevez, and J. Giraldo. *Vector spherical harmonics and their application to magnetostatics*, European Journal of Physics **6**., 287–294 (1985). DOI: 10.1088/0143-0807/6/4/014.

[147] Mizushima, M. $\Delta S{=}\pm 1$ *Magnetic Quadrupole Radiative Transitions in Atoms and Molecules*, Journal of the Physical Society of Japan **21**., 2335–2344 (1966). DOI: 10.1143/JPSJ.21.2335.

[148] Saleh, B. E. and M. C. Teich. *Fundamentals of photonics*. john Wiley & sons, 2019.

[149] Schmiegelow, C. T. and F. Schmidt-Kaler. *Light with orbital angular momentum interacting with trapped ions*, The European Physical Journal D **66**., 1–9 (2012). DOI: 10.1140/epjd/e2012-20730-4.

[150] Grimm, R., M. Weidemüller, and Y. B. Ovchinnikov. *Optical dipole traps for neutral atoms*, Advances in atomic, molecular, and optical physics **42**, 95–170 (2000). DOI: https://doi.org/10.1016/S1049-250X(08)60186-X.

[151] Savard, T. A., K. M. O'Hara, and J. E. Thomas. *Laser-noise-induced heating in far-off resonance optical traps*, Phys. Rev. A **56**, R1095 (1997). DOI: 10.1103/PhysRevA.56.R1095.

[152] Pichler, H., A. J. Daley, and P. Zoller. *Nonequilibrium dynamics of bosonic atoms in optical lattices: Decoherence of many-body states due to spontaneous emission*, Phys. Rev. A **82**, 063605 (2010). DOI: 10.1103/PhysRevA.82.063605.

[153] Trotzky, S., L. Pollet, F. Gerbier, U. Schnorrberger, I. Bloch, N. Prokof'Ev, B. Svistunov, and M. Troyer. *Suppression of the critical temperature for superfluidity near the Mott transition*, Nature Physics **6**., 998–1004 (2010). DOI: 10.1038/nphys1799.

[154] Blatt, S., A. Mazurenko, M. F. Parsons, C. S. Chiu, F. Huber, and M. Greiner. *Low-noise optical lattices for ultracold* ^{6}Li, Phys. Rev. A **92**, 021402 (Aug. 2015). DOI: 10.1103/PhysRevA.92.021402.

[155] Le Kien, F., P. Schneeweiss, and A. Rauschenbeutel. *Dynamical polarizability of atoms in arbitrary light fields: general theory and application to cesium*, The European Physical Journal D **67**., 1–16 (2013).

[156] Safronova, M. S., S. G. Porsev, U. I. Safronova, M. G. Kozlov, and C. W. Clark. *Blackbody-radiation shift in the Sr optical atomic clock*, Phys. Rev. A **87**, 012509 (2013). DOI: 10.1103/PhysRevA.87.012509.

[157] Steck, D. A. *Quantum and Atom Optics*. URL: http://steck.us/teaching.

[158] Rosenbusch, P., S. Ghezali, V. A. Dzuba, V. V. Flambaum, K. Beloy, and A. Derevianko. *ac Stark shift of the Cs microwave atomic clock transitions*, Phys. Rev. A **79**, 013404 (2009). DOI: 10.1103/PhysRevA.79.013404.

[159] Barakhshan, P., A. Marrs, A. Bhosale, B. Arora, R. Eigenmann, and M. S. Safronova. *Portal for High-Precision Atomic Data and Computation* (version 2.0). University of Delaware, Newark, DE, USA. URL: https://www.udel.edu/atom. 2022.

[160] A. Kramida, Yu. Ralchenko, J. Reader, and and NIST ASD Team. NIST Atomic Spectra Database (ver. 5.8), [Online]. Available: https://physics.nist.gov/asd [10/30/2020]. National Institute of Standards and Technology, Gaithersburg, MD. 2020. DOI: 10.18434/T4W30F.

[161] Safronova, M. S. *private communication*.

[162] Gerbier, F. and J. Dalibard. *Gauge fields for ultracold atoms in optical superlattices*, New Journal of Physics **12**., 033007 (2010). DOI: 10.1088/1367-2630/12/3/033007.

[163] DeTroye, D. J. and R. J. Chase. *The calculation and measurement of Helmholtz coil fields*. Tech. rep. Army Research Lab Adelphi MD, 1994.

[164] Bruus, H. *Theoretical microfluidics*. Vol. 18. Oxford university press, 2007.

[165] Raab, E. L., M. Prentiss, A. Cable, S. Chu, and D. E. Pritchard. *Trapping of Neutral Sodium Atoms with Radiation Pressure*, Phys. Rev. Lett. **59**, 2631–2634 (1987). DOI: 10.1103/PhysRevLett.59.2631.

[166] Katori, H., T. Ido, Y. Isoya, and M. Kuwata-Gonokami. *Magneto-Optical Trapping and Cooling of Strontium Atoms down to the Photon Recoil Temperature*, Phys. Rev. Lett. **82**, 1116–1119 (1999). DOI: 10.1103/PhysRevLett.82.1116.

[167] Mosk, A., S. Jochim, H. Moritz, T. Elsässer, M. Weidemüller, and R. Grimm. *Resonator-enhanced optical dipole trap for fermionic lithium atoms*, Opt. Lett. **26.**, 1837–1839 (2001). DOI: 10.1364/OL.26.001837.

[168] Raj, R. K., D. Bloch, J. J. Snyder, G. Camy, and M. Ducloy. *High-Frequency Optically Heterodyned Saturation Spectroscopy Via Resonant Degenerate Four-Wave Mixing*, Phys. Rev. Lett. **44**, 1251–1254 (1980). DOI: 10.1103/PhysRevLett.44.1251.

[169] Drever, R., J. L. Hall, F. Kowalski, J. Hough, G. Ford, A. Munley, and H. Ward. *Laser phase and frequency stabilization using an optical resonator*, Applied Physics B **31.**, 97–105 (1983).

[170] Haindl, R. "A Clock Laser System for Quantum Simulations with Ultracold Strontium Atoms". MA thesis. Ludwig Maximilians Universität München, 2019.

[171] Thorpe, J. I., K. Numata, and J. Livas. *Laser frequency stabilization and control through offset sideband locking to optical cavities*, Optics express **16.**, 15980–15990 (2008). DOI: 10.1364/OE.16.015980.

[172] Lewandowski, H. J., D. M. Harber, D. L. Whitaker, and E. A. Cornell. *Observation of Anomalous Spin-State Segregation in a Trapped Ultracold Vapor*, Phys. Rev. Lett. **88**, 070403 (2002). DOI: 10.1103/PhysRevLett.88.070403.

[173] Pertot, D., D. Greif, S. Albert, B. Gadway, and D. Schneble. *Versatile transporter apparatus for experiments with optically trapped Bose–Einstein condensates*, Journal of Physics B: Atomic, Molecular and Optical Physics **42.**, 215305 (2009). DOI: 10.1088/0953-4075/42/21/215305.

[174] Greiner, M. "Ultracold quantum gases in three-dimensional optical lattice potentials". PhD thesis. Ludwig Maximilians Universität München, 2003.

[175] Omran, A. "A microscope for Fermi gases". PhD thesis. Ludwig Maximilians Universität München, 2016.

[176] Léonard, J., M. Lee, A. Morales, T. M. Karg, T. Esslinger, and T. Donner. *Optical transport and manipulation of an ultracold atomic cloud using focus-tunable lenses*, New Journal of Physics **16.**, 093028 (2014). DOI: 10.1088/1367-2630/16/9/093028.

[177] Schmid, S., G. Thalhammer, K. Winkler, F. Lang, and J. H. Denschlag. *Long distance transport of ultracold atoms using a 1D optical lattice*, New Journal of Physics **8.**, 159–159 (2006). DOI: 10.1088/1367-2630/8/8/159.

[178] Klostermann, T., C. R. Cabrera, H. von Raven, J. F. Wienand, C. Schweizer, I. Bloch, and M. Aidelsburger. *Fast long-distance transport of cold cesium atoms*, Physical Review A **105**. (Apr. 2022). DOI: 10.1103/physreva.105.043319.

[179] Bao, Y., S. S. Yu, L. Anderegg, S. Burchesky, D. Gonzalez-Acevedo, E. Chae, W. Ketterle, K.-K. Ni, and J. M. Doyle. *Fast optical transport of ultracold molecules over long distances*, (2022). DOI: 10.48550/ARXIV.2205.06334.

[180] Peik, E., M. Ben Dahan, I. Bouchoule, Y. Castin, and C. Salomon. *Bloch oscillations of atoms, adiabatic rapid passage, and monokinetic atomic beams*, Phys. Rev. A **55**, 2989–3001 (1997). DOI: 10.1103/PhysRevA.55.2989.

[181] Traverso, A., R. Chakraborty, Y. N. Martinez de Escobar, P. G. Mickelson, S. B. Nagel, M. Yan, and T. C. Killian. *Inelastic and elastic collision rates for triplet states of ultracold strontium*, Phys. Rev. A **79**, 060702 (2009). DOI: 10.1103/PhysRevA.79.060702.

[182] Kokoouline, V., R. Santra, and C. H. Greene. *Multichannel cold collisions between metastable Sr atoms*, Physical Review Letters **90**., 253201 (2003).

[183] Blatt, S., J. W. Thomsen, G. K. Campbell, A. D. Ludlow, M. D. Swallows, M. J. Martin, M. M. Boyd, and J. Ye. *Rabi spectroscopy and excitation inhomogeneity in a one-dimensional optical lattice clock*, Phys. Rev. A **80**, 052703 (2009). DOI: 10.1103/PhysRevA.80.052703.

[184] Dicke, R. H. *The Effect of Collisions upon the Doppler Width of Spectral Lines*, Phys. Rev. **89**, 472–473 (1953). DOI: 10.1103/PhysRev.89.472.

[185] Leibfried, D., R. Blatt, C. Monroe, and D. Wineland. *Quantum dynamics of single trapped ions*, Rev. Mod. Phys. **75**, 281–324 (2003). DOI: 10.1103/RevModPhys.75.281.

[186] Wineland, D. J. and W. M. Itano. *Laser cooling of atoms*, Phys. Rev. A **20**, 1521–1540 (1979). DOI: 10.1103/PhysRevA.20.1521.

[187] McDonald, M., B. H. McGuyer, G. Z. Iwata, and T. Zelevinsky. *Thermometry via Light Shifts in Optical Lattices*, Phys. Rev. Lett. **114**, 023001 (2015). DOI: 10.1103/PhysRevLett.114.023001.

[188] Miyake, H., N. C. Pisenti, P. K. Elgee, A. Sitaram, and G. K. Campbell. *Isotope-shift spectroscopy of the* $^1S_0 \rightarrow^3 P_1$ *and* $^1S_0 \rightarrow^3 P_0$ *transitions in strontium*, Phys. Rev. Research **1**, 033113 (2019). DOI: 10.1103/PhysRevResearch.1.033113.

[189] Iwata, Y., D. Cheon, M. Miyabe, and S. Hasegawa. *Spectroscopic analysis of radioactive strontium with low isotopic abundance using laser resonance ionization*, Hyperfine Interactions **241**., 1–8 (2020). DOI: 10.1007/s10751-020-1700-x.

[190] Iwata, Y., M. Miyabe, K. Akaoka, and I. Wakaida. *Isotope shift and hyperfine structure measurements on triple resonance excitation to the autoionizing Rydberg state of atomic strontium*, Journal of Quantitative Spectroscopy and Radiative Transfer **275**, 107882 (2021). DOI: https://doi.org/10.1016/j.jqsrt.2021.107882.

[191] Stellmer, S. and F. Schreck. *Reservoir spectroscopy of* $5s5p\ ^3P_2$–$5snd\ ^3D_{1,2,3}$ *transitions in strontium*, Phys. Rev. A **90**, 022512 (2014). DOI: 10.1103/PhysRevA.90.022512.

[192] Born, M. and E. Wolf. *Principles of Optics: Electromagnetic Theory of Propagation, Interference and Diffraction of Light*. Elsevier, 2013.

[193] Flambaum, V. and V. Dzuba. *Search for variation of the fundamental constants in atomic, molecular, and nuclear spectra*, Canadian Journal of Physics **87**., 25–33 (2009).

[194] Lea, S. N. *Limits to time variation of fundamental constants from comparisons of atomic frequency standards*, Reports on Progress in Physics **70**., 1473–1523 (2007). DOI: 10.1088/0034-4885/70/9/r01.

[195] Dzuba, V. A., V. V. Flambaum, and S. Schiller. *Testing physics beyond the standard model through additional clock transitions in neutral ytterbium*, Physical Review A **98**. (2018). DOI: 10.1103/physreva.98.022501.

[196] Bhongale, S. G., L. Mathey, E. Zhao, S. F. Yelin, and M. Lemeshko. *Quantum Phases of Quadrupolar Fermi Gases in Optical Lattices*, Phys. Rev. Lett. **110**, 155301 (2013). DOI: 10.1103/PhysRevLett.110.155301.

[197] Huang, W.-M., M. Lahrz, and L. Mathey. *Quantum phases of quadrupolar Fermi gases in coupled one-dimensional systems*, Phys. Rev. A **89**, 013604 (2014). DOI: 10.1103/PhysRevA.89.013604.

[198] Stewart, M., J. Kwon, A. Lanuza, and D. Schneble. *Dynamics of matter-wave quantum emitters in a structured vacuum*, Phys. Rev. Research **2**, 043307 (2020). DOI: 10.1103/PhysRevResearch.2.043307.

[199] Hood, J. D., A. Goban, A. Asenjo-Garcia, M. Lu, S.-P. Yu, D. E. Chang, and H. Kimble. *Atom–atom interactions around the band edge of a photonic crystal waveguide*, Proceedings of the National Academy of Sciences **113**., 10507–10512 (2016). DOI: 10.1073/pnas.1603788113.

[200] Daley, A. J., I. Bloch, C. Kokail, S. Flannigan, N. Pearson, M. Troyer, and P. Zoller. *Practical quantum advantage in quantum simulation*, Nature **607**., 667–676 (2022). DOI: 10.1038/s41586-022-04940-6.

[201] Argüello-Luengo, J., A. González-Tudela, T. Shi, P. Zoller, and J. I. Cirac. *Analogue quantum chemistry simulation*, Nature **574**., 215–218 (2019). DOI: 10.1038/s41586-019-1614-4.

[202] Zhou, L., S.-T. Wang, S. Choi, H. Pichler, and M. D. Lukin. *Quantum Approximate Optimization Algorithm: Performance, Mechanism, and Implementation on Near-Term Devices*, Phys. Rev. X **10**, 021067 (2020). DOI: 10.1103/PhysRevX.10.021067.

[203] Huang, H.-Y., M. Broughton, J. Cotler, S. Chen, J. Li, M. Mohseni, H. Neven, R. Babbush, R. Kueng, J. Preskill, *et al. Quantum advantage in learning from experiments*, Science **376**., 1182–1186 (2022). DOI: 10.1126/science.abn7293.

[204] Biamonte, J., P. Wittek, N. Pancotti, P. Rebentrost, N. Wiebe, and S. Lloyd. *Quantum machine learning*, Nature **549**., 195–202 (2017). DOI: 10.1038/nature23474.

Acknowledgements

I would like to thank the many people who supported and guided me during my years as a Ph.D. student. Without them, this work would not have been possible. The following list is non-exhaustive and is in no particular order.

First and foremost, I want to thank our team leader Sebastian Blatt. During the last four years, he shared his wide range of knowledge with me. His knowledge, reaching from physics to computer science and electronics, showed me daily how many more exciting things there are to learn. He always had an open door to discuss physics and the many technical details of the experiments. He helped me to develop a more efficient working style and taught me how to simplify even challenging problems. I am extremely grateful that he calmed me down when things did not work out as planned and for his constant support.

Equally, I want to acknowledge Immanuel Bloch for granting me the opportunity to work in his research group with many fascinating and challenging experiments, where people are always willing to help and discuss. During our regular meetings, he helped us to stay on track to reach our bigger goals and not get lost in details. His enthusiasm and intuition about physics were always exciting and inspired me. He was always aware of what was going on in the experiments and provided solutions for technical challenges.

Special thanks go to my colleagues and friends Valentin Klüsener and Dimitry Yankelev. Working with them in the lab to constantly improve the machine and take data was fun, and I would not want to miss that time. While writing this thesis, they took over the machine and pushed its limits further. They did a great job achieving the first site-resolved images of strontium atoms. I really enjoyed discussing physics with them and various not-lab-related topics during lunch. As soon as he joined our team, Dimitry tremendously improved our ImageViewer to make it way more user-friendly. His good intuition about physics helped me so much to find bugs in my calculations. Valentin helped me a lot in upgrading the machine and keeping the laser running while taking data. His compensation coils around the experiment table are an attraction for most visitors. I was amazed at how calm and focused he could stay even when things did go very wrong in the lab. I also want to thank him that he took care of our Master's and intern students during the last year.

I would also like to thank my former colleagues André Heinz and Annie park, who became good friends. After I started in the lab, they introduced me to everybody and showed me how to work efficiently in the lab. André and I spent many hours in a dark lab characterizing the crossed-cavities, where he answered all my questions about cavities and optics. I really enjoyed working with him and the many times we met to get food in the city. Annie taught me everything about running the machine and how to debug it properly if anything goes wrong. I highly appreciated our discussions about physics and

research in general.

I also thank our Master's and intern students in recent years: Rudi Haindl, Etienne Staub, Florian Wallner, Eva Casotti, Dimitrios Tsevas, Yilong Yang, Romain Grainer, Soham Mukherjee, Christian Skinker, Luca Göcke, Ömer Ersahan, Andrew Whimstre, and Andreas Meyer. Each of them contributed to pushing the experiment forward by developing lab equipment and helping to complete various projects.

I would like to acknowledge the technical engineering team at MPQ. I want to thank Anton Mayer, who helped me with all the mechanical designs and actually made them useful. He also provided solutions within an amazingly short time if I faced urgent mechanical problems, such as producing a mount for a microscope to check the damaged surface of our viewport. Karsten Förster developed many important electronics for our lab. He also helped debug various electronic circuits. I also thank him for his ideas and effort in designing the control loop to stabilize the high current of the magnetic field coils. In addition, I would like to thank Olivia Mödel for debugging and fixing various circuits and instruments.

I highly appreciated the help and support of Kristina Schuldt, Doreen Seidl, and Ildiko Kecskesi. They organized many group activities and took care of all administrative-related work, guiding me through the jungle of bureaucracy.

I want to thank all the group members for sharing their ideas and enthusiasm about physics. The attitude to help whenever somebody needs it makes the group a great place to be. I would like to name a few in particular, but in no particular order: Marcel Duda, Roman Bause, Simon Hollerith, Pascal Weckesser, Sarah Hirthe, Dominik Bourgund, Nikolaus Lorenz, Lea Steinert and Philip Osterholz. They all made my time in Munich enjoyable.

A big thanks go to Sebastian Blatt, Valentin Klüsener, Annie Park, Dimitry Yankelev, Pascal Weckesser and Paul Wittmer for proofreading of my thesis.

Thanks to all my friends and family who supported me during my Ph.D. and for their patience. Without them, this work would not have been possible. I want to thank Paul Wittmer for his friendship and weekly phone calls that helped to calm me down when things went wrong. I also want to thank my friends from my home town for all the fun moments whenever we met. I thank my family: Monika, Dieter, Eva, Andreas, and Marie for their support and understanding. A special thanks go to Sarah for the countless help that cannot be described in words. Her patience and understanding gave me strength even in tough times. Most importantly, I thank her for the wonderful time we spent together.